Lecture Notes in Networks and Systems 1040

Marcelo Zambrano Vizuete ·
Miguel Botto-Tobar ·
Sonia Casillas · Carina Gonzalez ·
Carlos Sánchez · Gabriel Gomes ·
Benjamin Durakovic *Editors*

Innovation and Research – Smart Technologies & Systems

Proceedings of the CI3 2023, Volume 1

Springer

Lecture Notes in Networks and Systems 1040

The series “Lecture Notes in Networks and Systems” publishes the latest developments in Networks and Systems—quickly, informally and with high quality. Original research reported in proceedings and post-proceedings represents the core of LNNS.

Volumes published in LNNS embrace all aspects and subfields of, as well as new challenges in, Networks and Systems.

The series contains proceedings and edited volumes in systems and networks, spanning the areas of Cyber-Physical Systems, Autonomous Systems, Sensor Networks, Control Systems, Energy Systems, Automotive Systems, Biological Systems, Vehicular Networking and Connected Vehicles, Aerospace Systems, Automation, Manufacturing, Smart Grids, Nonlinear Systems, Power Systems, Robotics, Social Systems, Economic Systems and other. Of particular value to both the contributors and the readership are the short publication timeframe and the world-wide distribution and exposure which enable both a wide and rapid dissemination of research output.

The series covers the theory, applications, and perspectives on the state of the art and future developments relevant to systems and networks, decision making, control, complex processes and related areas, as embedded in the fields of interdisciplinary and applied sciences, engineering, computer science, physics, economics, social, and life sciences, as well as the paradigms and methodologies behind them.

Indexed by SCOPUS, INSPEC, WTI Frankfurt eG, zbMATH, SCImago.

All books published in the series are submitted for consideration in Web of Science.

For proposals from Asia please contact Aninda Bose (aninda.bose@springer.com).

Marcelo Zambrano Vizuete ·
Miguel Botto-Tobar · Sonia Casillas ·
Carina Gonzalez · Carlos Sánchez ·
Gabriel Gomes · Benjamin Durakovic
Editors

Innovation and Research – Smart Technologies & Systems

Proceedings of the CI3 2023, Volume 1

Springer

Editors
Marcelo Zambrano Vizuete
Instituto Tecnológico Superior Rumiñah
Sangolquí, Ecuador

Miguel Botto-Tobar
Eindhoven University of Technology
Eindhoven, The Netherlands

Sonia Casillas
universidad de salamanca
Salamanca, Spain

Carina Gonzalez
Universidad de La Laguna
Tenerife, Spain

Carlos Sánchez
Universidad de Zaragoza
Zaragoza, Spain

Gabriel Gomes
Universidad Estatal de Campinas
Campinas, Brazil

Benjamin Durakovic
International University of Sarajevo
Sarajevo, Bosnia and Herzegovina

ISSN 2367-3370 ISSN 2367-3389 (electronic)
Lecture Notes in Networks and Systems
ISBN 978-3-031-63433-8 ISBN 978-3-031-63434-5 (eBook)
https://doi.org/10.1007/978-3-031-63434-5

This Springer imprint is published by the registered company Springer Nature Switzerland AG
The registered company address is: Gewerbestrasse 11, 6330 Cham, Switzerland

Preface

The 4th edition of the International Research and Innovation Congress – Smart Technologies and Systems, CI3 2023, took place from August 30 to September 1, 2023, at the facilities of the Instituto Tecnológico Universitario Rumiñahui, located in the city of SangolquÍ, Pichincha, Ecuador.

The conference was organized by the Red de Investigación, Innovación y Transferencia de Tecnología RIT2, made up of the most relevant university institutes in Ecuador, among which are ITCA, BOLIVARIANO, ARGOS, VIDA NUEVA, ESPÍRITU SANTO, SUDAMERICANO, ISMAC, SAN ISIDRO, ARTES GRÁFICAS, ORIENTE, HUMANE, SUCRE, CENTRAL TÉCNICO, POLICÍA NACIONAL and RUMIÑAHUI.

Additionally, the event is sponsored by the Secretaría de Educación Superior, Ciencia, Tecnología e Innovación SENESCYT, Labortorio de Comunicación Visual de la Universidad Estatal de Campinas—Brazil, Universidad Ana G. Méndez—Puerto Rico, Centro de Investigaciones Psicopedagógicas y Sociológicas—Cuba, Instituto Superior de Diseño de la Universidad de La Habana—Cuba, GDEON and the Corporación Ecuatoriana para el Desarrollo de la Investigación y la Academia—CEDIA.

The main objective of CI3 2023 is to generate a space for dissemination and collaboration, where academia, industry and government can share their ideas, experiences and results of their projects and research.

"Research as a pillar of higher education and business improvement" is the motto of the Conference and suggests how research, innovation and academia must coincide with the productive sector to leverage social and economic development.

CI3 2023 had 145 papers submitted, of which 52 were accepted for publication and presentation. To guarantee the quality of the publications, the event has a staff of more than 70 experts, from different countries such as Spain, Argentina, Chile, Mexico, Peru, Brazil, Ecuador, among others, who carry out an exhaustive review of each proposal sent.

Likewise, during the event a series of keynote conferences were held, given by both national and international experts, allowing attendees to get in touch with the latest trends and technological advances around the world. Keynote speakers included: Ph.D. Carina González, University of La Laguna, Spain; Ph.D. Gabriel Gómez, State University of Campinas, Brazil; Ph.D. Carlos Sanchez, University of Zaragoza, Spain; Ph.D. Juan Minango, Instituto Tecnológico Superior Rumiñahui; Dr. Iván Cherrez, Universidad Espíritu Santo, Ecuador; and Ph.D. Nela Paustizaca, Escuela Politécnica del Litoral, Ecuador.

The content of this proceeding is related to the following topics:

- Smart Cities
- Innovation and Development
- Applied Technologies
- Economics and Management
- ICT for Educations.

Organization

General Chairs

Marcelo Zambrano Vizuete	Instituto Tecnológico Universitario Rumiñahui, Ecuador

Organizing Committee

Marcelo Zambrano Vizuete	Instituto Tecnológico Universitario Rumiñahui, Ecuador
Miguel Botto-Tobar	Eindhoven University of Technology, The Netherlands
Sonia Casillas	Universidad de Salamanca, Spain
Carina Gonzales	Universidad de La Laguna, Spain
Carlos Sánchez	Universidad de Zaragoza, Spain
Gabriel Gomes	Universidad Estatal de Campinas, Brazil
Benjamin Durakovic	International University of Sarajevo, Bosnia and Herzegovina

Steering Committee

Marcelo Zambrano	Instituto Tecnológico Superior Rumiñahui, Ecuador
Miguel Botto	Eindhoven University of Technology, The Netherlands
Karla Ayala	Instituto Tecnológico Superior Rumiñahui, Ecuador
Xavier Duque	Instituto Tecnológico Superior Rumiñahui, Ecuador
Ernesto Huerta	Instituto Tecnológico Superior Rumiñahui, Ecuador
Carmita Suárez	Instituto Tecnológico Superior Rumiñahui, Ecuador
Maritza Salazar	Instituto Superior Tecnológico Espíritu Santo, Ecuador
Wilfrido Robalino	Instituto Superior Tecnológico Vida Nueva, Ecuador

Roberto Tolozano	Instituto Superior Tecnológico Bolivariano, Ecuador
Carlos Pérez	Instituto Tecnológico Sudamericano, Ecuador
Alicia Soto	Instituto Superior Tecnológico ITCA, Ecuador
Lorena Ávila	Instituto Superior Tecnológico Policía Nacional, Ecuador
Denis Calvache	Instituto Superior Tecnológico ISMAC, Ecuador
Efraín Paredes	Instituto Superior Tecnológico IGAD, Ecuador
Paola Vasconez	Instituto Superior Tecnológico Oriente, Ecuador
Sandra El Khori	Instituto Superior Tecnológico San Isidro, Ecuador
Santiago Illescas	Instituto Superior Tecnológico Sucre, Ecuador
Jorge Calderón	Instituto Superior Tecnológico Argos, Ecuador
Trotsky Corella	Instituto Superior Tecnológico Central Técnico, Ecuador
Javier García	Instituto Superior Tecnológico Humane, Ecuador
Sandra Salazar	Instituto Superior Tecnológico American College, Ecuador
David Flores	Instituto Superior Tecnológico Cordillera, Ecuador
Marcelo Aguilera	Instituto Superior Tecnológico del Azuay, Ecuador

Program Committee

Carina González	Universidad de La Laguna, Spain
Carlos Sánchez	Universidad de Zaragoza, Spain
Sergey Balandin	Universidad de Helsinki, Finland
Silva Ganesh Malla	SKR Engineering College, India
Alberto Ochoa	Universidad Autónoma Ciudad de Juárez, Mexico
Antonio Orizaga	Universidad de Guadalajara, Mexico
Rocío Maciel	Universidad de Guadalajara, Mexico
Víctor Larios	Universidad de Guadalajara, Mexico
Yorberth Montes	Universidad de Zulia, Venezuela
Juan Minango	Universidad Estatal de Campinas, Brazil
Francisco Pérez	Universidad Politécnica de Valencia, Spain
Víctor Garrido	Universidad Politécnica de Valencia, Spain
Alberto García	Universidad Politécnica de Valencia, Spain
Javier Hingant	Universidad Politécnica de Valencia, Spain
Javier Prado	Universidad Técnica Federico Santa María, Chile
Marco Heredia	Universidad Politécnica de Madrid, Spain

Diego Paredes	Universidad de Zaragoza, Spain
Angela Cadena	Universitat de Valencia, Spain
Sonia Casillas	Universidad de Salamanca, Spain
Marco Cabezas	Universidad de Salamanca, Spain
Francesc Wilhelmi	Centre Tecnològic de Telecomunicacions de Catalunya, Spain
Santiago Vidal	Universidad Nacional Del Centro de la Provincia de Buenos Aires, Argentina
Adailton Antônio Galiza Nunes	Universidad Estatal de Campinas, Brazil
Leandro Bezerra De Lima	Universidad Federal de Mato Grosso Do Sul, Brazil
Andrea Carolina Flores	Embraer Defensa y Seguridad, Brazil
Elmer Levano Huamacto	Universidad Federal Do Parana, Brazil
Ari Lazzarotti	Universidad Federal de Goiás, Brazil
Ellen Synthia Fernandes de Oliveira	Universidad Federal de Goiás, Brazil
Fernanda Cruvinel Pimentel	Universidad Federal de Goiás, Brazil
Yuzo Lanoi	Universidad Estatal de Campinas, Brazil
Gabriel Gómez	Universidad Estatal de Campinas, Brazil
Pablo Minango	Universidad Estatal de Campinas, Brazil
Benjamin Durakovic	International University of Sarajevo, Bosnia and Herzegovina
Jhonny Barrera	Universidad Nacional de La Plata, Argentina
Daniel Ripalda	Universidad Nacional de La Plata, Argentina
Alonso Estrada Cuzcano	Universidad Nacional Mayor de San Marcos, Peru
Marcelo Zambrano	Instituto Tecnológico Superior Rumiñahui, Ecuador
Ana Zambrano	Escuela Politécnica Nacional, Ecuador
Angel Jaramillo	Universidad de las Américas, Ecuador
Ángela Cadena	Universidad de Guayaquil, Ecuador
Oscar Leon	Universidad de Guayaquil, Ecuador
Wladimir Paredes	Consejo de Aseguramiento de la Calidad de la Educación Superior, Ecuador
Miguel Angel Zúñiga	Universidad de Cuenca, Ecuador
Alex Santamaría	Universidad Laica Eloy Alfaro, Ecuador
Fabián Sáenz	Universidad de las Fuerzas Armadas ESPE, Ecuador
Darwin Aguilar	Universidad de las Fuerzas Armadas ESPE, Ecuador
Sergio Montes	Universidad de Las Fuerzas Armadas Espe, Ecuador
Jhenny Cayambe	Pontificia Universidad Católica del Ecuador Sede Ibarra, Ecuador

Santiago Ushiña	Likatelec, Ecuador
Raisa Bernal	Instituto Tecnológico Superior Rumiñahui, Ecuador
Aníbal Altamirano	Universidad de las Fuerzas Armadas ESPE, Ecuador
Moisés Toapanta	Universidad Católica Santiago de Guayaquil, Ecuador
Ricardo Rosero	Instituto Tecnológico Superior Rumiñahui, Ecuador
Danny De La Cruz	Universidad de las Fuerzas Armadas ESPE, Ecuador
Johana Tobar Quevedo	Universidad de las Fuerzas Armadas ESPE, Ecuador
Jhony Caucha	Universidad Nacional de Tumbes, Peru
Mariana Lima Bandeira	Universidad Andina Simón Bolívar, Ecuador
Norma Molina	Universidad Israel, Ecuador
Elfio Pérez	Universidad Indoamérica, Ecuador
Cristian Tasiguano	Instituto Superior San Antonio, Ecuador
Lizbeth Suarez Morales	Instituto Superior Vida Nueva, Ecuador
Carlos Ruiz	Instituto Superior Vida Nueva, Ecuador
Wilfrido Robalino	Instituto Superior Vida Nueva, Ecuador
William Venegas	Escuela Politécnica Nacional, Ecuador
César Ayabaca	Escuela Politécnica Nacional, Ecuador
Dario Morales	Instituto Superior Vida Nueva, Ecuador
Pamela Villareal	Instituto Superior Vida Nueva, Ecuador
Darwin Tituaña	Instituto Superior Vida Nueva, Ecuador
Ismenia Araujo	Instituto Superior José Chiriboga Grijalva, Ecuador
Luz Marina Rodríguez	Instituto Superior José Chiriboga Grijalva, Ecuador
Luis Alzate	Instituto Superior Bolivariano, Ecuador
Noemi Delgado	Instituto Superior Bolivariano, Ecuador
Marítza Salazar	Instituto Superior Espíritu Santo, Ecuador
Martha Fernández	Instituto Superior Espíritu Santo, Ecuador
Néstor Xavier Maya Izurieta	Instituto Superior Central Técnico, Ecuador
Michael Enrique Carrión Garzón	Instituto Superior Central Técnico, Ecuador
Nela Pastuizaca	Escuela Politécnica del Litoral, Ecuador
Marcelo Flores	Universidad Politécnica Salesiana, Ecuador
Diego Vizuete	Instituto Superior Sucre, Ecuador
Edgar Maya	Universidad Técnica del Norte, Ecuador
Mauricio Domínguez	Universidad Técnica del Norte, Ecuador
Fabián Cuzme	Universidad Técnica del Norte, Ecuador

Contents

Smart Cities

IoT Applied to Improve Production Controls in the Ecuadorian Floriculture Sector

Claudio Arcos[1](✉), Pablo Calvache[2], and Ricardo Calderón[3]

[1] San Francisco Global Foundation and ISMAC Technological Institute, Quito, Ecuador
claudioarcos@sanfranciscoglobal.org
[2] ISMAC Technological Institute, Quito, Ecuador
[3] World Roses Center Farm, Tabacundo, Ecuador

Abstract. For the development of this study, the internet of things IoT concept was used, in the context of which a network of sensors was deployed within a rose crop that is planted in an area of 30,000 m^2, which are covered under greenhouses. The crop is located at 2,900 m above sea level and, for a year and a half, humidity data, dew point data, temperature data and vapor pressure deficit VPD data were collected with the use of the sensor network. in such a way that a database of more than 49 million data was obtained that was used to contrast and analyze the data collected in the same period related to diseases and pests that can occur in rose production. The results show that there are levels of correlation that allow determining mechanisms for measuring environmental conditions in production to improve efficiency and effectiveness in the decision-making process for better crop management.

Keywords: IoT · Digital transformation · Precision agriculture

1 Introduction

Between the years 2018 and 2022, Ecuador exported 20.46% of a total of USD$15,850′580,000.00 of the fresh cut roses product, thus becoming the second most exporting country of this product during that period, below the Netherlands and above Columbia [1].

In this context, rose crops in Ecuador must implement control technologies in productive management to meet local and international demands in various areas. The phytosanitary field is one of the areas whose management, adequate or not, positively or negatively affects access to international markets, compliance with local controls, quality improvement and waste reduction.

The fact is that damage to the rose plant can occur in different ways. The main damage is caused by pests such as thrips and mites or diseases such as botrytis, powdery mildew and downy.

In this sense, the concept of precision agriculture is transcendental to implement mechanisms that favor the control and management of potential effects on plants. In this context, it is important to first understand what IoT is as a mechanism to promote precision agriculture in rose production, and secondly what are the main diseases and pests that affect the cultivation of roses.

M. Z. Vizuete et al. (Eds.): CI3 2023, LNNS 1040, pp. 3–17, 2024.
https://doi.org/10.1007/978-3-031-63434-5_1

1.1 IoT as a Mechanism to Promote Precision Agriculture in Rose Production

At present, the domain of agriculture results from the application of methods that, by using technological instruments, allow the improvement of traditional cultivation methods in the areas that are possible [2].

The fact is that knowledge-intensive solutions such as the use of sensors, drones, automated irrigation systems, real-time monitoring, timed disinfection, etc., make it possible to enhance the organization's resource and capacity management and favor productivity, efficiency, control of pests and diseases, quality of the final product and competitive access to markets, mainly.

For this reason, farmers are constantly looking for mechanisms to manage the risks of climate change. In this context, the Internet of Things, known as IoT, is a technological evolution that provides access to data, information and services of the activities in which it is applied, through intelligent networks that deliver data in real time [3].

The IoT applied to agriculture can improve several processes, because with better information it is possible to deploy actions to sustain the quality of the product during the production process and thus satisfy customer requirements [4].

In the flower sector, with the application of sensors within the IoT concept, it is possible to know what is happening with the production processes in terms of their incidence environment. In other words, in order to maintain optimal growth and development conditions for rose plants inside a greenhouse, it is necessary to control and manage, among other things, the temperature, humidity, vapor pressure deficit and the dew point within the crop environment [5].

The use of IoT technology can simplify this management by obtaining data from said measurements in real time and, with the analysis of these data, favor decision-making for the good of the production process, as well as the management and control of pests and diseases.

The diffusion of these technologies for the improvement of competitiveness in the flower sector of Ecuador is essential. This is because it has been shown that the presence of innovation activities depends on the execution of various skills within the organization, and its innovative approach is stimulated by mastering a portfolio of technological skills from which they are carried out. R&D activities and, if digital transformation and absorption are not promoted, innovation will not happen [6].

1.2 Diseases and Pests that Affect the Cultivation of Roses

Mainly: the development of cultural practices, adequate air circulation, correct protection of the growing area and irrigation, help prevent and control diseases and pests [7], This, plus the productive capacities of the peasants, which include their traditional and ancestral knowledge on sowing and harvesting mechanisms and practices, have contributed to the development of the flower sector in Ecuador [8].

Additionally, there are organic and chemical treatments to manage pests and diseases, mainly pests such as thrips and mites or diseases such as botrytis, powdery mildew and downy [9–11].

As for pests, thrips are small insects that feed on the petals and cause cosmetic damage to the flower. For their part, the mites that affect roses are sap suckers, therefore, they feed on the sap of the leaves, causing them to turn yellow and dry.

Among the most common diseases are: botrytis, which is a fungal disease that generates brown spots mainly on the petals. Powdery mildew is also a fungal disease that consists of the appearance of a white coating mainly on the leaves and stems, the same that is similar to dust on the leaves, buds and stems. For its part, downy is another fungal disease characterized by the appearance of reddish or orange pustules on the underside of the leaves [12].

The different affectations can cause decomposition of the flower, premature wilting, weakness of the plant, disorder of the growth cycle, deformations, premature fall of the leaves, affectation of the photosynthesis process; all of this decreases the quality of the flowers, reduces their life time in the vase, and therefore decreases the competitiveness of the final product, with the consequent loss of the export market.

The control of environmental conditions inside the greenhouse facilitates decision-making regarding agricultural activities as well as the application of fungicides to protect the health of plants. The fact is that both pests and diseases are the result of poor production management in the face of changing environmental conditions that favor the appearance of pests and diseases, mainly temperature, humidity, vapor pressure deficit and the dew point.

2 Materials and Methods

2.1 Database and Variables

For the development of the study, five sensors were installed on June 25, 2021, the same ones that were distributed in 30,000 m^2 of a rose farm located in Tabacundo - Ecuador, at 2,900 m above sea level.

The sensors used are dataloggers that record and store the data in their internal memory, and transmit it in real time through the internet or it can be downloaded via Bluetooth. For the present study, the data was obtained by the transmission via the internet to a PC.

The characteristics of the sensors are:

- Wireless access to data.
- The recorded data can be downloaded but cannot be edited.
- It has user-configurable alerts.
- Unlimited number of users that can monitor the same sensor.
- Connection to a portal to monitor in real time through a mobile application that allows the storage and download of data in CSV format.
- Measures temperature ranges from −40 °C to +60 °C.
- Measures relative humidity ranges from 0% to 100% (prolonged exposure to >80% can create a lag of up to +3% in readings, this effect gradually reverses after returning to < 80% conditions).
- Temperature accuracy (0 °C to 60 °C): +−0.3 °C typical, +−0.5 °C maximum.
- Temperature Accuracy (full range): +−0.7 °C typical, +−1.2 °C maximum.
- Humidity Accuracy (@25 °C, 20% to 80%): +−3% typical, +−4.5% maximum.
- Humidity Accuracy (@25 ºC, 0% to 100%): +−4.5% typical, +−7.5% maximum.

- Signal range: 100 m in line of sight. It is greater with the use of an amplifying antenna that increases the coverage radius to connect the sensor signal to a router.
- Battery: CR2477 × 1.3 V (duration of one year approximately).
- Dimensions: 40 × 40 × 16.5 mm.
- Weight: 40 gr.
- Compatibility: iOS 8+, Android 4.3+, Bluetooth 4.0+

Each sensor obtains data on temperature, humidity, vapor pressure deficit, and dew point. Sensors are IoT technology that record, store, and transmit data over the Internet in real time to one or more terminals with Android or iOS systems. The network architecture is shown below (see Fig. 1).

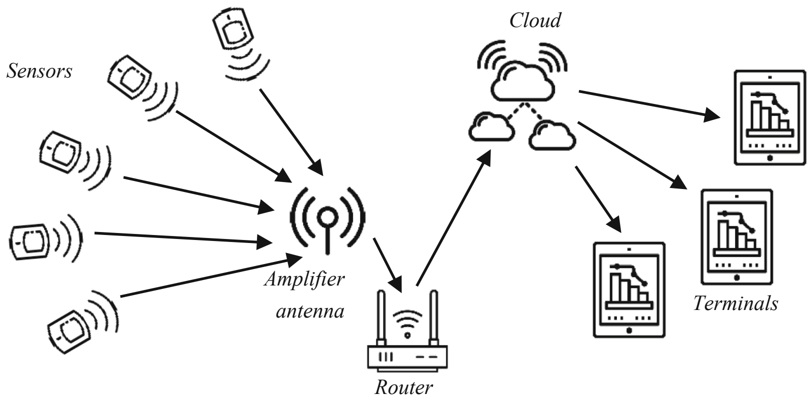

Fig. 1. Network architecture. Source: direct investigation.

Once the sensors were distributed, an amplifying antenna was fixed in the center of the five sensors at a distance of approximately 100 m from each sensor to the antenna. The antenna was connected to a router with internet access via a network cable. The router receives and transmits the data in real time to any terminal that has installed access to the information transmitted by the five sensors.

The data is permanently displayed in the sensors' own software, which allows all the data to be downloaded in CSV format. The databases constitute structured repositories with observations managed by storage systems and software packages of the sensors. In this sense, to obtain the data under study, observations collected from June 25, 2021 at 12:40 p.m. to January 19, 2023 at 5:40 p.m. were considered.

The database consists of minute-by-minute observations of four readings: temperature, relative humidity, vapor pressure deficit (VPD) and dew point, within the crop environment, obtaining the following observations and data:

- Block 1 database: 825,421 observations and 9,905,064 data
- Block 2 database: 825,407 observations and 9,904,884 data
- Block 3 database: 825,411 observations and 9,904,932 data
- Block 4 database: 825,411 observations and 9,904,932 data

- Block 5 database: 825,414 observations and 9,904,968 data

In order to compare the measurements of the five sensors with the state of the plants, the postharvest database of the company participating in the study was used. Said database stores daily information on harvest about production for exporting and discarded production. Discarded production is the number of stems discarded by pests and/or diseases caused in the rose, which go through the composting process because they do not comply with quality parameters for export. Within the discarded production, the different causes analyzed in this study are recorded, such as: in pests: mites and thrips; in diseases: botrytis, downy and powdery mildew. In the same way, the period of time considered for the analysis of the post-harvest database is from June 25, 2021 to January 19, 2023, obtaining the following observations and data:

- Postharvest database: 289,270 observations and 5,785,400 data

Since in Ecuador there are critical points in the productive systems, such as the precariousness of governance and management capacity [13], it is essential to consider that the determining factors of innovation in organizations include the adoption of digital transformation tools, understanding this action as the acquisition or absorption of innovation.

Therefore, demonstrating the application of a system based on IoT to improve production from the implementation of innovation solutions stimulates the mastery of technological skills as determinants of innovation [6].

In this sense, it is understood that the IoT applied acts as a catalyst for innovation, for which the question for this research is: how to improve efficiency in the Ecuadorian floriculture sector using IoT?

3 Results

Prior to the statistical analysis of the databases, these were refined and organized, disaggregating the date and time data as individual variables, to facilitate the grouping of data in intervals by hours, days, weeks, quarters, and years; and the days June 25, 2021 and January 19, 2023 were discarded as they did not have the total number of observations on those days.

To treat the database, a very important criterion for the study was incorporated, such as solar luminosity, so that the observations were grouped considering the sunrise from 6:00 a.m., and the sunset at 6:00 p.m., as well as the highest point (zenith) 12:00 pm. Therefore, a weighted average of four indicators per day was obtained considering the daily luminosity and a simple average was applied for grouping the days per week.

In reference to the postharvest database, the data was broken down by dates in format (mm/dd/yy), to facilitate their grouping by days and weeks. The production data were disaggregated to obtain the discarded production due to pests and diseases, and the data from each of the five sensors were grouped to obtain the discarded production and its causes. Sundays and holidays were not considered for not having postharvest records.

For the analysis, the databases were grouped and the observations were structured in years divided into weeks with the readings of the sensors and the causes of national production obtained from the postharvest record.

Once the data of the sensor variables and the causes of discarded production have been organized by years and weeks, the normality test is calculated. The normality test is performed because it is necessary to examine whether the data follows a normal distribution or not. For the normality test we use the Kolmogórov-Smirnov test, which is performed at a 95% confidence level. According to the result of this test, the statistical model should be selected, either for parametric or non-parametric data, and the following hypotheses are proposed:

H1: The data set does not follow the normal distribution
H0: The data set follows the normal distribution

If the result of the Kolmogórov-Smirnov test is less than 0.05, then the H0 hypothesis is rejected, that is, the data set does not follow a normal distribution.

The database was processed with the SPSS software, and the results show that the pest and disease variables obtain significance values less than 0.05 (see Table 1, 2, 3, 4 and 5), therefore the null hypothesis H0 is rejected and the alternative hypothesis H1 is accepted. Consequently, a statistical model for non-parametric data was then applied, it was Spearman Rho correlation coefficient, that is a nonparametric test used when the data does not follow a normal distribution.

Table 1. Normality test with data from sensor #1. Source: direct investigation.

Kolmogórov-Smirnov[a]			
	Stat	df	Sig
Humidity	,079	83	,200*
Dew point	,113	83	,011
Temperature	,058	83	,200*
VPD	,110	83	,015
Botrytis	,305	83	<,001
Powdery mildew	,306	83	<,001
Downy mildew	,308	83	<,001
Thrips	,191	83	<,001
Mites	,197	83	<,001

* This is a lower limit of the true meaning.
a. Lilliefors significance correction.

Table 2. Normality test with data from sensor #2. Source: direct investigation.

Kolmogórov-Smirnov[a]			
	Stat	df	Sig
Humidity	,064	83	,200*
Dew point	,124	83	,003
Temperature	,063	83	,200*
VPD	,096	83	,056
Botrytis	,271	83	<,001
Powdery mildew	,308	83	<,001
Downy mildew	,353	83	<,001
Thrips	,259	83	<,001
Mites	,220	83	<,001

* This is a lower limit of the true meaning.
a. Lilliefors significance correction.

Table 3. Normality test with data from sensor #3. Source: direct investigation.

Kolmogórov-Smirnov a			
	Stat	df	Sig
Humidity	,068	83	,200*
Dew point	,118	83	,006
Temperature	,063	83	,200*
VPD	,111	83	,013
Botrytis	,323	83	<,001
Powdery mildew	,302	83	<,001
Downy mildew	,273	83	<,001
Thrips	,283	83	<,001
Mites	,213	83	<,001

* This is a lower limit of the true meaning.
a. Lilliefors significance correction.

Table 4. Normality test with data from sensor #4. Source: direct investigation.

Kolmogórov-Smirnov a			
	Stat	df	Sig
Humidity	,122	51	,057
Dew point	,139	51	,016
Temperature	,209	51	<,001
VPD	,132	51	,026
Botrytis	,280	51	<,001
Powdery mildew	,260	51	<,001
Downy mildew	,402	51	<,001
Thrips	,346	51	<,001
Mites	,183	51	<,001

* This is a lower limit of the true meaning.
a. Lilliefors significance correction.

Table 5. Normality test with data from sensor sensor #5. Source: direct investigation.

Kolmogórov-Smirnov a			
	Stat	df	Sig
Humidity	,085	82	,200*
Dew point	,117	82	,008
Temperature	,092	82	,085
VPD	,102	82	,033
Botrytis	,291	82	<,001
Powdery mildew	,305	82	<,001
Downy mildew	,299	82	<,001
Thrips	,309	82	<,001
Mites	,204	82	<,001

* This is a lower limit of the true meaning.
a. Lilliefors significance correction.

Once the Spearman correlation coefficient statistical method was applied to the database, the respective correlation coefficient levels were obtained. The interpretation of Spearman's correlation coefficient ranges between -1 and + 1, indicating negative or positive associations respectively; 0 zero means that there is no correlation. The results can be seen in Table 6, 7, 8, 9 and 10.

Table 6. Correlation of pests and diseases with data from sensor #1. Source: direct investigation.

	Humidity				
	Botrytis	Powdery mildew	Downy mildew	Thrips	Mites
Rho =	0,122	0,204	0,041	−0,054	0,165
	Dew point				
	Botrytis	Powdery mildew	Downy mildew	Thrips	Mites
Rho =	0,081	0,245	−0,021	−0,09	0,097
	Temperature				
	Botrytis	Powdery mildew	Downy mildew	Thrips	Mites
Rho =	−0,003	0,072	−0,085	−0,034	−0,108
	VPD				
	Botrytis	Powdery mildew	Downy mildew	Thrips	Mites
Rho =	−0,086	−0,078	−0,057	−0,064	−0,15

Table 7. Correlation of pests and diseases with data from sensor #2. Source: direct investigation.

	Humidity				
	Botrytis	Powdery mildew	Downy mildew	Thrips	Mites
Rho =	0,533	0,093	−0,028	−0,434	0,382
	Dew point				
	Botrytis	Powdery mildew	Downy mildew	Thrips	Mites
Rho =	0,664	0,3	−0,144	−0,45	0,554
	Temperature				
	Botrytis	Powdery mildew	Downy mildew	Thrips	Mites
Rho =	0,251	0,317	−0,174	−0,038	0,267
	VPD				
	Botrytis	Powdery mildew	Downy mildew	Thrips	Mites
Rho =	−0,284	0,107	−0,024	0,318	−0,165

Table 8. Correlation of pests and diseases with data from sensor #3. Source: direct investigation.

	Humidity				
	Botrytis	Powdery mildew	Downy mildew	Thrips	Mites
Rho =	0,573	0,442	−0,014	−0,236	0,377
	Dew point				
	Botrytis	Powdery mildew	Downy mildew	Thrips	Mites
Rho =	0,698	0,62	−0,187	−0,128	0,477
	Temperature				
	Botrytis	Powdery mildew	Downy mildew	Thrips	Mites
Rho =	0,335	0,391	−0,296	0,118	0,292
	VPD				
	Botrytis	Powdery mildew	Downy mildew	Thrips	Mites
Rho =	−0,222	0,09	−0,123	0,229	−0,066

Table 9. Correlation of pests and diseases with data from sensor #4. Source: direct investigation.

	Humidity				
	Botrytis	Powdery mildew	Downy mildew	Thrips	Mites
Rho =	0,452	−0,009	−0,248	−0,142	0,22
	Dew point				
	Botrytis	Powdery mildew	Downy mildew	Thrips	Mites
Rho =	0,689	0,295	−0,233	−0,03	0,384
	Temperature				
	Botrytis	Powdery mildew	Downy mildew	Thrips	Mites
Rho =	0,455	0,393	−0,018	0,168	0,236
	VPD				
	Botrytis	Powdery mildew	Downy mildew	Thrips	Mites
Rho =	−0,071	0,18	0,181	0,178	−0,02

Table 10. Correlation of pests and diseases with data from sensor #4. Source: direct investigation.

	Humidity				
	Botrytis	Powdery mildew	Downy mildew	Thrips	Mites
Rho =	0,524	0,299	0,106	−0,298	0,405
	Dew point				
	Botrytis	Powdery mildew	Downy mildew	Thrips	Mites
Rho =	0,713	0,373	−0,081	−0,079	0,425
	Temperature				
	Botrytis	Powdery mildew	Downy mildew	Thrips	Mites
Rho =	0,449	0,227	−0,276	0,234	0,144
	VPD				
	Botrytis	Powdery mildew	Downy mildew	Thrips	Mites
Rho =	−0,116	−0,054	−0,219	0,348	−0,195

According to the statistical analysis of the data and its correlation, the following can be noted:

Humidity. It is verified that there is a positive correlation between the relative humidity variable with the presence of botrytis. The relationship is directly proportional with values of Rho min = 0.122 in sensor #1 and Rho max = 0.573 in sensor #3.

It is verified that there is a positive correlation between the relative humidity variable with the presence of powdery mildew. The relationship is directly proportional with values of Rho min = 0.093 in sensor #2 and Rho max = 0.442 in sensor #3. In this relationship, sensor #4 is the only one with a negative correlation with Rho = −0.009, so the possibility of an investigation by rose variety is opened considering the types of roses existing in the analysis radius measured by this sensor.

There is not enough significance to prove a correlation between the variable relative humidity with downy. The values shown are negative Rho max = −0.248 in sensor #4 and positive Rho max = 0.106 in sensor #5.

It is verified that there is a negative correlation between the relative humidity variable with the presence of thrips. The relationship is inversely proportional with values of Rho min = −0.054 in sensor #1 and Rho max = −0.434 in sensor #2.

It is verified that there is a positive correlation between the relative humidity variable with the presence of mites. The relationship is directly proportional with values of Rho min = 0.165 in sensor #1 and Rho max = 0.405 in sensor #5.

Dew Point. It is verified that there is a positive correlation between the dew point variable with the presence of botrytis. The relationship is directly proportional with values of Rho min = 0.081 in sensor #1 and Rho max = 0.713 in sensor #5.

It is verified that there is a positive correlation between the dew point variable with the presence of powdery mildew. The relationship is directly proportional with values of Rho min = 0.245 in sensor #1 and Rho max = 0.620 in sensor #3.

It is verified that there is a negative correlation between the variable dew point with the presence of downy. The relationship is inversely proportional with values of Rho min = −0.021 in sensor #1 and Rho max = −0.233 in sensor #4.

It is verified that there is a negative correlation between the dew point variable with the presence of thrips. The relationship is inversely proportional with values of Rho min = −0.030 in sensor #4 and Rho max = −0.450 in sensor #2.

It is verified that there is a positive correlation between the dew point variable with the presence of mites. The relationship is directly proportional with values of Rho min = 0.097 in sensor #1 and Rho max = 0.554 in sensor #2.

Temperature. It is verified that there is a positive correlation between the temperature variable with the presence of botrytis. The relationship is directly proportional with values of Rho min = 0.251 in sensor #2 and Rho max = 0.449 in sensor #5. In this relationship, sensor #1 is the only one with a negative correlation with Rho = −0.003, so the possibility of an investigation by rose variety is opened considering the types of roses existing in the analysis radius measured by this sensor.

It is verified that there is a positive correlation between the temperature variable with the presence of powdery mildew. The relationship is directly proportional with values of Rho min = 0.072 in sensor #1 and Rho max = 0.391 in sensor #3.

It is verified that there is a negative correlation between the variable temperature with the presence of downy. The relationship is inversely proportional with values of Rho min = −0.085 in sensor #1 and Rho max = −0.296 in sensor #3.

There is not enough significance to prove a correlation between the variable temperature with thrips. The values shown are negative Rho max = −0.038 in sensor #2 and positive Rho max = 0.234 in sensor #5.

It is verified that there is a positive correlation between the temperature variable with the presence of mites. The relationship is directly proportional with values of Rho min = 0.236 in sensor #4 and Rho max = 0.292 in sensor #3. In this relationship, sensor #1 is the only one with a negative correlation with Rho = −0.108, so the possibility of an investigation by rose variety is opened considering the types of roses existing in the analysis radius measured by this sensor.

VPD. It is verified that there is a negative correlation between the VPD variable with the presence of botrytis. The relationship is inversely proportional with values of Rho min = −0.086 in sensor #1 and Rho max = −0.284 in sensor #2.

There is not enough significance to prove a correlation between the variable VPD with powdery mildew. The values shown are negative Rho max = −0.078 in sensor #1 and positive Rho max = 0.078 in sensor #2.

There is not enough significance to prove a correlation between the variable VPD with downy. The values shown are negative Rho max = −0.219 in sensor #5 and positive Rho max = 0.181 in sensor #4.

It is verified that there is a positive correlation between the VPD variable with the presence of thrips. The relationship is directly proportional with values of Rho min = 0.178 in sensor #4 and Rho max = 0.348 in sensor #5. In this relationship, sensor #1 is the only one with a negative correlation with Rho = −0.064, so the possibility of an investigation by rose variety is opened considering the types of roses existing in the analysis radius measured by this sensor.

It is verified that there is a negative correlation between the VPD variable with the presence of mites. The relationship is inversely proportional with values of Rho min = −0.020 in sensor #4 and Rho max = −0.195 in sensor #5.

4 Discussion

The use of IoT technology helps to obtain data in real time so a farm is able to take decisions also in real time looking to improve the production process, as well as the management and control of pests and diseases.

Controlling affectations that cause damage of the flower can help to get a better competitive level with the consequent increase of the possibilities for exporting.

As a result of the present study, the control of environmental conditions inside the greenhouse can help decision-making regarding agricultural activities as well as the application of fungicides to protect the health of plants. In this sense, this research proposes a data sheet that combines both, pests and diseases, to show when the farm should be alert about the changing environmental conditions that favor the appearance of pests and diseases, considering temperature, humidity, vapor pressure deficit and the dew point, to deploy actions to prevent the damage of the roses.

Table 11 shows a set of indicators that consider the conditions of temperature, humidity, dew point and VPD, which when combined, resulted in the 20% of highest presence and incidence of diseases and pests. These indicators represent the possibility of improving production control through the IoT applied to the production of roses, and mean a guide for daily work on a farm that decides to implement digital transformation tools such as IoT and data analytics.

Table 11. Data sheet of estimated conditions for the prevention of pests and diseases in the production of roses. Source: direct investigation.

Estimated conditions for the incidence of botrytis				
Range	*Humidity*	*Dew point*	*Temperature*	*VPD*
MIN:	49.20	6.95	16.57	0.54
MAX:	77.50	14.77	22.02	1.66
Estimated conditions for the incidence of powdery mildew				
Range	*Humidity*	*Dew point*	*Temperature*	*VPD*
MIN:	57.72	9.80	16.03	0.59
MAX:	77.50	12.89	23.60	1.95
Estimated conditions for the incidence of downy mildew				

(*continued*)

Table 11. (*continued*)

Estimated conditions for the incidence of botrytis				
Range	*Humidity*	*Dew point*	*Temperature*	*VPD*
Range	*Humidity*	*Dew point*	*Temperature*	*VPD*
MIN:	55.57	7.11	13.82	0.36
MAX:	79.40	12.95	20.16	1.39
Estimated conditions for the incidence of thrips				
Range	*Humidity*	*Dew point*	*Temperature*	*VPD*
MIN:	48.90	8.36	16.56	0.66
MAX:	71.69	12.83	21.30	1.86
Estimated conditions for the incidence of mites				
Range	*Humidity*	*Dew point*	*Temperature*	*VPD*
MIN:	49.20	6.95	14.73	0.45
MAX:	79.10	14.02	21.27	1.71

5 Conclusions

In all cases it was evidenced that the incidence of pests and diseases has different levels of correlation with the environmental conditions inside the greenhouses. This information is useful to establish a data sheet with a set of indicators that allow the producer to know when it must be carried out preventive and even corrective actions due to the effect of knowledge about environmental conditions in real time.

The present study demonstrates the importance of the IoT applied to control production in the floriculture production sector, however, this study does not cover the economic impact and administrative management due to the fact of handling data on environmental conditions that could affect the crop. Nevertheless, the data sheet of estimated conditions for the prevention of pests and diseases in the production of roses is an important advance for this agricultural sector, the same one that should be measured in a new study.

The possibility of deepening the current study and developing decision-making methods based on statistical information built from the IoT applied to the flower sector remains open.

References

1. Trade Map: Trade Map, 21 05 2023. [En línea]. www.trademap.org
2. Tamoghna, O., Sudip, M., Narendra, S.R.: Wireless sensor networks for agriculture: The state-of-the-art in practice and future challenges. Comp. Electron. Agric. **118**, 66–84 (2015)
3. Want, R., Schilit, B., Jenson, S.: Enabling the Internet of Things. Computer **48**, 28–35 (2015)
4. Alagarsamy, G., Gowthaman, N.: Intelligent IoT (IIoT)-based food supply monitoring system with alert messages in transmission and distribution environment. In: de Technology, Business, Innovation, and Entrepreneurship in Industry 4.0, Gewerbestrasse, EAI/Springer Innovations in Communication and Computing, pp. 353–368 (2023)

5. Grower Talks: Grower Talks, 01 11 2018. [En línea]. www.growertalks.com
6. Arcos, C., Padilla, A.: Model of technological competencies as determinants of innovation: a comparative intersectoral study in Ecuador. In: de Trends in Artificial Intelligence and Computer Engineering. ICAETT 2022. Lecture Notes in Networks and Systems, vol. 619. Springer, Cham, pp. 561–574 (2023)
7. Gostinchar, J.: Cultivo del rosal. Cofisa, Madrid (1954)
8. Arcos, C.: Obstacles to innovative activities: case of the floriculture sector in Ecuador. In: de Technology, Business, Innovation, and Entrepreneurship in Industry 4.0, Gewerbestrasse. EAI/Springer Innovations in Communication and Computing, pp. 67–94 (2023)
9. Calvache, Á.: Elaboración de un manual técnico-práctico del cultivo de rosas para exportación. Researchgate (2010)
10. Messelink, G., Kruidhof, M.: Advances in pest and disease management in greenhouse cultivation. In: de Achieving sustainable greenhouse cultivation, London, Burleigh Dodds Science Publishing, p. 46 (2019)
11. Yong, A.: El cultivo del rosal y su propagación. Cultivos Tropicales **25**(2), 53–67 (2004)
12. Daughtrey, M., Buitenhuis, R.: Integrated pest and disease management in greenhouse ornamentals. In: de Integrated Pest and Disease Management in Greenhouse Crops, Berna, Plant Pathology in the 21st Century book series (ICPP, vol. 9), pp. 625–679 (2020)
13. Heredia, M., Falconí, V., Silva, J.H., Amores, K., Endara, C., Ausay, K.F.: Technological innovation for the sustainability of knowledge and natural resources: case of the Choco Andino biosphere reserve,» de innovation and research: a driving force for socio-econo-technological development. In: Botto-Tobar, M., Zambrano Vizuete, M., Díaz Cadena, A. (eds.). Springer, Cham, pp. 464–476 (2021)

Transesterification of Waste Oils for Sustainable Transport in the Tourism Sector

Edwin Chiliquinga[1(✉)], Dennis Ugeño[1], Edwin Machay[1], and Viviana Silva[2]

[1] Instituto Tecnológico Universitario Vida Nueva, Quito, Ecuador
omar.chiliquinga@istvidanueva.edu.ec
[2] Instituto Tecnológico Universitario Central Técnico, Quito, Ecuador

Abstract. This research aims to analyse the properties of biodiesel obtained from residual oils that have been collected in sites dedicated to community tourism, taking into consideration that at present, Ecuador does not have solid strategies to recycle and rationally reuse the volume of residual oils generated in the preparation of food in different sectors. In the tourism field, the generation of residual oils is not an isolated case, residual oils, produced in food preparation, are generally discarded; However, this work developed a strategy for obtaining biodiesel from waste oils, defining the reagents necessary for the development of the chemical reaction called transesterification, from which biodiesel was obtained that will be used as biofuel and on the other hand the glycerine which will be used as a degreaser, the necessary reagents were fixed from the bibliographic investigation, and then proceeded to characterise the oil used as raw material, for later carry out the experimental phase to analyse the physical and chemical properties at laboratory level, finally used in an internal combustion engine diesel obtaining an average opacity level of 16%, with these values proceeds to validate the application of the product obtained in agricultural machinery commonly used in tourism community.

Keywords: Transesterification · Biodiesel · Sustainability · Pollution · Opacity

1 Introduction

Currently tourism in Ecuador is among the four main sources of non-oil economic income in the country, in general the flow of national and foreign tourists to different tourist destinations report a considerable income of foreign currency in establishments dedicated to the service of food and beverages, many of these places offer great gastronomic variety that are mostly prepared with palm oil, soybean, soybean, colsa, palm kernel, olive, sunflower, among others; This undoubtedly entails an environmental problem that must be solved urgently, since these establishments do not have good environmental practices or resources for the management of residual oils produced in cooking, today it has caused great environmental and public health problems by polluting rivers and lands [1].

For years it has been known that oils should not be reused in the kitchen, at least not very often, since the high temperatures used for food preparation by frying can release

M. Z. Vizuete et al. (Eds.): CI3 2023, LNNS 1040, pp. 18–29, 2024.
https://doi.org/10.1007/978-3-031-63434-5_2

water vapour that when mixed that when reacting with triglycerides cause the formation of fatty acids, monoglycerides, diglycerides, glycerol and even some carcinogenic substances such as benzopyrene, an element also found in tobacco smoke. Most common diseases caused by eating trans fats are related to colon problems, blood vessel problems, and possibly stomach cancer [2].

Cooking by frying is one of the most important techniques in food preparation, this technique was used since 1600 BC; however, after preparing food with this technique, some people continue to use the oils indiscriminately either because of working conditions or because of the cost of the oil, in other cases, the residual oil is poured directly into the soil, rivers, oceans, etc., affecting the local ecosystem. This situation has led to the search for alternatives worldwide through the development of biofuels as a solution to this problem [1].

The main objective of the development of biofuels is to reduce the rate of environmental pollution left by the consumption of petroleum-based fuels. Currently biodiesel can replace diesel completely or can be used as an additive for internal combustion engines in the form of mixtures containing 20% and 50% biodiesel (B 20, B 50) thus offering improvement of the properties and characteristics of diesel [3].

The purpose of this research is the manufacture of an industrial equipment used to obtain biodiesel through the transformation of vegetable waste oils, through the transesterification process that combines the oil with methanol and sodium hydroxide (NaOH), which allows the production of a compound that can be used directly in the burner, electricity generator or in a diesel combustion engine, also as a residual product of this reaction glycerol is obtained, commonly called glycerine, it can be used in other industries such as pharmaceuticals for the manufacture of cleaning products, degreasers, etc. [4].

The evaluation of the biodiesel obtained focuses on the development of physical, chemical tests and opacity measurement, thus determining the feasibility of using this biofuel as an advantage from the energy point of view and recommended from the environmental point of view, since it has a lower emission of harmful gases, especially carbon dioxide (CO2), which is the main cause of the greenhouse effect; In this way, the production and use of alternative energies, friendly to the environment and in turn progressively reduce the use of fossil fuels, renewed interest in the efficient management of energy and economic resources that allow a globalised growth in the production and economy of the country in different social sectors [5].

2 Biodiesel

The ASTM (American Society for Testing and Materials) defines biodiesel as “the long-chain monoalkyl ester of fatty acids derived from renewable resources, such as vegetable oils or animal fats, for use in diesel engines”. It is presented in a liquid state and is obtained from renewable resources such as vegetable oils of soybean, rapeseed/canola, sunflower, palm and others, as well as animal fats, through a process called Transesterification [2].

Transesterification consists of mixing vegetable oil or fats with an alcohol (usually methanol) and an alkali (caustic soda). After a resting time, by decantation, the biodiesel is separated from its by-product glycerol. This process requires a reactor that is the heart of every biodiesel plant. Despite different experiences made since the 1920s in the production of biodiesel, it achieved real notoriety in the early years of the twenty-first century caused by the increase in international oil prices [13].

According to the research of Tejada Tovar [6], the different possibilities of obtaining biodiesel from fatty waste generated in the livestock farm: chicken, pork, and beef fat, for this the variables molar alcohol/animal fat ratio and amount of catalyst are analysed, “since they are the ones that most affect the quality of biodiesel, when evaluating their characteristics and yields of the transesterification reaction.

In addition, Tejada Tovar [6] mentions that the yield in the process of extracting fat from chicken waste material is 70.5%, and pork fat 90%, so they are proposed as viable alternatives from the technical point of view, allowing the valorisation of these organic wastes and alleviating the pollution generated in this type of industries. From the characterization of chicken and pork fat, it was established that both raw materials are low acidity, which guarantees a high degree of transesterification, taking into account that it had a yield of 96% from chicken fat and 91.2% from pork fat.

2.1 Raw Materials for the Production of Biodiesel

The most used raw material for the manufacture of biodiesel should be one that contains a high triglyceride index such as: sunflower oil, rapeseed, soybean, used frying oil, tallow, etc. Table 1 shows the main feedstocks used to make biodiesel.

Table 1. Raw material for the production of biodiesel

Conventional oils	Alternative vegetable oils	Other Sources
Sunflower	Brassica carinata	Genetically modified seed oil
Colsa	Cynara curdunculus	Animal fats (beef and buffalo tallow)
Coconut	Camelina sativa	Microalgae oils
Soybean	Cambre abyssinica	Microbial production oils
Palm	Pogianus	Frying oils

Each type of feedstock used for biodiesel production is described below.

Conventional vegetable oils: The most common raw materials used are oilseed oils such as sunflower oil, canola oil (Europe), soybean oil (USA) and coconut oil (Philippines); and oily fruits such as palm oil used in Malaysia and oil in Indonesia [7].

Alternative vegetable oils: These are better adapted to the conditions of the countries where they are developed and are more beneficial for energy crops. It highlights, for example, camelina, camellia and jatropha oil, in Spain, the crops most suitable to the conditions of the country are Brassica carinata and Cynara cur-dunculus [8].

GMO vegetable oil: The main difference between oil and fat is the fatty acid content. Oils with a high proportion of unsaturated fatty acids, such as sunflower oil or camelina oil, can improve the performance of biodiesel at low temperatures, but reduce its oxidative stability, resulting in a high iodine index. Therefore, highly unsaturated oils that have been genetically modified to reduce the establishment ratio, such as sunflower oil with high oil content, can be considered as feedstock for biodiesel production [9].

Used frying oils: It is an alternative for the production of biodiesel with better prospects, since it is the most economical raw material for the production of this fuel. The use of used oil promotes good treatment and waste disposal [3].

Animal fats: Animal fats, especially cow tallow, can also be used for the production of biodiesel [10].

2.2 Use of Biodiesel in Internal Combustion Engines

The use of biodiesel has several environmental benefits, compared to diesel, it reduces the pollution load caused by the engines. Reported biodiesel test results where a 20% reduction in sulphur compound emissions, a 10% reduction in carbon monoxide (CO), a 14% reduction in hydrocarbons (HC), and a 26% reduction in particulate matter for diesel fuel were observed. As for nitrogen oxide (NOx) emissions, there is no single standard, as some studies reported an increase in NOx emissions, while others reported a decrease (Piloto Rodríguez, 2010). Adding biodiesel to diesel has several advantages [16]. Biodiesel has a higher cetane number. Biodiesel improves lubrication, which prolongs the life of engine components. Biodiesel also has a higher flash point than diesel. Although the flash point does not directly affect combustion, it makes biodiesel safer for storage and transportation [9].

2.3 Transesterification

Vegetable oils usually contain free fatty acids, phospholipids, sterols, water and other impurities. Therefore, the oil cannot be used directly as fuel [20]. To overcome these problems, vegetable oils undergo a slight chemical modification called transesterification. As a result of this modification, a cleaner and more environmentally safe fuel (biodiesel) was obtained, whose main components are mono alkyl esters of long-chain fatty acids [11].

Transesterification, or alcoholysis, named for the use of short-chain alcohols such as methanol or ethanol, is the replacement of an alcohol group in an ester provided by triglycerides of animal or vegetable fats by another alcohol in a process similar to hydrolysis. Use alcohol instead of water. This process is widely used to reduce the high viscosity of triglycerides. Figure 1 shows the general reaction for transesterification [14].

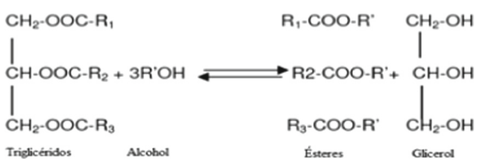

Fig. 1. General equation of the transesterification reaction [11]

For transesterification methanol or ethanol can be used. If methanol is used the process is called methanolysis, and if ethanol is used it is called ethanolysis, as shown in Fig. 2.

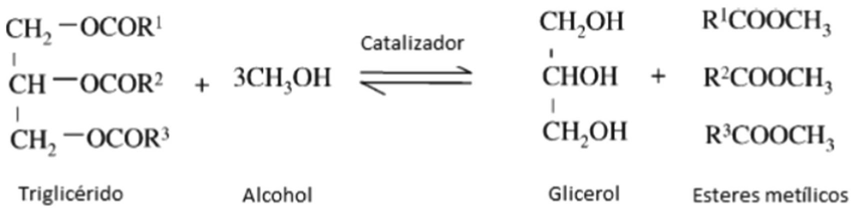

Fig. 2. General equation for triglyceride ethanolysis [11]

Both processes can be catalysed by acids or bases. The most commonly used bases are sodium hydroxide, potassium hydroxide and carbonates. Commonly used acid catalysts are: sulfuric acid, sulfonic acid, hydrochloric acid [15]. After transesterification of triglycerides, the product is a mixture of esters, glycerol, alcohol, catalyst and triglycerides, diglycerides and monoglycerides, which are then separated. A layer of glycerine was deposited at the bottom of the reaction vessel. The formation of diglycerides and monoglycerides is an intermediate step in the process. Figure 3 shows the mechanism of the transesterification reaction [11].

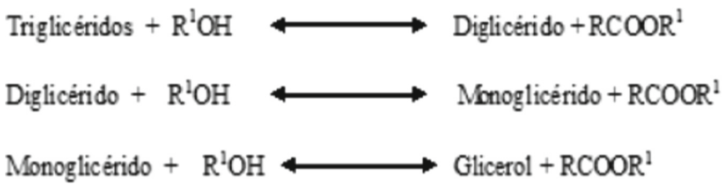

Fig. 3. Reaction Mechanisms [11]

3 Methodology

To obtain biodiesel it is important to analyse the density and viscosity of animal, automotive and hydraulic oils, allowing the selection of the appropriate oil to apply the transesterification process in obtaining biodiesel, therefore, density measurements of the different types of oils are carried out for the previous selection of the most appropriate raw material and thus obtain the biofuel (Fig. 4).

Fig. 4. Density measurement of vegetable and animal oils

With the data obtained, a table is generated showing the relative density of each of the oils (Table 2).

Table 2. Relative density of oils

Type of oil	Relative density
Vegetable Oils	0,90
Animal Oils	0,93
Automotive Oil	0,95
Hydraulic oil	0,98

At this point the Ford viscosity cup is used, which helps to quickly and accurately determine viscosity in liquids." However, you should keep in mind that it is only possible with dense liquids, since this method is applied to determine other mechanical variables, such as the average speed which will allow the selection of the pipe necessary for the construction of the biodiesel distillation system [17] (Fig. 5).

Fig. 5. Viscosity Measurement by FORD Cup Method # 4

Table 3 shows the values of the times obtained from each of the raw materials with the Ford cup, using these data, we proceed to calculate the viscosities as a function of the time of each of the oils.

Table 3. Time obtained from Ford Cup #4

Type of oil	Average time(s)
Vegetable oils	10,40
Animal oils	11,00
Automotive oil	11,80

Next, the mathematical model for calculating the viscosity of oils is presented.

$$Vp = |2{,}74 \times t - 100 \times t| \tag{1}$$

where: Vp = Viscosity (mPa.s) and t = Time (s). Then we proceed to replace the average time in the equation previously raised to obtain the viscosity of the different types of oils considered as raw material.

Calculation of the viscosity of vegetable base oil. Time of 10,40 s.

$$Vp = |2{,}74 \times t - 100 \times t|$$

$$Vp = |2, 74(10{,}40) - 100(10{,}40)|$$

$$Vp = 1011{,}50 mPa.s$$

Calculation of the viscosity of animal base oil for time of 11,00 s.

$$Vp = |2{,}74 \times t - 100 \times t|$$

$$Vp = |2{,}74(11{,}00) - 100(11{,}00)|$$

$$Vp = 1069{,}86 mPa.s$$

Calculation of automotive oil viscosity for time of 11,00 s.

$$Vp = |2{,}74 \times t - 100 \times t|$$

$$Vp = |2{,}74(11{,}80) - 100(11{,}80)|$$

$$Vp = 1147{,}66 mPa.s$$

Calculation of the viscosity of hydraulic systems for time of 11,00 s.

$$Vp = |2{,}74 \times t - 100 \times t|$$

$$Vp = |2{,}74(12{,}20) - 100(12{,}20)|$$

$$Vp = 1186{,}57 mPa.s$$

Through the measured and calculated values, the following table is made which indicates the physical and chemical properties of each of the raw material analysed to select the most optimal substance that serves the transesterification process.

Table 4. Properties of oils.

Type of oil	Density kg/m^3	Viscosity mPa s	Temperature °C
Vegetable oils	900	1011,50	100 a 180
Animal oils	930	1069.86	180 a 200
Automotive oil	950	1147.66	200 a 250
Hydraulic oil	980	1186,57	250 a 300

The results obtained presented in Table 4, show the density of each of the oils, taking into account that higher density oils need a higher temperature (200 °C to 300 °C) for decomposition and lower density oils decompose at a lower temperature (100 °C to 180 °C), reaching the conclusion that vegetable and animal oils are suitable for the process of obtaining biodiesel using the transesterification process [18].

3.1 Property Analysis

After obtaining the biodiesel, the properties of the resulting product are extracted through experiments and calculations to compare with some national and international specifications that validate whether the biodiesel obtained is suitable for consumption (Table 5).

Table 5. Density of diesel and biodiesel at 15 °C.

Fuel	ISO 12185 kg/m^3	NTE INEN 1498 kg/m^3	ASTM D6751 kg/m^3	Measured Value kg/m^3
Commercial diesel	820–845	850	–	–
Commercial biodiesel	–	–	860 – 900	–
Biodiesel obtained	–	–	–	880

Another property to be evaluated was the kinematic viscosity, for which it was necessary to heat the biodiesel obtained since the NTE INEN 1498 standard specifies the measurement of this parameter at 37.8 °C [19] (Table 6).

Table 6. Kinematic viscosity of diesel and biodiesel cSt

Fuel	NTE INEN 1498 cSt	ASTM D975 cSt	Measured Value cSt
Diesel 1	1,3–3	–	–
Diesel 2	2,5–6	–	–
Premium diesel	2,5–6	–	–
Commercial biodiesel	–	1,9 – 6	–
Obtained biodiesel	–	–	4

The average kinematic viscosity value obtained from tests allows the product obtained to be validated, since it is of the national and international parameters of commercial diesel from Ecuador and international biodiesel.

The pH mediation was developed with the aim of identifying if the substance obtained is acidic or not, this would allow to validate the application of the biofuel in an internal combustion engine, if the result is acidic it could cause severe damage to the metal parts of the engine (Table 7).

Table 7. pH index of commercial biodiesel and biodiesel obtained.

Fuel	EN 14214 pH	pH Measured value
commercial biodiesel	6–8,4	6
obtained biodiesel	–	6–7

The measured pH value of biodiesel allows to define as a fuel suitable for internal combustion engines.

The determination of density, kinematic viscosity and pH index support the application of biodiesel for the operation of an internal combustion engine.

Below, the opacity results obtained when running a diesel internal combustion engine with the biofuel produced are detailed, the results will be compared with the NTE INEN 017 standards (ENVIRONMENTAL MANAGEMENT. AIR. MOTOR VEHICLES. DETERMINATION OF THE OPACITY OF EXHAUST EMISSIONS OF DIESEL ENGINES BY STATIC TEST FREE ACCELERATION METHOD) (Table 8).

Table 8. Results obtained from opacity (%) [12].

Temp: (85–90) °C	Model and year: Motor Great Wall 2016			Fuel type: Biodiesel	
	Acceleration 1 (%)	Acceleration 2 (%)	Acceleration 3 (%)	Acceleration 4 (%)	Acceleration 5 (%)
Test 1	15	17	14	15	15
Test 2	17	17	15	18	18
Test 3	17	18	18	15	15
Opacity result					
Test 1: 15%					
Test 2: 17%					
Test 3: 16%					

Note. To obtain more realistic measurements, three tests were performed

The average result of the opacity of the engine using biodiesel as an alternative fuel is 16%, which guarantees that the engine produces a low level of particulate matter (PM) according to the regulations is within the ranges.

4 Conclusions

With the studies carried out in the research it was possible to determine the most appropriate process such as transesterification to obtain biodiesel from waste oils produced by animal fats that are often used in the cooking of food in the tourism sectors.

Through mathematical expressions I can identify the parameters and modifiable variables within the transesterification process to select the raw material that allows to obtain diesel 2 also known as biodiesel.

The values obtained in the calculations will help the design of the prototype for the biodiesel distillation machine. By means of a thermodynamic process that will decompose the oil molecules for the transesterification process and the obtaining of the product.

The research carried out allowed the generation of biodiesel from residual oils with physical and chemical properties that meet national and international specifications which guarantee the optimal operation of the engine, avoiding damage due to overheating, oxidation, corrosion or lubrication.

The community must have knowledge of waste management so, in the first instance, it is necessary to guide citizens on the initial classification of the same and then, on activities such as reuse, recovery, recycling; breaking the traditional scheme of "collection - final disposal" reaching the conclusion that it is necessary to generate a program of collection of residual oils in the community to promote sustainable tourism.

References

1. de León Benítez, J.B., Abreu Rodríguez, L., Matiauda, M., Miño Valdés, J.E.: Diseño de una planta de obtención de Biodiesel a partir de un residual de la industria azucarera (cachaza, Centro Azúcar, vol. 43, no. 1, pp. 1–9 (2019)
2. García-Díaz, M., Gandón-Hernández, J., Maqueira-Tamayo, Y.: Estudio de la obtención de biodiesel a partir de aceite comestible usado, Tecnología Química, vol. 33, no. 2, pp. 162–169 (2019)
3. Marquínez, A.N.M., et al.: Obtención de biodiesel a partir de aceite de coco (Cocos nucifera L.), Revista de Iniciación Científica, vol. 6, no. 1, pp. 9–14 (2020)
4. Pardal, A.C.D.V.: Obtención de biodiesel por transesterificación de aceites vegetales: nuevos métodos de sínteses, 2012, Accedido: 21 de junio de 2022. [En línea]. Disponible en: https://repositorio.ipbeja.pt/handle/20.500.12207/738
5. Diseño de un reactor de transesterificación para la obtención de biodiesel a partir de aceites vegetales. https://riunet.upv.es/handle/10251/73470 (accedido 21 de junio de 2022)
6. Tejada Tovar, C., Tejeda Benítez, L., Villabona Ortiz, Á., Monroy Rodríguez, L.: Obtención de biodiesel a partir de diferentes tipos de grasa residual de origen animal, Luna Azul, no. 36, pp. 10–25 (2019)
7. Tejeda Benitez, L.: Obtención de biodiesel a partir de diferentes tipos de grasa residual de origen animal, Extracting biodiesel from different types of animal origin residual fat, 21 de septiembre de 2022. http://www.scielo.org.co/scielo.php?script=sci_arttext&pid=S1909-24742013000100002 (accedido 21 de junio de 2022)
8. Oliva-Montes, J., Flores-Rodríguez, J., López-Medina, R., Santos-Camacho, J., Contreras, J., Vaca-Mier, M.: Producción de biodiesel a partir de grasa animal utilizando catálisis heterogénea, vol. 2, no. 5, p. 10
9. Garrido, S.M.: Tecnología, territorio y sociedad. Producción de biodiesel a partir de aceites usados, Íconos, vol. 0, no. 37, p. 75 (2013). https://doi.org/10.17141/iconos.37.2010.422
10. Valderrama Negrón, A., Jacinto Hernández, C., Ponce García, S., Manrique Pollera, L.: Uso del diseño factorial en los ensayos de liberación controlada del ácido 1,3 indolacético cargado en matrices de quitosano, Revista de la Sociedad Química del Perú, vol. 83, no. 3, pp. 354–365 (2017)
11. Esterificación y transesterificación de aceites residuales para obtener biodiesel. http://www.scielo.org.co/scielo.php?script=sci_arttext&pid=S1909-24742015000100003 (accedido 21 de junio de 2022)
12. INEN: RTE INEN 017 Control de emisiones contaminantes de fuentes móviles terrestres. Quito (2016)
13. Rožić, M., Babac, M.T., Radić Stojanović, D., Božić, M.: Trans-esterification reactions in the synthesis of bioactive compounds. Molecules **26**(12), 3503 (2021)

14. Zhu, S., et al.: Bio-diesel production and environmental impacts. Renew. Sustain. Energy Rev. **123**, 109758 (2020)
15. Pousa, J.R., Ballesta Claver, J., Piqueras Céspedes, J., Rodríguez Avi, J., Viola, E.: Biodiesel production: raw material and extraction methods of lipids from vegetable oils and animal fats. Grasas Aceites **70**(3), e318 (2019)
16. Phan, A.N., Phan, T.M.: Biodiesel production from non-edible plant oils. In Biodiesel-A feasible alternative in present scenario, pp. 75–98. IntechOpen (2018)
17. Kryvda, V., Pisárčik, M., Matúš, M., Lazor, M.: Energy properties of biodiesel fuels. In: MATEC Web of Conferences, vol. 157, p. 02020. EDP Sciences (2018)
18. Silitonga, A.S., Atabani, A.E., Mahlia, T.M.I.: A review on pro-spect of Jatropha curcas for biodiesel in Indonesia. Energy Convers. Manage. **181**, 197–215 (2019)
19. Li, G., Xue, J., Han, B.: Emission characteristics of biodiesel–diesel blends: a review. Renew. Sustain. Energy Rev. **118**, 109512 (2020)
20. Freedman, B., Butterfield, R.O., Pryde, E.H.: Transesterification kinetics of soybean oil. J. Am. Oil Chem. Soc. **63**(10), 1375–1380 (1986)

LoRaWAN Applied to WSN as Support for Sustainable Agriculture in Rural Environments. Case Study: Pedro Moncayo Canton, Pichincha Province

Evelyn Bonilla-Fonte, Edgar Maya-Olalla, Alejandra Pinto-Erazo, Ana Umaquinga-Criollo, Daniel Jaramillo-Vinueza, and Luis Suárez-Zambrano(✉)

Universidad Técnica del Norte, Avenida 17 de Julio 5-21 y General María Córdoba, 100105 Ibarra, Ecuador
{eamaya,lesuarez}@utn.edu.ec

Abstract. This work describes the development of a Long-Range Low-Power Wireless Sensor Network (LPWAN) implemented in a rural environment to monitor environmental variables that influence the growth of grass crops. The sensor node collects and transmits data on soil moisture, UV radiation, temperature, and rainfall in a cultivation area covering 1000 m^2. The data collected by the sensor node is sent to the central node or gateway via LoRa communication, where it is processed and transmitted to a cloud platform called ThingSpeak using the MQTT protocol. The data is displayed in the form of graphs. The analysis, design, implementation, and testing of the wireless link are carried out, and the data is sent to an IoT platform where it is collected, visualized, and analyzed in real-time using MQTT as the central communication protocol. Functional tests are performed, including path loss, receiver power, signal-to-noise ratio, receiver sensitivity, link budget, Fresnel zone, azimuth angle, and elevation angle. Finally, a stable scenario for data transmission and reception is determined, which can be applied to an optimization system for crop cultivation in rural agricultural areas.

Keywords: LoRaWAN · MQTT · propagation loss · scattering factor

1 Introduction

Tocachi, a rural parish in the province of Pichincha, located in the Pedro Moncayo canton, is internationally recognized for its cultivation and production of roses. However, livestock farming is also important in this region. In the area, there is a dairy association made up of small-scale farmers who raise cattle for this purpose. These animals require quantities of green forage for their feed, making pasture cultivation essential and cost-effective. It is common to find large tracts of land with cattle. The farmers are a fundamental part of the economic growth in the area, both in milk and meat production [1].

M. Z. Vizuete et al. (Eds.): CI3 2023, LNNS 1040, pp. 30–45, 2024.
https://doi.org/10.1007/978-3-031-63434-5_3

The duration and performance of grasses depend on factors such as crop planning, fertilization, proper cutting, and especially irrigation [2]. Plants in their early stages are highly sensitive to lack or excess moisture, so it is crucial to maintain constant moisture for the crops to achieve optimal growth and production.

The local farmers have traditionally implemented sprinkler irrigation systems, but the water distribution is not adequate, resulting in wastage as they cannot determine which part of the land needs irrigation and how much water should be provided. Additionally, climatic factors such as temperature, rainfall, and solar radiation significantly affect the production and quality of the Grass [3]. It is important for the person in charge of the cultivation to consider these parameters for proper pasture management.

In the study area, the average annual precipitation varies from 400 to 1300 mm, with a dry period between July and October, resulting in a water deficit of 0 to 330 mm [4]. The daily growth rate of grass in summer ranges from 5–20 kg/MS/ha/day, while in winter it increases to levels of 60–80 kg/MS/ha/day [5]. Therefore, it is important to apply irrigation to increase grass production. Improving the efficiency of the sprinkler irrigation system will allow farmers to reduce unnecessary water consumption.

In [6], the design of a Wireless Sensor Network (WSN) for the control and monitoring of a drip irrigation system in a strawberry plantation is presented. The primary objective is to collect data from multiple sensor nodes distributed throughout the crop, which are then transmitted to a central node and stored in a local database. Zigbee technology is employed for communication between the sensor nodes and the central node. Additionally, the system uses reference values for soil moisture and temperature to activate or deactivate the solenoid valve and a fan, respectively.

In [7], the design of an intelligent irrigation system based on fuzzy logic for vegetable crops at the La Pradera farm of the Technical University of the North is presented. The main goal of this research is to develop a drip irrigation system based on fuzzy logic, which includes a WSN defined in the IEEE 802.14 protocol. Sensor data is wirelessly transmitted to a control station using Zigbee technology. In this station, the data is analyzed, and the opening time of the solenoid valve for crop irrigation is determined.

In [8], a system for irrigation control using machine learning techniques is designed for alfalfa crops at the La Pradera farm of the Technical University of the North. The collected data comes from a sensor network developed in [9] and is stored in a local database. Wireless communication is carried out using LoRaWAN modules.

Considering the aforementioned works, the present work proposes the design of a long-range and low-power wireless sensor network (LPWAN) for a grass crop in a rural environment. The system collects data from variables through a WSN located in the cultivation area, which covers an area of 1000 m^2. The analysis, design, implementation, and testing of the prototype are carried out. Subsequently, the data is sent to an IoT platform where it is collected, visualized, and analyzed in real time using the MQTT protocol as the central point of communication [10]. Path loss, receiver power, signal-to-noise ratio, receiver sensitivity, link budget, Fresnel zone, azimuth angle, and elevation angle are analyzed.

2 Methods

A methodology was followed to design and develop the proposed system, considering the requirements, analysis, design, and testing. The WSN LoRa wireless sensor network was designed with its corresponding design phases:

2.1 Hardware and Software Selection

The selection of components is based on the developer's requirements and the system architecture, considering coverage, compatibility, compact size, cost, and availability in the national market. For the node responsible for sensing environmental variables, the Arduino UNO board based on the ATmega328 microchip is chosen, as it has the necessary number of analog/digital pins to establish wireless communication with the central node. For wireless communication between the sensor node and the central node, as well as between the central node and the actuator node, the Dragino LoRa Shield based on the Sx1276 chip, and the Raspberry Pi 3 board are selected. These components allow for coverage of distances greater than 2 km. The chosen platform for registering the data sent by the sensors is ThingSpeak, as it provides suitable visualization of the collected data. The selected sensors are capacitive soil moisture sensor, LM35 temperature sensor, GUVA-S12SD UV radiation sensor and MH-RD YL-83 water or rain sensor. Figure 1 shows the general architecture of the WSN nodes with LoRa technology.

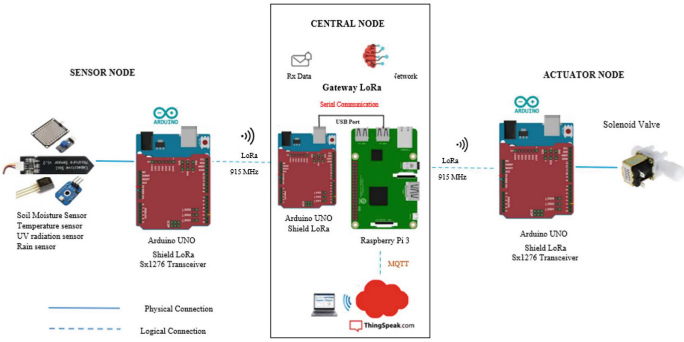

Fig. 1. General System Architecture.

2.2 Analysis of the Current Situation

There is access to a grass crop owned by one of the dairy association members, which covers a total area of 3400 m^2. For the development of this project, a sample of 1000 m^2 will be used, as shown in Fig. 2, the distribution of spaces between the plot, water source, and control center is shown.

Fig. 2. The blue area is the water source, the orange area is the control center.

2.3 Design of the System

In this phase, a star-type communication is established using LoRa technology be- tween the sensor and actuator nodes towards the gateway located in the central node. The central node receives sensor data through the MQTT protocol and visualizes it on an IoT platform.

2.4 Power Supply

Lithium batteries of 3.7 V and 6000 mAH are used to power the sensor node and actuator node. Additionally, a solar panel is available to recharge the batteries. On the other hand, the gateway is powered through a connection to the electrical grid using a 110 VAC to VDC power adapter.

2.5 Wireless Communication Design

The wireless communication is designed using a simulated radio link in Radio Mobile, with a frequency of 915 MHz, within the LoRa technology operating range of 902 to 928 MHz. Figure 4 shows the network diagram with the parameters of the nodes and the distances between them and the gateway (Fig. 3).

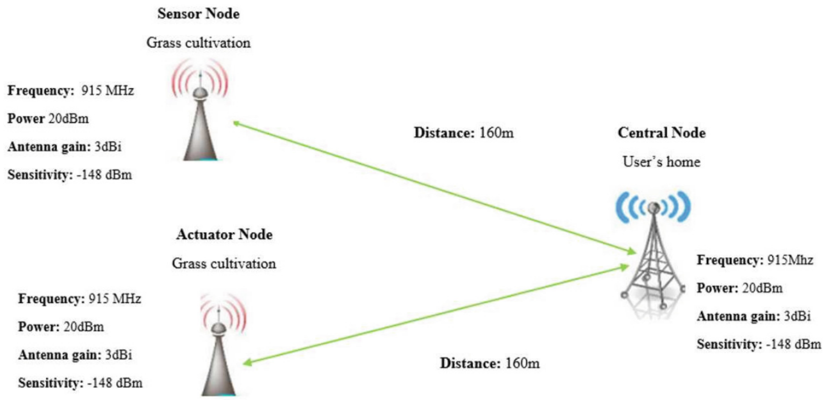

Fig. 3. Network diagram of the system.

Table 1. Coordinates of each node that forms the network.

Nodes	(Latitude)	(Longitude)	(Latitude)	(Longitude)
Gateway	0° 2′35.21″ N	78°17′35.03″ O	0.0431	−78.2930
Sensor Node	0° 2′31.65″ N	78°17′38.81″ O	0.0421	−78.2941
cre Actuator Node	0° 2′31.58″ N	78°17′38.77″ O	0.0421	−78.2941

Google Earth allows setting the latitude and longitude of the nodes and gateway, as specified in Table 1.

The communication yielded the following results: path loss between the gateway and the sensor node in free space of 75.75 dB, receiver power of 25 dBm, signal-tonoise ratio for LoRa communication between −20 dB and +10 dB, receiver sensitivity of −125 dBm, link margin of 150 dBm, link budget of 145 dBm, Fresnel zone of 3.62 m, azimuth angle of 47.72°, and elevation angle of 1.611°, see Fig. 4. Also, the heights of the antennas are varied to achieve a completely clear Fresnel zone, and the different simulated scenarios are detailed in Table 2.

Table 2. Propagation Characteristics

	Antenna height Sensor-Central	Worst Fresnel	Free Space Loss (dB)	Obstruction (dB)	Propagation loss (dB)	Worst (dB) reception (dB)
1	0.5–6	0.6 F1	75.8	0.5	81.3	91.7
2	1–6	0.8 F1	75.8	−0.5	80.3	92.7
3	1.5–6	1.0 F1	75.7	−0.8	80.0	93.0
4	3–6	1.2 F1	75.7	0.0	80.8	92.2
5	4.5–6	1.6 F1	75.7	0.2	81.0	92.0

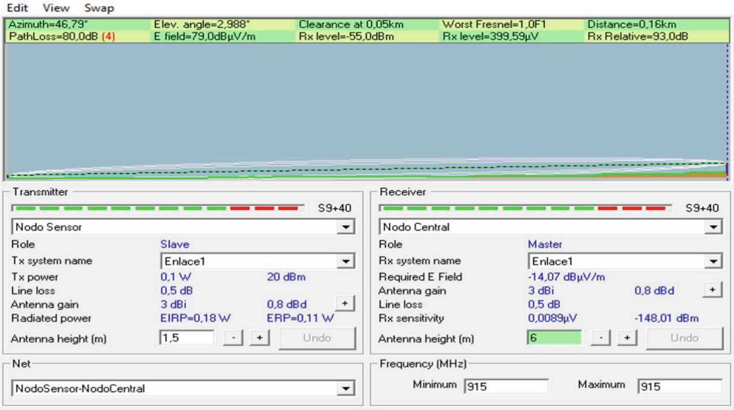

Fig. 4. Radio Mobile simulation - LoRa link between the sensor and gateway nodes.

In the link profile, free space losses remain unchanged with the antenna heights, while total propagation losses decrease as the antenna heights vary. A minimum Fresnel clearance of 0.6F1 is achieved, ensuring a smooth signal, as it should always be greater than or equal to 60%. The worst reception varies from 91.7 to 93 dB, indicating a safety margin with respect to the receiver sensitivity. The higher this value, the greater the assurance that the signal reaches the receiver. Figure 5 shows the results of the link between the sensor node and the central node. Also, the line of sight between the central node and the actuator node with the different simulated scenarios is observed in Table 3.

Table 3. Propagation Characteristics

	Antenna height Central-Actuator	Worst Fresnel	Free Space Loss (dB)	Obstruction (dB)	Propagation loss (dB)	Worst (dB) reception (dB)
1	6-0.5	0.6 F1	75.8	0.3	81.2	91.9
2	6-1	0.9 F1	75.8	−0.6	80.2	92.8
3	6-1.5	1.1 F1	75.8	−0.8	80.1	92.9
4	6-3	1.3 F1	75.8	0.7	81.6	91.4
5	6-4.5	1.6 F1	75.8	−0.2	80.7	92.4

The worst Fresnel value is 0.6 F1, the free space losses are approximately 76 dB, and the obstructions range from −0.8 dB to 0.7 dB. The total propagation losses reach 81.6 dB, and the worst reception approaches 93 dB. Based on the data obtained from the different scenarios, it can be concluded that all radio links are acceptable, as the first Fresnel zone exceeds 60%. However, for this project, Scenario 3 is implemented, with an antenna height of 1.5 m for the sensor and actuator nodes, and a height of 6 m for the central node.

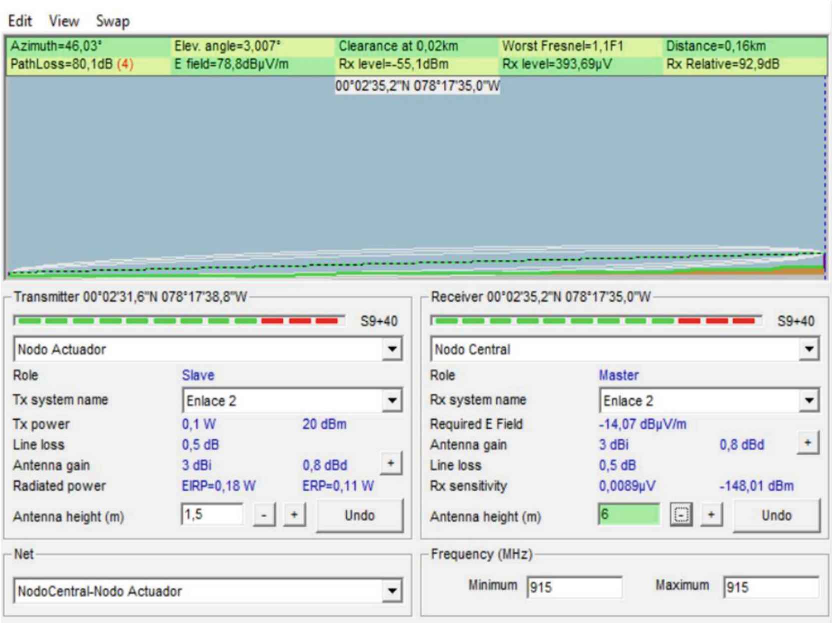

Fig. 5. Link between central node and actuator node.

2.6 Software Encoding of the System

The sensor and central nodes are encoded with the same configuration parameters to enable communication. The sensor node is responsible for reading the environmental variables, while the central node configures the gateway to send the data to the cloud using the MQTT protocol.

In Fig. 6 shows the flowchart of the sensor and gateway nodes. The sensor node waits to receive a request from the gateway and then sends the data obtained from the sensors. In the central node, the data sent by the sensor node is read. Finally, the sensor data is retrieved and sent to the ThingSpeak cloud server using the MQTT protocol.

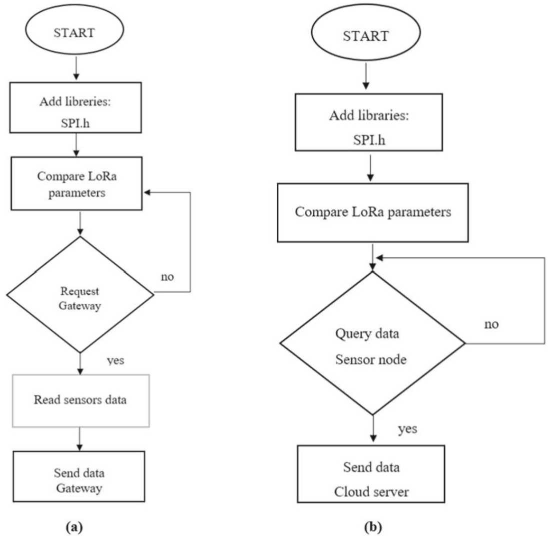

Fig. 6. Flowchart of the sensor node and central node.

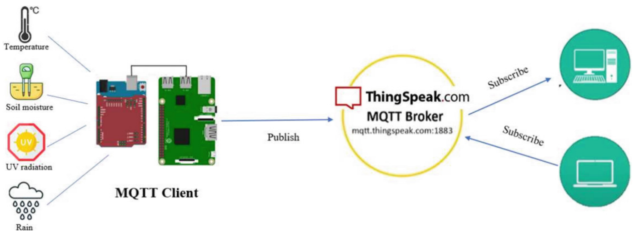

Fig. 7. Publish/Subscribe MQTT Architecture.

The system utilizes a basic star topology with the MQTT protocol, where all clients connect directly to the central point, known as the broker, which acts as a server. The system architecture is shown in Fig. 7. The Raspberry Pi3 board configures MQTT using the paho.mqtt.publish library. The corresponding Channel ID and Write API Key for the created channel are entered. Additionally, the MQTT host address is stored in a variable, and the topic is created for publishing the data. Finally, the temperature, humidity, UV radiation, and rain values are assigned to the fields created in the platform, allowing the updated values of each field to be observed in the channel.

3 Results and Discussion

The following aspects are verified: the electrical test of the sensor node, data collection, data reception, data presentation and wireless communication tests.

3.1 Sensor Node Electrical Test

The successful powering on of all system devices and proper voltage supply are verified. It is also ensured that the solar panel is charging the battery, as shown in Fig. 8.

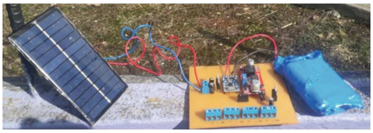

Fig. 8. Sensor Node powered by a lithium battery and solar panel.

3.2 Information Collection, Data Reception and Presentation

The sensor node measures environmental variables such as soil moisture, UV radiation, temperature, and rainfall. These data are sent through the LoRa wireless network to the gateway located in the central node. Measurements are taken both in the morning and in the afternoon. After collecting the data, the sensor node sends it to the central node, where the gateway is located. This process is carried out through wireless communication using the LoRa module at a frequency of 915 MHz. The results are shown in Fig. 9. Figure 10 graphically shows the data of the environmental variables from the communication between the sensor node and the gateway, taken at a specific time.

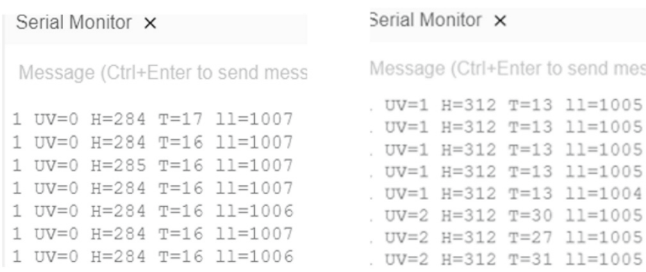

Fig. 9. Sending and receiving data from the central node-gateway.

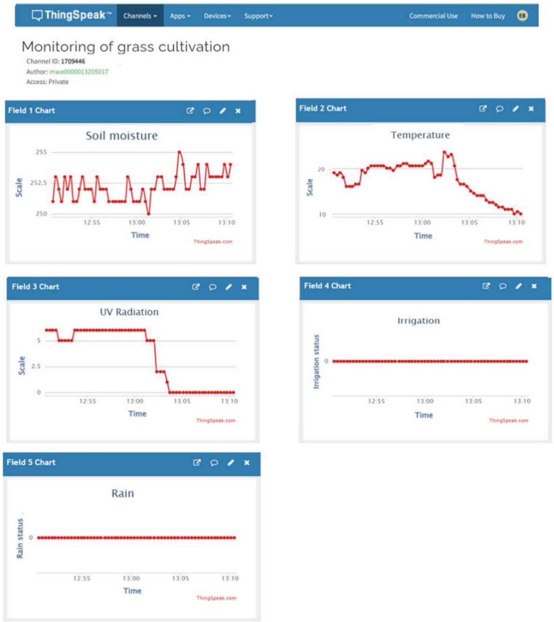

Fig. 10. Data Presentation in ThingSpeak.

3.3 Wireless Communication Testing

The wireless communication tests with LoRa technology proved to be adequate between the sensor node and the gateway at a maximum distance of 205 m without any data loss.

3.4 Airtime of Transmission

The airtime of a LoRa packet is calculated, which is the time it takes for a signal to be transmitted from a sensor node to be received by the gateway (receiver) node. This calculation is based on the spreading factor (SF), coding rate (CR), and signal bandwidth (BW). The airtime can be determined using the Eq. 1 [11].

$$ToA = T_{\text{preamble}} + T_{\text{payload}} \tag{1}$$

Where the preamble time is calculated using Eq. 2, where n_preamble is the preamble length, which according to the Semtech datasheet is programmed as 8 for the transceivers SX1276/77/78/79.

$$T_{\text{preamble}} = (n_{\text{preamble}} + 4.25) \cdot T_{\text{symbol}} \tag{2}$$

The symbol time is calculated using Eq. 3, where SF is the spreading fac-tor and BW is the bandwidth.

$$T_{\text{symbol}} = 2^{\frac{SF}{BW}} = 2^{\frac{7}{125}} = 1024 \tag{3}$$

By substituting this value into Eq. 2, we obtain that the preamble time is 12.54 ms.

$$T_{\text{preamble}} = (8 + 4.25) \cdot 1024 = 12.54 \tag{4}$$

To calculate the Payload time, it is necessary to know the symbol length in the payload. This can be calculated using Eq. 5.

$$N_{\text{payload}} = 8 + \frac{8PL - 4SF + 28 + 16CRC - 20IH}{4(SF - 2DE)}(CR + 4) \tag{5}$$

where:

- IH: Header, when enabled, the value IH is equal to 0; otherwise, it is 1.
- DE: Low Data Rate Optimize, the value DE is 1 when enabled, and the value DE is 0 for the other case.
- PL: Indicates the payload size in bytes.
- SF: Indicates the spreading factor.
- CRC: Indicates the cyclic redundancy check used for error detection. When enabled, it takes a value of 1; otherwise, it is 0. By default, it is disabled.
- CR: Indicates the coding rate, which can be in the range of 1 to 4 (1 corresponding to 4/5, 4 corresponding to 4/8).

By replacing this value in Eq. 5, we obtain a value of 58 symbols in the payload.

$$N_{\text{payload}} = 8 + \max\left(\left\lceil \frac{8(35) - 4(7) + 28 + 16(0) - 20(0)}{4(7 - 2(0))} \right\rceil \cdot (1 + 4), 0\right) = 58 \text{ symbols}$$

Once this value is obtained, we can calculate the duration of the payload using Eq. 7.

$$T_{\text{payload}} = N_{\text{payload}} \cdot T_{\text{symbol}} \tag{6}$$

Replacing the values, we obtain a payload time of 59.392 ms.

$$T_{\text{payload}} = 58 \cdot 1.024 = 59.39 \text{ ms} \tag{7}$$

Finally, we obtain the value of the airtime by replacing it in Eq. 1.

$$ToA = T_{\text{preamble}} + T_{\text{payload}} = 12.54 + 59.39 = 71.93\,\text{ms} \tag{8}$$

Figure 11 shows that the airtime is 71.94 ms, which is consistent with the calculations performed. This value can be verified using an online calculator for LoRa packets from Semtech modems, where the transmission parameters are entered, and the duration performance is obtained, including symbol time, airtime, preamble duration, and equivalent bit rate.

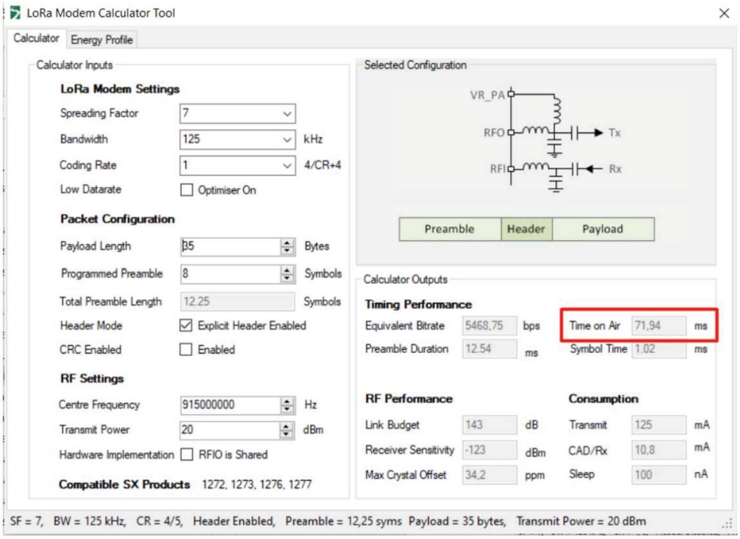

Fig. 11. LoRa Calculator for Airtime Calculation.

3.5 Spectral Analysis of LoRa Transmission

The Keysight N9322C spectrum analyzer is used to record and playback the captured signal traces. The spectrogram is used to visualize the spectrum of the signal in a LoRa transmission with different spreading factors (SF7 to SF12) in the LoRa nodes. The results obtained from the spectrum analyzer are presented in the Fig. 12.

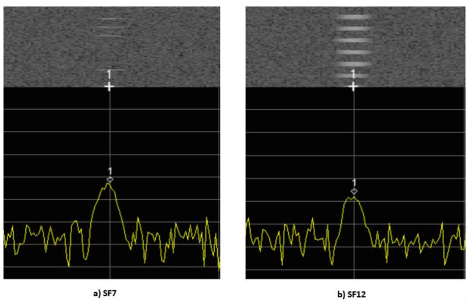

Fig. 12. Spectrum of the signal when varying the spreading factor from SF7 to SF12.

Each spectrum shows a colored horizontal line representing different signal amplitudes. In Fig. 13, the spectrum of a signal in MATLAB can be observed using a spreading factor SF7, with a packet airtime of 71.94 ms. Due to the short duration of this airtime, the signal is very faint and shorter compared to the spectrum of the signal using a spreading factor SF12. The latter signal has a longer airtime of 1646.59 ms., which allows for the distinction of a longer-duration signal.

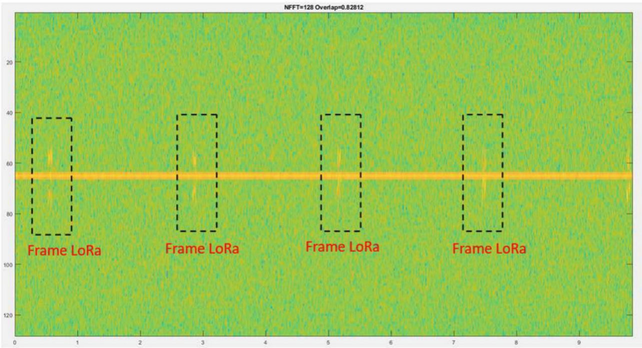

Fig. 13. Transmitted packets from the sensor node to the central node at 915 MHz.

3.6 MQTT Protocol Analysis

Once the TCP three-way handshake is completed, the client can connect to the MQTT broker to publish and subscribe to messages. The client sends a CONNECT packet to the broker to establish the connection. Then, access is granted, and a CONNECT ACK packet is responded, which contains return codes indicating the transmission status (success or error). Once the connection is accepted, messages can be published (PUBLISH) from the client to the broker or vice versa. In this field, the Topic is specified, which identifies the ThingSpeak channel ID. The last captured message is the DISCONNECT, indicating the closure of the connection sent from the client to the broker or vice versa. In this case, the client only publishes sensor data, so only the mentioned MQTT messages are captured. See Fig. 14.

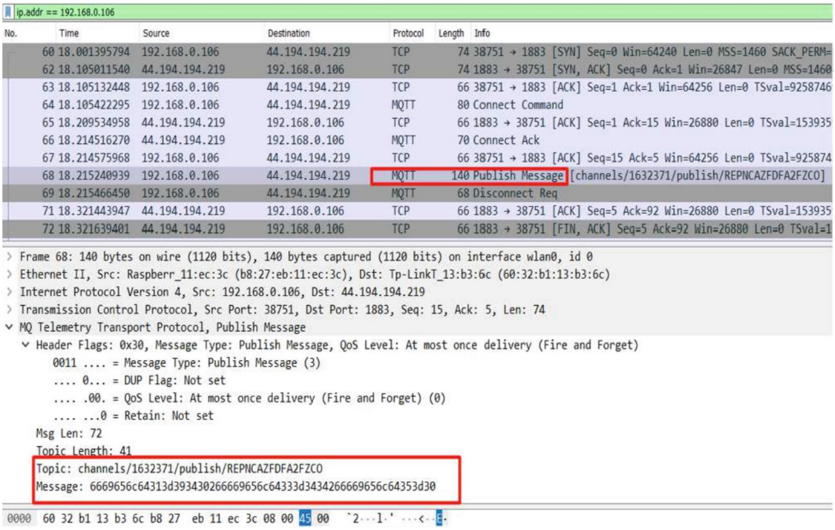

Fig. 14. MQTT Messages: Connect, Connect ACK, Publish, Disconnect.

4 Conclusions

– Appropriate devices were used for the sensor node, actuator, and central node, meeting the system requirements to establish a stable communication and perform data transmission and reception.
– An electrical test was conducted to verify that the power board supplies power to the sensor nodes, actuator, and gateway for approximately 24 h. If necessary, the battery can be recharged using the micro-USB port of the TP5046 charging module with 5 V.
– The transmission of environmental variables data from the sensor node to the central node was successfully carried out, complying with the parameters established in the radio link simulation to ensure an obstruction free transmission.
– For communication using LoRa technology, the following parameters were determined: spreading factor (SF7), bandwidth of 125 KHz, error coding rate of 4/5, and transmission power of 20 dBm, resulting in an approximate airtime of 70 ms.
– The data of the environmental variables sent by the sensor node were published via the MQTT protocol on the ThingSpeak platform, where they are represented through graphs with an update frequency of every 15 s.
– A LoRa WSN wireless sensor network was designed with four components (humidity, temperature, UV radiation, and rainfall sensors), enabling the monitoring of environmental variables. Historical records and graphs were generated based on the measurements from the sensor node, which will serve as background information for future studies.

– To facilitate the presentation of clear and accurate results, the ThingView software was used. It is a mobile application that provides access to ThingSpeak channels through a user-friendly interface. The data can also be displayed on the LCD screen of the central node in case the user doesn't have internet access.
– The implementation of a wireless sensor network using LoRa technology is versatile, as there are various solutions available from different manufacturers, catering to different budgets, objectives, and ranges. Although in this case it was implemented in a plot with less than one kilometer between the sensor node and the gateway, LoRa technology offers coverage of over two kilometers, allowing for implementation in larger areas without difficulties.

5 Recommendations

– The gateway requires a stable internet connection to ensure efficient packet routing and enable data visualization in the cloud.
– It is recommended to perform an initial charge of the lithium batteries of the sensor and actuator nodes through the micro-USB port.
– It is important to ensure a clear line of sight between the sensor node and the gateway, as obstacles can weaken the transmitted signal. This may require adjustments in the network design during development.
– It is recommended to adjust the airtime of the transmission to optimize performance and minimize propagation losses, maximizing the power used.

6 Future Work

This phase and its preliminary results lay the foundation for the implementation of crop-oriented systems in rural environments.

References

1. Castro, M., Espin, F.: Análisis de los factores que determinan la sostenibilidad y sustentabilidad de la economía social y solidaria para la crianza y comercialización de vacuno en pie y faenado en los cantones Quito, Cayambe y Pedro Moncayo. Tesis **1**, 17 (2016)
2. Chacón, P.: Cultivo de pastos. SN Power Proyecto Cheves **1**, 40 (2015)
3. Red IAPD. Libro de actas del I Congreso en Investigación en Agricultura para el Desarrollo (2011)
4. Hidalgo, K., et al.: Plan de Desarrollo y Ordenamiento Territorial-Pedro Moncayo 2018-2025 (2018)
5. Leon, R., Bonifaz, N., Gutierrez, F.: Pastos y Forrajes del Ecuador (2018)
6. Jhomaira, B.: Red WSN para el control y monitoreo de un sistema de riego por goteo de una plantación de fresas en la granja experimental Yuyucocha - UTN. Universidad Técnica del Norte (2014)

7. Leandro, S.: Diseño de un sistema de riego inteligente para cultivos de hortaliza basado en Fuzzy Logic en la granja La Pradera de la Universidad Técnica del Norte. Universidad Técnica del Norte (2019)
8. Dario, C.: Diseño de un sistema para el control de riego mediante técnicas de aprendizaje automático aplicadas a la agricultura de precisión en la granja La Pradera de la Universidad Técnica del Norte. Universidad Técnica del Norte (2020)
9. Dominguez, A.: Diseño de una red de sensores inalámbricos LPWAN para el monitoreo de cultivos y materia orgánica en la granja experimental La Pradera de la Universidad Técnica del Norte," Universidad Técnica del Norte (2020)
10. Nettikadan, D., Raj, S.: Smart community monitoring system using thingspeak IoT plaform. Int. J. Appl. Eng. Res. **13**(October), 13402–13408 (2018)
11. Semtech. Semtech SX1276 (2020)

Artificial Intelligence, Towards the Diffusion of Cultural Tourism in the D.M. Quito

Geovanny Javier Cujano Guachi(✉) and Victoria Estefanía Segovia Mejia

Instituto Tecnológico Vida Nueva, Quito 170126, Ecuador
geovanny.cujano@istvidanueva.edu.ec

Abstract. The need to generate a digital participatory experience approach requires the adaptation of tourism to the automation of processes, these induce the digitalization and revolution of the immersive experience of tourists, through virtual reality, management of big data and artificial intelligence (AI).). It is therefore essential to analyze the AI to process opinions and interests of the visitors and determine the effectiveness of the interaction of the AI with the tourist. The use of methodologies and models such as safety and security, lean and agile, georeferenced information systems, seek to articulate tourism products to the digital environment. The study applies an AI model with social interaction in cultural visiting sites, the results demonstrate the feasibility of analog conversion to a digital environment, presenting schemes and necessary means for the adoption and adaptation of cultural tourism to the digital world.

Keywords: Cultural tourism · Artificial intelligence · Digital transformation

1 Introduction

The concepts of artificial intelligence (AI) are present in the data analysis process, mainly from those businesses that massify and universalize products or services. [1] considers that a corporate strategy used is the use of an information system, tourism faces the need to generate an experience design focused on the user in addition to combining the participatory experience. That is why the research seeks to formulate the analysis of the AI to process the opinions and interests of the visitors, determine the active interaction of the AI with the tourist, to achieve the purpose the research focuses on parameters and methodology of [2] who develops the term safety and security in tourism, and the Lean and Agile methodology. The results will allow to establish the changing preferences of tourists, to apply it to the AI so that the algorithm understands the preference qualities. All this embodied in a web page that collects the data and presents results. The main function is to digitize the tourism sector, providing both establishments and tourists with information and preference profiles, while ensuring the data and well-being of the visitor in matters of health and integrity. So that the research question is answered: Is it necessary to generate a user-focused experience design that can combine the participatory experience through tourist contact with AI, to determine preferences? [2] When the tourist experience enters a virtual world, [1] The application of Virtual

M. Z. Vizuete et al. (Eds.): CI3 2023, LNNS 1040, pp. 46–58, 2024.
https://doi.org/10.1007/978-3-031-63434-5_4

Reality (VR) in conjunction with Artificial Intelligence (AI) represents a revolution in the sector such as those led by the arrival of the first websites dedicated to tourism or applications for mobile devices with services tourist.

1.1 Technological Disruption

[3] artificial intelligence is in an embryonic state. Despite the condition, 3 stages are developed that the process of adopting technological innovation must follow, focused on the implementation of artificial intelligence.

- Progressive process innovation
- Innovation in new products and services (incremental)
- Disruptive technology innovation [4]

The interpretation of artificial intelligence, through processes, takes the following scenarios.

- Replacement: ratio of readaptation of human tasks by technology
- Increase: increase of attributes of the machines
- Symbiosis: mutual interaction of each of the individuals [4]

When engaging the service sector, it is necessary to categorize [5] Artificial Narrow Intelligence, (ANI), the cognitive capacity in relation to common sense is not very objective, inferior to human capacity [6] Artificial General Intelligence (AGI), objective ability to solve broad problems. In this sense, projects such as receptionist robots in hotels in Japan are being developed, or human symbiotic-empathic translator machines, such as assistants with artificial intelligence (Google, Alexa…).

Digital Tourism Sector. The trace of tourists on the internet, based on their products and search for destinations, through mobile devices, payments, consumption of both suppliers and opinions, rating of platforms and services as well as social networks.

By combining artificial intelligence and tourism, data is obtained on behaviors, information, needs, heterogeneous nature. Data that can be potentiated once the type of user is defined, offering successful tourist products and solutions, and at the same time personalized [7] Technological generation has an impact on the tourism industry Perfection and the search for process perfection drive digitalization [8].

The contribution of artificial intelligence to tourism has been framed in the ease of communication with the tourist, in this way both; Machines like robots carry artificial intelligence and perform some service, [9] the interaction of elements in the digital composition of a service involves the ability of AI, in continuous learning this allows perfection in customer preferences based on the service.

The AI applications used in tourism are:

Internet Of Things [10]. It is the interrelation between elements with AI principles, it interconnects, monitors, manages and identifies preferences in a product or service.

Virtual assistants and chatbots: [11] blend hybrid skills integrating human qualities that bring AI closer to learning tasks including natural language processing.

Blockchain: time chain information blocks in digital transaction actions

Tourism as an interdisciplinary study [12] tourism is a phenomenon that encompasses open systems that make it an interdisciplinary study, it is from this point the opening of tourism to work with ICTs and therefore with the digitization process. The structuring of the tourist market classifies the tourist activity as follows [13].

From this foundation, the definition based on the digitization of tourism, openness to the application of the safety and security methodology, this type of environment generates an analysis of the content to be presented based on the priorities of the tourist and their profile.

Tourism in cultural places of visit In this category are considered the tourist activities carried out to Museums, monuments, historical sites [14]. The fundamental purpose is to know the history, art, and culture found in a destination. From this perspective, it can be defined that:

Museums monopolize the distribution and syncretism of a culture [15], Museums monopolize the distribution and syncretism of a culture, it is considered as a center that presents culture and preservation through the collection of cultural manifestations that influence lifestyle [8].

Within the category of historical monument, it focuses on places with particular historical background determined by a structure that mixes urbanity and identity [8].

Historical ensembles: A historical ensemble or [10] historic center involve aspects that represent social development [16] the preservation of this style of resource allows to preserve the identity and cultural knowledge of a locality [18] the following stages should be considered:

- Control of load capacity, through controls of crowded areas
- Use of AI, to reduce intermediation
- Unique digital identification of the traveler (Safety and security)

The benefits of the implementation of AI, in the cultural sites of visit, allows to save costs of productivity, interpret the quality of the service and innovation.

To revolutionize the tourist experience through the use of ICTs, 3 dimensions must be considered to follow [3]:

- Digitization of content: this process will make it possible to visit the destination from a controlled environment, in addition to providing a universal panorama due to the availability of dialects
- Technological scope: platforms and means of reaching Artificial Intelligence
- Marketing: focuses on the lines of promotion that maintain social relations.
- Security: through public-private cooperation they must regulate the sector to be digitized [3].

2 Methods

2.1 Desing

The study methodology focused on the review of the literature, this with the purpose of obtaining quantitative and qualitative aspects through primary studies, with the objective of understanding the information on a particular topic, for its subsequent analysis, comparison and description of results [19].

For the review and orientation of the research, the quantitative study was proposed, based on the statistics of technical aspects of artificial intelligence, in cultural sites visited, for which models of digital transformation of services are used based on of cultural policies [13].

The focus of the research is of a simple descriptive nature, due to the intention of detailing the phenomenon of artificial intelligence in a cultural interpretation center, be it a museum, historic center or monument.

As a phenomenon for the study, the environment of the museums within the MD Quito is considered, which have their expression in painting, sculpture or architecture, combining the elements corresponding to cultural tourism [20] For the implementation of artificial intelligence, the approach of the [21] an agile museum, which applies in the context of a cultural center the deployment of virtual assistants with artificial intelligence for relative interaction with the visitor.

The methodology, used in the model of [22] It covers the articulation of artificial intelligence and a museum: this method called Lean and Agile, covers the design of a digital, multimedia experience between the tourist and the object.

The theoretical axis of the research is based on models proposed in various investigations.

- Geographic information systems: articulation of businesses focused on tourism, forms of digitization of georeferenced tourism products and services.
- Virtual reality/big data and artificial intelligence: Immersive virtual reality application format
- Internet of things: Management of virtual environments in areas of universal access to tourism
- Cultural and arts digital organizational development model: attributes to the organization the hierarchical pyramid, organization and work forces, for hybrid work, human and artificial intelligence
- Agile Museum: Applies in the context of a cultural center the deployment of virtual assistants with artificial intelligence for relative interaction with the visitor.
- Safety and security: Tourist card or passport model with tourist profiles and preferences, which protects integrity.
- Virtual assistants/chartboots and Blockchain: Applications for tourism with artificial intelligence
- Lean and Agile: Implementation of digitization in museums focused on the visitor experience.

The exposed models articulate the process of implementation of artificial intelligence in cultural visiting sites.

2.2 Population and Sample

For the purpose of the population, all the tourist companies involved in the physical and digital market are incurred, through the SITURIN and MINTUR records, the establishments considered in the study are. Food and beverages, Cafeterias, Restaurants, Intermediation Operation, Tourist transport and museums, in addition to the number of tourists who visit the D.M Quito, the total result is 4542. The population is classified as indefinite due to lack of updated data in the records of government entities. Once the total amount has been determined with the statistical calculation of an infinite sample, the total of 202 tourists who receive the product is determined, this will allow defining their preferences before the study created, and 123 tourist establishments, which will be surveyed randomly.

2.3 Instrument and Data Collection

For the data collection of tourists, a questionnaire used in the investigation is adapted and taken: exploration of social benefits for tourism Performing arts and industrialization in culture - tourism integration based on deep learning technology and artificial intelligence. The questionnaire is applied in dimensions of a social nature, taking cultural tourism (performing art and industrialization) and artificial intelligence as the central axis. It uses 11 items, to which a 5-point Likert scale is adapted. The questionnaire is divided by indices (G1, G2, G3).

G1 Index: From the perspective of (kim & others, 2022), it is necessary to analyze the social benefit in the city in relation to cultural tourism, use of resources, that is, how cultural tourism contributes to improving the living conditions through the inclusion of social economic relationship.

- Cultural heritage: articulates cultural identity and collective memory, safeguards the values of social heritage through the transferability of values
- Employment: Virtual Reality (VR) and Artificial Intelligence (AI) to tourism will mean a new revolution in the sector such as those led by the cheaper means of transport or the arrival of the first websites dedicated to tourism or the appearance of applications for mobile devices with tourist services, therefore, better living and employment conditions
- Quality of life: Data that can be potentiated once the type of user is defined, offering successful tourism products and solutions, and at the same time personalized.
- Infrastructure: the infrastructure of services interrelates the disruptive innovation of services

G2 Index: The importance of environmental care is part of large cities and their culture, [17] the cities carry the cultural heritage of the aboriginal peoples and these are promoted with cultural tourism, the higher the level of conservation, the greater the probability of maintaining and sustaining a representative tourist resource.

- Ecological environment: focuses on concepts of sustainability through the preservation of a legacy for future generations, uses the potential of tourism to conserve natural and cultural areas.
- Cultural protection: it constitutes a fundamental anthropological element for social sustainability.
- Environmental protection: focuses on the cultural component from the proactivity of individuals for the conservation of ecological zones.

G3 Index [18] the importance of cultural tourism in relevant social benefit in the economic aspect, which allows covering the implementation of digital systems.

- Economy: The use of economic systems through articulated information allows the digitization of processes focused on social and tourism benefits.
- Profitability: forms a visible finite chain by studying social enactment factors
- Utilities: the benefits of technologies are considered based on connectivity
- Return: tourism is a phenomenon that encompasses open systems that make it an interdisciplinary study, it is from this point the opening of tourism to work with ICTs

Dimensions: For the structure of internal coherence, the development of dimensions is incurred as:

- Cultural tourism: In the publication of ICOMOS in the Charter of Cultural Tourism (1976) it has the function of promulgating the historical and artistic social relationship.
- Environmental cultural heritage includes digitization actions in the conservation of customs and traditions of tourist spaces.
- Artificial Intelligence Artificial Narrow Intelligence (ANI), and Artificial General Intelligence (AGI) is one that can only provide solutions to one or a spectrum of cognitive and common-sense abilities that are inferior to human capacity.

Items for Validity Analysis

Table 1. Questionnaire adapted from the publication [18] exploration of social benefits for tourism Performing arts and industrialization in culture - tourism integration based on deep learning technology and artificial intelligence.

Variable	Item
cultural tourism	
TC1	Building artificial intelligence systems can link local cultural resources and the developing city
TC2	Cultural tourism generates jobs for the local population
TC3	The economy grows and the quality of life improves with cultural tourism
TC4	The infrastructure focused on cultural tourism, such as transportation, provision of basic services, improves considerably
Environmental cultural heritage	
HCA1	The ecological environment linked to cultural tourism as a heritage of the peoples is adequately treated
HCA2	The cultural environmental environments of the city are preserved and valued

(*continued*)

Table 1. (*continued*)

Variable	Item
HCA3	Local residents feel the benefit of protecting and conserving a cultural natural asset
Artificial intelligence	
IA1	The implementation of artificial intelligence can attract foreign tourists to promote local development and related industries
IA2	The implementation of artificial intelligence is capable of generating a net benefit of profitability to a cultural tourism project
IA3	The generation of artificial intelligence projects can cover its operating costs with the dissemination of cultural tourism
IA4	The inclusion of companies related to cultural tourism to artificial intelligence programs may reflect the ability to use capital to generate income

The data adapted from the questionnaire were analyzed through the validity of constructs and dimensions (Table 1).

Reliability analysis of the construction of the questionnaire: According to, [26] This process makes it possible to define the validity and precision of an instrument before its application, considering this aspect for the execution, 10% of the sample was taken so that a vision and perspective of the formulation of the questions can be obtained, contrasted with the previous results. The results reflect the 0.824 level of reliability, in Cronbach's Alpha.

Once the data collection instruments have been applied, the analysis is carried out based on the following antecedents:

- To determine the valid variables applied in the questionnaire addressed to tourists and the instrument focused on tourism companies, the construction of the tourist passport was defined through the analysis of communalities of each one.
- Structure of constructs of and dimensions of the variables adopted.

Analysis and Data Processing

[19], determines that the validity of constructs is fundamental to determine the data and the design that will be used to evaluate them, so that the applied instruments are within the variables and results presented, which is why in the processing of cases in SPSS the data was established in two parameters, one for the population of 202 tourists and 123 tourist companies.

The approach that was given to the processing of cases, to the companies related to the tourism field, who contribute their criteria to the development of the investigation based on this new form of content dissemination.

Analysis of construct strengths and information relationship in the instrument applied to tourists. Once the data is processed, the relationship of the two instruments is considered, determining that there is a relationship between the data and these will allow as a result to know the aspects with the greatest impact to be reflected in the development of the virtual passport (Tables 2 and 3).

Table 2. Analysis of the intelligence system construct

Construct	Number of indicators	Reliability	Cronbach's alpha
TC	6	0.96	0.955
HCA	3	0.86	0.770
IA	5	0.90	0.869

Table 3. Result of the analysis of the tourist passport construct

Construct	Number of indicators	Reliability	Cronbach's alpha
IAT	5	0.90	0.871
AV	4	0.97	0.967
CTU	5	0.93	0.911

Finally, the proportions of communalities obtained were analyzed so that the questions and results of the proposed items can be related (Table 4).

Table 4. Analysis of the tourist intelligence system

Construct items	C	CF
Building artificial intelligence systems can link local cultural resources and the developing city	.821	.507
Cultural tourism generates jobs for the local population	.596	.618
The economy grows and the quality of life improves with cultural tourism	.552	.363
The infrastructure focused on cultural tourism, such as transportation, provision of basic services, improves considerably	.804	.657
The ecological environment linked to cultural tourism as a heritage of the peoples is adequately treated	.751	.409
The cultural environmental environments of the city are preserved and valued	.552	.423
Local residents feel the benefit of protecting and conserving a cultural natural asset	.708	.485
The implementation of artificial intelligence can attract foreign tourists to promote local development and related industries	.547	.524

(*continued*)

Table 4. (*continued*)

Construct items	C	CF
The generation of artificial intelligence projects can cover its operating costs with the dissemination of cultural tourism	.678	.536
La generación de proyectos de inteligencia artificial puede cubrir sus costes operativos con la difusión del turismo cultural	.607	.364
The inclusion of companies related to cultural tourism to artificial intelligence programs may reflect the ability to use capital to generate income	.529	.494

Table 5. Analysis of the tourist intelligence system

Items of the tourist passport construct	C	CF
Do you believe in the reinvention of tourism through artificial intelligence?	.670	.534
Is artificial intelligence part of tourism competitiveness?	.799	.539
Do you think artificial intelligence favors the tourism industry?	.636	.559
What kind of tourists do you receive in your travel agency?	.560	.553
Can a personalized service be provided through the virtual passport?	.722	.417
With the creation of a virtual passport, what types of services would it include?	.716	.554
Can the needs of tourists be identified with the virtual passport?	.754	.427
What would you like to see inside the virtual passport?	.708	.478

Result of the communities found tourist passport variable (Table 5)

Analysis of communalities of the virtual passport variable

Once the data has been analyzed, the means that the development of the project will cover can be defined, especially the presentation and common data that will be placed in the tourist passport such as:

- Active tourism companies
- Contribution of tourism companies to the sustainable development of the truism
- Acts to protect and conserve a cultural natural asset.

3 Discussion

Tourism products maintain a level of degradation due to physical contact with the tourist. Artificial intelligence, and digitization means allow to preserve elements of the cultural heritage, for future generations [4] Immersive virtual reality allows you to explore beyond time and space and even beyond other barriers such as language. From the results obtained, it can be defined that the main function of AI is to digitize the tourism sector, providing both establishments and tourists with information and preference profiles, while ensuring data and well-being. of the visitor in matters of health and integrity. Thus, it is considered necessary to generate a user-focused experience design that can combine the participatory experience through tourist contact with AI, to determine preferences.

To achieve this purpose, it is essential to consider that immersive VR can improve historical and geographical knowledge and the sensory approach allows you to enjoy a different tourist experience in a specific destination. To this same sense joins [10], who defends the context of the use of artificial intelligence as a strength of tourism as a means of sustainability of resources and tourist attractions, becoming a tool in favor of cultural destinations (Fig. 1).

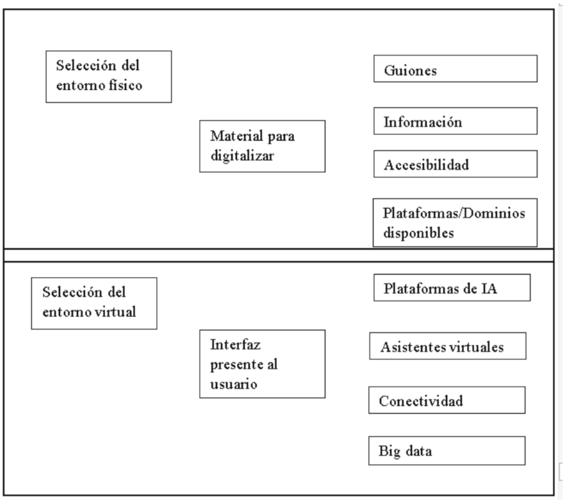

Fig. 1. Initial outline of the AI application

Schemes focused on the analysis of [13] The approaches of artificial intelligence in the tourist experience are determined in three perspectives (Table 6).

The models approach takes the analysis and transcription of [13]. By adopting the Lean and Agile model. In this way, the results are articulated in the provision of the page in which the tourist passport is hosted, as an initiative for the dissemination and virtualization of the experience through companies dedicated to tourist activity (Fig. 2).

Table 6. Models applied to cultural centers through AI

Design	*Model and methodology*	*Approach*
User-focused experience design	Hybrid experience model that qualifies human-computer interaction	AI must process the opinions and interests of visitors
Participatory experience design	Qualitative experience model (HISTOQUAL/SERVPERF/SERVQUAL)	Analyze the interaction of AI with the tourist
Agile experience design	Lean and Agile model, adapted to AI in a tourist space	Analyzes the changing goals and preferences of tourists, to apply it to AI so that the algorithm understands the qualities of preference

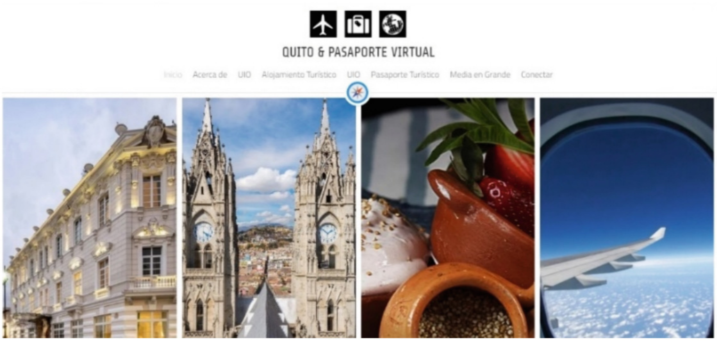

Fig. 2. The page is located at the address: https://pasaporteuio2023.mystrikingly.com/

4 Conclusion

The feasible means for the application of artificial intelligence are available to tourism, Models such as Safety and security, guarantee the integrity of the tourist in addition to determining the profile and preferences, shortening the intermediation process, the qualities of the Lean and Agile Model, focus on the transformation of a physical environment into a universal digital space within the reach of tourists. Artificial intelligence is the future of cultural tourism, the physical means are degrading, but the elements stored in the big data allow us to obtain a retelling of the lived history. Artificial intelligence, from the results obtained, allows to disseminate visitor preferences, in addition to keeping updated records of visits and even generating habits and frequency of visits, the models considered analyze social, economic and even political aspects of visitors.

The proposed methodological approach determines that, in the tourism field, especially in the approach to consumer experiences through artificial intelligence, the methodology of the hybrid experience model qualifies the human-computer interaction, the qualitative model of experiences (HISTOQUAL/SERVPERF/SERVQUAL) makes it possible to define satisfaction through the expectations and perception of the tourist and the Lean and Agile model, adapted to AI, adapts a service to a digital environment. The results, embodied in the development of the page, allow us to identify the articulated qualities of the interaction necessary for the development of a tourist adaptation system through the digitization of needs, taking the use of artificial intelligence as a strength of tourism. as a means of sustainability of natural and cultural resources and tourist attractions.

Work presented is an adaptation to artificial intelligence, thus increasing efficiency and tourist quality, giving a technological turn to tourist services, through the analysis of outbound tourists and tourism companies that collaborate actively with the product obtained. Project follow-up is vital, to correct alternative methodologies to the application, from the perspective of the study, the Safety and security and Lean and Agile methodology, allow defining the preferences for product selection, in future research, These methodologies could focus the tourism sector on the development of digitization.

References

1. Sastre, D., Martín, I., Martín, L.: La experiencia 5G en el turismo: el caso de Segovia, Ciudad Patrimonio de la Humanidad. Rev. Ibérica Sistemas Tecnol. Inf. **E24**, 336–348 (2019)
2. de Oliveira, D.: Tarjeta turística safety and security: el pasaporte para turistas y destinos seguros. Cuadernos Turismo **46**, 489–504 (2020)
3. de Oliveira, D.P.: Safety and security tourist card: the passport for tourists and safe destinations. Cuadernos Turismo **46**, 653–654 (2020)
4. González, D.: Modelos de gestión de museos con Inteligencia Artificial. Editorial Universitat Politècnica de València, pp. 685–697 (2022)
5. Almeida, M.: Robots, inteligencia artificial y realidad virtual: una aproximación en el sector del turismo. Cuadernos Turismo **44**, 13–26 (2019)
6. Barrera, C., González, J., Cáceres, G.: Toma de decisiones en el sector turismo mediante el uso de Sistemas de Información Geográfica e inteligencia de negocios. Rev. Científica **38**(2), 160–173 (2020)
7. Car, T.: Internet of things (IoT) in tourism and hospitality: opportunities and challenge. Tour. South East Eur. **5**, 163–175 (2019)
8. Chión, S., Charles, V.: Analítica de datos para la modelación estructural. Pearson Educación, Lima (2016)
9. Hegley, D., Tongen, M., David, A.: The Agile museum. In: MW2016: Museums and the web (2016). https://mw2016.museumsandtheweb.com/paper/the-agile-museum/
10. Lulia, D.: Aplicaciones de la inteligencia artificial en el sector turístico (2020). http://repositori.uji.es/xmlui/bitstream/handle/10234/194538/TFG_2020_Diana%20Iulia%20Iosivan.pdf?sequence=1
11. Melançon, M.: The USPTO's sisyphean plan: Increasing manpower will not match artificial intelligence's inventive capabilities. Texas Law Rev. **96**(4), 873–889 (2018)
12. Rodriguez, J.: Conocimiento y aprendizaje en las grandes cadenas hoteleras españolas en Iberoamérica: internet como herramienta de aprendizaje organizativo. Cuadernos Turismo **21**, 135–137 (2008)
13. Sabiescu, A.: A critical reflection on three paradigms in museum experience design. In: Vermeeren, A., Calvi, L., Sabiescu, A. (eds.) Museum Experience Design. Springer Series on Cultural Computing, pp. 259–276. Springer, Cham (2018). https://doi.org/10.1007/978-3-319-58550-5_13

14. Canavire, B.: Inteligencia artificial, cultura y educación: una plataforma latinoamericana de podcast para resguardar el patrimonio cultural. Rev. Científica Ciencias Soc. **21**, 59–71 (2023)
15. Cortes, S.S.: Evolución del concepto de servicescape: revisión sistemática de literatura 1995–2017. Rev. Espacios **39**(04) (2018)
16. Determinación de indicadores pertinentes para utilizar dentro de un sistema de gestión de información turística para el departamento de Casanare. Turismo Soc. XX **20**(10), 191–209 (2018)
17. Hui-Min, Y.W.: Design of eco-tourism service quality evaluation model based on artificial neural network. In: 2020 IEEE International Conference on Industrial Application of Artificial Intelligence (IAAI), pp. 119–124. IEEE (2020)
18. Zhang, R.: Exploración de beneficios sociales para el turismo Artes escénicas Industrialización en la integración cultura-turismo basada en tecnología de aprendizaje profundo e inteligencia artificial. Front. Psychol. **12**, 1–11 (2021)
19. Arévalo, D.S.G.: La gestión de departamentos y destinos turísticos de Colombia según el Índice de Competitividad Turística Regional (ICTRC). Rev. Int. Turismo Empresa Territorio **4**(2), 158–177 (2020)
20. Manterola, C., Astudillo, P., Arias, E., Claros, N.: Revisiones sistemáticas de la literatura. Qué se debe saber acerca de ellas. Cirugia Española **91**(3), 149–155 (2013)
21. Olmos, L., Garcia, R.: Estructura del Mercado turístico. Paraninfo, España (2016)
22. Panosso, A., Lohmann, G.: Teoria del Turismo. Trillas, Colombia (2012)

Real-Time Data Acquisition Based on IoT for Monitoring Autonomous Photovoltaic Systems

Fernando Jacome(✉), Henry Osorio, Luis Daniel Andagoya-Alba, and Edison Paredes

Instituto Superior Universitario Rumiñahui, Sangolquí, Ecuador
fernando.jacome@ister.edu.ec

Abstract. Technological development has made photovoltaic systems more accessible for applications in domestic self-generation microsystems. In this context, new monitoring techniques are necessary to visualize the operating status of photovoltaic systems components. The main objective of this work is to monitor the operation status of a photovoltaic system through remote measurements in real-time using IoT technology. The study used IoT technology for the remote acquisition of principal elements of a photovoltaic system data to show them in time series through a graphical interface. The study resulted in a real-time remote monitoring system that allows the observation of photovoltaic system variables. The study concludes that through IoT technology, complex real-time monitoring systems of photovoltaic system operating variables can be configured to store them in a database that allows the visualization and analysis of historical data behavior of photovoltaic systems.

Keywords: Photovoltaic System · Remote Monitoring · IoT · Electrical Variables

1 Introduction

Technological development has made photovoltaic systems more accessible for domestic self-generation microsystems. In this context, new challenges are presented for network operators and for end users who implement these systems, for self-consumption and for distributed generation. These new challenges not only have to do with the installations and their impacts but also with the monitoring and management systems of this type of equipment. In this context, new monitoring techniques are needed to visualize the state of the components of the photovoltaic systems [1].

The current technological advances in the field of monitoring techniques present a constant evolution, going from being manual to being carried out through automatic processes using advanced devices and complex processing procedures, both for the acquisition and analysis of data. In [2], a review of the development of some data monitoring techniques for the diagnosis of the state of photovoltaic panels is carried out.

M. Z. Vizuete et al. (Eds.): CI3 2023, LNNS 1040, pp. 59–70, 2024.
https://doi.org/10.1007/978-3-031-63434-5_5

In this study, a general classification is made into three groups. Manual methods that are applied to small systems, these techniques include visual inspection, reflectometry methods, and ground capacitance measurements. Semi-automatic methods, in this group are thermal cameras, infrared or electroluminescent images for locating faults in a large-scale system. The automatic methods used in a general way with algorithms based on modern techniques of analysis and data treatment are also proposed.

One of the ways used in automatic methods is the development of monitoring systems based on IoT applications, these have become a viable alternative in remote monitoring systems development that could be very useful in places with difficult access and where is difficult to have the necessary infrastructure to carry out some type of manual or semi-automatic monitoring [3, 4]. IoT-based monitoring systems are mainly made up of sensors, Arduino brand prototype development boards and Raspberry Pi microcomputers which, depending on the configuration, obtain data from a photovoltaic system that are displayed on display screens and/or mobile applications or also stored. in a physical database or in a data cloud. Initially, these methodologies were developed for monitoring the variables of the photovoltaic panels, but later they have been used for other applications such as estimates of the operating state of the system in general [3, 5–8].

In other studies, new methodologies are developed to improve the processes of acquisition, presentation and treatment of data. In [9], a data acquisition methodology based on IoT technology is presented. This study develops a data acquisition scheme with three levels, in the first one the current, voltage, temperature and solar irradiance data are taken through sensors. At the next level, these data are sent through the internet to finally present them in a third phase on a web platform or stored in a database. The device is made with Arduino technology both for the data acquisition from the sensors and for the transmission of them for them to be presented in real-time. In this same context, the study [10], presents a methodology where the use of a SCADA system is proposed as a means of monitoring variables. This methodology also uses sensors, an Arduino device to receive the variables and Raspberry Pi to manage and send the data.

IoT-based methodologies have also been developed as automatic techniques for monitoring photovoltaic operating variables through remote data acquisition. In general, these methodologies use sensors, data acquisition devices such as Arduino and data processing through a Rasberry Pi, however, the last one is not always used, but a remote server can also be used for the analysis of the data obtained. The variables that are taken through sensors are voltages, currents, temperature and irradiance at certain points of a photovoltaic system, this can be variable depending on the study to be carried out [11–14].

The main objective of this work is to monitor a photovoltaic system operation state through remote measurements in real-time using IoT technology. For this, the process has been divided into four stages, data acquisition, data processing, sending the data to a cloud database and displaying them. The main contribution of the project is related to the unification of the data acquisition process, treatment and presentation of them in online visualization platforms, which makes this model a remote and real-time monitoring system, in addition to show of a backup of the monitored variables stored in time series data, all of this, based on IoT technology. These systems are suitable to be applied in autonomous photovoltaic systems, especially in those with difficult access and where the necessary infrastructure to establish conventional communication systems is not available.

2 Methodology

The proposed methodology consists of four stages as indicated in Fig. 1. The first consists of the variables measurement through the sensors installed in certain points of the photovoltaic system, the second consists of the acquisition of sensor data through an Arduino device and the sending to a cloud through a Rasberry Pi. The third consists of the treatment of the data obtained in a Rasberry Pi microcomputer and finally a fourth stage where the data from the sensors are sent through the Internet to a display device which can be a mobile or a server. Each of the stages is detailed below in Fig. 1.

For filtering of data obtained from the sensors, the Arduino MeanFilter library was used, which implements a moving average filter. This filter stores a certain number of samples to define the window used by the filter to later obtain the average. A window

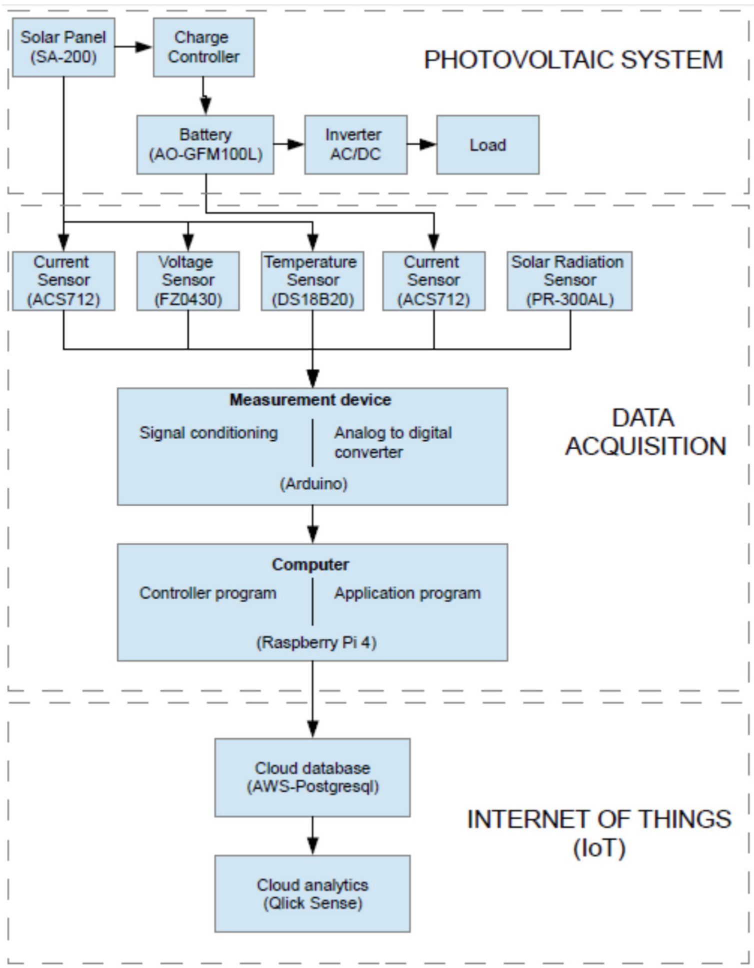

Fig. 1. Photovoltaic Monitoring System Diagram Using IoT.

of 10 samples was used. The moving average filter is widely used in signal acquisition systems and does not have a high computational cost to be implemented on a prototyping board such as Arduino.

2.1 Variable Measurement Process.

The measurement process is carried out through sensors located at specific points of the photovoltaic system. The variables taken are Voltages, Current, Irradiance, Temperature in the photovoltaic panel and Current in the battery. ACS712 Current [15], FZ0430 Voltage [16], DS18B20 Temperature [17] and Radiation PR-300AL [18] sensors are used.

To minimize the measurement error, the values from sensor of the solar irradiance variable were contrasted with a commercial solar irradiance meter such as the TES 132 DataLogging Solar Power Meter. In the same way, Current and voltage measurements were contrasted with Proskit MT-3109 Multimeter. TES 132 is showed in the Fig. 2.

Fig. 2. TES 132 Data-logging Solar Power Meter.

2.2 Data Acquisition and Sending

The data acquisition and filtering process is carried out through an Arduino device that is responsible for converting the analog signals of the sensors to digital signals and then sending them through the Raspberry Pi 4 device to a storage cloud and a visualization platform in real-time through IoT technology. In this stage, there is a remote measurement process through sensors, IoT devices and data storage in time series.

2.3 Data Processing

Data processing for visualization is done through IoT processes directly on the Rasberry Pi, which acts as a central node that receives, processes, and sends the data. The data collected from the sensors and monitoring devices is processed on the Raspberry Pi using specific algorithms and models designed to identify normal operation patterns and detect possible parameters whit any error that could affect the complete measurement process.

The monitored variables are Radiation, Solar Panel Voltage, Solar Panel Current, Solar Panel Temperature and Battery Current.

2.4 Results Visualization

Data processing for visualization is done through IoT processes; in the case of storage, it was done through an open-source relational database AWS-PostgreSQL. This database management system is known for its open source, reliability, scalability, and ability to manage a large volume of data. Choosing AWS-PostgreSQL ensures secure and efficient storage of collected data in the system.

For data visualization, the Qlik Sense application has been used, which is a tool that allows the interactive dashboards and graphics creation to analyze and visualize data effectively, with Qlik Sense.

The flow diagram of the proposed methodology is presented in Fig. 2.

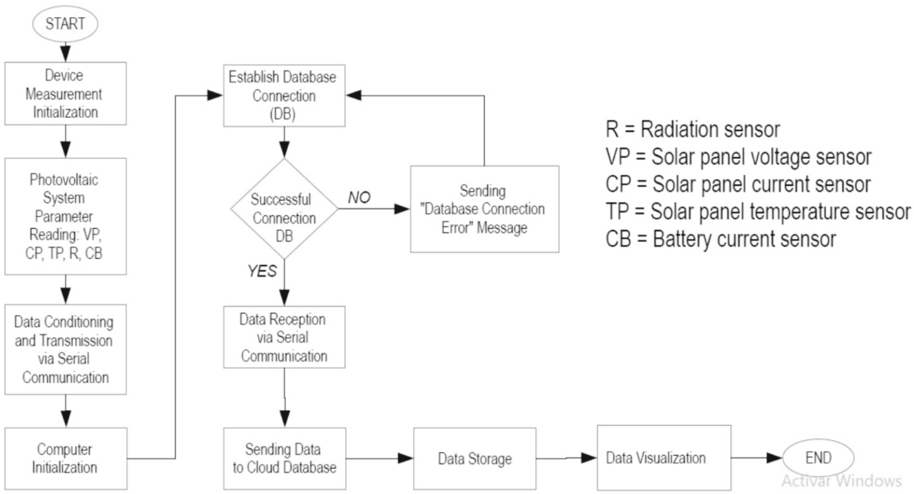

Fig. 3. Monitoring System Flowchart of photovoltaic system using IoT.

3 Results

The present work is based on the data acquisition system development for a photovoltaic system characteristic variables observation. The project is based on IoT technology for data acquisition from a photovoltaic system.

The methodology has been applied in a real test photovoltaic system located in the Instituto Superior Tecnológico Rumiñahui building located in the Pichincha province.

The test system consists of the next elements:

Photovoltaic module: 200 W photovoltaic panel, 21 V of open circuit voltage and 12.82 A of short circuit current.
Battery module: Gel battery, capacity of 100 Ah at 12 V.
Charge regulator: Solar Charge Controller PWM, nominal voltage of 12–24 V and maximum current of 20A.
Voltage Inverter: 1KW DC/AC inverter, nominal voltage 12 VDC/110 VAC.
Current sensors: ACS712.
Loads: 4 LED lights of 9 W.
Raspberry Pi: Model 4 with 8 GB of RAM and 32 GB of SSD.
Arduino: UNO R3 Model.
Voltage Sensor: FZ0430.
Temperature Sensor: DS18B20.
Radiation Sensor: PR-300AL.

The complete test of the Photovoltaic System is shown in Fig. 4.

Fig. 4. Test Photovoltaic System.

The application results of this methodology are detailed below:

The first process of the present study is focused on the remote acquisition of data through IoT technology use. This methodology allowed the collection of relevant information for the analysis of the test photovoltaic system state. These data are related to voltage, current, temperature in the solar panel and solar irradiation that it receives. For this, the system was configured to monitor, acquire and record the data every 5 min during an initial period of 3 months. This sampling frequency made it possible to obtain a large amount of data in a significant time interval, which is essential to perform a representative analysis and understand the behavior of the system in real-time. The results obtained were validated by real measurements with the respective equipment intended for these purposes.

The collection and storage of this data have two main purposes. To observe clearly the values of the photovoltaic system operating variables in real time to verify its operation, which allows observing the efficiency of the system and determining the need to carry out some type of maintenance in it.

The data obtained from the IoT system during the week of June 11 to June 15, 2023, are presented below. These data are of great importance because they will provide detailed information about the behavior of the system under specific conditions and will be useful as a guide for the analysis and estimation of the photovoltaic system operation state.

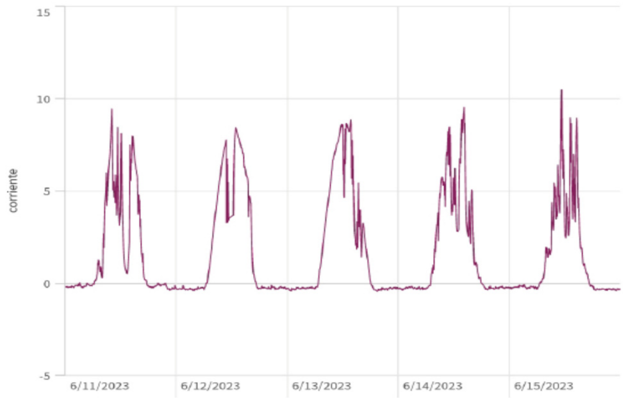

Fig. 5. Current at Photovoltaic Panel output obtained by the Monitoring System.

The graphic of Fig. 5 presents the current data obtained at the photovoltaic panel output of the test system, it clearly shows the variation of the current generated by the photovoltaic panel, which allows us to identify patterns, trends, and potential irregularities in panel performance. The fluctuations in the generated current values are influenced by solar radiation and ambient temperature. During the hours of maximum solar radiation, it is expected that the generated current reaches its highest values, while, in periods of less solar radiation, the current may decrease.

The graphic of Fig. 6 represents the voltage values recorded by the monitoring and measurement device for five days. This graphic provides detailed information on how the voltage varies in time, which helps us to identify patterns, trends and possible problems in the operation of the panel through the voltage values recorded in time series. The voltage variation in a day is directly influenced by solar radiation and ambient temperature. During the hours of greatest solar radiation, it is supposed that the voltage reaches its maximum values, while, at times of less solar radiation, the voltage can decrease to its minimum values.

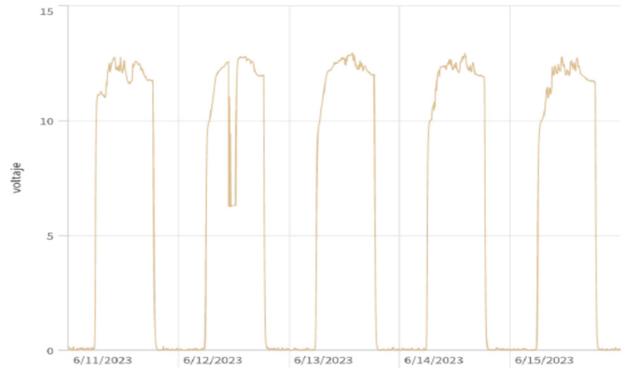

Fig. 6. Voltage at Photovoltaic Panel output obtained by the Monitoring System.

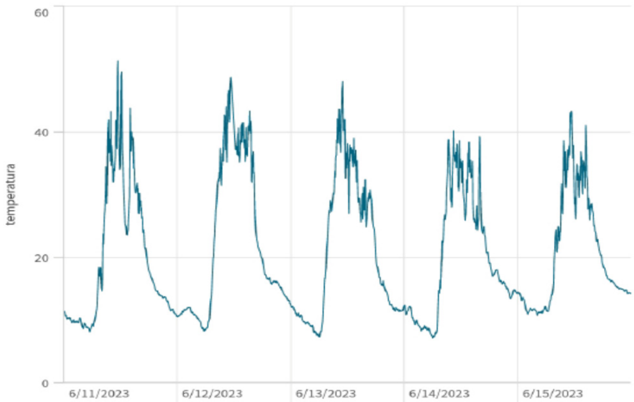

Fig. 7. Temperature on Photovoltaic Panel obtained by the Monitoring System.

The graphic in Fig. 7 provides detailed information about the temperature fluctuations produced on the photovoltaic panel throughout the day. The efficiency of the photovoltaic panel is influenced by its temperature, an increase in temperature can decrease the efficiency of solar cells and reduce energy production. Therefore, it is important to monitor this parameter to assess system performance and take corrective actions on time.

The graphic in Fig. 8 provides detailed information about the incident solar radiation on the photovoltaic panel and its variation during the day, which allows us to understand how solar radiation affects the energy production of the photovoltaic panel. The graphic shows how solar radiation varies throughout the day, with radiation peaking during the hours of greatest solar intensity, generally at noon. The graphic could also give radiation information based on seasonal patterns and differences in solar radiation between cloudy and clear days.

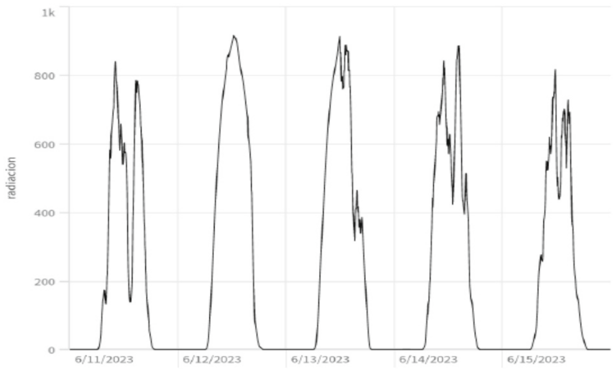

Fig. 8. Radiation on Photovoltaic Panel obtained by the Monitoring System.

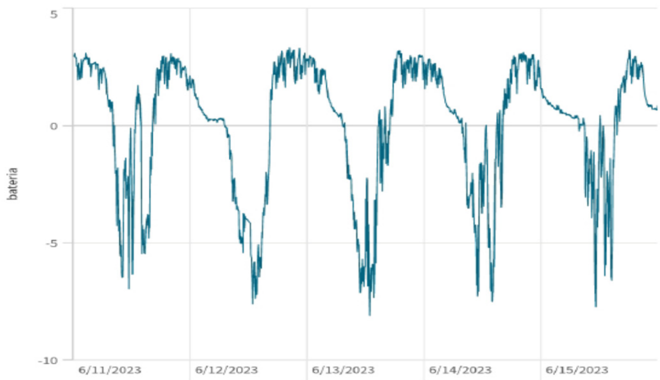

Fig. 9. Current from the battery obtained by the Monitoring System.

The graphic of Fig. 9 shows the current measurements in the battery throughout a week, in it, we can see positive values that represent an energy contribution to the load and negative values that correspond to the battery charge with the energy from the photovoltaic panel. With these values, it is possible to have patterns of battery behavior that could give information about the battery state operation.

Table 1 shows a descriptive statistic applied to data acquired from the monitoring system. In this table, solar irradiance has a maximum of 1100 W/m^2 with standard deviation of 414.19 W/m2 that represents solar irradiation of one day. Instead, module temperature has a maximum temperature of 56.75 ºC with a standard deviation of 11.59 ºC and a minimum of 5.88 ºC.

Table 2 shows a correlations analysis of measurement variables. In the table, Solar irradiance and PV temperature have a high correlation with PV power generation.

Compared to the method presented in [3] and [4] which use the ThingSpeak Platform, the data of the present work is stored in a cloud database for further analysis and visualization in different time frames. In this way, you can see how the measured variables behave over days, weeks or months.

Table 1. Descriptive Statistics of measured variables

	Voltage	Current	Solar Irradiance	Temperature	Power > 0
Mean	11.228	3.208	594.529	25.960	36.936
Standard Error	0.031	0.026	3.741	0.105	0.305
Mode	9.877	0.481	0.000	12.500	0.107
Median	11.402	2.270	658.540	24.000	26.262
First Quartile	10.037	0.744	154.086	15.937	8.385
Third Quartile	12.081	5.071	1024.525	34.687	58.189
Variance	11.591	8.127	171553.990	134.537	1140.081
Standard Deviation	3.405	2.851	414.191	11.599	33.765
Kurtosis	4.680	−0.508	−1.589	−0.839	−0.226
Skewness	0.080	0.833	−0.180	0.437	0.902
Range	23.056	11.399	1100.351	50.875	149.866
Minimum	0.123	0.005	−0.001	5.875	0.100
Maximum	23.179	11.404	1100.350	56.750	149.966
Sum	137598.389	39318.393	7285953.798	318143.546	452651.517
Count	12255.000	12255.000	12255.000	12255.000	12255.000

Table 2. Correlation analysis of measured variables

Correlations	Voltage	Current	Solar Irradiance	PV Temperature	Power
Voltage	1.0000				
Current	0.0941	1.0000			
Solar Irradiance	0.4486	0.8024	1.0000		
PV Temperature	0.4313	0.8250	0.9095	1.0000	
Power	0.1828	0.9876	0.8127	0.8431	1.0000

As mentioned in [2], the most widely used technology is WIFI, which shows good performance for distances of up to 100 m. Regarding security, the device with WIFI connection and Internet access is the Raspberry PI that has a Linux-based operating system installed that is less prone to security flaws, although updates to this operating system must be made regularly.

4 Conclusions

IoT technology is an effective and promising solution in the field of remote monitoring photovoltaic systems variables, the main advantage of these systems is the ability to present real values of the monitored variables and facilitates the visualization of the monitored system operating status.

The study demonstrated the feasibility of using IoT technology for real-time remote monitoring of photovoltaic systems variables. The results obtained allowed us to observe the variability of the characteristic variables of monitored systems by time series analysis techniques.

The adequate treatment of the data acquired through IoT technology, especially through time series analysis techniques, provides important information for decision-making based on data and the implementation of corrective actions in a timely manner in the case to detect any anomaly in the data obtained by the monitoring system.

The remote monitoring system based on IoT technology can be the initial point for the development of new advances in the field of remote monitoring. The system stores the results obtained in time series in a database, which makes it possible to identify behavior patterns and therefore the possibility of observing an anomaly that could be due to a fault at some point in the photovoltaic system.

References

1. Masson, G., Bosch, E., Kaizuka, I., Jäger-Waldau, A., Donoso, J.: Snapshot of global PV markets 2022 task 1 strategic PV analysis and outreach PVPS (2022)
2. Mellit, A., Kalogirou, S.: Artificial intelligence and internet of things to improve efficacy of diagnosis and remote sensing of solar photovoltaic systems: challenges, recommendations and future directions. Renew. Sustain. Energy Rev. **143**, 110889 (2021). https://doi.org/10.1016/j.rser.2021.110889
3. Priharti, W., Rosmawati, A.F.K., Wibawa, I.P.D.: IoT based photovoltaic monitoring system application. J. Phys. Conf. Ser. **1367**(1), 012069 (2019). https://doi.org/10.1088/1742-6596/1367/1/012069
4. Muthusamy, S.: Fault detection and monitoring of solar PV panels using internet of things. Int. J. Ind. Eng. **2**, 146–149 (2018)
5. Tellawar, M.P., Chamat, N.: An IOT based smart solar photovoltaic remote monitoring system. Int. J. Eng. Res. **8**(09) (2019)
6. Gopal, M., Prakash, T.C., Ramakrishna, N.V., Yadav, B.P.: IoT based solar power monitoring system. In: IOP Conference Series: Materials Science and Engineering, vol. 981, no. 3, p. 032037 (2020). https://doi.org/10.1088/1757-899X/981/3/032037
7. Rerhrhaye, F., et al.: IoT-based data logger for solar systems applications. In: ITM Web Conference, vol. 46, p. 01003 (2022). https://doi.org/10.1051/itmconf/20224601003
8. Vujović, I., Koprivica, M., Đurišić, Ž.: Monitoring and management solution for distributed PV systems based on cloud and IoT technologies. In: 2022 30th Telecommunications Forum (TELFOR), pp. 1–4 (2022). https://doi.org/10.1109/TELFOR56187.2022.9983768
9. Sasikala, G.: Arduino based smart solar photovoltaic remote monitoring system. Malays. J. Sci. 58–62 (2022). https://doi.org/10.22452/mjs.vol41no3.8
10. Aghenta, L.O., Iqbal, M.T.: Development of an IoT based open source SCADA system for PV system monitoring. In: 2019 IEEE Canadian Conference of Electrical and Computer Engineering (CCECE), pp. 1–4 (2019). https://doi.org/10.1109/CCECE.2019.8861827

11. Ahmad, S., Shakir, M., Ahmad, B., Aslam, Z., Qaiser, M., Aslam, S.: Development of an IoT based DAQ system for PV monitoring and management. In: 2022 International Conference on Engineering and Emerging Technologies (ICEET), pp. 1–6 (2022). https://doi.org/10.1109/ICEET56468.2022.10007393
12. Hojabri, M., Kellerhals, S., Upadhyay, G., Bowler, B.: IoT-based PV array fault detection and classification using embedded supervised learning methods. Energies **15**(6), Art. No. 6 (2022). https://doi.org/10.3390/en15062097
13. Mellit, A., Hamied, A., Lughi, V., Pavan, A.M.: A low-cost monitoring and fault detection system for stand-alone photovoltaic systems using IoT technique. In: Zamboni, W., Petrone, G. (eds.) ELECTRIMACS 2019. LNEE, vol. 615, pp. 349–358. Springer, Cham (2020). https://doi.org/10.1007/978-3-030-37161-6_26
14. Hamied, A., Boubidi, A., Rouibah, N., Chine, W., Mellit, A.: IoT-based smart photovoltaic arrays for remote sensing and fault identification. In: Hatti, M. (ed.) Smart Energy Empowerment in Smart and Resilient Cities. LNNS, vol. 102, pp. 478–486. Springer, Cham (2020). https://doi.org/10.1007/978-3-030-37207-1_51
15. Current Sensor ACS712 (AC or DC) 30A. Future Electronics Egypt. https://store.fut-electronics.com/products/current-sensor-acs712-ac-or-dc-30a. Accessed 19 Mar 2023
16. Módulo Sensor Medidor de Voltaje Breakout FZ0430. Carrod. https://www.carrod.mx/products/modulo-sensor-fz0430-medidor-de-voltaje-breakout. Accessed 19 Mar 2023
17. J. A. K. Electronics. DS18B20+PAR Maxim Integrated - Analog Output Temperature SensorsJAK Electronics. https://www.jakelectronics.com/productdetail/maximintegrated-ds18b20par-6131397 Accessed 19 Mar 2023
18. Intelligent Detection of Solar Radiation Energy. https://rainbowsensor.en.made-in-china.com/product/uwrtdLzYggRo/China-Intelligent-Detection-of-Solar-Radiation-Energy.html Accessed 19 Mar 2023

Georeferenced Maintenance Management of Public Lighting Systems Using IoT Devices

Angel Toapanta(✉), Daniela Juiña, Byron Silva, and Consuelo Chasi

Instituto de Investigación Geológico y Energético IIGE, Quito, Ecuador
angel.toapanta@geoenergia.gob.ec

Abstract. Public lighting plays an essential role in our communities; it not only provides visibility during the nighttime hours, but also has a significant impact on safety, quality of life, economic activity, and social cohesion in urban areas. Its importance stems from its ability to create secure, attractive, and functional environments for all citizens. Quito's city reports of failures or breakdowns in luminaires or lamp pole are typically obtained from users who detect the issues and the time it takes to resolve the reported problem is high, making the lighting service inefficient for pedestrians and drivers. In the present work, a public lighting maintenance management system has been developed to optimize maintenance tasks for luminaires and lamp pole. This system employs technologies like the Internet of Things (IoT), data-driven planning, and automated tracking to improve efficiency, costs reduction, and maintain reliable and safe public illumination. The proposed system includes an IoT device responsible for real-time data collection about the state of luminaires, lamp pole, energy consumption, operation, and other relevant parameters. This is possible due to integrated sensors that detect faults, changes in lighting intensity, and other anomalies. The data collected by the IoT device is transmitted to a broker and stored in a NoSQL database. Subsequently, this information is analyzed using the proposed software, enabling pattern and trend identification, set thresholds and alerts to detect issues like inactive lights, changes in energy consumption, or performance deterioration, planning maintenance, task tracking, and route optimization.

Keywords: Street Lighting · IoT · Maintenance · Management · LoRa · MQTT · NOSQL

1 Introduction

About 2900 TWh of electrical energy is consumed annually for indoor and outdoor lighting; considering the expansion of cities and companies worldwide, in the next 20 years, there will be an approximate increase of 50% in current demand levels [1].

We use lighting daily in all the spaces where we live and work. Artificial lighting systems are a tool that greatly impacts productivity and the quality of life of living beings. Environments with an adequate lighting system provide safety and allow road and pedestrian mobility [2].

M. Z. Vizuete et al. (Eds.): CI3 2023, LNNS 1040, pp. 71–82, 2024.
https://doi.org/10.1007/978-3-031-63434-5_6

The public lighting system is one of the sources of the greatest energy consumption and also requires good management and investment to maintain and control energy consumption [3]. In Ecuador, public lighting systems are in charge of the electric companies around the country [4].

When thinking about new lighting installations, must be a strategy integrated to concentrate services such as internet, lighting, and fiber optic connections for building within the same infrastructure; this is how, in recent years, there has been interest from tell managers in the field of public lighting systems to integrate intelligent devices through a network with internet with which it is possible to: monitor, control, and even keep historical records of the inventory of street lighting luminaires [5], as well as the status of all its components, thus allowing to reduce the time of attention to failures to maintain the quality indexes of the street lighting service [2].

To repair a luminaire, it is crucial to know the technical specifications such as the type of technology, auxiliary equipment for its operation, power, voltage, current, the height at which the luminaire is installed, and many other details that facilitate the maintenance of this and thus reduce operating costs for this type of corrective maintenance. When there is a record of damage to the components or the installed luminaire itself, can perform failure analysis, can be planned preventive and corrective maintenance that may require. This action reduces operating costs and the acquisition of consumables, accessories, and spare parts.

1.1 Previous Works

In the literature, there are different proposals for the design and implementation of monitoring and control of public lighting systems to reduce energy consumption and maintenance costs.

Chunguo Jing et al. in their work show a wireless sensor network system consisting of a sensor node installed on each pole to detect and control the luminaires; the remote terminal unit that serves as a transmission station using the GPRS network between the control center and the sensor nodes; and the control center that monitors and controls all the luminaires in real time [6].

Lavric et al. presents a monitoring and control system based on a WSN network that allows remote control of street lighting luminaires. When the system detects a vehicle, the light intensity of the luminaires is increased to a predetermined level so as not to affect traffic safety and reduced in the opposite case; furthermore, employing current sensors, allows the identification of any possible malfunction of the luminaires [7].

Also, one of the most popular and versatile schemes proposed is the Zigbee network-based scheme; several authors use them effectively in their models; Yusoff et al. suggest a system for street lighting control based on Zigbee. The wireless Zigbee network monitors street lighting from a base station. In addition, it incorporates an automatic mode of operation that uses light sensors to automatically turn on the luminaires when the daylight intensity drops below a certain level [8].

On the other hand, Kurman et al. proposes a system that uses ZigBee-based wireless devices and also combines with sensors to control and guarantee the lighting parameters of the system. They have designed and implemented a monitoring system based on Internet technology integrated with street lighting. The mode adopted in this monitoring system is the Browser/Server mode, which uses the technologies of an embedded web server (standard web browser over the Internet) [9].

Other authors present schemes for the control and monitoring of public lighting systems, focusing mainly on providing facilities and information for the maintenance of these systems; Bezbradica et al. present a system for measuring the light intensity and GPS positioning of public lighting luminaires, creating a database that stores more than just the coordinates. This intelligent system consists of a central control and database which allows the management, programming, and analysis of the lighting system and coordinates information from traffic and weather sensors; communication between the software and the switch is established via Ethernet, fiber optics, and GPRS. The switch cabinet allows data collection from street lighting sensors for every 50 luminaires [10].

Additionally, Kumar et al. propose a system for collecting and analyzing information about street lighting infrastructure. They develop an automobile-mounted sensor platform that allows for collecting and recording data from luminaires during nighttime tours. This platform enables mapping street lighting levels, identifying luminaires, estimating their heights, and geo-tagging them. It highlights an image recognition algorithm to identify luminaires from the video data collected by the sensor platform and its subsequent use in estimating heights. With this, they develop a semi-live virtual three-dimensional street lighting model at an urban scale [9].

2 Methodology

The proposed block diagram for the geo-referenced maintenance management system for street lighting using IoT devices is shown in Fig. 1 shows the proposed block diagram for the geo-referenced maintenance management system for public lighting luminaires using IoT devices [11]; The system consists of three stages:

1. IoT Public Light Device: This is responsible for data collection and transmission. It replaces traditional photocells and will be installed on each luminaire.
2. Maintenance Management System: This is responsible for analysis, monitoring, and maintenance management. It is hosted on the free tier of Amazon Web Services (AWS), which offers flexibility, scalability, security, and a variety of cloud services [12] cal interface through which the end user can interact with the system [13].

The block diagram in Fig. 2 shows the components of the IoT field devices, which are constituted by a VAC/VDC converter that will provide power to all the electronic components of the device, a microcontroller with built-in memory for processing and treatment of signals from the sensors, a wireless communication module to transmit the information from each luminaire to the router reaching stage 2, a GPS module to provide the location of the luminaire, a current sensor to determine the operating status of the luminaire, an ambient light sensor to provide information for switching the luminaire on or off, an accelerometer to detect events such as impacts and changes in orientation on the lamp pole, a power relay to activate the output of the luminaire's power supply circuit [14].

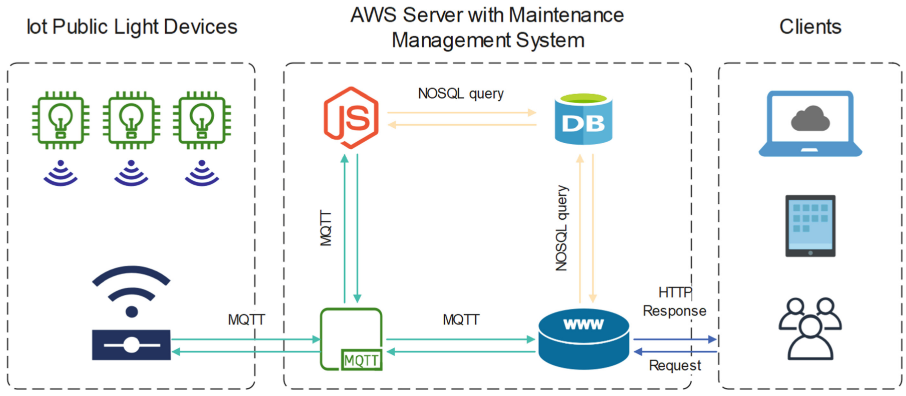

Fig. 1. Proposed system block diagram

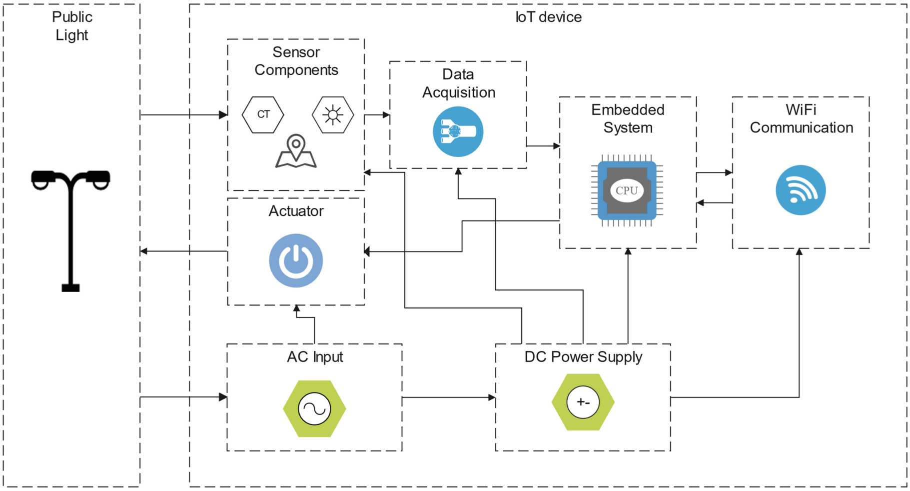

Fig. 2. Block diagram corresponding to IoT field devices.

2.1 Sensors of the IoT Field Device

Current Sensor TA12–200. El sensor de corriente TA12–200 permite adquirir los datos de corriente que circula a través de la luminaria para establecer su estado de funcionamiento. Las principales características de este sensor son:

Transformation ratio: 2000:1
Input current: 0-5A
Non-linearity: $\leq 0.2\%$
Phase shift: $\leq 5°$

BH1750 Light Sensor. The BH1750 photodetector is based on a photodiode, a trans-impedance amplifier, and a filter. Its single-chip construction reduces noise sources as a result of the integration of the amplifier and the photodiode; the sensor has a spectral response capability close to the response of the human eye in the 400 nm and 700 nm range, and the amplifier output signal is digitized by a 16-bit ADC [15].

NEO-6M GPS Positioning Sensor. The NEO-6M GPS is a 50-channel device with a time-to-first-correction (TTFF) of less than 1 s; its design and technology suppress sources of interference and mitigate the effects of multiple trajectories. In addition, it has a dedicated acquisition engine, with 2 million correlators, capable of performing massively parallel searches in time/frequency space, allowing it to find satellites instantly. The information is extracted from the minimum recommended position data of the $GPRMC sentence NMEA 0183 standard packet protocol Quetec: L80 GPS Protocol Specification (2014) [16].

MPU-6050 Accelerometer. The MPU-6050 accelerometer is a six-axis sensor that combines accelerometer and gyroscope on a single chip. It uses I2C communication and offers accurate measurement with configurable sensitivity. It has digital filters to improve measurement quality and can detect events such as impacts and changes in orientation. Low power and compact size [17].

2.2 Acquisition of Data

Each IoT device has a conditioning stage for the signals of each analog sensor for which an ADC converter of 4 analog channels with a resolution of 16 bits with a sampling rate of up to 860sps and an I2C serial data bus is used.

In the case of the current sensor, a precision resistor of 800 ohms recommended by the manufacturer is used to convert the current signal to a voltage signal of 2V, and this signal enters the ADC for further processing.

The light, gps and accelerometer sensors have embedded conditioning and transmit data through I2C serial data buses.

2.3 Embedded System

IoT applications generally use embedded SoC (System-On-Chip) controllers and Open Source Hardware, as is the case of Arduino and ESP32; this type of Hardware does not usually carry an operating system, and its programming is based on C and C++ [18]. This component performs the logic (algorithms) related to acquisition, conversion, quantification, and co-communication. The proposed IoT field device is developed on a 240 MHz Tensilica LX6 dual-core + 1 ULP, 600 DMIPS ESP32 SoC, including a 19 dB maximum output power SX1276/SX1278 LoRa chip. The ESP32 SoC is dual-core so that separate tasks can be assigned to the different cores, which is a great advantage as it alleviates CPU usage and allows having more than one task running at the same time, each on a different core [19, 20].

2.4 Communication

The IoT device based on the ESP32 SoC has several wireless communication channels such as WiFi 802.11 b/g/n, Bluetooth V4.2, and Node-To-Node Lo-RaWAN with a frequency of 915 MHz in the ISM band without a license due to geographical location and corresponding regulations. This allows it to connect to existing wireless networks deployed in smart cities. The MQTT protocol is used for messaging transport, which is built to provide orderly, lossless, and bidirectional connections. MQTT is widely used because it is lightweight, open, and designed for low bandwidth, high latency networks. MQTT comprises three members: publisher, broker, and subscriber; the broker manages messages between publishers and subscribers without needing to identify a publisher and consumer based on physical aspects. MQTT allows data acquisition in a simple and simplified way [21, 22].

For sending messages, the IoT device will process all the information and send it to the MQTT broker hosted in the cloud. The QoS QoS for MQTT is defined and controlled by the sender, i.e., each IoT device can have a different policy; for our case, and to alleviate the bandwidth, we will select a QoS = 0.

The software developed for our management system allows the registration of unique topics for each IoT device in a structured hierarchy, and the MQTT broker only processes the data of each device previously registered.

2.5 Power Supply

The IoT device is designed to be powered with a voltage between 100V to 240V, which will depend on the nominal voltage of the luminaire so that it works with the same power supply already available in lighting networks. This alternating voltage is converted into 5V DC voltage to operate all electronic components.

2.6 Description of Software

The management system allows to visualize the data in real time or the historical values of all the parameters configured in each IoT device. The data is published to the MQTT broker, this information is requested by the software for real-time visualization or by the node JS server, which in turn is responsible for storing the data in the NoSQL database and its subsequent visualization in the software as historical data. The software was developed using the Laravel framework in its version 10 in the backend and VueJs in the frontend and its implementation has been done based on design patterns so that developers can understand it in order to ensure that the software can be updated.

This software allows:

- Analyze data to identify patterns and trends.
- Establish thresholds and alerts to detect problems such as luminaires going out, changes in energy consumption or deterioration in performance.
- Maintenance planning based on the analyzed data.
- Automatically generate preventive and corrective maintenance schedules. This includes scheduling work orders using location and geolocation data so that technical personnel perform their tasks efficiently and reduce mobilization times.
- Maintain historical data of the parameters sent by each IoT device, as well as maintenance and work orders performed.
- Report generation.

The software has five modules:

1. User authentication
   a. Login
   b. Email verification
   c. Password reset
   d. Two-factor authentication
2. User administration and permissions
   a. Register new users
   b. Edit user information
   c. Create roles and permissions
   d. Associate users with roles and permissions
3. Inventory Management
   a. Create, view, and edit technical specifications for luminaires, poles, and fixtures
4. Installation and maintenance manager
   a. Register facilities
   b. Maintenance planning
   c. Alarms for luminaire and pole failures.
   d. Automatic elaboration of work orders
   e. Maintenance record
   f. Equipment change log
5. Reports

Module 1 user authentication and module 2 user administration and permissions are related to program security for user authentication and user authorizations. Also, module 1 allows the creation and edition of information for all users, while Module 2 establishes user authorizations through roles and permissions so that each based role has defined access to each part of the software.

Module 3, inventory management, is in charge of inventory management, i.e., it allows storing the technical specifications of luminaires, auxiliary equipment, and poles, as well as their availability.

Module 4, installation and maintenance manager, allows the automatic creation of work orders, which are created based on the parameters established in the maintenance planning, whether preventive or corrective, for luminaires and poles.

If a luminaire or the pole on which it is installed presents failures, the system automatically displays alerts and notifications so that system users are informed. The application identifies the number of failures of nearby luminaires and sets it as a decision parameter. In case the first parameter is not met, a time limit is set since the loss has occurred.

This information is analyzed in order, to deploy maintenance personnel automatically, optimizing the response time by the claimant; in addition, the application has a connection to Google Maps so that the person follows the route optimally chosen to perform the maintenance.

If the failure is in the pole structure, the application instantly generates the work order since these failures are structural and can cause accidents to pedestrians and vehicles.

All this can be done thanks to the field device proposed in this document, which provides the necessary information to know the status of the luminaires in real time.

Module 5 allows for generating dynamic reports through the use of filters.

3 Results and Discussion

The software has been deployed on Amazon's free Amazon EC2 server with 99.99% service availability, which allows up to 750 h per month at the free level (Fig. 3).

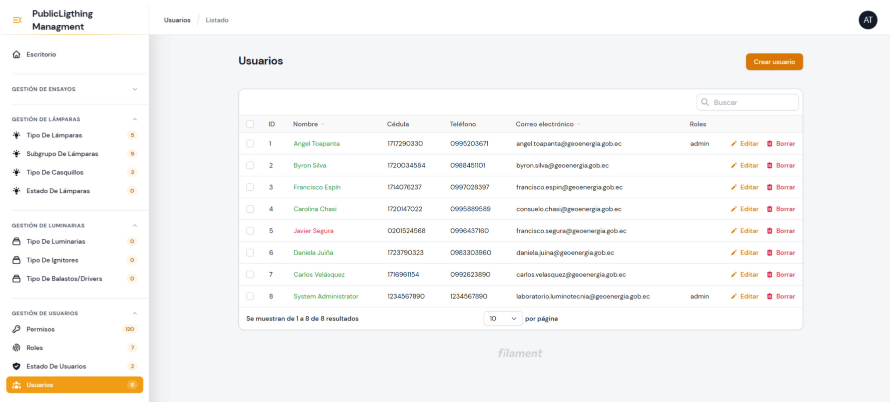

Fig. 3. Public Lighting Maintenance Management System

The IoT devices proposed in this document are installed on 10 street lighting poles with an average installation distance of 30 m (Fig. 4).

Fig. 4. Layout of public lighting poles

The first test performed is to the IoT device by console so that the parameters of the luminaire in which it is installed can be seen. The message received (topic) has the following format: Syste Name/Company/Gateway Code/Circuit Identification/Luminaire Code/option. Example: PLM/EEQ/2R-GW1/2R/258/data(field1, field2,…, fieldn). The data of the luminaire and pole states come from field 5, a defined code depending on their state (Table 1).

Table 1. Pole and luminaire status codes

Code	Description
M0100	Ok
M0101	ON
M0102	OFF
E0300	Fault: powered, but does not turn on
E0301	Fault: circuit without energy
E0302	Fault: pole broke down
E0303	Fault: lost of communication

```
MQTT connection Ok
Suscription ok
Processing msg...
{
    field1: '2R258',
    field2: '-0.162583',
    field3: '-78.480033',
    field4: '8',
    field5: 'M0100',
    field6: '220.03',
    field7: '0.968',
    field8: '0.08',
    field9: '70.05',
    field10: '-',
    field11: '-',
    topic: "'PLM/EEQ/2R-GW1/2R/258/'"
}
Device registered: True
Insert data...
Affected rows: 1
Inserted row ID: ObjectId("64714f7abb41448adc0fd819")
```

Fig. 5. IoT device test run

Once the IoT devices have been configured and registered in the management software, we proceed to test the operation of the proposed Maintenance Management System by simulating failures in different IoT nodes (Figs. 5, 6 and 7).

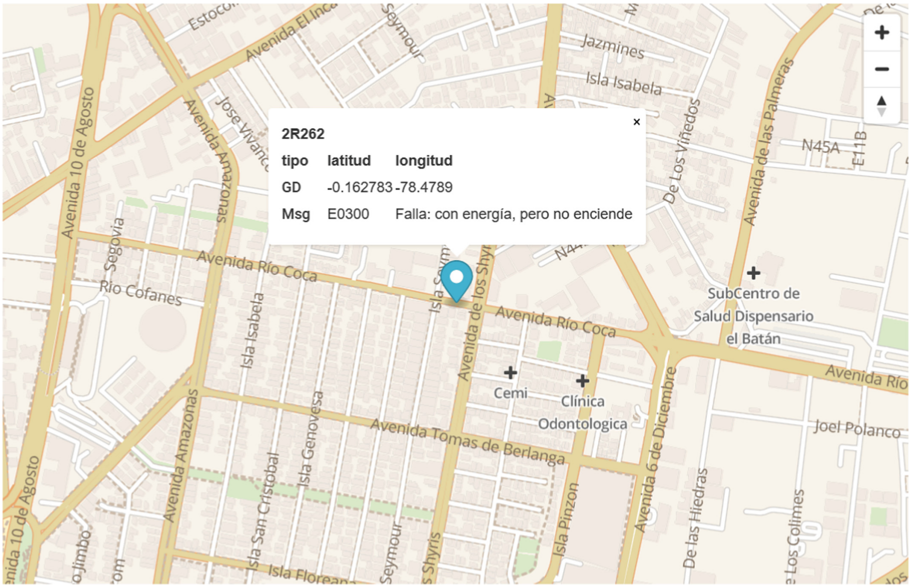

Fig. 6. Message E0300, Fault: powered, but does not turn on

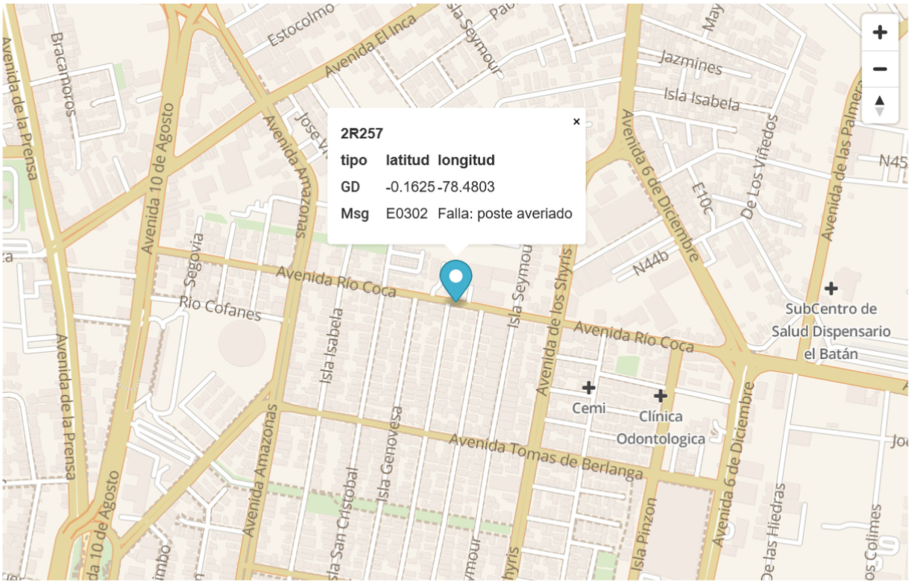

Fig. 7. Message E0302, Fault: pole broken down

4 Conclusion

The management of georeferenced maintenance of public lighting systems through the "internet of Things" IoT arises from the need to have energy savings to regulate, schedule, and manage the use of lighting efficiently.

The damage report in the city of Quito is currently obtained from the user who detects the failure or breakdown of a luminaire; the time it takes to solve the reported problem is high. Therefore, the lighting service becomes inefficient for passers-by and drivers. However, it is now within reach of managers to implement a management system that allows monitoring and storing information so that after the corresponding analysis, preventive maintenance routes can be planned and created, effectively managing the inventory of luminaires and increasing the quality index of the Public Lighting service.

The information collected can also be used to differentiate the levels of illumination required by each lighting system, whether for road or pedestrian traffic, guaranteeing, depending on vehicle traffic, adapting the lighting to the context of traffic and time, providing a feeling of greater security combined with aesthetically pleasing designs.

The initiative to implement these georeferenced management systems is a stepping stone to achieving an integrated system that will allow in the near future to control an intelligent city that can obtain data with motion sensors, which in addition to controlling lighting control traffic through traffic lights, which acquire images and videos of the conflict zones in the city to create safe spaces for citizens.

All these changes will allow us to evolve the behavior of the operation and management of public lighting, lighting when it is needed, where it is needed, reducing the light pollution that is caused, and even conserving the environment.

References

1. PNUMA, FMAM, U4E: Aceleración de la adopción mundial de la iluminación energéticamente eficiente (2016)
2. Szalai, A., Szabó, T., Horváth, P., Timár, A., Poppe, A.: Smart SSL: application of IoT/CPS design platforms in LED-based street-lighting luminaires. In: 2016 IEEE Lighting Conference of the Visegrad Countries (Lumen V4), pp. 1–6 (2016)
3. Ageed, Z.S., et al.: A state of art survey for intelligent energy monitoring systems. Asian J. Res. Comput. Sci. **8**, 46–61 (2021). https://doi.org/10.9734/ajrcos/2021/v8i130192
4. Conelec: Regulación Nro. CONELEC 005/14 Prestación del Servicio de Alumbrado Público General (2014)
5. Pachamanov, A., Pavlov, D., Kassev, K., Nikolova, K.: Individual control of street luminaries by speed of change of natural light in the evening and by calendars in the morning. In: 2021 Sixth Junior Conference on Lighting (Lighting), pp. 1–4 (2021)
6. Jing, C., Shu, D., Gu, D.: Design of streetlight monitoring and control system based on wireless sensor networks (2007)
7. Lavric, A., Valentin, P., Finis, I., Simion, D.: The design and implementation of an energy efficient street lighting monitoring and control system. Przeglad Elektrotechniczny. **88**, 312–316 (2012)
8. Yusoff, Y.M., Rosli, R., Karnaluddin, M.U., Samad, M.: Towards smart street lighting system in Malaysia. In: 2013 IEEE Symposium on Wireless Technology & Applications (ISWTA), pp. 301–305 (2013)

9. Kumar, S., Deshpande, A., Ho, S., Ku, J., Sarma, S.: Urban street lighting infrastructure monitoring using a mobile sensor platform. IEEE Sens. J. **16**, 1 (2016). https://doi.org/10.1109/JSEN.2016.2552249
10. Bezbradica, M., Trpovski, Ž.: Advanced street lighting maintenance using GPS, light intensity measuring and incremental cost-effectiveness ratio. In: 2014 International Conference on High Performance Computing & Simulation (HPCS), pp. 670–675 (2014)
11. Gupta, A.K., Johari, R.: IOT based electrical device surveillance and control system. In: 2019 4th International Conference on Internet of Things: Smart Innovation and Usages (IoT-SIU), pp. 1–5 (2019)
12. Domínguez-Bolaño, T., Campos, O., Barral, V., Escudero, C.J., García-Naya, J.A.: An overview of IoT architectures, technologies, and existing open-source projects. Internet Things. **20**, 100626 (2022). https://doi.org/10.1016/j.iot.2022.100626
13. Toapanta, R., Chafla, J., Toapanta, A.: Physical variables monitoring to contribute to landslide mitigation with IoT-based systems. In: Botto-Tobar, M., S. Gómez, O., Rosero Miranda, R., Díaz Cadena, A. (eds.) Advances in Emerging Trends and Technologies, ICAETT 2020, Advances in Intelligent Systems and Computing, vol. 1302, pp. 58–71. Springer, Cham (2021). https://doi.org/10.1007/978-3-030-63665-4_5
14. Sanchez-Sutil, F., Cano-Ortega, A.: Development and implementation of a PQ analyser to monitoring public lighting installations with a LoRa wireless system. Internet Things. **22**, 100711 (2023). https://doi.org/10.1016/j.iot.2023.100711
15. Araguillin, R., Toapanta, A., Juiña, D., Silva, B. (2022). Design and characterization of a wireless illuminance meter with IoT-based systems for smart lighting applications. In: Botto-Tobar, M., Zambrano Vizuete, M., Diaz Cadena, A., Vizuete, A.Z. (eds.) Latest Advances in Electrical Engineering, and Electronics, LNEE, vol. 933, pp. 129–140. Springer, Cham (2022). https://doi.org/10.1007/978-3-031-08942-8_10
16. Quectel: L80 GPS protocol specification (2014)
17. Chokshi, R.: MPU-6000 and MPU-6050 register map and descriptions revision 4.0 (2012)
18. Mohamed, K.S.: The era of internet of things: towards a smart world (2019)
19. Prade, L., Moraes, J., de Albuquerque, E., Rosário, D., Both, C.B.: Multi-radio and multi-hop LoRa communication architecture for large scale IoT deployment. Comput. Electr. Eng. **102**, 108242 (2022). https://doi.org/10.1016/j.compeleceng.2022.108242
20. Leonardi, L., Lo Bello, L., Patti, G.: MRT-LoRa: a multi-hop real-time communication protocol for industrial IoT applications over LoRa networks. Comput. Commun. **199**, 72–86 (2023). https://doi.org/10.1016/j.comcom.2022.12.013
21. Alahmadi, H., Bouabdallah, F., Al-Dubai, A.: A novel time-slotted LoRa MAC protocol for scalable IoT networks. Futur. Gener. Comput. Syst. **134**, 287–302 (2022). https://doi.org/10.1016/j.future.2022.04.003
22. Nakamura, K., et al.: A LoRa-based protocol for connecting IoT edge computing nodes to provide small-data-based services. Digit. Commun. Netw. **8**, 257–266 (2022). https://doi.org/10.1016/j.dcan.2021.08.007

Degradation of Synthetic Oils: Physicochemical Viscosity Tests

José Vicente Manopanta-Aigaje(✉), Fausto Neptali Oyasa-Sepa, Oswaldo Leonel Caiza-Caiza, and Marcela Liliana Herrera-Mueses

Instituto Universitario ISMAC (ISMAC University Institute), Quito, Ecuador
vmanopanta@tecnologicoismac.edu.ec

Abstract. The oils used in compression-ignition engines involving the running time of the automobiles under certain mileages within the preventive and corrective maintenance, were established as the object of this study, being analyzed the 15w 40 CI synthetic base oil to validate the degradation level of a lubricant in compression-ignition engines. The sample was taken in containers with capacity of 120 ml. International standards were considered the procedures: kinematic viscosity testing, ASTM D 445 Standard; total alkalinity and acidity value, ASTM D 4739/ASTM D 664 Standards; infrared spectrum in used oils, NVE 751 Standard: oxidation, water, sulfation, nitration, fuel, soot; metal content by spectrometry, wear metals, contamination metals and additive metals, ASTM D 6595 Standard; oil spot test. For this study, literary analysis was used based on a comprehensive review of scientific papers, academic impact projects and reports that will make the readers have a clear view of the physical and mechanical characteristics of the lubricant. In the tribology analysis in engine oils, establishing the wear due to the movement of internal motor components, the degradation of a lubricant should be lower to maintain a better performance in a combustion engine, thus establishing a physicochemical test to determine at different mileages its durability with respect to friction and wear in a given sample of the lubricant.

Keywords: Lubrication · Degradation · Viscosity · Tests · Oxidation · Standard

1 Introduction

The lubricant used for engines contains various chemical compounds such as heavy metals (e.g., chromium, cadmium, arsenic, lead, among others), polycyclic aromatic hydrocarbons, benzene and sometimes chlorinated solvents, PCBs, etc. [1]. Some researchers have analyzed the combustion and emission of recycled engine oil-diesel blends. The recycled oil was prepared in two stages. First, waste engine lubricant was treated and blend with diesel in different proportions. Properties such as flash point, kinematic viscosity, calorific value, cetane number, cloud point, pour point and density were measured according to (ASTM) Standards. The blends were fed into a diesel engine and the tests indicate an increase in brake thermal efficiency, gas temperature compared to that of diesel. A decrease in brake specific fuel consumption and NOx emissions in the exhaust

M. Z. Vizuete et al. (Eds.): CI3 2023, LNNS 1040, pp. 83–98, 2024.
https://doi.org/10.1007/978-3-031-63434-5_7

gas combustion phase is determined [2]. In the local market, the oil used for category N3 engines belongs to the class called semi-synthetic, which depending on the parameters and quality can extend its change period, depending on the package of additives added, which can be antioxidant, detergent, diluent or anti-corrosive [3]. The analysis and monitoring of engine oil provide greater reliability about the real condition of the engine and prevents unexpected corrective maintenance. In diesel and gasoline internal combustion engines, where fuel is burned, lubrication is extremely difficult due to the additional and more demanding phenomena that must be faced: high temperatures, combustion products and residues that can contaminate the lubricant, high stresses, among others [4]. Using the standards of the Ecuadorian standardization service (INEN, D445, ASTM D5185, D2896, E2412), we will verify the correct change interval of the semi-synthetic oil used in the wear, viscosity, degradation and total base number tests [5]. Sampling is the most critical aspect of oil analysis. If a representative sample is not obtained, all subsequent oil analysis efforts will be nullified. The main objectives for obtaining a representative sample are: 1. To maximize information density. To obtain as much information as possible per milliliter of oil. 2. To minimize information distortion. The concentration of information should be represented in tables of results, and graphs at different mileage where the metals present in the lubricant are visualized. It is important that the sample is not contaminated during the analysis procedure in the tests. Limits in oil analysis are sometimes referred to as alarms, which are devices created to assist in the interpretation of reports [6]. During the analysis and verification of the physicochemical degradation tests of an engine lubricating oil by means of results obtained from the sampling used in compression-ignition engines, kinematic viscosity and infrared analysis were determined establishing parameters by mileage in oxidation, nitration and sulfation.

2 Theoretical Framework

2.1 Lubricating Oils

Lubricating oils are constituted by a base, which provides the primary lubrication characteristics; the base can be mineral, synthetic or vegetable. Viscosity is a factor that is affected by temperature. It is important to consider the operating temperatures to which the oil will be subjected [30]. Engine lubricants are a combination of paraffinic, naphthenic and aromatic hydrocarbons obtained by distillation of crude oil (mineral oils) or by synthesis from petrochemical products (synthetic oils). The variation in the proportion of the different types of hydrocarbons in the mixture determines the physical and chemical characteristics of the oils. A high proportion of paraffinic hydrocarbons gives the oil a higher resistance to oxidation, while a high content of aromatic hydrocarbons favors thermal stability [31].

2.2 Types of Lubricating Oils

Mineral Oil. Base oil or lubricant base is one of the products derived from the distillation of crude oil. During petroleum refining, lubricant bases are produced, which must strictly comply with the viscosity range that characterizes them [32]. Mineral oils are derived from the distillation of petroleum and, therefore, their origin is 100% natural. Mineral base oils are made up of three types of compounds: paraffinic, naphthalenic and aromatic, the first ones being the those found in greater proportion (60 to 70%), because they have the best lubricating properties, but there are naphthalenic and aromatic compounds that provide properties that paraffins do not have, such as good behavior at low temperatures and solvent power, among others [17].

Semi-synthetic Oil. They are the result of mixing or combining minerals and synthetics. No more than 30% of synthetic compounds and the remaining 30% of mineral. Thanks to this combination, excellent advantages of both are obtained, since they are more economical than synthetic compounds.

The superior characteristics of a semi-synthetic oil are:

- Higher viscosity index (withstands extreme temperatures better).
- It extends oil change intervals, because it withstands oxidation better than synthetic oils.
- Semi-synthetic lubricant improves lubrication with the help of another synthetic lubricant.
- Semi-synthetic oil is more environmentally friendly.
- Certain benefits provided by synthetic oils are obtained without having to invest in the oil [18].

Synthetic Oil. It is a highly refined lubricant to prevent premature engine wear, which has outstanding flow characteristics at low temperatures. As a result, the components are lubricated avoiding frictional wear, being very effective in cold starting where a significant amount of wear can occur in the moving parts of the engine [28].

Viscosity stability. A higher viscosity index is synonymous with a more stable viscosity over a wider temperature range produced in the engine.

Higher thermal and oxidation stability.- The higher thermal and oxidation stability of synthetic lubricants results in a lower increase in viscosity over time with respect to engine operation, thus prolonging the respective change of lubricating oil by working hours or mileage [29].

2.3 Use of Lubricating Oils

The lubricating oils inside the internal combustion engine of a diesel vehicle have an exclusive function with the care of the internal mobile mechanisms inside the automobile. This is how the fishing industry in the last years has prioritized to use an ideal lubricant for its diesel engines since the high cost of repairs in the short term has been a disadvantage in the last years is. For that reason, it should be clarified that the corrective maintenance of an engine is inevitable in the short or long term, but in the automotive industry it is important that a lubricating oil with excellent characteristics prolongs the useful life of the engine for a longer period of time. The study of the viscosity index at different temperatures is essential to analyze it by means of parameters with respect to its additives [9].

2.4 Synthetic Oil for Diesel Engines

A synthetic lubricant has base oils that are highly refined in a laboratory more than those used in usual mineral engine oils, obtaining better protection and performance features in the moving and fixed parts of the engine. Synthetic lubricants are manufactured with more advanced refining processes and therefore have a special chemical treatment and have a higher purity and quality as opposed to a mineral oil. This not only removes more impurities from the crude oil, but also allows the individual molecules in the lubricant to be modified to match the demands of today's automobiles [29]. When the engine is started, the mineral lubricant takes considerable time to circulate throughout the engine system, resulting in frictional wear between moving engine parts. On the other hand, synthetic oil begins to circulate quickly, protecting every moving part within the engine. Synthetic oils can also significantly increase fuel economy. During the warm-up period of a normal truck run, mineral oils have the disadvantage of being thicker and circulating slowly throughout the engine's internal mechanism, causing wear, making the engine more fuel-intensive and less efficient. In contrast, synthetic lubricants start working faster and the engine reaches its maximum operating efficiency effectively prolonging its service life [28].

3 Method

The research paper is presented with the literature review methodology, whose purpose is to consult several authors to discuss conclusions and results. Literature review means to discover, consult and obtain references, and other materials useful for research, from which the inquiry, plus the collection of important and necessary information to pose the research problem (Hernandez et al., 2014). On the one hand, it is of the documentary type since researchers perform a second-hand information search when looking for and selecting information that is already documented: recorded, compiled and classified.

This research was conducted in a review of several articles, books, theses, projects, scientific journals and verifiable sources that ensure the credibility of the concepts and analyses presented.

3.1 Viscosity

As an example of viscosity in a diesel road transport vehicle, a quantitative and qualitative analysis of the lubricant is considered necessary, the same that complies with the operating conditions suitable for a diesel engine, with respect to its durability under progressive operating conditions. Laboratory tests in relation to the study of the lubricant is a trend of relevant importance since a baseline that represents an interpretation of the engine wear can be determined through statistical limits and if the lubricant meets the ideal characteristics through the frequency of use of the same engine, so that, through a chemical data report, it can be established by means of indicators and color codes whether the oil has a favorable engine characterization [8].

Taking as a reference a heavy equipment, it is deduced that there is one of the most relevant advantages since the lubricant allows to establish a wide durability and reduces the corrective maintenance postponing it to a longer time, therefore, the study of the ideal lubricant is reflected in the preventive maintenances having to be carried out in the established period after the pertinent oil change, and an accompaniment of the viscosity study in a specialized chemical laboratory establishing parameters of temperature, mileage, and elements that produce the oxidation phase in the moving and fixed parts of the engine, being the ideal indicator for warning tests, and establishing limit results according to the hours of operation if it is construction equipment such as backhoes, caterpillars and mechanical shovels [9] (Table 1).

Table 1. Lubricants according to the equipment in operation [9]

Engine Manufacturer			
Oil Analysis	Caterpillar	Cummins	Detroit Diesel
	All models	All models	All models
Iron	100 ppm.	84 ppm.	150 ppm.
Copper	45 ppm.	20 ppm.	90 ppm.
Lead	100 ppm.	100 ppm.	–
Aluminum	15 ppm.	15 ppm.	–
Chromium	15 ppm.	15 ppm.	–
Spectroscopy	20 ppm.	20 ppm.	–
Sodium	40 ppm.	20 ppm.	50 ppm.
Boron	20 ppm.	25 ppm.	20 ppm.
Silicon	10 ppm.	15 ppm.	None specified
Viscosity	+20% to −10% of SAE nominal grade	±1 SAE grade or 4 cSt of new oil (Visc. at 100 °C)	+40% to −15% of the nominal value (Visc. at 40 °C)
Water	0.25% max.	0.2% max.	0.3% max.
TBN	1.0 mg KOH/g min. Estimate	2.0 mg KOH/g min. or half the new oil or equivalent to TAN	1.0 mg KOH/g min. Estimate
Fuel dilution	5% max.	5% max.	2.5% max.
Coolant dilution	0.1% max.	0.1% max.	0.1% max.
Ferrography	In exceptions	In exceptions	In exceptions

One of the quick test alternatives to determine the degradation and wear of a diesel lubricating oil can be achieved by means of an oil spot test, establishing comparative image parameters to determine the continuous wear with respect to the oil. This basic procedure comes from an analysis with a suitable diagnostic tool to determine the scope of ideal lubrication. These images determine the wear that this oil has through color spectra. This verification can be determined as a quick test to observe the oil condition after a certain time of use. Additionally, CNG engines show a higher demand due to their high thermal and mechanical demand, exposing a high degradation after a certain time of use [10] (Table 2).

Table 2. Database of Maxter Multigrade CI-4 SAE 15W40 oil [10]

Name	TBN (mgKOH)	Viscosity AT 100 °C (cSt)	Soot FT-IR (abs/1 mm)	DI	CI	WD
M01-A	9.06	14.07	0.74	94.5168	2.3854	13.0794
M02-A	9.08	12.35	0.63	90.6937	2.3664	22.0229
M03-A	9.88	13.42	0.85	94.7259	2.3766	12.5346
M04-A	6.25	13.34	0.58	93.0169	2.3832	16.6424
M05-A	9.63	14.01	0.63	88.9408	2.3585	26.0832
M06-A	8.81	13.68	0.84	95.3611	2.3826	11.0525
M07-A	6.94	13.33	0.91	93.1826	2.3687	16.1481
M08-A	8.68	13.91	1.01	95.7843	2.4104	10.1615

3.2 Engine Category

Machinery manufactured by Caterpillar shown in a data sheet according to its engine characteristics is considered [13] (Table 3).

Table 3. Main characteristics of the Caterpillar 2014 excavator engine [13]

Engine model	Cat•C6.6 ACERT^{TM}
Lubrication:	Circulating pressure
Gross power: SAE J1995	111 kW
Piston diameter	105 mm
Stroke	127 mm
Displacement	6.6
Pistons:	Inline-six
Compression Ratio:	16.2: 1

3.3 Measurement of Wear Elements in the Lubricant

For the collection of the samples, initially the cleaning of the oil intake port that is right on the oil filter was performed as in Fig. 1, then the sample was taken in a transparent plastic container of 120 ml that has an airtight lid. The label has information on the customer, unit, unit code, date of sampling, type of oil, oil hours, unit hours, so that the recommendations given regarding the condition of the oil are as accurate as possible.

In addition, the volume to be collected in each sample is 100 ml of oil and an oil sampling kit was used for this purpose. It was established to take the oil sample at intervals of 250 working hours, which corresponds to the preventive maintenance time suggested by the manufacturer [11].

Fig. 1. Oil sampling points in the engine [12]

4 Analysis of Results

4.1 SAE 15W-40 Oil Properties

Nomenclature of SAE 15W-40 oil, represented by the letter W, meaning Winter, referring to the degree of cold viscosity in temperature, the second numbering represents the lubricant viscosity in hot temperature. The higher the percentage of viscosity, the greater the protection to the mechanical parts. It is also emphasized that an excess of viscosity can cause internal friction and decrease the performance of the vehicle, which means a deterioration of the engine. In reference to the characteristics of the manufacturer of (2020) 15W40 Bardahl oil, it is understood that it is a multigrade oil, designed for the lubrication of 4-stroke turbocharged and naturally aspirated diesel engines. Therefore, these vehicles require a specific lubrication according to the type of engine. As an outstanding point about the 15W40 oil, it fulfills the function of protecting the engine from wear and corrosion to which it is exposed according to the activity it regularly performs, thus allowing the lubricant to adapt to the temperature diversity according to the climate to which the engine is exposed [27].

4.2 Infrared Oil Analysis

Over time, diesel engine oil degrades due to exposure to high temperatures and contact with combustion products. Infrared spectroscopy can detect the presence of degradation products, such as acids, resins and varnishes, which can affect the viscosity and lubricating properties of the oil. Early detection of oil degradation allows timely changes to be made and potential engine downtime to be avoided. Infrared analysis of diesel engine oil is a technique used to determine the chemical composition and quality of diesel engine lubricant by using infrared spectroscopy. This technique makes it possible to identify and quantify the different molecular components present in the oil, as well as to detect the presence of contaminants or degradation. Among those are:

- Measurement of elements in oil: Cu, Fe and Cr.
- Measurement of elements in oil: Al, Pb and Sn.
- Measurement of elements in oil: Si, Na and K.
- Measurement of elements in oil: Mo and Ni.

The measurement of elements such as aluminum Cu, Fe and Cr, Al, Pb and Sn, Si, Na and K, Mo and Ni in diesel engine oil is commonly performed through Optical Emission Spectroscopy (ICP-OES) or Atomic Absorption Spectroscopy (AA) analysis techniques. These techniques experimentally obtain the manifestation of metals in the engine lubricant and are widely used in the analysis of oils and fluids. Figure 2 shows the evolution of the acidity and alkaline reserve depletion measurements in mg KOH/g of the samples analyzed for diesel engines, respectively. It is indicated in the first instance that the intersection of the trend curves of the TAN and TBN measurements show the oil change intervals for each of the lubricating oils. As we can see, type II oil shows a clear reduction of the established period by approximately 50% (15,000 km).

Reaching the oil change intervals established by the manufacturer (30,000 km) using this type could pose serious risks of engine failure. The better performance of type I compared to type II can be attributed to its additive packages and probably to its lubricant base. It should be noted that type I has higher levels of TBN than type II, thus neutralizing the high levels of acidification of the oil at the end of the oil change interval. Diesel engines undoubtedly show a lower demand from the point of view of oil acidity, being not too much affected by this variable. Their alkaline reserve reaches without any problem the periods that have been established for these engines and can reach higher levels if we extrapolate the data obtained [26] (Table 4).

Table 4. Comparative Table

Characteristics	Type I	Type II	Type III
SAE Grade	10W40	15W40	15W40
Density at 15 °C (kg/m^3)	865	865	881
Viscosity at 40 °C (cSt)	91.8	112.0	108.0
Viscosity at 100 °C (cSt)	14.3	14.5	14.5
Viscosity Index	160	125 min.	130 min.
T.B.N. (mg KOH/g)	13.2	7.0	10
Aminic additives (Abs cm^{-1}/0.1 mm)	17,991*	12,978*	1,275*

(*continued*)

Table 4. (*continued*)

Characteristics	Type I	Type II	Type III
Antiwear additives (Abs cm^{-1}/0.1 mm)	8,048*	10,903*	12,950*
Flash point, open cup (°C)	>220	215	215 min.
Pour point (°C)	<−33	−27	−27 max.
Specifications	IVECO 18-1809	API CF-4	ACEA E7/E5, API CI – 4/CH-4/SL

Table 4: Main characteristics of the lubricating oils
(*) These results correspond to measurements carried out in the laboratory using the FT-IR technique.

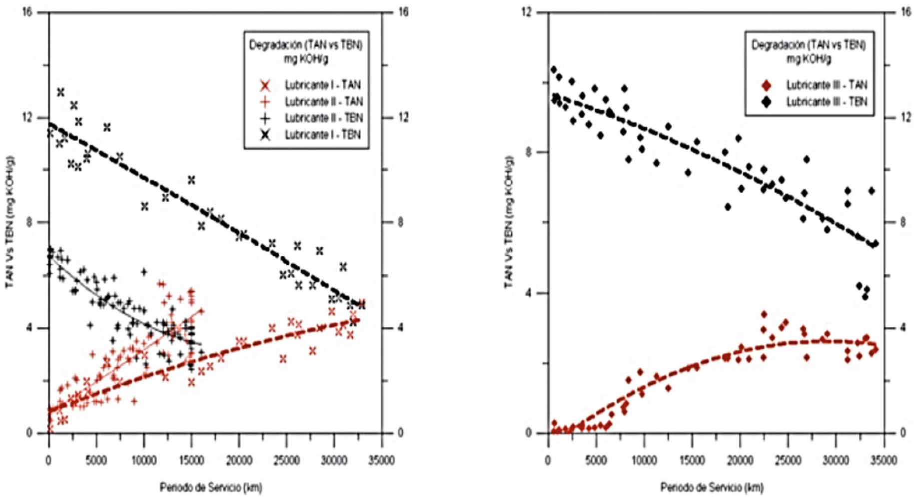

Fig. 2. Evolution of acidity measurements [26].

5 Discussion

5.1 Interpretation of the Wear of New 15W40 Oil

It can be seen in Table 5 that the proportion of polymer additives was similar in almost all the lubricants in the tests, and they are between 7% by weight and 8% by weight. Some irregularities were found for engine lubricants C and H, where the amount of polymer additives was above or below this range, proportionally. With reference to the absolute values of the polymeric additives, they can be somewhat overestimated due to the mechanism of size-exclusion chromatography [19].

Kinematic viscosity is relatively unaffected in all long-range automotive lubricant tests, gasoline cars identify a minor increase, diesel cars a minor decrease. Although the changes are not relevant, at least in this mileage range, it is suggested to involve these

Table 5. Chromatographic segmentation of SAE 15W- 40 lubricants [19]

	Polymer additives in oil (wt%)	Composition of base oil + low MW additives (wt%)				
		Saturates	Monoaromatics	Diaromatics	Polyaromatics	Polar compounds
Oil A	8.0	72.5	17.7	2.7	1.6	5.5
Oil B	8.2	71.4	15.2	2.7	2.9	7.8
Oil C	10.4	69.6	16.9	3.3	3.2	6.9
Oil D	8.1	67.3	18.3	4.2	3.4	6.8
Oil E	7.2	83.7	10.9	1.7	1.6	2.1
Oil F	7.4	84.7	7.2	1.4	0.6	6.1
Oil G	8.0	93.6	2.9	0.5	0.3	2.8
Oil H	6.4	73.1	16.4	3.3	2.3	4.8

fundamentally different trends in viscosity change in engine development, particularly when considering modern extended operating ranges exceeding 20,000 km covered [20].

The 15W-40 API CI-4 and M7ADS V 15W-40 API CI-4 CH-4/SL oils show similar lubrication. The M7ADS III 15W-40 API CF-4/SG engine lubricant shows the highest surface wear, in other words, the lowest lubrication of the new engine lubricants seen in the tests. Correlation analysis of the experimental values found that the fuel content that penetrated the lubricants correlates negatively with viscosity ($R = -0.87$). Low water contamination in the engine oil does not cause a revealing negative effect on lubrication. A significant correlation was confirmed between the oxidation, nitration and sulfation products of chemical degradation of the lubricants used in the tests ($R \geq 0.90$). These degradation products improve lubrication due to their polarity, i.e., they caused better lubrication of worn lubricants compared to new engine oils [21].

In the case of tests of used 15W-40 engine oils, those are shown in samples no. 2-2, 2-3, 2-4 (see Fig. 3 and Table 6) with 12,335 km, 25,888 km and 25,900 km covered. The concentration of the ZDDP additive was inspected at the level of 74%, 67% and 59%, i.e., it did not exceed the limit amount of 30%. Based on the identification of the fuel in the oil in relation to the viscosity of the new engine lubricant [21].

The change in KV at 100 °C was less than 15.96%. The oxidative-onset temperature (OOT) of the lubricants decreased gradually with the working mileage. All OOT values of the worn lubricants are at 210 °C effectively. A general test indicated that the used engine

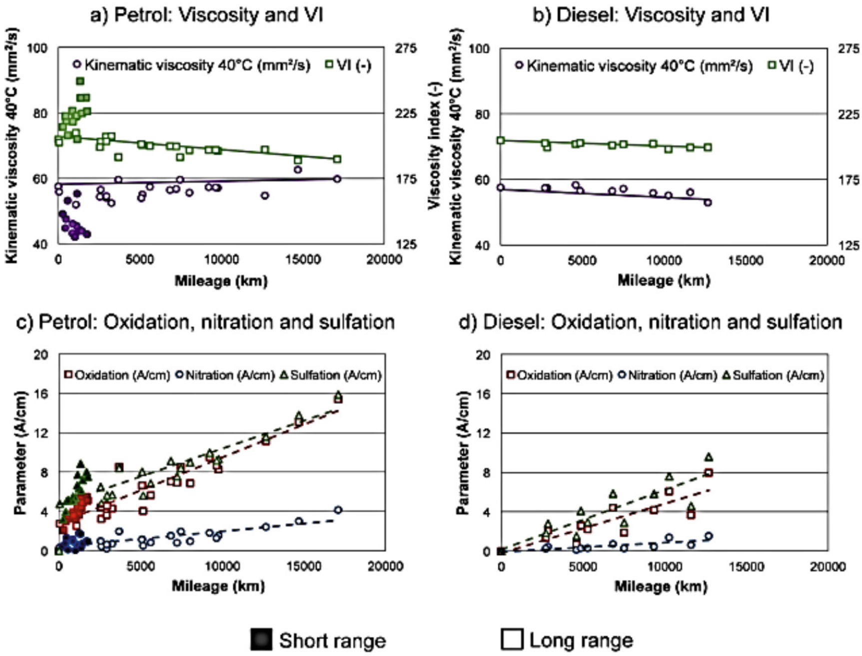

Fig. 3. Kinematic viscosity and viscosity index (VI) as a function of mileage. a) Gasoline cars, b) diesel cars. Oxidation, nitration and sulfation according to mileage. c) Gasoline cars, d) diesel cars. The lines shown only facilitate the appreciation of the results with respect to the tests carried out [20].

Table 6. Engine oil test assessment [21]

Oil sample No.	WS (mm^2)	$KV_{100°C}$ ($mm^2.S^{-1}$)	ZDDP (%)	Soot (%T)	Fuel (wt. %)	Water (wt. %)	Oxidation (A/0.1 mm)	Nitration (A/0.1 mm)	Sulfation (A/0.1 mm)
1-1	9.0	14.62	100.0	100	0.0	0.0	0.00	0.00	0.00
1-2	7.9	12.15	69.3	72	4.4	0.0	0.17	0.08	0.16
1-3	8.3	9.23	69.3	72	20.0	0.0	0.17	0.08	0.16
1-4	8.8	7.47	69.3	72	30.0	0.0	0.17	0.08	0.16
1-5	6.3	14.75	63.4	54	2.7	0.2	0.05	0.08	0.14
2-1	5.9	14.29	100.0	100	0.0	0.0	0.00	0.00	0.00
2-2	7.6	12.94	74.0	81	17.0	0.0	0.21	0.12	0.19
2-3	6.3	13.30	67.0	78	0.0	0.1	0.07	0.10	0.14
2-4	7.9	15.48	59.0	79	7.0	0.0	0.07	0.09	0.17
3-1	5.8	14.14	100.0	100	0.0	0.0	0.00	0.00	0.00
3-2	5.9	14.07	11.5	93	0.0	0.0	0.15	0.23	0.26

(*continued*)

Table 6. (*continued*)

Oil sample No.	WS (mm^2)	$KV_{100°C}$ ($mm^2.S^{-1}$)	ZDDP (%)	Soot (%T)	Fuel (wt. %)	Water (wt. %)	Oxidation (A/0.1 mm)	Nitration (A/0.1 mm)	Sulfation (A/0.1 mm)
3-3	6.1	14.07	13.8	93	0.0	0.0	0.14	0.22	0.26
3-4	6.3	14.68	5.0	88	0.0	0.0	0.26	0.40	0.38
3-5	5.8	14.65	6.0	88	0.5	0.0	0.26	0.40	0.38
4-1	3.5	14.37	100.0	100	0.0	0.0	0.00	0.00	0.00
4-2	2.1	15.58	23.2	75	0.0	0.2	0.42	0.62	0.57

oils retained their useful detergent and dispersant characteristics in an adequate amount. The four-ball wear scar diameters and coefficient of friction of the worn lubricants did not increase significantly after the road tests were completed. These tests are a reference for the next oil change to be performed on the automobile [22].

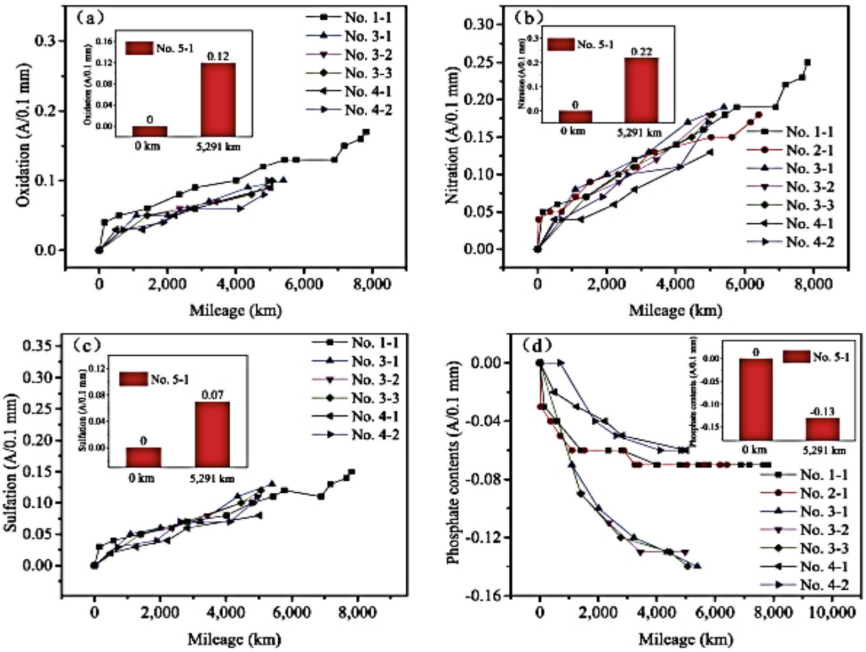

Fig. 4. Existing component test parameters of engine lubricant: (a) oxidation value, (b) nitration value, (c) sulfation value and (d) phosphate content [22].

The results of the tested lubricant components tend to be assessed by means of Fig. 4. As Figs. 4(a)–4(c) show, all oxidation, nitration and sulfation values of the tested engine lubricants increased with the operating mileage, and phosphate content decreased with an amplification of the tests (Fig. 4(d)). The oxidation, nitration and sulfation values increased rapidly, while the phosphate content declined rapidly during the primary test period. This was caused by the mix of residual lubricant and dissolution of residues of the previous lubricant. The phosphate content changed during the parallel tests with the same car model (1-1 and 2-1), the repeated test with mineral oil (3-1, 3-2 and 3-3) and the repeated test with synthetic lubricant (4-1 and 4-2). These had excellent prolongation, indicating that the consumption of antiwear components over the course of the road tests was well repeated. The experimental car 5-1 was brand new and was started with 5,291 km. The lubricant component change characteristics of car 5-1 were almost identical to those of the other road tests. The total oxidation, nitration and sulfation values of the worn lubricants were below the warning limit (1.0 A/0.1 mm) reported in Ref. [23]. Briefly, it can be stated that the authors focused on the study of the most common form of degradation of engine lubricating oil. Oxidation occurs under mild conditions by the gradual weakening of antioxidants. Concurrently with the oxidation products, nitrates are formed. Nitration originates in the crankcase due to the occurrence of combustion gases from the explosion time in the engine. Due to the mixing of oil with air and combustion gases at high temperatures, ideal conditions are created in the crankcase for oxidation and nitration. On the same principle [21, 22], the formation of sulfates is argued, in experimental words, the formation of SOx, reactions of combustion gases with lubricant. Soot also contributes to increase the viscosity of lubricants in a diesel engine. Soot generated in the engine can cause consistent sludge, high oil viscosity or gelling of the lubricant itself [24]. Contamination of these compounds in the lubricant with soot did not cause a significant increase in viscosity due to dispersants that dispersed them in isolation [25].

5.2 Mathematical Models - Tribology “Wear Coefficient”

The normalization method represents an important contribution to the use of techniques in wear evaluation and failure diagnosis, since it makes the analysis independent of engine type and size, lubricant capacity and operating conditions. The normalized concentration for a metallic element in the oil sample Cn is obtained by multiplying the concentration of the wear element by coefficients that adjust this concentration according to the ratios of size (Kt), volume of lubricant in the system (Kv) and chemical composition of the engine components (Km) [14].

The correction of the concentrations measured by the spectrometer with the objective of considering the effect of particle loss in the sample taken was performed through the constant velocity model for systems with leakage and additives, developed by Espinoza [15], and which is summarized in the following equations:

$$Cm(t) = \frac{P}{Z * Vo}\left(C_{mo} - \frac{P}{Z * V_o}\right) * e^{Z.t} \tag{1}$$

where:

$$Z = \frac{Qa}{Vo} \tag{2}$$

With Eq. (1), (P) is determined. In this investigation, the effect of the filter was not considered since the tests were carried out with the engine without oil filter. The corrected concentrations, which represent the number of particles that would exist in the crankcase if there were no leaks, additives or filters at time (t), are calculated through Eq. (3) and (4).

If (t0) is the time of oil change, so it is equal to zero, the above equation changes to this:

$$Cc = Co + \frac{P}{V_o}(t_1 - t_0) \tag{3}$$

The normalization model showed below was developed by Espinoza [15, 16] in 990. The normalized concentration for a metallic element (i) in the oil sample Cn(i) is obtained by multiplying the concentration of the wear element measured in the oil by coefficients that adjust this concentration according to the ratios of size (Kt), volume of lubricant in the system (Kv) and chemical composition of the components of tribology (Km(i)) [15].

$$Cc = Co + \frac{P}{V_o}t \tag{4}$$

$$\mathrm{Cn(i) = Cd(i)\,Kt\,Kv\,Km(i)} \tag{5}$$

$$\mathrm{Kt = Z/Zn * 1/\lambda^2} \tag{6}$$

$$\mathrm{Kv = V/Vn} \tag{7}$$

$$\mathrm{Km(i) = Yn(i)/Y(i)} \tag{8}$$

In Eq. 6, Z is the number of cylinders, λ is the similarity ratio between the analyzed engine, V is the volume of lubricant in the system. The subscript n refers to the normalized or reference engine, as expressed in Eq. 9.

$$\mathrm{D/D_n = \lambda} \tag{9}$$

6 Conclusion

In the use of lubricants for vehicles, a diversity of analyses has been reported, where it is shown that lubricants, based on the components of which they are a part, can produce wear in the engine, so it is feasible to use a type of lubricant that minimizes wear through proactive maintenance.

Lubricating oils start from a general identification of category with respect to their initial manufacture, whereby mineral, semi-synthetic and synthetic oils are denoted, showing diverse physicochemical analyses in combustion engines depending on the additive that are included in the manufacture.

The diverse qualitative bibliometric analyses by description of physicochemical test methods generalize a study of kinematic viscosity considering the current viscosity trends present in synthetic oils. Additionally, the quantitative results focus on infrared analyses to determine the quantity and chemical composition of the degradation agents by concentration of metallic elements.

The analyses show that if an oil was contaminated, its hydrodynamic lubrication will lose its lubrication, which will cause severe wear in the engine, directly affecting the rings, cylinders, oil pump and in the latter producing foam, which will cause it to break, inducing cavitation. Another cause can be the content of dirt or soot in the lubricant, damaging the crankshaft, camshaft, valves and other parts. Thus, due to the above-mentioned causes, it is highly important that the oil is in perfect condition to promote the good performance of the vehicle.

In a lubricant, the presence of oxidation is observed, which is the main cause of degradation of engine oils and in general of any organic compound, therefore, synthetic oils must have agents and additives that produce a better lubricant that acts effectively in hard conditions and high working temperatures inside the engine to better preserve the moving parts of the engine.

References

1. Hamawand, I., Yusaf, T., Rafat, S.: Recycling of waste engine oils using a new washing agent. Energies **6**(2), 1023–1049 (2013)
2. Prabakaran, B., Zachariah, Z.: Production of fuel from waste engine oil and study of performance and emission characteristics in a diesel engine. Int. J. Chem Tech Res. **9**(5), 474–480 (2016)
3. Caiza, S.D.S., Martínez, S.A.B., Terán, J.C.R.: Análisis Físico-Químico de la vida útil en aceites sintéticos. Dominio de las Ciencias **8**(3), 49 (2022)
4. Saldivia, F.: Aplicación de mantenimiento predictivo. Caso Estudio: analisis de aceite usado en un motorde combustion interna. In: XI Latin American and Caribbean Conference for Engineering and Technology (LACCEI'2013), Mexico (2013)
5. Saldivia, F.: Comportamiento de las propiedades físico-químicas de un aceite lubricante usado en un motor ce combustion interna (2013)
6. Troyer, D., Fitch, J.: Oil analysis basics en español (2004). Gómez García, C. -(2012)
7. Rondón, P.P., Pereira, A.G., Meneces, M.D.L.Á.R., Kruskova, E.R., Águila, M.V.G. (2015)
8. Manjon Patiño, Á.A., Villadiego del Villar, J.D., Salazar Salcedo, S. (2022)
9. Apaza Pastor, J.H.: Prueba de desempeño de motor con el aceite Chevron en la flota de camiones CAT 785D-Mina Shougang Hierro Perú para el cliente San Martín Contratistas Generales-San Juan de Marcona-Ica (2022)
10. Arellano, G., Helguero, M.: Implantación de Análisis de Aceite en Motores de Combustión Interna de Ciclo Diesel. Revista ESPOL 1–6 (2022)
11. Buchelli-Carpio, L., García-Granizo, V.: Detección temprana de fallas en motores de combustión interna a diésel mediante la técnica de análisis de aceite. Revista Ciencia UNEMI **8**(15), 84–85 (2015)
12. Cummins. The Complete Guide to Fluid Analysis (2012)
13. CATEPILLAR: Cat SOS Services. Understanding Your Results (2007)
14. Espinoza, H.: La normalización de las concentraciones de particulasde desgaste en aceite aplicada a motores diésel, vol. 8, no. 2, pp. 1–6. Instituto de Investigación y Desarrollo Anzoátegui, Universidad de Oriente, AVANCES Investigación en Ingeniería (2011)
15. Espinoza, H.: Diagnostico de fallos en motores de encendido por compresión de automoción. Tesis doctoral, Universidad Politécnic a de Valencia, España (1990)

16. Espinoza, H.: Diagnóstico de motores de encendido por compresión mediante análisis de aceite. Universidad Politécnica de Valencia, SPUPV-90-1018, España (1990)
17. García, A.: Diseño, selección y producción de nuevos biolubricantes. Tesis Doctoral Universitat Ramon Llull IQS-Bioenginyeria (2011)
18. Pérez, D.S., et al.: El ciclo de evolución de los lubricantes. ContactoS No. 97, 62 (2015)
19. Cerny, J., Strnad, Z., Sebor, G.: Composition and oxidation stability of SAE 15W–40 engine oils. Tribol. Int. **34**(2), 127–134 (2001). https://doi.org/10.1016/s0301-679x(00)00150-x
20. Agocs, A., et al.: Comprehensive assessment of oil degradation patterns in petrol and diesel engines observed in a field test with passenger cars – conventional oil analysis and fuel dilution. Tribol. Int. **161**, 107079 (2021). Cited 16 times
21. Sejkorová, M., Hurtová, I., Jilek, P., Novák, M., Voltr, O.: Estudio del efecto de la degradación fisicoquímica y la contaminación de los aceites de motor en su lubricidad. Revestimientos **11**(1), 60 (2021)
22. Wei, L., Duan, H., Jin, Y., et al.: Degradación del aceite de motor durante las pruebas de ciclismo urbano. Fricción **9**(5), 1002–1011 (2021)
23. Kral Jr, J., Konecny, B., Kral, J., Madac, K., Fedorko, G, Molnar, V. (2014)
24. Ziółkowska, M.: Wpływ sadzy na proces żelowania oleju silnikowego. Nafta-Gaz **3**, 178–184 (2019)
25. Wolak, A., Zając, G., Fijorek, K., Janocha, P., Matwijczuk, A.: Investigación experimental de los rangos de parámetros de viscosidad: estudio de caso de aceites de motor en el grado de viscosidad seleccionado. Energías **13**, 3152 (2020)
26. Macian-Martinez, V., Tormos-Martinez, B., Gomez, Y., Bermudez-Tamarit, V. (2013)
27. Bardahl (2020). https://www.bardahl.com.mx/ventajas-del-aceite-15w-40/
28. Robles, M., David, K.: Re-refinación de Aceites Lubricantes Usados Mediante Procesos Físico-Químicos (2016)
29. E. M. Corporation: ¿Qué es un lubricante sintético? (2015)
30. Corella Jiménez, F.D.: Caracterización de Aceites por sus Propiedades Ópticas (2016)
31. Ziolo, L.F.B., Gómez, J.R., Prieto-Cadavid, S., Gallo, S.C.: Biorremediación de suelos contaminados con aceites usados de motor. Revista CINTEX **20**, 69–96 (2015)
32. Dubois, R.A.: Introducción a la refinación del petróleo, Eudeba (2005)

CONNECTED Project. Connecting to the Disconnected

Marcelo Zambrano-Vizuete[1](✉), Juan Minango-Negrete[1], Segundo Toapanta-Toapanta[1], Edgar Maya-Olalla[2], Patricia Nuñez-Panta[3], and Eddye Lino-Matamoros[3]

[1] Instituto Tecnológico Superior Rumiñahui, Av. Atahualpa 1701 and 8 de febrero, 171103 Sangolquí, Ecuador
marcelo.zambrano@ister.edu.ec
[2] Universidad Técnica del Norte, Av. 17 de julio 5-21, 100105 Ibarra, Ecuador
[3] Instituto Espíritu Santo, Av. Juan Tanca Marengo and Av. Las Aguas, 090510 Guayaquil, Ecuador

Abstract. The pandemic caused by COVID19 had a disruptive effect throughout the planet, bringing to light the social, economic, and technological gaps that exist in current societies around the world, including such important aspects as connectivity (internet service) and education. Within the educational field, the closure of schools and colleges, as well as the lack of internet service in rural areas, prevented millions of children from continuing with their formal education. The CONNECTED project uses cutting-edge telematics tools and technologies to develop a communications system that allows delivering internet service to rural areas lacking this service; This, in turn, makes it possible for children and young people residing in these areas to continue with their formal education through tele-education processes.

Keywords: Rural Communications · Teleeducation · School Dropout

1 Introduction

During 2020 and part of 2021, COVID19 caused a third of the world's population to be subjected to confinement and strong mobility restrictions [1]. The first case of this virus (SARS-CoV-2.67 - Covid19) was identified in December 2019, in the city of Wuhan, capital of Hubei province, in the People's Republic of China. The World Health Organization (WHO) recognized it as a pandemic on March 11, 2020; By date, more than 118,000 cases had already been reported in 114 countries, and 4,291 people had lost their lives [2]. As of January 16, 2022, more than 350 million confirmed cases of this disease have been reported, with more than 5 million deaths, in more than 250 countries [3].

In addition to the human losses mentioned above, the measures adopted to combat the virus brought with them a drastic reduction in socioeconomic activities such as employment, tourism and education. One of the most important problems has been

M. Z. Vizuete et al. (Eds.): CI3 2023, LNNS 1040, pp. 99–109, 2024.
https://doi.org/10.1007/978-3-031-63434-5_8

reflected in the education sector: in more than 138 countries, schools and colleges were closed, affecting more than 1.37 billion children and young people who were unable to continue with their basic and secondary academic training [3, 4]. Under these conditions, connectivity and internet service became critical since they made it possible to compensate for the lack of physical contact and distancing using telematic applications and virtuality [5].

In the case of Ecuador, nearly one million children and young people were unable to continue with their formal education due to the difficulties in carrying out effective tele-education processes, mainly due to connectivity problems and the lack of internet service [6, 7]. Approximately, during the 2020–2021 period, more than 150,000 dropouts were registered in the basic and secondary education system of Ecuador [8].

According to figures from the National Institute of Statistics and Censuses (INEC), by April 2021, only 50% of Ecuadorian households, in the urban sector, had internet access and, for the rural sector, the figures worsen, only 40% of households have access to this service. This technological gap has a direct impact on the existing economic and social gaps between the urban and rural sectors [9–11].

To solve the problems, the CONNECTED project is developed, using cutting-edge tools and technologies that make it possible to provide connectivity and internet service to rural areas not covered by conventional providers of this service (dark areas).

It is important to emphasize that the objective of the project has a strictly social nature: to enable children and young people residing in rural areas without internet service to have a formal basic and intermediate level education. This, in turn, enable to improve the quality of life of citizens residing in these areas, reducing the existing socioeconomic gaps between this rural and urban sector.

This document is organized as follows: first, an introduction is made regarding the topics related to the project; second, the methodology used during its development and implementation is described; Third, the tests and results obtained are presented and, finally, fourth, the main conclusions resulting from the project are presented.

2 Methodology

This project is part of applied, qualitative and quantitative research. Applied, since its objective is the practical implementation (prototype) of a technical and technological solution that provides a solution to a real problem. Qualitative, the ultimate goal of the project is to provide connectivity and internet service, yes or no, to rural areas not covered by conventional Internet providers. Quantitative, the quality of Internet service is measured through quantitative variables such as transmission speed and bandwidth.

In general, the methodology used in this project is experimental, that is, after the design and sizing of the solution, the implementation and functionality tests (trial and error) will be carried out. If this is the case, the necessary corrective measures will be made to re-run tests and verify the functionality of the system.

The project is divided into four phases or stages:

1. Literature review and determination of the state of the art. It allowed us to learn about the advances, challenges and current state of the Internet service and tele-education processes in rural areas, as well as the successful models and implementations that

have been developed around this topic. According to this study, the problem was established, determining that in Ecuador, there is a significant lack of this service in rural areas.

2. Design and sizing of the solution. First, the generic architecture of the system was designed, which establishes the requirements, conditions and general structure of the system so that it can provide a solution to the identified problem. Second, the Target Geographic Area that will benefit from the development of this project was determined. Third, the specific architecture was designed taking into consideration the particular characteristics of the geographical area taken as the objective and adapting the generic architecture to these particularities. Finally, the characteristics and quantity of the equipment, devices and electrical and communications elements required for the implementation were determined.
3. Implementation. A prototype of the communications system is implemented in accordance with the area chosen as the objective, the specific architecture and the sizing of the equipment previously carried out.
4. Functionality tests. Since the main objective of the project is to allow the effective execution of tele-education processes within the Target Area, functionality tests were carried out using computer applications such as Microsoft Teams [12] and Zoom [13]. Measurements of bandwidth and data transmission speeds were taken both in the communications backbone and in each of the end users.

2.1 Architecture

The generic architecture of communications system is shown in Fig. 1 and consists of the following elements:

1. Donor, institution that donates a portion of its internet bandwidth for the development of the project.
2. Target Geographic Area, beneficiary area of the project and in which the donated bandwidth will be used.
3. Communications backbone, a set of point-to-point radio links that provides connectivity between the Donor and the Target Geographic Area. It is important to consider that, for licensing reasons, radio links must operate in free bands such as 2.4 GHz or 5 GHz. At these frequencies, the existence of line of sight between the transmitters and receivers of each of them becomes essential. Links deployed for communications backbone can be made up of one or several radio frequency links (hops), everything will depend on the distance between the donor and the Target Geographic Area, as well as the physical obstacles that prevent the line of sight between transmitters and receivers.
4. Base Station, point multipoint telecommunications equipment that allows wireless coverage of the Target Geographic Area. The base station must have connectivity with the last node of the communications backbone installed in the Target Geographic Area.
5. User terminals, telecommunications equipment, installed in the end user locations and that enable communication with the Base Station.
6. Access points, telecommunications equipment that receives the Internet signal from user terminals and distributes it to user locations through an IEEE 802.11 network.

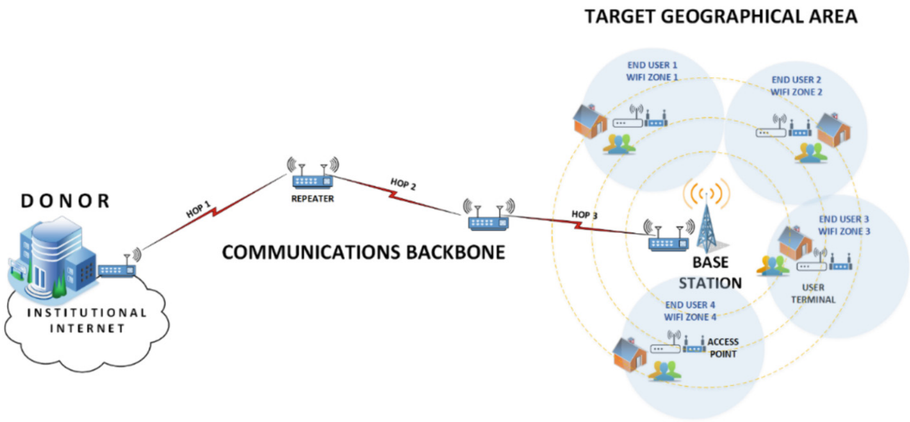

Fig. 1. Generic CONNECTED project architecture.

The San Antonio neighborhood (Ecuador country, Pichincha Province, Rumiñahui canton) was chosen as the Target Geographic Area; a small town located on the slopes of the Pasochoa volcano, at an approximate distance of 15 km from the Rumiñahui Higher Technological Institute (ISTER), which serves as a donor for this project. It was identified that in this area there was a group of approximately 15 people, including children and young people, who had not been able to continue with their formal education during the COVID19 pandemic due to lack of internet service and the impossibility of carrying out teleeducation processes. Figure 2 shows the geographic location of the San Antonio neighborhood and the line of sight study that demonstrates the feasibility of reaching the Target Geographic Area through a single radio link.

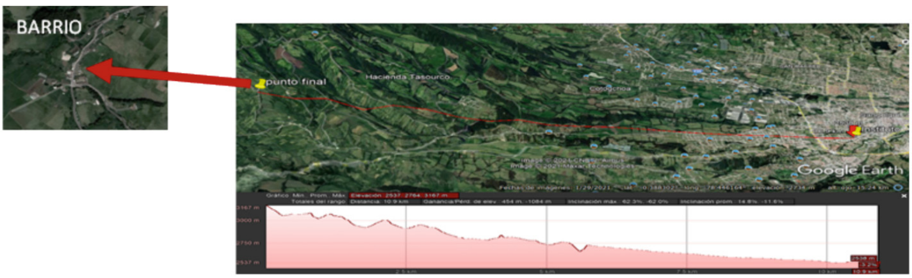

Fig. 2. Line of sight study for the Target Geographic Area: Barrio San Antonio/Pichincha/Rumiñahui.

Once the Target Geographic Area was established, the generic architecture was adapted to the characteristics of that area (geographic, accessibility, electric energy, etc.). Figure 3 shows the specific architecture of the communications system for the San Antonio neighborhood, taking ISTER as a donor, with a bandwidth of 100 Mbps.

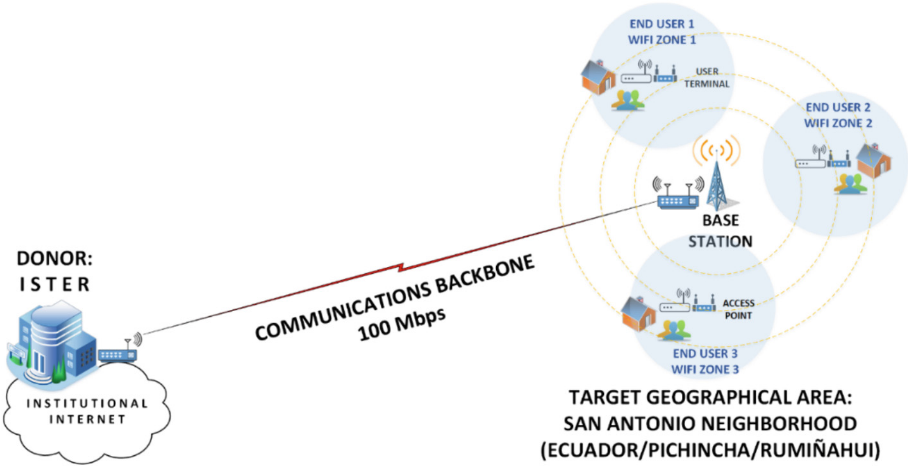

Fig. 3. Specific architecture of the CONNECTED project for the San Antonio neighborhood (Ecuador/Pichincha/Rumiñahui).

2.2 Sizing, Implementation, and Functionality Testing of the System

For the implementation of the system, LigoWave brand equipment [14] was chosen, given its operating frequency characteristics, protection against dust and liquids, traffic management, high tolerance to noise and interference, among others. Although LigoWave equipment can operate under the IEEE 802.11 standard [15, 16], many of the aforementioned features are related to its proprietary layer 2 protocol called Ipoll3 [17, 18].

Ipoll3 makes an improvement to the HCF (Hybrid Coordinate Function) medium access technique, changing the typical control carried out sequentially by the base station, for an intelligent polling carried out individually by each of the access points (APs) subscribed to that station base. Each AP sends a polling frame to the base station and must receive a response before starting to send data. Before polling other APs, the base station must receive data from the AP in question. APs that require less airtime are registered to a low activity or inactivity list, while stations that generate more traffic are registered to an active list. This allows the network to self-regulate so that each wireless link gets the maximum bandwidth with the lowest possible latency.

The equipment used is described in Table 1 below.

Table 1. Equipment used for the implementation of the prototype of the CONNECTED project.

No.	Description	Model	Quantities	Ubication
1	Radio (Antenna included)	LigoPTP 5-23 RapidFire [19]	2	Donor Target Geographical Area
2	Switch layer 2	TPLINK TL-WR840N V2 [20]	1	Donor
3	Base Station (Antenna included)	LigoDLB 5-90n [21]	1	Target Geographical Area
4	User Terminal (Antenna included)	LigoDLB 5-20ac [22]	3	End User site 1 End User site 2 End User site 3
5	Access Point	LigoWave NFT 2ac [23]	3	End User site 1 End User site 2 End User site 3

In addition to the equipment described above, an instance of the LigoWave network management software, called WNMS [24], was implemented. Among the functionalities of this software, can highlight the collection of inventory data, generation of alarms, statistical reports, remote configuration of equipment, among others. In the case of the CONNECTED project, WNMS allowed continuous and real-time monitoring of the radio links and the wireless communications network deployed in the Target Geographic Area.

A prototype of the communications system was implemented, for which ISTER serves as a donor, providing 100 Mbps of its institutional bandwidth for this project. All equipment operates at a frequency of 5 GHz. Figure 4 shows a diagram of the installed equipment.

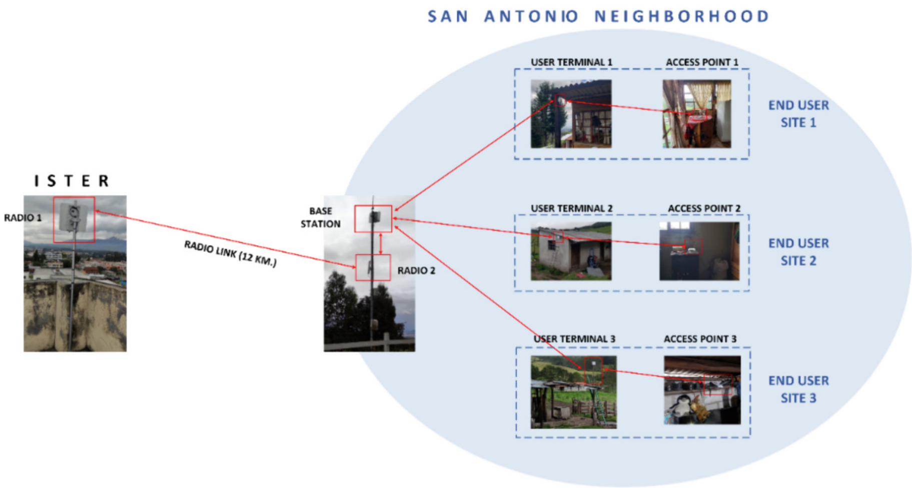

Fig. 4. Prototype of the communications system for the CONNECTED project, San Antonio neighborhood (Ecuador/Pichincha/Rumiñahui).

3 Results and Functionality Test

To verify the functionality of the system, multiple audio and video tests were carried out with 9 recurring users, 4 of them used Microsoft Teams and the remaining 5 using ZOOM. 7 of the end users used their smartphone during the tests and 2 used their laptops. The results obtained were satisfactory in 100% of the cases. No packet losses or significant delays were detected during test communications.

Additionally, 4 transmitters and 4 receivers were chosen at random to carry out text file transfer tests (.docx), each with an approximate size of 10 MB. As in the previous case, the tests were carried out successfully.

Although LigoWave equipment allows it, quality of service (QoS) was not implemented, with the objective of verifying the response of the Ipoll3 protocol to network traffic. It is important to highlight the stability of LigoWave equipment, maintaining minimal variations in transmission speeds and delays in transmissions.

Figure 5 shows the results of the network parameter measurements carried out through the LigoWave WNMS software, both at the donor site and at the Target Geographical Area.

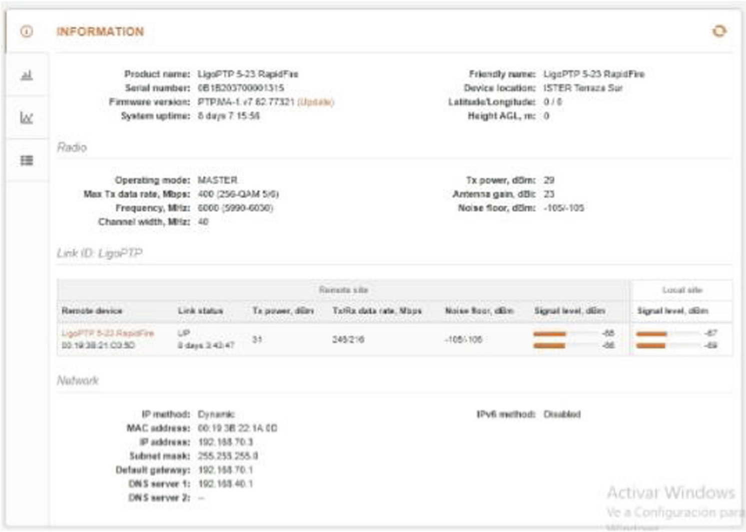

(a)

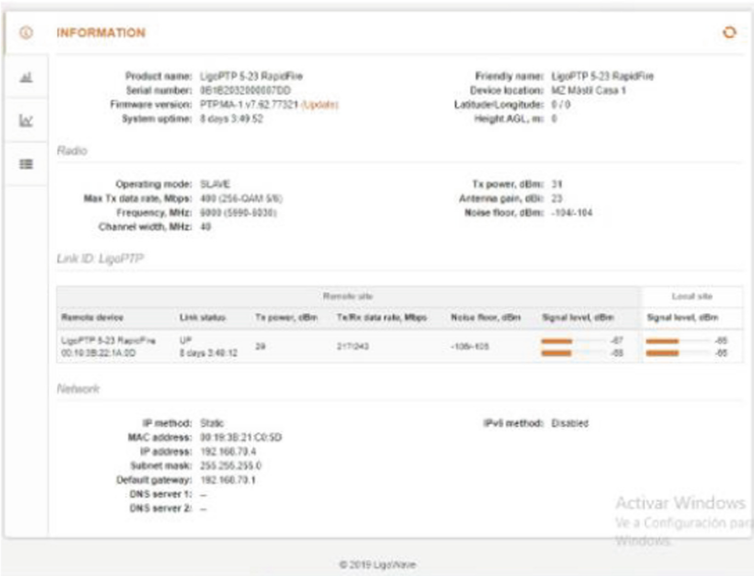

(b)

Fig. 5. **(a)** Network parameters LigoWave 5-23 RapidFire – ISTER. **(b)** Network parameters LigoWave 5-23 RapidFire – Target Geographical Area. **(c)** Network parameters LigoWave 5-90 Base Station – Target Geographical Area. **(d)** Network parameters LigoWave 5-20ac User Terminal – End User site 3.

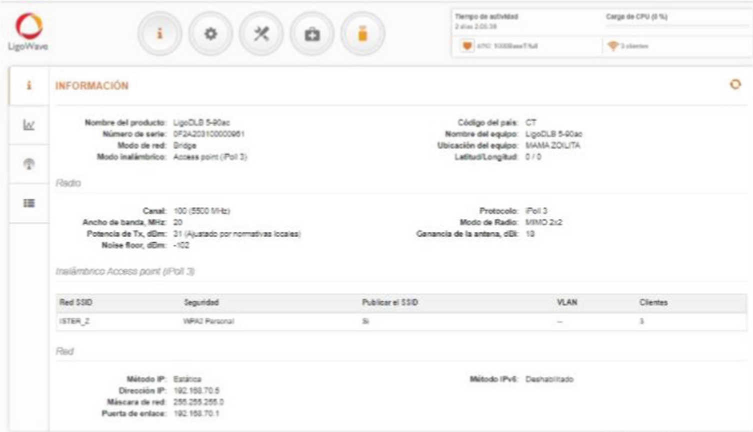

(c)

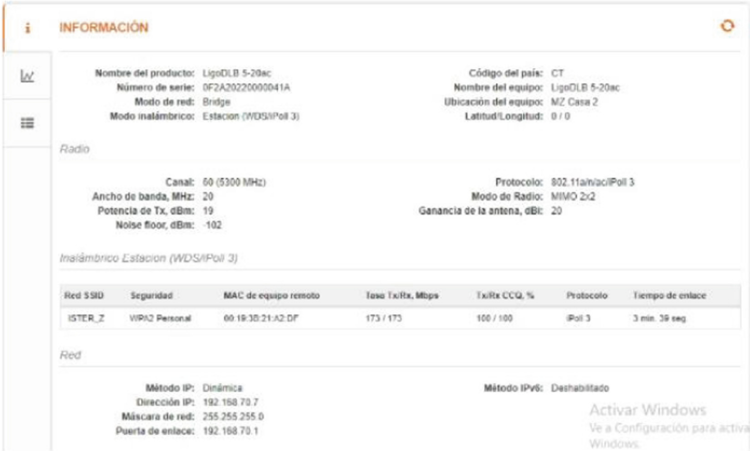

(d)

Fig. 5. (*continued*)

4 Conclusions

The CONNECTED project has a strictly social character, that is, it does not seek economic but social profitability. In the case of this first prototype of the system, the *Instituto Tecnológico Superior Rumiñahui* (ISTER) functions as a donor of the internet service, assigning the project a bandwidth of 100 Mbps. All functionality tests were successful, corroborating the feasibility of the system for the development of Teleeducation effective processes.

It is important to remember that the CONNECTED project is developed jointly by the ISTER and the *Instituto Espíritu Santo* (TES). In addition, it has the support of the *Corporación Ecuatoriana para el Desarrollo de la Investigación y la Academia* (CEDIA).

One of the most difficult activities to accomplish was establishing the location of the radio equipment in the Target Geographic area, since the trees in the area (forested area) are an impediment to reaching the line of sight required between transmitters and receivers to form the link. At first, it was planned to make two jumps to reach the objective point, however, after carrying out the site visit and the field study, it was verified that with the installation of a 6-m-high mast it was possible to reach the line of sight between the radios with a single jump, this, considering that the Ligowave RapidFire equipment has a range of 30 km.

As future work, it is expected to be able to replicate this communications system in other rural locations that have the same problem, considering, if necessary, multiple hops or radio links to reach the Target Geographic Area (this makes it possible to overcome the lack of a line of sight between the donor and the Target Geographic Area). For this, the use of layer 2 switches must be considered in each of the implemented hops, allowing signal regeneration and preventing the bit error rate from increasing. Likewise, it is planned to implement a portable system solution that allows providing communications and/or internet service to areas that have suffered some type of disaster and are cut off.

References

1. Dalponte, B.: COVID-19 y seguridad regional. Macro-seguritización global, adaptaciones locales y dilemas de la cooperación latinoamericana. URVIO. Revista Latinoamericana de Estudios de Seguridad (2021)
2. Maguiña Vargas, C., Gastelo Acosta, R., Tequen Bernilla, A.: El nuevo Coronavirus y la pandemia del Covid-19. Revista Médica Herediana **31**(2), 125–131 (2020)
3. United Nations News Home Page, Más de 156 millones de estudiantes están fuera de la escuela en América Latina debido al coronavirus. https://news.un.org/es/story/2020/03/1471822,2020. Accessed 25 Sept 2023
4. Sanz, I., Sainz, J.: Organización de Estados Iberoamericanos para la Educación, la Ciencia y la Cultura (OEI), Efectos del Coronavirus en la Educación (2020)
5. Bonilla-Guachamin, J.A.: Las dos caras de la educación en el COVID-19. Ciencia América (2020)
6. El Pais. Ecuador: la educación online desde casa es imposible e injusta. Planeta Futuro (2020)
7. El Universo. Un millón de estudiantes sin acceso a educación virtual durante la emergencia sanitaria (2020)
8. Primicias. La pandemia empujó a 150.0000 estudiantes hacia la deserción escolar (2020)
9. Instituto Nacional de Estadísticas y Censos. Indicadores de tecnologías de la información y comunicación. Gobierno en cifras (2021)
10. CEPAL. Pandemia provoca aumento en los niveles de pobreza sin precedentes en las últimas décadas e impacta fuertemente en la desigualdad y el empleo (2021)
11. Reliefweb. El choque COVID-19 en la pobreza, desigualdad y clases sociales en el Ecuador: Una mirada a los hogares con niñas, niños y adolescentes. OCHA Services (2020)
12. Microsoft, Microsoft Teams (2023). https://www.microsoft.com/es/microsoft-teams/group-chat-software. Accessed 16 June 2023
13. Zoom Home Page (2023). https://zoom.us/es. Accessed 16 June 2023
14. LigoWave Home Page. https://www.ligowave.com/es. Accessed 16 June 2023
15. Bellalta, B.: Delay Analysis of IEEE 802.11 be multi-link operation under finite load. IEEE Wireless Commun. Lett. **12**(4), 595–599 (2023)

16. Zubow, A., Memedi, A., Dressler, F.: Towards hybrid electronic-mechanical beamforming for IEEE 802.11 ad. In: 18th Wireless On-Demand Network Systems and Services Conference (WONS). IEEE (2023)
17. LigoWave Ipoll Protocol Home Page. https://www.ligowave.com/wiki/faq/apc-ipoll-protocol/. Accessed 16 June 2023
18. LigoWave, iPoll™- PTMP Protocol, Technical Paper (2016)
19. LigoWave Rapidfire Home Page. https://www.bhphotovideo.com/c/product/1411609-REG/ligowave_ptp_rapidfire_5_23_5ghz_ptp_mimo_700mbps.html?ul=S&gclid=CjwKCAjwyNSoBhA9EiwA5aYlb9w-ytkL6xqdcVAc-TDWSxMw5E3cYO41sD3I_selnEc3_nAyU4mmWxoCX-cQAvD_BwE. Accessed 21 Aug 2023
20. TPlink Wireless Router TL-WR840 Home Page. https://www.tp-link.com/ec/home-networking/wifi-router/tl-wr840n/. Accessed 21 Aug 2023
21. LigoWave LigoDBL-590n Home Page. https://www.ligowave.com/products/ligodlb-5-90n. Accessed 21 June 2023
22. LigoWave LigoDBL-520ac Home Page. https://www.ligowave.com/es/products-2/ligodlb-5-20-ac-3. Accessed 21 June 2023
23. LigoWave NFT-2AC Home Page. https://www.ligowave.com/es/products-2/nft-2ac-3. Accessed 21 June 2023
24. LigoWave Network Monitoring Software Home Page. https://www.ligowave.com/network-monitoring-software. Accessed 21 June 2023

Performance Analysis of Coherent and Non-coherent Detection Techniques in Chirp Spread Spectrum for Internet of Things Applications

Juan Minango[1(✉)], Marcelo Zambrano[1], Moisés Toapanta[1], Patricia Nuñez[2], and Eddye Lino[2]

[1] Instituto Tecnológico Superior Universitario Rumiñahui, Av. Atahualpa 1701 and 8 de Febrero, 171103 Sangolquí, Ecuador
juancarlos.minango@ister.edu.ec

[2] Instituto Espirítu Santo, Av. Juan Tanca Marengo and Av. Las Aguas, 090510 Guayaquil, Ecuador

Abstract. This paper presents an analysis of Chirp Spread Spectrum (CSS) for Internet of Things (IoT) applications, focusing on the performance of coherent and non-coherent detectors in various channel environments. The study evaluates scenarios with additive white Gaussian noise (AWGN), frequency-selective channels, and Rayleigh fading channels, considering a system with 10 receiving antennas. The results demonstrate that the coherent detector outperforms the non-coherent detector in terms of performance. However, the non-coherent detector offers the advantage of lower complexity. To further improve the performance of non-coherent detection in CSS-based IoT systems, the need for exploring new techniques is emphasized. Future research should aim to bridge the performance gap between coherent and non-coherent detection, considering adaptive signal processing algorithms, advanced filtering techniques, or hybrid detection schemes. By addressing the challenges associated with non-coherent detection, CSS can become a reliable and efficient modulation scheme for low signal-to-noise ratio conditions in IoT applications. This research contributes to the advancement of CSS in IoT, enabling seamless connectivity and data exchange in diverse IoT scenarios.

Keywords: Chirp Spread Spectrum (CSS) · Internet of Things (IoT) · Coherent detection · Non-coherent detection · Performance analysis

1 Introduction

In recent years, the Internet of Things (IoT) has emerged as a transformative technology, connecting an unprecedented number of devices and enabling a wide range of applications that enhance efficiency, convenience, and productivity in

M. Z. Vizuete et al. (Eds.): CI3 2023, LNNS 1040, pp. 110–122, 2024.
https://doi.org/10.1007/978-3-031-63434-5_9

various domains. With the explosive growth of IoT deployments, there is a pressing need for robust and efficient communication protocols that can handle the unique challenges posed by IoT environments. Chirp Spread Spectrum (CSS) has emerged as a promising modulation technique for overcoming some of these challenges, providing a reliable and versatile solution for IoT communication [1].

The concept of Chirp Spread Spectrum dates back to the early 1940s when it was initially used in military applications such as radar systems. However, it is only in recent years that CSS has gained significant attention as a viable modulation technique for IoT applications. Unlike traditional modulation schemes like frequency shift keying (FSK) or amplitude shift keying (ASK), CSS employs a unique approach that allows for increased range, improved robustness, and enhanced coexistence with other wireless systems [2].

CSS utilizes the principles of spread spectrum communication, which involves spreading the signal energy across a wide frequency band. This spreading not only provides inherent resistance to interference but also enables multiple devices to transmit simultaneously without causing significant mutual interference [2,3]. By employing linear frequency modulation, known as chirping, CSS achieves enhanced spectral efficiency and resilience against fading and multipath effects.

The Internet of Things, often referred to as the "network of smart devices," encompasses a vast ecosystem of interconnected sensors, actuators, and embedded systems, all working together to gather and exchange data. From smart homes and industrial automation to healthcare monitoring and environmental sensing, the IoT promises to revolutionize how we interact with technology and the world around us [4]. However, the massive number of IoT devices, their varied communication requirements, and the presence of other wireless systems demand innovative solutions to ensure reliable and efficient data transmission.

This is where CSS shines. By leveraging its unique characteristics, CSS addresses several key challenges encountered in IoT deployments. Its inherent resistance to interference makes it particularly suitable for crowded frequency bands, where numerous devices coexist, such as in urban environments or industrial settings. The low power requirements of CSS enable energy-efficient operation, making it well-suited for battery-powered IoT devices that are often deployed in remote or inaccessible locations [5].

Moreover, CSS enables long-range communication, allowing IoT devices to transmit data reliably over extended distances. This capability is especially valuable in applications such as environmental monitoring, precision agriculture, and asset tracking, where seamless connectivity across large areas is essential.

The purpose of this paper is to explore the applications and advantages of Chirp Spread Spectrum in the Internet of Things domain, with a specific focus on the comparison between coherent and non-coherent detection in CSS. We will investigate the performance of these detection schemes in two different environments: one with only noise and another with additive white Gaussian noise (AWGN) and Rayleigh fading.

The structure of the rest of the paper is as follows. Section 2 provides an in-depth explanation of Chirp Spread Spectrum modulation, including its principles, signal processing techniques, and advantages over traditional modulation schemes. In Sect. 3, the concept of coherent and non-coherent detection in CSS is discussed focusing on their benefits and limitations. Section 4 analyzes the performance comparison in terms of bit error rate (BER) between coherent and non-coherent detectors in the presence of additive white Gaussian noise (AWGN) and Rayleigh fading. Finally, the conclusions are presented in Sect. 5.

2 Chirp Spread Spectrum Concepts

From a mathematical standpoint, Chirp Spread Spectrum (CSS) is a modulation technique that utilizes linear frequency modulation to spread the signal energy across a wide frequency band [5]. This spreading technique provides inherent resistance to interference and enables multiple devices to transmit simultaneously without significant mutual interference [6]. In this introduction, we will explore the mathematical concepts underlying CSS and its advantages in the context of the Internet of Things (IoT).

CSS modulation is based on the principle of linear frequency modulation, also known as chirping. It involves sweeping the frequency of the transmitted signal linearly over time, resulting in a chirp waveform. Mathematically, the chirp waveform can be described as:

$$s(t) = \cos\left(2\pi\left(f_c t + \frac{K}{2}t^2\right)\right) \tag{1}$$

where $s(t)$ represents the chirp signal as a function of time t, f_c is the carrier frequency, and K represents the chirp rate. The chirp rate, defined as the change in frequency over time, determines the spread of the signal across the frequency band. A larger chirp rate results in a wider spread, providing increased resistance to interference.

CSS offers several advantages in IoT applications. Firstly, its resistance to interference allows for reliable communication in crowded frequency bands where multiple devices coexist [7]. By spreading the signal energy over a wide frequency band, CSS reduces the impact of narrowband interference sources, enabling robust communication in challenging environments. Additionally, CSS enables long-range communication, making it ideal for IoT deployments requiring connectivity over extended distances. The ability to transmit data reliably over larger distances enhances the coverage and scalability of IoT networks.

Furthermore, CSS exhibits low power requirements, making it energy-efficient and well-suited for battery-powered IoT devices. The efficient utilization of power resources ensures prolonged battery life, enabling long-term operation and reducing maintenance needs. This characteristic is particularly valuable for IoT deployments in remote or inaccessible locations, where frequent battery replacement or recharging may not be feasible.

Firstly, it is important to note that Chirp Spread Spectrum (CSS) is closely related to orthogonal Frequency Shift Keying (FSK) modulation, as both techniques employ orthogonal modulation schemes in different domains. While FSK modulation operates in the frequency domain, CSS operates in the time domain [8].

In FSK modulation, the transmitted signal is modulated by switching between different discrete frequencies, with each frequency representing a specific symbol. This modulation scheme is widely used in various communication systems, including wireless networks and digital audio broadcasting. FSK enables efficient transmission of digital data by using a set of orthogonal frequency carriers, ensuring minimal interference between symbols [3].

On the other hand, CSS takes a different approach by modulating the transmitted signal using linear frequency modulation, also known as chirping, in the time domain. This linear frequency sweep creates a chirp waveform, which spreads the signal energy across a wide frequency band. The spreading of the signal in CSS provides inherent resistance to interference and allows for the simultaneous transmission of multiple devices without significant mutual interference.

Despite the differences in the modulation domains, CSS and FSK share similarities in terms of their use of orthogonal modulation. Both techniques aim to minimize interference and improve the reliability of data transmission. While FSK achieves orthogonality in the frequency domain through the use of orthogonal frequency carriers, CSS achieves orthogonality in the time domain through the spreading of the signal energy [9].

Understanding the relationship between CSS and FSK can provide valuable insights into the principles and benefits of CSS modulation. By leveraging the orthogonal modulation characteristics, CSS enables robust and efficient communication in IoT applications, overcoming challenges such as interference, multipath fading, and coexistence with other wireless systems.

The complex base-band of the basic chirp $x_0(t)$, which has a frequency that linearly increases from $\frac{-BW}{2}$ at $t = \frac{-T}{2}$ to $\frac{BW}{2}$ at $t = \frac{T}{2}$ is given by:

$$x_0(t) = \exp\left\{ j\pi \frac{BW}{T} t^2 \right\} p_T(t), \quad \forall t \in R \tag{2}$$

where BW denotes the bandwidth of the signal, and T the time to transmit a symbol, then $\log_2(BW.T) = SF$ is the spreading factor which gives the number of bits carried by a single symbol that can take $M = BW \times T = 2^{SF}$ values and $p_T(t) = 1$ for all $t \in [-T/2, T/2[$, and $p_T(t) = 0$ otherwise.

To modulate a symbol $m \in M$, the initial frequency of $x_0(t)$ is shifted by $m\frac{BW}{M} = \frac{m}{T}$ Hz and the chirp must be wrapped between $[-BW/2; BW/2]$, that we have:

$$x_m(t) = \exp\left\{ j2\pi(\frac{BW}{2T} + \frac{m}{T})t \right\} \exp\left\{-j2\pi lBWt\right\} p_T(t), \tag{3}$$

$$\forall t \in Rl \in Z \;\; \text{s.t.} \frac{BW}{T}t + \frac{m}{T} \in [lBW - \frac{BW}{2}; lBW + \frac{BW}{2}].$$

Thus, the modulated signal consists of multiple symbols sent sequentially, with a time spacing of T seconds:

$$s(t) = \sum_{n=0}^{L/SF} x_{\mathbf{m}_n}(t - nT), \forall t \in R, \tag{4}$$

where $\mathrm{m}_n \in M$ is the n-th element of $\mathbf{m}$.

To obtain the discrete-time of $s(t)$, we must sample at the rate $F_{samp} = \frac{1}{T_{samp}} = BW$. Using the relation $BWT = M$, we have $T = MT_{samp}$. Thus, the discrete-time expression of $s(t)$ is:

$$s[k] = s(kT_{samp}) = \sum_{n=0}^{L/SF} x_{\mathbf{m}_n}(kT_{samp} - nT) = \sum_{n=0}^{L/SF} x_{\mathbf{m}_n}[k - nM] \quad \forall k \in Z. \tag{5}$$

Therefore, the discrete-time expression of a modulated chirp is:

$$\begin{aligned} x_m[k] &= x_m(kT_{samp}) \\ &= \exp\left\{j2\pi\left(\frac{BW}{2T}kT_{samp} + \frac{m}{T}\right)kT_{samp}\right\} \\ &\quad \times \exp\left\{-j2\pi lBWkT_{samp}\right\} \\ &\quad \times p_T(kT_{samp}), \end{aligned} \tag{6}$$

$$\forall k, l \in Z \ \text{ s.t.} \frac{BW}{kT_{samp}} + \frac{m}{T} \in [lBW - \frac{BW}{2}; lBW + \frac{BW}{2}].$$

where $p_T(kT_{samp}) = p_{\frac{T}{T_{samp}}}(k) = p_M[k]$ and $\exp\{-j2\pi lBWkT_{samp}\} = \exp\{-j2\pi lk\} = 1 \forall l, k \in Z$. Thus, the expression of $x_m(t)$ is simpler in the discrete-time domain:

$$x_m[k] = \exp\left\{j2\pi(\frac{B}{2T}kT_{samp} + \frac{m}{T})kT_{samp}\right\} p_M[k] = \exp\left\{j\pi\frac{k^2}{M}\right\}\exp\left\{j2\pi\frac{m}{M}k\right\} p_M[k]. \tag{7}$$

$$x_m[k] = \exp\left\{j2\pi(\frac{B}{2T}kT_{samp} + \frac{m}{T})kT_{samp}\right\} p_M[k] = \exp\left\{j\pi\frac{k^2}{M}\right\}\exp\left\{j2\pi\frac{m}{M}k\right\} p_M[k]. \tag{8}$$

Incorporating (8) in (5), we obtain:

$$s[k] = \sum_{n=0}^{L/SF} p_M[k - nM]\exp\left\{j\pi\frac{(k - nM)^2}{M}\right\}\exp\left\{j2\pi\frac{\mathbf{m}_n}{M}(k - nM)\right\} \tag{9}$$

$$s[k] = \underbrace{\exp\left\{j\pi\frac{k^2}{M}\right\}}_{Chirp}\underbrace{\sum_{n=0}^{L/SF} p_M[k - nM]\exp\left\{j2\pi\frac{\mathbf{m}_n}{M}k\right\}}_{M-FSK} \tag{10}$$

The Eq. 10 shows that CSS signals are basically chirped versions of M-arry Frequency Shift Keying (M-FSK) signals [6].

3 Coherent and Non-coherent Detector in CSS

Considering an AWGN channel, we have that:

$$y[k] = s[k] + z[k] \quad \forall k \in Z, \tag{11}$$

where $z[k]$ is a zero-mean, complex-circular white Gaussian noise. Later, we proceed with dechirping operation:

$$y_d[k] = y[k]\exp\left\{-j\pi\frac{k^2}{M}\right\} \quad \forall k \in Z, \tag{12}$$

where $y_d[k]$ is the dechirped observed signal. This process does not change the statistical properties of the noise, thus, the system involving $y_d[k]$ instead of $y[k]$ is equivalent to $M-FSK$ over AWGN.

3.1 Coherent Detector

Coherent detectors play a crucial role in Chirp Spread Spectrum (CSS) by extracting the transmitted information from the received CSS signal. These detectors rely on maintaining phase and frequency coherence between the transmitted and received signals, enabling precise demodulation and recovery of the original data [1].

In CSS, coherent detection involves aligning the carrier frequencies of the received signal with a replica of the transmitted chirp signal. This alignment is achieved through carrier synchronization, ensuring that the local replica of the transmitted chirp signal is accurately matched in frequency and phase with the received signal. By multiplying the received signal with the synchronized replica, the coherent detector can extract the information embedded in the CSS signal [1].

Coherent detection is essential for separating the desired signal from other interference sources, as it takes advantage of the alignment of the carrier frequencies. This alignment allows for precise demodulation, resulting in accurate recovery of the original data. It is particularly useful in environments with low signal-to-noise ratio or when dealing with interfering signals that are closely located in the frequency spectrum.

Overall, coherent detectors in CSS enable reliable and accurate demodulation, making them an important component in the successful implementation of CSS-based communication systems.

Over perfect AWGN channels, it allows for maximum likelihood detection (MLD). Its use is mandatory for demodulating derivative of CSS that use the phase to encode symbols [16]. Thus, a MLD strategy for M-CSS in the presence of AWGN is to find the symbol m whose associated signal $\exp\left\{2\pi\frac{m}{M}k\right\}$ correlates the best with the observed signal $y_d[k]$. This is given by:

$$\hat{\mathbf{m}}_n = \text{argmax } Real\left\{\sum_{k=-\infty}^{\infty} p_M[k]\exp\left\{-2\pi\frac{m}{M}k\right\} y_d[k+nM]\right\}. \tag{13}$$

From the above expression, we observe the term in the real part is the M point Discrete Fourier Transform (DFT), denoted by $F_M\{.\}$ of the received signal:

$$\hat{\mathbf{m}}_n = \text{argmax } Real\left\{F_M\left\{y_d[k+nM]\right\}[m]\right\}. \quad (14)$$

Expanding (16), we have:

$$\begin{aligned} F_M\left\{y_d[k-nM]\right\}[m'] &= F_M\left\{s[k-nM]\right\}[m'] + F_M\left\{z[k]\right\}[m'] \\ &= M\delta_{n-n'}\delta_{m_n-m'_n} + F_M\left\{z[k]\right\}[m'], \end{aligned} \quad (15)$$

where $\delta_n = 1$ if $n = 0$ and zero otherwise. As we can see, the correlator output corresponding to the symbol that was sent has its amplitude augmented by M, as opposed to the other correlators. This means that this modulation, along with coherent demodulation gets more robust to noise as M increases.

3.2 Non-coherent Detector

In Chirp Spread Spectrum (CSS), a non-coherent detector is an alternative to the coherent detection scheme. Unlike coherent detection, which relies on maintaining phase and frequency coherence between the transmitted and received signals, non-coherent detection does not require such synchronization [5].

In non-coherent detection, the received CSS signal is processed without aligning the carrier frequencies or maintaining phase coherence. Instead, the detector focuses on extracting the modulating information from the received signal using techniques that do not rely on precise carrier synchronization [6].

One common non-coherent detection technique used in CSS is energy detection. This technique involves measuring the energy level of the received signal over a certain integration period. By comparing the energy level to a predetermined threshold, the detector makes a decision on the presence or absence of the transmitted signal.

Since non-coherent detection does not require precise synchronization, it offers several advantages in certain scenarios. Non-coherent detectors are more robust in environments where carrier frequency offsets or phase variations occur, as they are not affected by these impairments. They also eliminate the need for complex carrier recovery circuits, simplifying the receiver design and reducing implementation complexity.

However, non-coherent detection typically has lower performance compared to coherent detection, particularly in terms of signal detection sensitivity and demodulation accuracy. Non-coherent detectors may suffer from higher detection error rates and reduced data throughput, especially in low signal-to-noise ratio (SNR) conditions. Additionally, non-coherent detection may have limitations in scenarios where high-precision demodulation or decoding is required [4].

Nonetheless, non-coherent detection is suitable for applications where carrier synchronization is challenging or not feasible, or when the emphasis is on simplicity and robustness rather than achieving the highest possible performance. It offers an alternative approach for CSS systems in certain environments where precise synchronization is difficult to achieve or maintain.

Non-coherent detector replaces the real part operator by the magnitude operator in (16):

$$\hat{\mathbf{m}}_n = \text{argmax } |F_M \{y_d[k+nM]\}[m]|. \tag{16}$$

3.3 Quadrature Demodulation

In sub-section, we have included the description about quadrature demodulation for comparison purposes which is a technique used in communication systems to extract information from a modulated signal. It is commonly employed in various modulation schemes, including amplitude modulation (AM), frequency modulation (FM), and phase modulation (PM).

The term "quadrature" refers to the use of two separate signal paths, known as the in-phase (I) and quadrature (Q) channels, which are 90° out of phase with each other. The modulated signal is split into these two channels, allowing for simultaneous processing of both the in-phase and quadrature components.

The quadrature demodulation process typically involves two main steps: mixing and low-pass filtering. In the mixing stage, the received signal is multiplied by two local oscillators, one in-phase and one quadrature, which are synchronized with the carrier frequency of the modulated signal. This mixing process results in the separation of the modulated signal into its in-phase and quadrature components.

After mixing, the resulting signals are passed through low-pass filters to remove high-frequency components and noise. These filters are designed to allow only the baseband information, typically the amplitude, frequency, or phase modulation, to pass through. The filtered in-phase and quadrature signals can then be further processed or demodulated to recover the original modulating information.

Quadrature demodulation offers several advantages in communication systems. By using the I/Q channels, it enables the receiver to capture both the amplitude and phase characteristics of the modulated signal simultaneously. This allows for accurate demodulation and recovery of the original information, even in the presence of noise and interference.

Additionally, quadrature demodulation is compatible with various modulation schemes, making it a versatile technique in modern communication systems. It is widely used in applications such as wireless communication, software-defined radio (SDR), and digital broadcasting.

Quadrature demodulation can be used in M-CSS signal, once the M-CSS signal has passed by the dechirping process, we have a M-FSK signal which can be seen as frequency modulated M-arry Amplitude Shift Keying (ASK) modulations. Thus, we have two-stage demodulation process. The first stage performs quadrature detection of the frequency variation in $y_d[k]$, and the second performs M-ASK demodulation on this frequency variation.

Quadrature demodulation computes the product of $y_d[k]$ with a unit delayed and conjugated version of itself. In order to determine its frequency variation. Thus, we have:

$$a[k] = \arg \{y_d[k] y_d^*[k-1]\}. \tag{17}$$

Once the frequency is the derivative of the phase, we have that quadrature demodulator corresponding to the digital derivative of the phase of $y_d[k]$. After quadrature detection, the signal is analogous to an M-ASK modulated signal:

$$a[k] = \frac{2\pi}{M} \sum_{n=0}^{L/SF} p_M[k - nM]\mathbf{m}_n + z'[k], \tag{18}$$

where $z'[k]$ has no guarantee to be Gaussian nor white. Later, a hard decision by comparing its amplitude to $M - 1$ thresholds can be taken in order to obtain the transmitted symbols $\mathbf{m}$.

4 Performance Results Comparisons

In this section, we analyze and compare the performance of CSS in different physical environments, such as AWGN, frequency-selective and Rayleight channels. We evaluate the performance metrics, including signal-to-noise ratio (SNR) and bit error rate (BER).

4.1 AWGN Channel

Figure 1 compares the three demodulators described in Sect. 3 for a CSS with SF = 9. We note that quadrature demodulation has the worst performance, which can however be improved by oversampling the received signal with a factor of 2. However, quadrature demodulation continues to present an E_b/N_0 difference as high as 23 dB for a BER of 10^{-4} in comparison with coherent demodulation.

4.2 Frequency-Selective Channel

In a frequency-selective channel in order to evaluate the performance of coherent and non-coherent demodulation, we have considered a static frequency-selective channel with impulse response $h[k] = 0.407\delta_{k-1} + 0.815\delta_k + 0.407\delta_{k+1}$ with $\delta_k = 1$ if $k = 0$ and $\delta_k = 0$ otherwise. Note that this channel is non-invertible. The received signal is given by:

$$y[k] = \sum_{l=-\infty}^{\infty} h[l]s[k - l] + z[k] \tag{19}$$

From Fig. 2 we note that CSS performs better than FSK on this channel due to the fact that it is better at spreading the information in frequency.

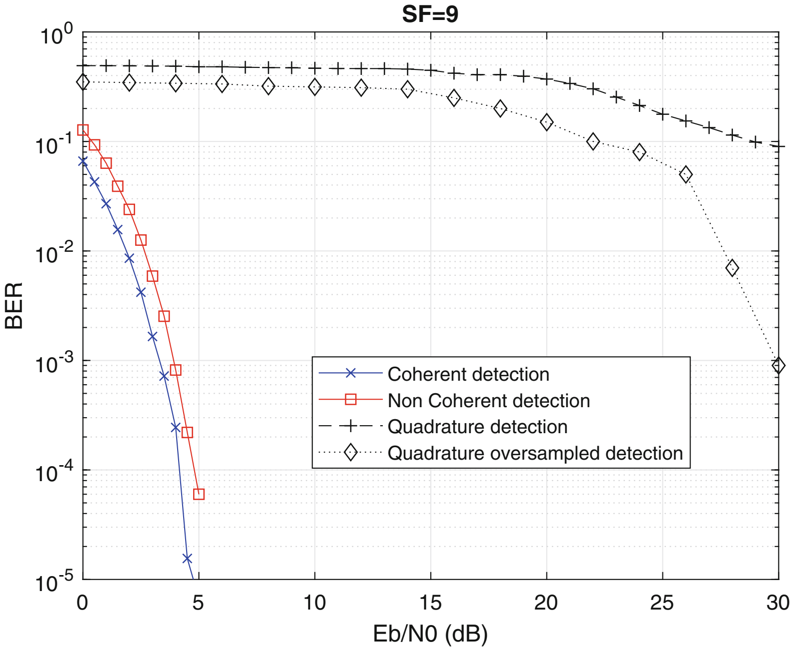

Fig. 1. Comparison between different detectors for CSS with SF = 9 in an AWGN channel

4.3 Rayleigh Channel

In this analysis, a slow and flat fading channel is assumed. Thus, the received signal is given by:

$$y[k] = h[k]s[k] + z[k], \tag{20}$$

where $h[k] = \alpha[k]\exp\{j\theta\}$ with $\alpha[k]$ and θ being attenuation factor and uniformly distributed phase variations.

Figure 3 shows the comparison between coherent and non-coherent CSS modulation with SF = 6 in a Rayleigh channel. As it is evident coherent detection presents a better performance of about 0.5 dB in comparison with non-coherent detection. For the theoretical non-coherent detection BER curve the 'beading' tool from Matlab was used. However, this same tool for the case of the theoretical coherent detection BER curve is only defined for $M = 2$.

Figure 4 compares the performance of a CSS modulation with SF = 6 employing $N_r = 1$ and $N_r = 10$ receive antennas for coherent and non-coherent detection. We can observe better performance when we use more than 1 receive antenna. For this case, we note that the performance difference between coherent and non-coherent detection increase as N_r increase. Thus, for $N_r = 10$ the performance difference is about 4 dB for a BER$= 10^{-3}$.

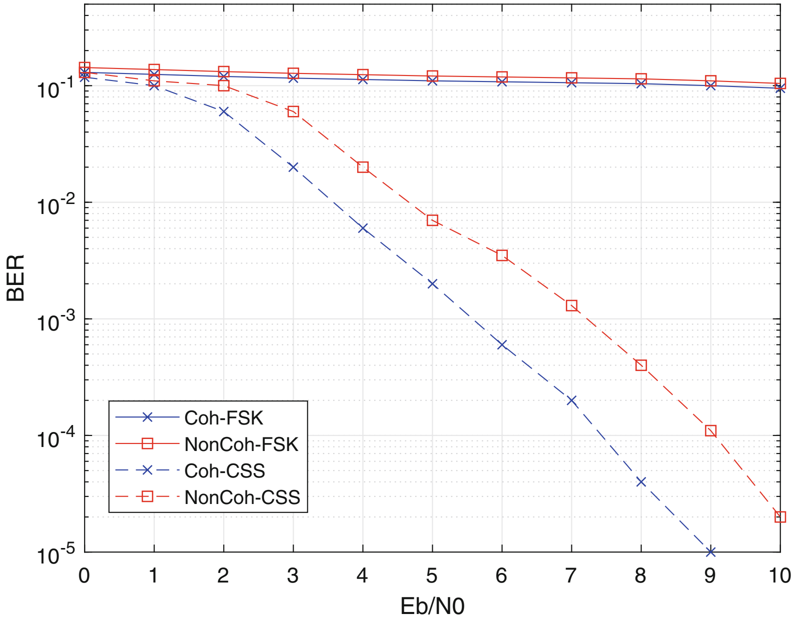

Fig. 2. Comparison between CSS and FSK in a Frequency-selective Channel.

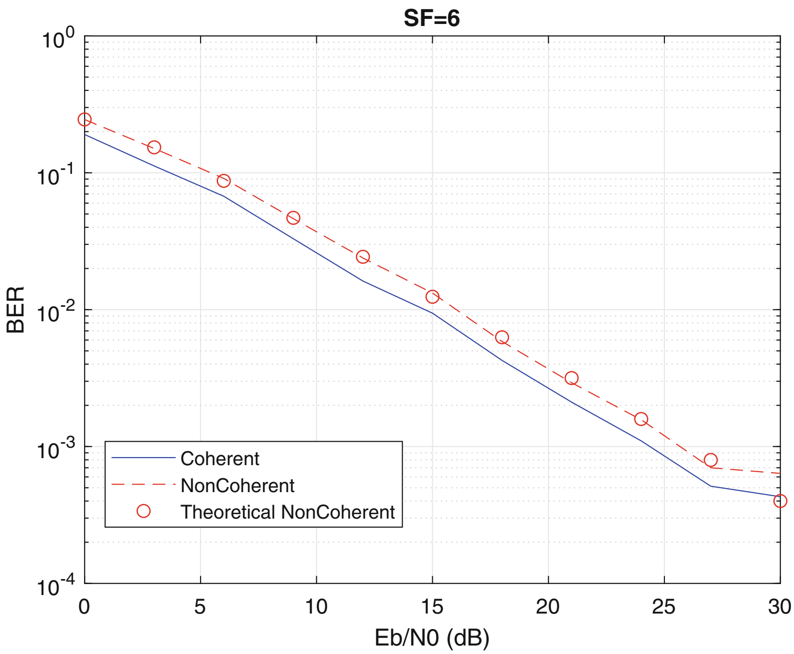

Fig. 3. CSS with coherent and non-coherent detection in a Rayleigh Channel.

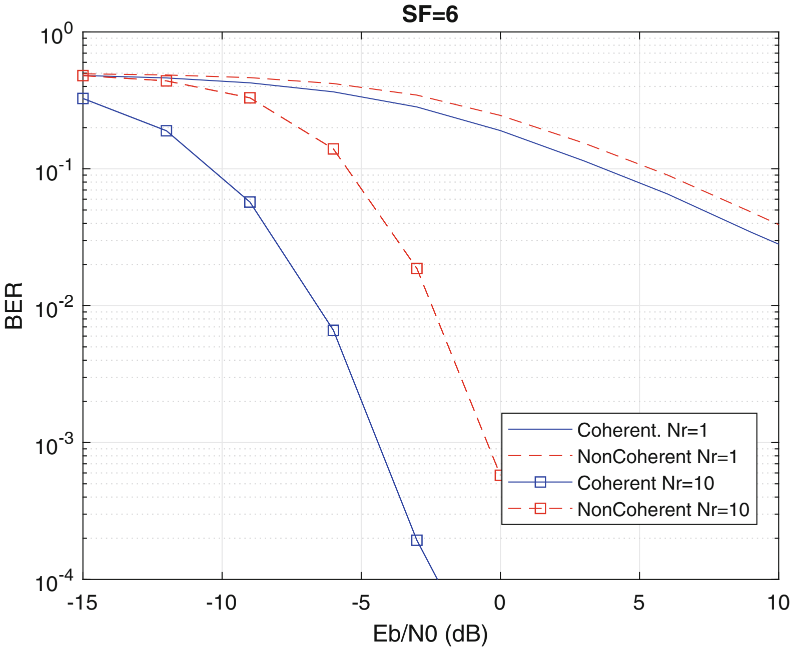

Fig. 4. CSS with coherent and non-coherent detection and diversity $N_r = 10$ receive antennas in a Rayleigh Channel.

5 Conclusion

In conclusion, the utilization of Chirp Spread Spectrum (CSS) in Internet of Things (IoT) applications has been presented and discussed in this paper. The performance of both coherent and non-coherent detectors was thoroughly analyzed in various channel environments, including scenarios with additive white Gaussian noise (AWGN), frequency-selective channels, and Rayleigh fading channels.

The results demonstrate that the coherent detector exhibits superior performance compared to the non-coherent detector in the studied system with 10 receiving antennas. The coherent detection scheme, with its ability to maintain phase and frequency coherence between the transmitted and received signals, proves to be more effective in extracting the desired information from the CSS signal.

However, it is worth noting that the non-coherent detector offers the advantage of lower complexity due to its independence from precise carrier synchronization. This makes it an attractive option for resource-constrained IoT devices or scenarios where maintaining synchronization may be challenging.

Nevertheless, to further enhance the performance of non-coherent detection in CSS-based IoT systems, it is essential to explore and evaluate new techniques. Future research should focus on developing innovative methods that can mitigate the performance gap between coherent and non-coherent detection. These advancements may include adaptive signal processing algorithms, advanced filtering techniques, or hybrid detection schemes that combine the strengths of both coherent and non-coherent approaches.

By addressing the challenges associated with non-coherent detection, such as increased bit error rates or reduced data throughput, the potential of CSS in low signal-to-noise ratio conditions can be fully realized. This will contribute to the advancement of reliable and efficient IoT communication systems, enabling seamless connectivity and data exchange in diverse IoT applications.

In summary, this study highlights the significance of coherent and non-coherent detectors in CSS-based IoT systems. While the coherent detector currently demonstrates superior performance, the exploration of new techniques for improving the performance of non-coherent detection holds great promise. By bridging the performance gap, we can leverage the advantages of both detection schemes and unlock the full potential of CSS in IoT applications.

Acknowledgments. We would like to express our sincere gratitude to CEDIA for their generous financial support, which played a pivotal role in the successful realization of this project. Their commitment to our vision has been instrumental, and we appreciate the confidence they have shown in our mission. This project would not have been possible without the invaluable contribution from CEDIA, and we extend our deepest thanks for their unwavering support.

References

1. Tselikis, G., Askoxylakis, I.G.: Chirp spread spectrum for IoT applications: challenges and opportunities. IEEE Commun. Mag. **55**(11), 147–153 (2017)
2. Zheng, Y., Dong, X., Chen, L.: Chirp spread spectrum in Internet of Things: a comprehensive survey. IEEE Internet Things J. **8**(8), 6604–6617 (2021)
3. Ali, S., Ismail, M., Anpalagan, A.: Chirp spread spectrum modulation for energy-constrained IoT systems. IEEE Access **8**, 214312–214327 (2020)
4. Shah, D., Garg, S.: Chirp spread spectrum-based IoT localization technique for smart cities. In: Proceedings of the International Conference on IoT in Social, Mobile, Analytics and Cloud, pp. 143–148 (2019)
5. Han, Y., Han, C.: Chirp spread spectrum communication scheme for IoT applications in wireless sensor networks. Sensors **21**(6), 2129 (2021)
6. Ahmad, N., Rahman, A.F., Isa, N.A.M.: Chirp spread spectrum modulation for secure and reliable IoT communications. In: Proceedings of the International Conference on IoT in Social, Mobile, Analytics and Cloud, pp. 223–228 (2019)
7. Suh, J., Oh, C., Hong, D.: Chirp spread spectrum-based communication for cooperative Internet of Things. In: Proceedings of the International Conference on Information Science and Applications, pp. 1–4 (2019)
8. Haq, R.U., Baig, I., Khan, M.A.U.: Chirp spread spectrum modulation for reliable communication in IoT. In: Proceedings of the International Conference on Advanced Communication Technologies and Networking, pp. 8–13 (2021)
9. Gupta, S., Nath, B., Pandey, V.: Performance evaluation of chirp spread spectrum modulation for IoT applications. In: Proceedings of the International Conference on Inventive Computation Technologies, pp. 384–389 (2021)

Exploring the Use of Blockchain for Academic Certificates: Development, Testing, and Deployment

Juan Minango(✉), Marcelo Zambrano, and Cesar Minaya

Instituto Tecnológico Superior Universitario Rumiñahui, Av. Atahualpa 1701 and 8 de Febrero, 171103 Sangolquí, Ecuador
juancarlos.minango@ister.edu.ec

Abstract. This study presents the development and deployment of a smart contract for issuing academic certificates on the Sepolia network. The smart contract, built using the Solidity language and the ERC721 standard, enables secure and decentralized certification, ensuring the integrity and immutability of academic records. The deployment process was facilitated by the use of the Alchemy development tool, allowing for seamless interaction with the blockchain network. The successful deployment was confirmed through the acquisition of the contract address and the verification of transaction details on Etherscan. Unit tests were conducted to ensure the functionality and reliability of the smart contract, validating its ability to mint and verify academic certificates. The results demonstrated the potential of blockchain technology in transforming traditional certification systems by providing transparency, tamper-proof records, and enhanced security. This study contributes to the growing field of blockchain applications in the academic sector, highlighting the importance of decentralized solutions for efficient and trustworthy certification processes.

Keywords: Smart contract · Academic certificates · Blockchain · deployment · Alchemy · ERC721 · Decentralized certification

1 Introduction

Blockchain technology has emerged as a groundbreaking innovation with far-reaching implications across industries. Its decentralized and transparent nature has the potential to disrupt traditional systems, establishing new standards of trust, security, and efficiency [1,2]. By providing a decentralized ledger that records transactions and information across a network of computers, blockchain eliminates the need for intermediaries, reduces the risk of fraud, and enhances transparency [3].

One of the key advantages of blockchain is its ability to establish trust in a trustless environment. Through cryptographic techniques and consensus

M. Z. Vizuete et al. (Eds.): CI3 2023, LNNS 1040, pp. 123–137, 2024.
https://doi.org/10.1007/978-3-031-63434-5_10

mechanisms, blockchain ensures the integrity and immutability of data, making it resistant to manipulation and tampering. This feature has the potential to revolutionize industries such as finance, supply chain management, healthcare, the academic sector, and many more, where trust and transparency are paramount [4].

In finance, blockchain technology enables secure and efficient peer-to-peer transactions without the need for traditional intermediaries such as banks [5]. It provides a decentralized and tamper-proof record of transactions, enhancing security and reducing costs associated with traditional payment systems. Additionally, blockchain-based smart contracts automate and enforce the terms of agreements, streamlining processes and minimizing the risk of disputes [5,6].

In supply chain management, blockchain facilitates end-to-end traceability, enabling businesses and consumers to track the journey of products from origin to destination. This transparency helps in verifying the authenticity and quality of goods, ensuring compliance with regulations, and combating issues such as counterfeiting and supply chain fraud. By providing an immutable record of transactions and product information, blockchain enhances trust among participants and simplifies complex supply chain processes [7].

In the healthcare industry, blockchain has the potential to revolutionize data sharing and patient records management. With blockchain, patients can have control over their medical records, granting access to healthcare providers as needed. This decentralized approach improves the security and privacy of sensitive medical information while enabling interoperability and efficient sharing of data among healthcare providers, leading to better patient outcomes and more effective research [8].

Furthermore, blockchain technology has demonstrated adaptability across different sectors, including energy, voting systems, intellectual property, and more. Its decentralized and transparent nature can enhance the efficiency, security, and accountability of various processes. By utilizing blockchain, organizations can streamline operations, reduce costs, mitigate risks, and establish new business models that were previously not feasible [9].

Besides, the academic sector can also benefit significantly from the implementation of blockchain technology. One of the key applications is in the issuance and verification of academic certificates. By leveraging blockchain, educational institutions can create tamper-proof digital certificates as non-fungible tokens (NFTs). These NFT-based certificates provide a secure and decentralized record of achievements, enabling easy verification by employers and other educational institutions. This eliminates the risks associated with counterfeit certificates and simplifies the verification process, enhancing trust and reliability in academic credentials [10].

Thus, in this paper, we present the development of a smart contract[1] for the emission of academic certificates by Instituto Tecnológico Universitario Rumiñahui (ISTER). The smart contract was deployed on a blockchain net-

[1] We have included the link of the repository of the Academic Certificate smart contract [https://github.com/jminangoIster/corn_leaves_diseases] for reproducibility.

work, allowing us to interact with it using the Metamask wallet. By leveraging the capabilities of blockchain technology and the Ethereum network, we aim to change the certification process and enhance the transparency, security, and accessibility of academic credentials issued by ISTER.

The remainder of this paper is organized as follows. Section 2 provides an introduction to the Ethereum network, specifically the Sepolia network, which was utilized for deploying and testing our smart contracts. In Sect. 3, we provide a concise overview of the development tools and network connection, which served as the foundation for the implementation and interaction with our smart contracts. Section 4 delves into the details of the smart contract developed specifically for issuing academic certificates, highlighting its key functionalities and mechanisms. The deployment results of the smart contract are presented in Sect. 5, showcasing the outcomes and performance metrics. Finally, in Sect. 6, we draw conclusions based on our findings and discuss the implications and potential future directions for further research in this domain.

2 Ethereum and the Sepolia Network

The Ethereum network has gained significant attention as a decentralized, open-source blockchain platform that enables the development and deployment of smart contracts. With its native cryptocurrency, Ether (ETH), Ethereum provides a robust and versatile environment for building decentralized applications (dApps) and executing programmable transactions [4,11].

In this section, we introduce the Sepolia network, a specific instance of the Ethereum network that we utilized for deploying and testing our smart contract for issuing academic certificates. Sepolia is a test network specifically designed for development and experimentation purposes, providing developers with a sandbox-like environment to deploy and interact with smart contracts before deploying them on the Ethereum mainnet [12].

Sepolia offers several advantages for blockchain tests. Firstly, it allows us to test the functionality and performance of our academic certificate smart contract without incurring any real-world costs or risks associated with the deployment on the mainnet. This enables us to iterate and refine our implementation before taking it live [13].

Secondly, Sepolia provides a network with a similar architecture and consensus mechanism to the Ethereum mainnet, allowing us to simulate real-world conditions and gauge the scalability and efficiency of our smart contract deployment [10]. By using Sepolia, we can evaluate the network's transaction processing capabilities, gas costs, and potential bottlenecks that may affect the issuance and verification of academic certificates.

2.1 Faucet in the Sepolia Network

A faucet is a service specifically designed for test networks like Sepolia. Its purpose is to distribute test ETH to developers, allowing them to cover transaction costs and simulate real-world scenarios without incurring any expenses. Test ETH obtained from the faucet serves as a valuable resource for deploying and interacting with smart contracts in a risk-free environment [14,15].

To obtain test ETH through the Sepolia faucet, we must follow these steps:

1. Visit the Sepolia testnet faucet website or a compatible faucet service designed for the Sepolia network.
2. Provide the Ethereum address associated with the wallet that will be used for interacting with the academic certificate smart contract on Sepolia.
3. Submit a request to receive test ETH by clicking on the "Request" or "Get Test ETH" button.
4. The faucet service will process the request and verify the provided Ethereum address.
5. Upon successful verification, the faucet will transfer a predetermined amount of test ETH to the provided Ethereum address.
6. By obtaining test ETH through the faucet, we can seamlessly engage with the academic certificate smart contract on Sepolia without the need for real funds. This enables thorough testing, debugging, and validation of the smart contract's functionality before deploying it on the live Ethereum network.

3 Development Tools and Network Connection

3.1 Hardhat: A Development Framework

In the development of the academic certificate smart contract, the Hardhat framework was utilized. Hardhat is a popular development environment for Ethereum smart contracts, providing a robust set of tools and utilities that facilitate the entire development lifecycle. It offers features such as smart contract compilation, deployment, testing, and debugging.

Hardhat simplifies the development process by providing a command-line interface (CLI) for executing tasks related to smart contracts. It supports the Solidity programming language and integrates seamlessly with various Ethereum networks, including the Sepolia network. With Hardhat, developers can efficiently write, compile, and deploy their smart contracts, making it an ideal choice for this research.

3.2 Alchemy: Connecting to the Sepolia Network

To interact with the Sepolia network and deploy the academic certificate smart contract, the Alchemy platform was used. Alchemy acts as an infrastructure provider, offering developers easy access to Ethereum networks and providing powerful APIs for blockchain connectivity.

Alchemy simplifies the process of establishing a connection with the Sepolia network by providing a reliable and user-friendly interface. It offers advanced features such as transaction monitoring, debugging tools, and real-time network analytics. By leveraging Alchemy, developers can seamlessly interact with the Sepolia network, deploy smart contracts, and monitor their transactions.

Figure 1 showcases the Ister Academic Certificates decentralized application (DApp) running on the Alchemy platform. The DApp interface displays the network connection details, including the Sepolia network, which enables seamless interaction with the academic certificate smart contract. Users can mint and verify academic certificates securely through the user-friendly interface provided by the DApp. The integration of Alchemy ensures reliable and efficient network connectivity, enhancing the overall experience of issuing and verifying academic certificates on the blockchain.

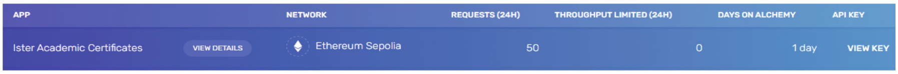

Fig. 1. Ister Academic Certificates DApp on Alchemy.

3.3 Metamask: Interacting with the Academic Certificate and Faucet

Metamask is a widely used browser extension that serves as a digital wallet and allows users to interact with Ethereum-based applications. In the context of the academic certificate smart contract, Metamask plays a crucial role in facilitating user interactions and accessing the Sepolia network.

By installing the Metamask extension in our web browser, users can create Ethereum wallets and securely store their cryptographic keys. Metamask also provides an intuitive user interface for interacting with the academic certificate smart contract, enabling users to mint and verify certificates.

Metamask was configured to connect to the Sepolia network by adding the appropriate network details, including the network name, chain ID, RPC URL, and optionally the faucet's address. Once connected, users can seamlessly interact with the smart contract deployed on the Sepolia network, minting and verifying academic certificates.

Figure 2 shows the Metamask browser extension interface with an account named "Ister" connected to the Sepolia network. The account balance of 0.5 SepoliaETH indicates that the account has successfully received faucet funds. The integration of Metamask provides a user-friendly and convenient experience for managing blockchain transactions and interacting with the academic certificate system.

By combining Hardhat for development, Alchemy for network connection, and Metamask for user interactions, the academic certificate smart contract can be efficiently developed, deployed, and interacted with on the Sepolia network. This combination of tools and technologies ensures a seamless and user-friendly experience for all stakeholders involved.

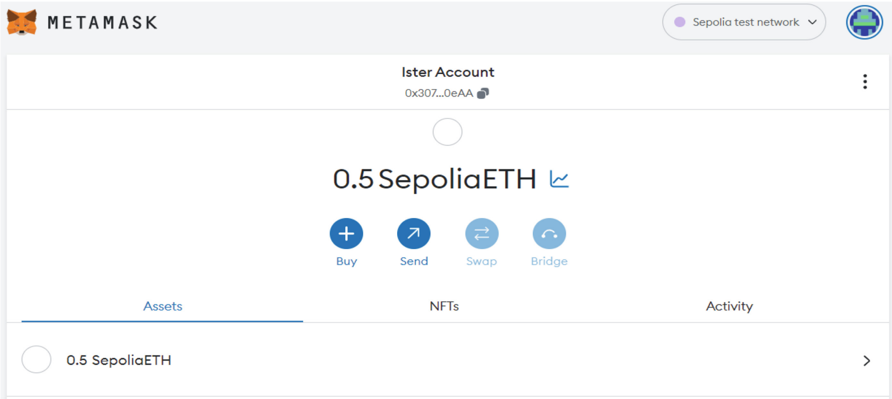

Fig. 2. Metamask Browser Interface with Ister Account on Sepolia Network.

4 Academic Certificate Smart Contract: Functionality and Mechanisms

In this section, we provide an in-depth explanation of the smart contract developed for issuing academic certificates. The smart contract, named "Academic-Certificate", is built on the Ethereum blockchain using the Solidity programming language.

The contract inherits from the ERC721 standard which is shown in Listing 1.1, which is a widely adopted standard for non-fungible tokens (NFTs) on Ethereum. Unlike fungible tokens, which are interchangeable and identical to each other (like cryptocurrencies), non-fungible tokens represent unique assets that can have distinct characteristics and properties. Each ERC721 token is assigned a unique identifier, or token ID, which distinguishes it from other tokens in the same contract. Thus, our contract ensures that each academic certificate issued is unique and can be easily transferred and verified.

Listing 1.1. AcademicCertificate contract

```
contract AcademicCertificate is ERC721 {
}
```

The structure of an academic certificate is defined within the contract using a struct. It includes fields such as recipient name, date of issue, issuer, course, grade, and duration. These fields capture the essential information associated with each certificate and it is presented in Listing 1.2.

Listing 1.2. AcademicCertificate contract

```
 struct Certificate {
        string recipientName;
        uint256 dateOfIssue;
        string issuer;
```

```
        string course;
        string grade;
        string duration;
    }
```

To mint a new certificate NFT, the contract includes a function named “mintCertificate”. This function requires that the caller is the designated “Ister Account”, which ensures that only authorized entities can emit academic certificates. Upon minting, a new certificate ID is generated, and the certificate data is stored in a mapping. See Listing 1.3.

Listing 1.3. AcademicCertificate contract

```
function mintCertificate(
        string memory _recipientName,
        uint256 _dateOfIssue,
        string memory _issuer,
        string memory _course,
        string memory _grade,
        string memory _duration
    ) public {
        require(_isterAccount == msg.sender, ``Just Ister Account can emit Academic Certificates'');
        uint256 certificateId = _totalCertificates + 1;
        certificates[certificateId] = Certificate(
            _recipientName,
            _dateOfIssue,
            _issuer,
            _course,
            _grade,
            _duration
        );
        _mint(msg.sender, certificateId);
        _totalCertificates ++;
        emit NewCertificate(
            certificateId,
            _recipientName,
            _dateOfIssue,
            _issuer,
            _course,
            _grade,
            _duration
        );
    }
```

The contract also includes a function named “verifyOwnership” which allows anyone to verify their ownership of a certificate NFT by providing its ID. This function returns a boolean value indicating whether the caller is the owner of the specified certificate as is shown in Listing 1.4.

Listing 1.4. AcademicCertificate contract

```
function verifyOwnership(uint256 _certificateId) public
    view returns (bool) {
        return ownerOf(_certificateId) == msg.sender;
    }
```

Additionally, the contract emits an event named "NewCertificate" whenever a new certificate is minted. This event includes the certificate ID, recipient name, date of issue, issuer, course, grade, and duration. See Listing 1.5.

Listing 1.5. AcademicCertificate contract

```
event NewCertificate(
        uint256 indexed certificateId,
        string recipientName,
        uint256 dateOfIssuem,
        string issuer,
        string course,
        string grade,
        string duration
    );
```

5 Results and Performance Metrics

5.1 Unitary Tests

In the repository accompanying this article, a comprehensive set of test cases has been developed to validate the functionality and performance of the AcademicCertificate smart contract. These tests utilize the Mocha and Chai testing frameworks, along with the Hardhat development environment.

The tests cover various aspects of the contract, including the deployment process, the minting of new certificate NFTs, and the verification of ownership. By running these tests, it is possible to ensure that the smart contract behaves as expected and meets the desired requirements.

The first test case, "should mint a new certificate NFT," verifies that the contract successfully mints a new certificate with the specified details and assigns ownership to the correct address. It ensures that the certificate data is correctly stored and retrievable.

The second test case, "should verify ownership of a certificate NFT," ensures that the contract correctly verifies the ownership of a certificate NFT. It validates that only the rightful owner can claim ownership and that unauthorized users are unable to do so.

These test cases provide a solid foundation for ensuring the robustness and reliability of the AcademicCertificate contract. They enable developers and users to have confidence in the contract's functionality and its ability to issue and verify academic certificates securely and accurately.

Figure 3 shows the successful execution of the tests using the command 'npx hardhat test'. The tests verify the functionality of the AcademicCertificate smart contract, ensuring that it properly mints a new certificate NFT and verifies the ownership of the certificate. The tests were executed using the Hardhat development environment, which provides a robust and reliable framework for testing Ethereum smart contracts."

```
PS C:\ws-ethereum\educationalCertificates> npx hardhat test


  AcademicCertificate
    Deployment
      ✓ should mint a new certificate NFT (924ms)
      ✓ should verify ownership of a certificate NFT (46ms)


  2 passing (977ms)
```

Fig. 3. Successful execution of tests using 'npx hardhat test'. The tests verify the functionality of the AcademicCertificate smart contract, ensuring proper certificate issuance and ownership verification.

5.2 Deployment Results and Verification on Alchemy and Etherscan

To deploy the AcademicCertificate smart contract, we execute the command 'npx hardhat run scripts/deploy.ts –network sepolia' which will run the deployment script using the sepolia network.

Upon successful deployment, we received a message indicating that the "Academic Certificate" contract has been deployed. The contract address was displayed as: "Contract deployed at address: 0x4e86B73205B95c6537B307e778158 01b2ee7F7e4" as it is shown in Fig. 4.

```
PS C:\ws-ethereum\educationalCertificates> npx hardhat run scripts/deploy.ts --network sepolia
Academic Certificate Successfully Deployed!
Contract deployed at address: 0x4e86B73205B95c6537B307e77815801b2ee7F7e4
```

Fig. 4. Successful Deployment of the Academic Certificate Smart Contract.

The contract address shown in Fig. 4 represents the unique identifier assigned to the deployed Academic Certificate smart contract on the blockchain network. This address serves as a reference or identifier to interact with the specific instance of the smart contract.

In simpler terms, the contract address can be thought of as the location of the smart contract on the blockchain. It allows users to interact with the deployed contract, such as minting new certificate NFTs or verifying ownership of existing certificates.

Alchemy Dashboard Results. In this subsubsection, the results from the successful deployment of the Academic Certificate smart contract on the Alchemy dashboard are presented and discussed.

Figure 5 shows the Alchemy Dashboard, displaying important deployment statistics of the Academic Certificate smart contract. The dashboard reveals key metrics such as the median response time of 22 ms, indicating the efficiency and responsiveness of the deployed contract. Additionally, the success rate of 98% highlights the robustness and reliability of the deployment process. These results demonstrate the successful deployment and smooth operation of the Academic Certificate smart contract on the Ethereum network, ensuring seamless issuance and verification of academic certificates.

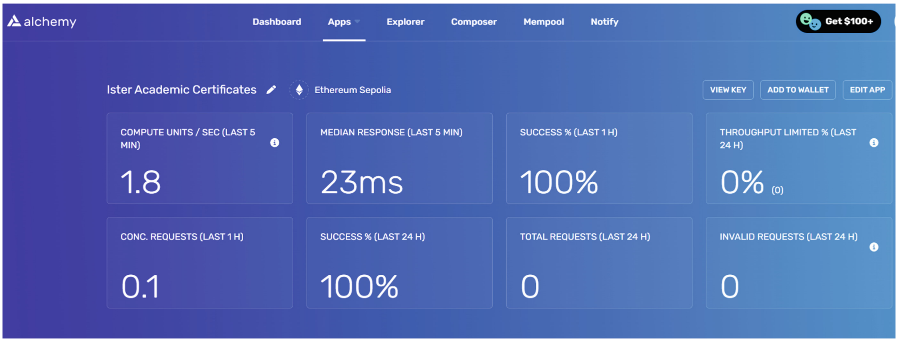

Fig. 5. Alchemy Dashboard showing deployment statistics of the Academic Certificate smart contract.

Figure 6 showcases the Alchemy Explorer, providing detailed information about the Ister Account and various Ethereum network parameters. The public key associated with the Ister Account is displayed, ensuring secure and authenticated interactions with the blockchain. Additionally, key network parameters such as eth_chainId, eth_getTransactionReceipt, eth_blockNumber, and eth_getTransactionCount are visible, providing insights into the current state of the Ethereum network. These parameters play a crucial role in facilitating transactions, verifying blocks, and ensuring the integrity of the blockchain. Thus, the Alchemy Explorer serves as a valuable tool for monitoring and analyzing blockchain activity, enhancing transparency and reliability in the deployment and utilization of the Academic Certificate smart contract.

Figure 7 provides essential information about individual transactions related to our academic certification smart contract. This information includes:

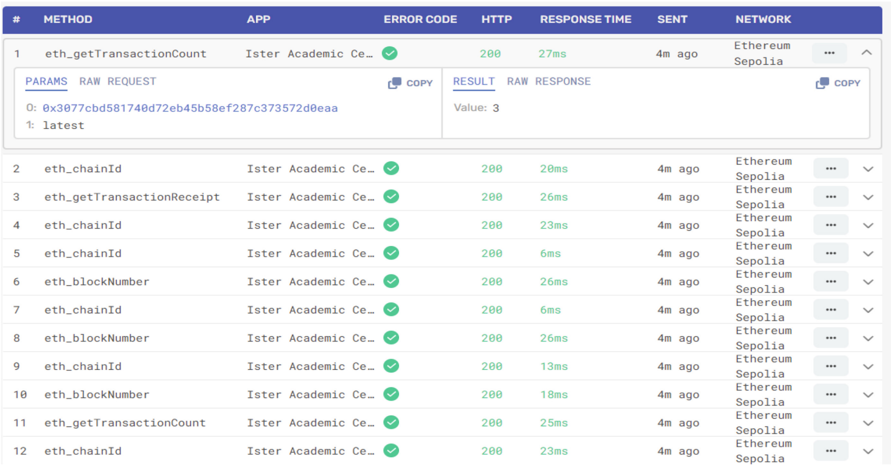

#	METHOD	APP	ERROR CODE	HTTP	RESPONSE TIME	SENT	NETWORK
1	eth_getTransactionCount	Ister Academic Ce…		200	27ms	4m ago	Ethereum Sepolia
	PARAMS RAW REQUEST COPY 0: 0x3077cbd581740d72eb45b58ef287c373572d0eaa 1: latest			RESULT RAW RESPONSE COPY Value: 3			
2	eth_chainId	Ister Academic Ce…		200	20ms	4m ago	Ethereum Sepolia
3	eth_getTransactionReceipt	Ister Academic Ce…		200	26ms	4m ago	Ethereum Sepolia
4	eth_chainId	Ister Academic Ce…		200	23ms	4m ago	Ethereum Sepolia
5	eth_chainId	Ister Academic Ce…		200	6ms	4m ago	Ethereum Sepolia
6	eth_blockNumber	Ister Academic Ce…		200	26ms	4m ago	Ethereum Sepolia
7	eth_chainId	Ister Academic Ce…		200	6ms	4m ago	Ethereum Sepolia
8	eth_blockNumber	Ister Academic Ce…		200	26ms	4m ago	Ethereum Sepolia
9	eth_chainId	Ister Academic Ce…		200	13ms	4m ago	Ethereum Sepolia
10	eth_blockNumber	Ister Academic Ce…		200	18ms	4m ago	Ethereum Sepolia
11	eth_getTransactionCount	Ister Academic Ce…		200	25ms	4m ago	Ethereum Sepolia
12	eth_chainId	Ister Academic Ce…		200	23ms	4m ago	Ethereum Sepolia

Fig. 6. Alchemy Explorer displaying information related to the Ister Account and Ethereum network parameters.

- Transaction Hash: This is a unique identifier for each transaction. It serves as a reference point to track and verify the transaction's details and status on the blockchain.
- Network: Indicates the specific network on which the transaction is taking place. This helps ensure that the transaction is being executed on the intended network.
- Block Number: The block number in which the transaction is included. It helps determine the position of the transaction in the blockchain's chronological order.
- Gas: Gas represents the computational cost required to execute the transaction. It is a fundamental concept in Ethereum and ensures that participants are fairly incentivized for their computational work.
- From Address: The address of the sender who initiated the transaction. In the context of our academic certification smart contract, this could be the address of the academic institution or the authorized issuer.
- To Address: The address of the recipient or the destination of the transaction. In the case of academic certifications, this would typically be the address of the individual receiving the certificate.
- Transaction Type: Indicates the type of transaction being executed. In this case, it is labeled as EIO-1559, which refers to a specific type of transaction related to the Ethereum Improvement Proposal (EIP) 1559. EIP-1559 aims to improve transaction fee predictability and efficiency on the Ethereum network.

Etherscan. Etherscan is a widely used blockchain explorer and analytics platform for the Ethereum network. It provides users with a comprehensive view

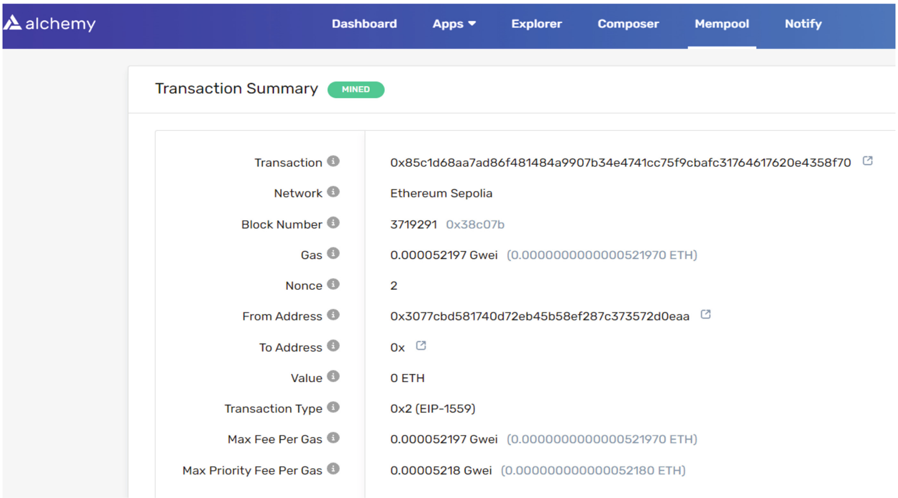

Fig. 7. Transaction Summary in Alchemy Mempool.

of the Ethereum blockchain, allowing them to explore and verify transactions, smart contracts, addresses, and other on-chain activities. Etherscan offers various features, including the ability to search for specific transactions, view account balances, track token transfers, and monitor contract interactions. It also provides detailed information about block confirmations, gas fees, and network statistics. Overall, Etherscan is a valuable tool for individuals and businesses to gain insights and transparency into the Ethereum blockchain ecosystem.

Figure 8 shows the transaction details on Etherscan for the deployment of the Academic Certificate smart contract. It includes important information such as the contract address and transaction hash.

The contract address represents the unique identifier of the deployed smart contract on the Ethereum blockchain. It serves as the entry point for interacting with the contract and accessing its functionalities.

The transaction hash is a unique identifier for the transaction that deployed the smart contract. It can be used to track and verify the transaction's status and details, including the sender, recipient, gas used, and block confirmation.

Etherscan provides a comprehensive view of these transaction details, enabling users to validate and audit smart contract deployments. It also offers additional information such as the transaction timestamp, gas price, and cumulative gas used. This data helps ensure transparency and accountability in the deployment process.

Finally, Fig. 9 displays the transaction details on Etherscan for the successful deployment of the Academic Certificate smart contract on the Sepolia network. The information presented in this figure is similar to the transaction summary shown in the Alchemy dashboard.

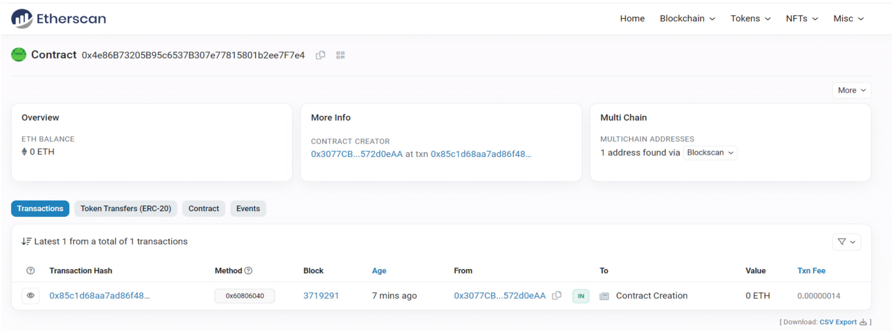

Fig. 8. Etherscan Transaction Details for Academic Certificate Deployment.

The transaction details include the transaction hash, which uniquely identifies this specific transaction on the blockchain. Additionally, it provides essential information such as the network (Sepolia), block number, gas used, and the sender and recipient addresses. These details confirm that the Academic Certificate smart contract was deployed on the Sepolia network and validate its successful execution.

The inclusion of this figure reinforces the successful deployment of the smart contract and highlights the transparency and public accessibility of transaction details on the Ethereum blockchain through platforms like Etherscan.

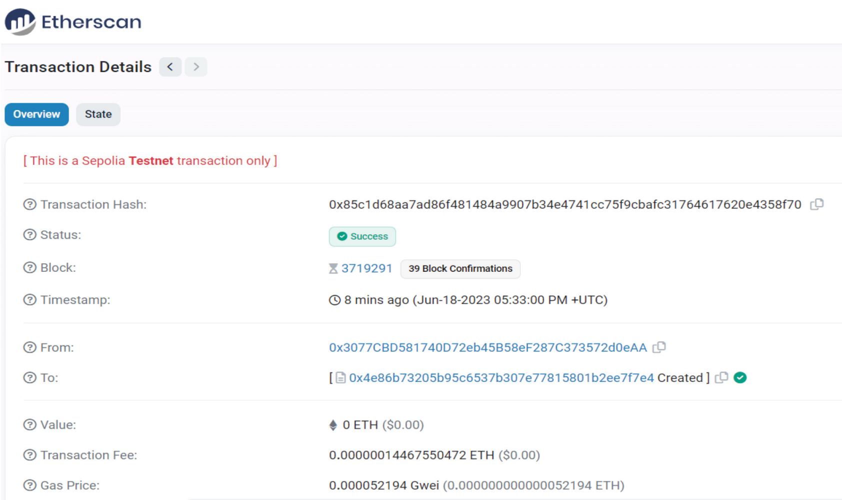

Fig. 9. Etherscan Transaction Details for Academic Certificate Deployment.

6 Conclusion

This study focused on the development and deployment of an academic certificate smart contract on the Sepolia network. Through rigorous unit testing, we ensured the reliability and functionality of the smart contract, validating its ability to issue and verify academic certificates securely on the blockchain. Utilizing Alchemy as our development tool, we successfully deployed the smart contract on the Sepolia network. The deployment process was smooth, and we observed positive outcomes, including the acquisition of the contract address and confirmation of successful deployment. The use of Alchemy provided us with valuable insights into network performance metrics, such as median response time and success percentage, further reinforcing the efficiency and effectiveness of the deployed smart contract. Furthermore, our exploration of Etherscan allowed us to delve deeper into the transaction details, confirming the transparency and accessibility of blockchain data. This demonstration solidifies the successful deployment of the academic certificate smart contract on the Sepolia network. Overall, this study showcases the potential of blockchain technology, specifically smart contracts, in revolutionizing academic certification systems. By leveraging the capabilities of the Sepolia network, Alchemy, and Etherscan, we have achieved a robust and transparent solution for issuing and verifying academic certificates. Moving forward, further research and development in this area can unlock even more opportunities for secure and decentralized certification systems.

References

1. Nakamoto, S.: Bitcoin: a peer-to-peer electronic cash system (2008). https://bitcoin.org/bitcoin.pdf
2. Buterin, V.: A next-generation smart contract and decentralized application platform (2014). https://github.com/ethereum/wiki/wiki/White-Paper
3. Antonopoulos, A.M.: Mastering Ethereum: Building Smart Contracts and DApps. O'Reilly Media, Sebastopol (2018)
4. Atzei, N., Bartoletti, M., Cimoli, T.: A survey of attacks on ethereum smart contracts (SoK). In: Maffei, M., Ryan, M. (eds.) POST 2017. LNCS, vol. 10204, pp. 164–186. Springer, Heidelberg (2017). https://doi.org/10.1007/978-3-662-54455-6_8
5. Luu, L., Chu, H., Olickel, H., Saxena, P., Hobor, A.: Making smart contracts smarter. In: Proceedings of the 2016 ACM SIGSAC Conference on Computer and Communications Security, pp. 254–269 (2016)
6. Swan, M.: Blockchain: Blueprint for a New Economy. O'Reilly Media, Sebastopol (2015)
7. Yli-Huumo, J., Ko, D., Choi, S., Park, S., Smolander, K.: Where is current research on blockchain technology? a systematic review. PLoS ONE **11**(10), e0163477 (2016)
8. Li, Q., Xu, L.D., Zhao, S.: Blockchain-based smart homes: a survey. IEEE Access **5**, 22927–22942 (2017)
9. Sivaraman, V., Maesa, D.D.: Blockchain applications and use cases: a systematic review. Futur. Gener. Comput. Syst. **97**, 512–529 (2019)

10. Koens, T., Harmsze, F.: Blockchain in education: an overview of opportunities and challenges. In: Proceedings of the 2017 IEEE Frontiers in Education Conference (FIE), pp. 1–9 (2017)
11. Choo, K.K.R., Dhillon, G., Sun, H.: Security of blockchain: a systematic review. Digital Commun. Netw. **4**(2), 118–137 (2018)
12. Tödling, F., Quirchmayr, G., Seufert, M.: Blockchain for academic certificates: what are the requirements? In: Proceedings of the 2nd International Workshop on Cryptocurrencies and Blockchain Technology (CBT), pp. 105–116 (2019)
13. Nascimento, A.F., Silva, A., Moreira, E., Peixoto, G.: An overview of blockchain technology: architecture, consensus, and future trends. J. Inf. Syst. Eng. Manag. **4**(3), 17 (2019)
14. Xu, M., Chen, Y., Yu, S.: A blockchain-based framework for secure and efficient certificate verification. In: Proceedings of the 2019 IEEE International Conference on Communications (ICC), pp. 1–6 (2019)
15. Bhargava, B., Garg, S., Kapoor, A.: Blockchain technology for secure storage of academic certificates. In: Proceedings of the 2019 IEEE International Conference on Smart Computing and Electronic Enterprise (ICSCEE) (2019)

Designing a Water Level Measurement System to Monitor the Flow of Water from the Primary Catchment Source of Tulcán City Using LoRa Communication Technology

Paul Ramírez Ortega[1], Edgar Maya-Olalla[1](✉), Hernán M. Domínguez-Limaico[1], Marcelo Zambrano[1,2], Carlos Vásquez Ayala[1], and Marco Gordillo Pasquel[1]

[1] Universidad Técnica del Norte, Avenida 17 de Julio 5-21 y General María Córdoba, 100105 Ibarra, Ecuador
eamaya@utn.edu.ec

[2] Instituto Superior Tecnológico Rumiñahui, Avenida Atahualpa 1701 y 8 de Febrero, 171103 Sangolquí, Ecuador

Abstract. This study focuses on utilizing LoRa wireless communication technology to create a sensor network that measures the water level of a river. The collected data can help assess the current state of the river and detect any changes in its level. Alerts can be sent via email if any changes are detected. The system consists of various components. Firstly, sensor nodes are utilized that employ HC-SR04 sensors for level calculation. Secondly, the ESP32 microcontroller is connected to the LoRa RFM95 module for wireless transmission using LoRa. Finally, the microcontroller handles the processing tasks. The central node acts as a receiver for the data gathered by the sensor nodes. It consists of an Arduino Uno compatible with the LoRa RFM95 module. The central node is connected to a Raspberry PI 4 for processing and then sending the data using the MQTT protocol to the server. The information can then be viewed on the ThingSpeak platform. Tests have been conducted to verify the established communication between the nodes and the Gateway. The results have shown that the LoRa communication parameters are accurately established in the RFM95 modules. Additionally, the data sent from the nodes to the Gateway is visualized on ThingSpeak.

Keywords: LoRa · LoRa Gateway · ThingSpeak · catchment source

1 Introduction

Low-power communications and data transmission are the main objectives of the LoRa Alliance association, which developed and promoted the LoRa technology.

M. Z. Vizuete et al. (Eds.): CI3 2023, LNNS 1040, pp. 138–152, 2024.
https://doi.org/10.1007/978-3-031-63434-5_11

In addition, the use of physical layer techniques allows for coverage of wide areas in terms of kilometers, as reported by [1].

LoRa has been chosen as the technology for designing the wireless sensor network because it provides advantages over its primary rival, SigFox. In contrast to SigFox, LoRa's standard modules serve as both transmitters and receivers without any limitation on data transmission. The acronym LoRa represents 'long-range', indicating one of its primary features. This is achieved through the utilization of a spread spectrum modulation technique known as spread spectrum chirp technology or CSS. LoRa technology is ideal for usage in wireless sensor networks and the Internet of Things due to its ability to implement a wide area network with low power consumption. This enables the maintenance of hundreds of devices connected through a wireless link to a hub or Gateway, which communicates with all network nodes, manages traffic, and shares information to the required destination [2].

A system for measuring the water level of Tulcan City's main water supply source will be developed using wireless communication technology. The system will use a network of wireless sensors connected through LoRa communication technology to identify high and low water levels witnessed in the source's channel.

Awareness of the water level in a water source is vital due to climate change leading to fluctuations in ambient temperature, rainfall frequency, and volume. Knowledge of this physical variable can indicate the potential for floods or droughts and can enable measures to decrease or increase water levels. The water resource level will be measured using an ultrasonic sensor that operates non-invasively without direct water contact. The microcontroller board equipped with a LoRa module processes the sensor signal to facilitate long-range communication with the concentrator node or the dedicated LoRa Gateway board. Processed data will be sent to the cloud and can be accessed via the Internet. The system monitors the water resource level daily, enabling frequent checks to identify changes in water levels and detect increasing or decreasing trends within the flow.

2 Related Work

The paper [3] addresses the problem of efficiently monitoring water levels in natural environments as a disaster prevention measure. Developed by Shinshu University in Japan, the system's objective is to effectively transmit water level, temperature, and humidity data. To achieve this, it employs LoRa technology in the 429 MHz band and a technique called Packet Level Index Modulation (PLIM). The system was implemented in Nagano City, Japan, for real-world testing. The study's conclusions indicate that the system demonstrated stable information aggregation and the ability to avoid packet collisions.

The study [4] tackles the challenge of real-time monitoring and predicting flash floods in Uttarakhand, India, using the Internet of Things (IoT). The aim is to create a low-cost, energy-efficient system that employs a variety of sensors and an Arduino UNO microcontroller. This data is then analyzed using a Long

Short-Term Memory (LSTM) model to issue real-time flood alerts. The system has shown high accuracy, with F1 scores of 97–98% for different alert levels, making it a valuable tool for disaster management.

In [5], the study focuses on addressing the issue of unanticipated flooding by developing an IoT-based monitoring system. Using an ultrasonic sensor and a NodeMCU microcontroller, the system sends data to the ThingSpeak platform for real-time monitoring and alert generation. Although tested in an academic setting, the system has the potential for application in flood-prone areas. The findings indicate that the system is effective in detecting changes in water levels and issuing alerts, which could be crucial for flood preparedness and response.

The authors of the paper [6], addresses the issue of inefficient water level management in dams, which can lead to either man-made or natural disasters. The aim is to develop an IoT-based monitoring system that can automatically route water from dams into canals. This system was tested using a model that includes an Arduino Uno microcontroller and an ultrasonic sensor to measure water levels in real-time. The data is sent to a base station and then stored in the cloud, where a command center makes decisions about opening or closing the dam gates. The findings suggest that the system could be effective in managing water resources and preventing calamities.

The paper [7] addresses the issue of real-time monitoring of water levels in the Al-Gharraf river in Wasit city, Iraq. The aim is to design a low-cost system that uses a microprocessor and an ultrasonic sensor to track water levels and relay the data via GPRS technology. The system was implemented at regulator No.1 in Al-Hay city and utilizes an Arduino Uno board and a JSN-SR04T ultrasonic distance sensor. The data is visualized on a ThingSpeak platform and updates every three minutes. The system achieved an accuracy rate of 96.84% and suggests that it could be improved with an additional network of sensors.

The study [8] tackles the issue of water pollution in the river in Riau Province, Indonesia. It aims to develop a smart sensor node to monitor multiple water parameters such as temperature, pH, dissolved oxygen, and electrical conductivity using Wireless Sensor Networks (WSN). The system was implemented in a laboratory setting and plans to be tested on the actual site. It utilizes a microcontroller and a variety of sensors, and the data is sent to a back-end system for analysis. Initial results show good agreement between theoretical and measured data, suggesting that the system is ready for real-environment testing.

The paper [9] focuses on the issue of water pollution in the Citarum River in Indonesia. The aim is to develop a fuzzy logic-controlled floating robot to monitor water quality in real-time. The system was tested in a controlled environment and uses an Arduino Uno microcontroller and sensors like the MPU6050 for stabilization. The robot can be manually or automatically controlled and sends data via an HC05 Bluetooth module. Although the robot is still not perfect in maintaining its position and has a tendency to sink due to the PLA material used, the results show that the system has a 92.67% accuracy in distance calculation using the Haversine Formula.

3 Development of the Water Level Monitoring System

The project is being developed in the parish of Rio Chico, Tufiño, which corresponds to the city of Tulcán in the province of Carchi. Rio Chico is a tributary of the river of the same name, which is recognised as a source for purifying water due to its special characteristics.

3.1 System Design

The system has been designed with three stages in mind: the sensing stage, the control stage, and the visualization stage. The system comprises three stages. The first stage collects data, specifically the water level variable. The control stage utilizes a control board for data processing while the visualization stage presents detailed information of the measured physical variable.

The system has been designed with three stages in mind: the sensing stage, the control stage, and the visualization stage. The system comprises three stages. The first stage collects data, specifically the water level variable. The control stage utilizes a control board for data processing while the visualization stage presents detailed information of the measured physical variable.

The control stage utilizes a printed circuit controller board and a LoRa module, which establish communication with the sensors. The data collected is subsequently processed by this element and sent to the next respective stage.

The visualization stage involves observing different level measurements obtained from ultrasonic sensors on a web page accessible on the internet. This enables the variation of the water flow level to be viewed, along with other relevant information.

3.2 System Block Diagram

In Fig. 1 describe the system block diagram consists of the layers of the IoT architecture. It describes the essential elements and requirements to be employed in each layer for designing the proposed system in a general manner.

The device layer comprises ultrasonic sensors that acquire data for measurement. These sensors are connected to a micro-controller board, which executes the respective programming. Furthermore, a LoRa module facilitates wireless communication to the LoRa Gateway via this technology. In the Gateway layer, the printed circuit board or controller board with high processing capabilities is present. It is connected to a LoRa module to enable communication with the sensor nodes, forming the central node, or LoRa Gateway. This is the element of the network that receives all data collected from the sensors. The network layer establishes an internet connection, which can be achieved through wired or wireless media. In this case, the data from the LoRa Gateway is transmitted wirelessly to the servers using the MQTT connection protocol. At the Cloud layer or data center, received data is stored before being transmitted to the final layer, i.e., the application layer. Here, the data is displayed using graphical tools, such as a dashboard.

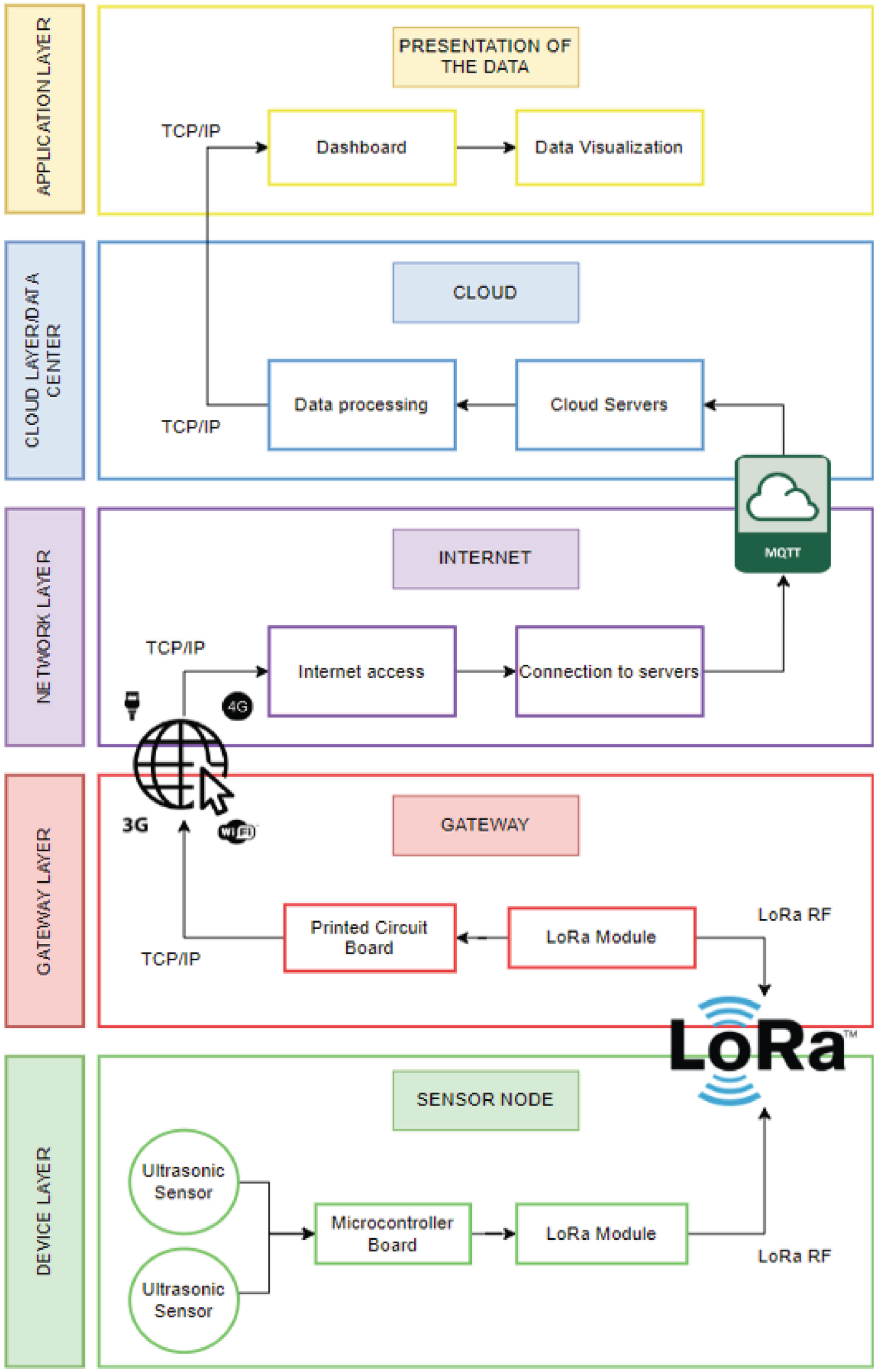

Fig. 1. The block diagram of the system with each layer of the IoT architecture.

3.3 System Architecture of the Water Level Monitoring System

The system architecture, shown in the figure below Fig. 2, represents a star network consisting of the first element, namely the collector nodes, which utilize ultrasonic sensors for measuring water levels. The ESP32 board, acting as a microcontroller, is responsible for the functioning of the sensors and the programming code. For communication between the sensors and the LoRa Gateway, LoRa RF95 modules are employed. The Gateway itself involves communication between an Arduino UNO and a Raspberry Pi 4, linked through a serial port. The final stage consists of processing data in the cloud, after which it is visualized through the use of the IoT platform ThingSpeak and made available for subsequent access by end devices.

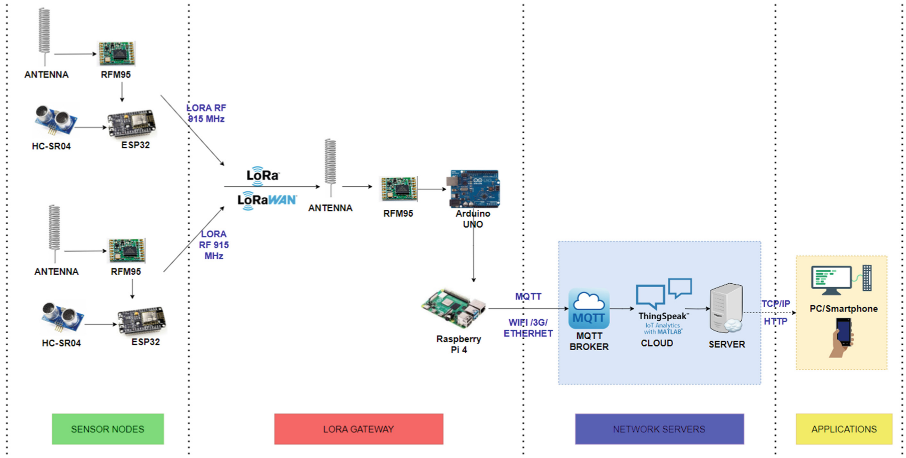

Fig. 2. System Architecture of the Water level monitoring system.

3.4 Interconnection Diagrams

After analyzing the hardware requirements and selecting the components for the sensor network development, connection diagrams for each element are presented to ensure their proper operation, including the sensor node and the LoRa Gateway node.

Sensor Node. The sensor node is composed of an ESP32 microcontroller and an ultrasonic sensor to measure water levels in a flow. The accompanying diagram outlines the connections between the two elements for their respective operation. In Fig. 3, below are the details of how each element is connected to the corresponding pins:

- The Vcc power supply pin of the HC-SR04 sensor is connected to the 5V power supply pin of the ESP32.
- The Trigger pin of the HC-SR04 sensor is connected to pin 16 of the ESP32.
- The Pin Echo of the HC-SR-04 sensor is connected to pin 17 of the ESP32.
- The GND pin, corresponding to the ground of the HC-SR04 sensor, is connected to the GND pin of the ESP32.

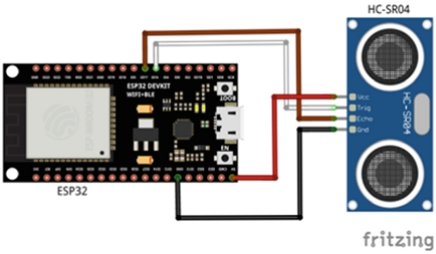

Fig. 3. C-SR04 and ESP32 sensor connection diagram.

LoRa Gateway. The central node is the network component to which all sensor nodes are connected. Its main function is to receive data from the sensors and transmit it to the internet. In this setup, a LoRa Gateway is built using a Raspberry Pi and an Arduino UNO. About other development boards, the Raspberry Pi has superior processing capabilities. This element functions as the gateway within the network that facilitates communication with the sensor nodes that require LoRa communication technology. For this purpose, the RFM95 [13] module is connected to the Arduino UNO as illustrated in the diagram in Fig. 4. The Arduino UNO, in turn, is connected to the Raspberry Pi through a serial connection. The connections made are further detailed below:

- The 3.3 V power pin of the RFM95 module should be connected to the 3.3V pin on the Arduino UNO.
- The ground pin of the RFM95 module must be connected to the ground pin of the Arduino UNO.
- Pin 2 on the Arduino UNO should be connected to the DIO0 pin on the RFM95 module.
- The RST pin of the RFM95 module must be connected to pin 9 on the Arduino UNO.
- Pin 10 on the Arduino UNO should be connected to the NSS pin on the RFM95 module.
- Pin 11 of the Arduino UNO is connected to the MOSI pin of the RFM95 module.
- Pin 12 of the Arduino UNO is connected to the MISO pin of the RFM95 module.

- Pin 13 of the Arduino UNO is connected to the SCK pin, which corresponds to the clock signal of the RFM95 module.
- The antenna is connected to the ANT pin and operates at the required frequency based on its size.
- To read the data via serial communication, the Arduino UNO is connected to the Raspberry PI through a USB cable.

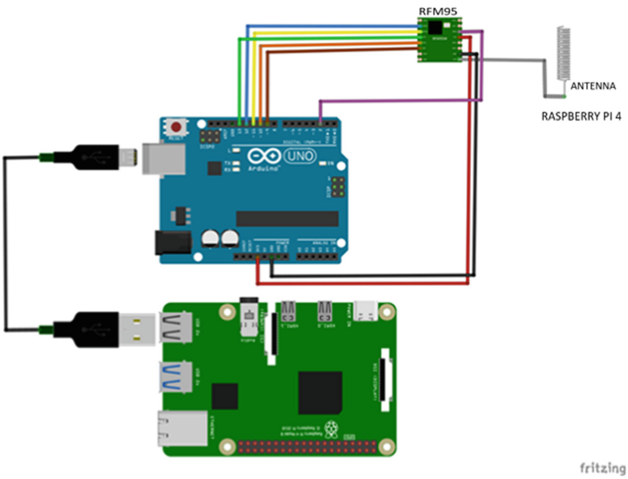

Fig. 4. Connection diagram of LoRa Gateway.

System Flow Diagram. The system flow diagram shows the processes involved and the different functions described in Fig. 5. The process begins with connecting the LoRa RFM95 modules to the ESP32 microcontroller using digital pins to establish wireless communication via LoRa technology. The modules are then verified for proper initialization, which is necessary for establishing a connection to the LoRa Gateway. To measure river flow level, the ultrasonic sensors are connected to the ESP32 microcontroller using its pins. Verification is done to ensure that the sensors are operating correctly, and the data obtained from them is then sent to the LoRa Gateway. Specifically, the LoRa Gateway consists of an Arduino UNO board connected to the Raspberry Pi 4 via serial port. Afterwards, the system confirms that the data is received at this network element and then measures whether the flow level increased or decreased compared to the average value. This information is then used to send out an email alert. Following this, the data is sent to the ThingSpeak platform for cloud storage, which can later be accessed online.

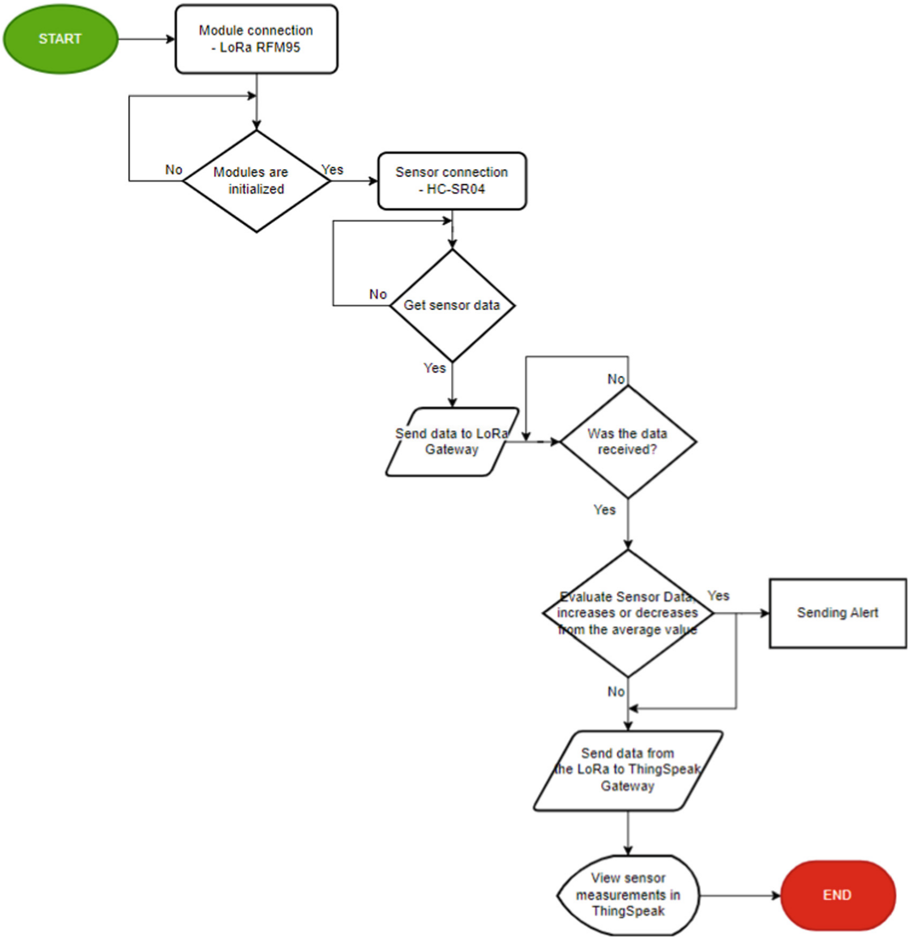

Fig. 5. System flow diagram.

4 Results

4.1 Component Integration

After selecting the appropriate hardware for each network element, the equipment is physically connected according to the established configurations in the previous step.

Peripheral devices are connected to the ESP32 board for the sensor node. Figure 1 illustrates the implementation of the sensor node. It comprises of an HC-SR04 ultrasonic sensor connected to the ESP32 board and a LoRa RFM95 module also connected to the ESP32 board. These are powered by a lithium battery with 5 V input for autonomous operation. The assembled sensor node inside its case looks as Fig. 6:

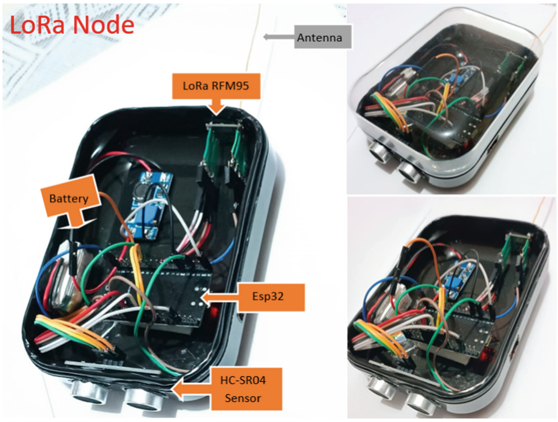

Fig. 6. LoRa sensor node.

The LoRa Gateway obtained the data collected through the RFM95 module using serial communication between the Arduino UNO and the Raspberry PI. The Raspberry PI 4 processed the data, and it was sent to the ThingSpeak platform. The assembled LoRa Gateway, or central node, can be viewed in its casing. Refer to Fig. 7 for details.

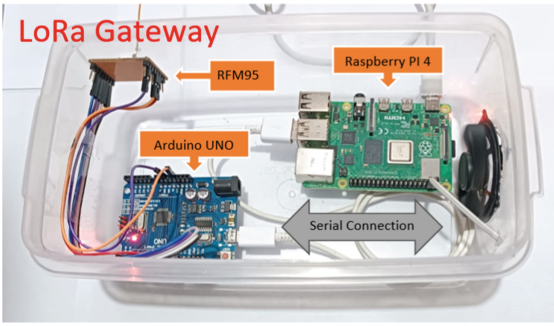

Fig. 7. Gateway LoRa.

4.2 Performance Tests

During the system operation tests, data is obtained from each sensor node, confirming the correct initialization of the LoRa RFM95 module and accuracy of the level value (in centimeters) retrieved from the sensors. Moreover, the LoRa Gateway's capability to receive the data correctly is verified. This ensures the data can be further processed and sent to the ThingSpeak platform without loss.

System Implementation. As previously analyzed in the requirements and system design phase, the project will be implemented in Rio Chico. Two sensor nodes will be placed to measure the level of the river water at two different geographic locations. The placement of sensor nodes takes into account that the water level can be calculated by measuring the cross-section of the river, which includes the distance from the bottom to the surface. In addition, to obtain the river level in centimeters, it is essential to know the total distance between the bottom of the river and the node. This can be calculated by subtracting the two measurements. Figure 8 displays a visual representation of this process.

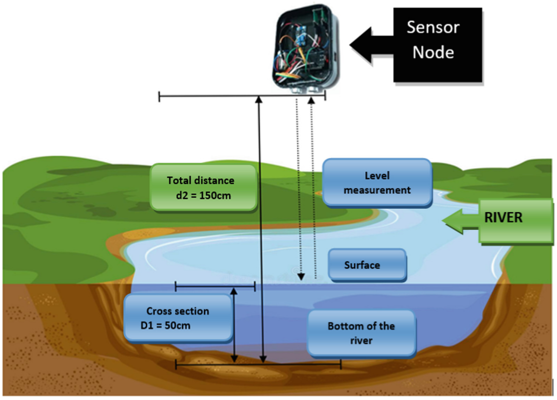

Fig. 8. Sensor node location and measurements.

We will now proceed to physically position the sensor in the chosen location, considering the measures presented in Fig. 8 for proper sensor functionality. Figure 9 displays the sensor node positioned on the river and supported by a PVC pipe structure. This allows for obtaining the required level measurement.

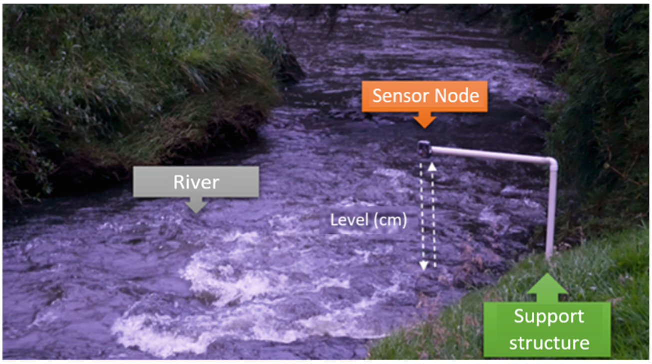

Fig. 9. Location of the sensor node on the river.

Communication Between the Sensor Node and the LoRa Gateway. In this test in Fig. 1, the sensor node is powered by a lithium battery, which allows it to operate autonomously without the need for a USB cable. This feature provides mobility to the node, which can collect and transmit data from its current location (Fig. 10).

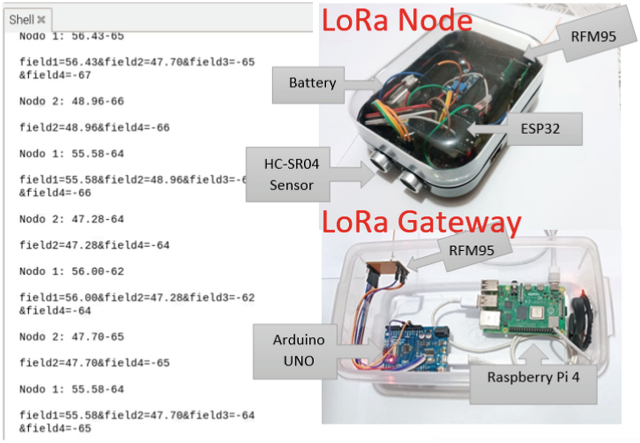

Fig. 10. Receiving data from the sensor node at the Gateway.

Receiving and Displaying Data in the ThingSpeak Platform. Data is sent to the ThingSpeak platform using the MQTT protocol as observed Fig. 11. One can observe the measurements for both Node 1 and Node 2 levels on the platform. Additionally, the RSSI of the signal, expressed in dBm, can be seen to check the signal quality for both nodes.

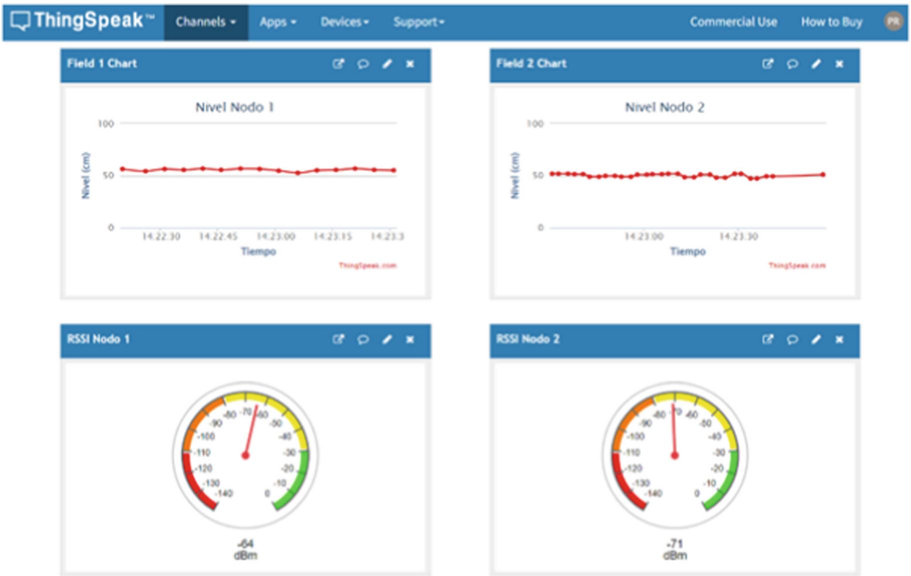

Fig. 11. Visualization platform ThingSpeak.

The data is transmitted to the ThingSpeak server through the MQTT protocol as observed Fig. 11. To verify this, we used the Wireshark sniffer to capture the packets sent, which revealed the used protocol, the payload corresponding to the fields intended for publication in the broker, the TCP port used, the address of the server, and the packet size (Fig. 12).

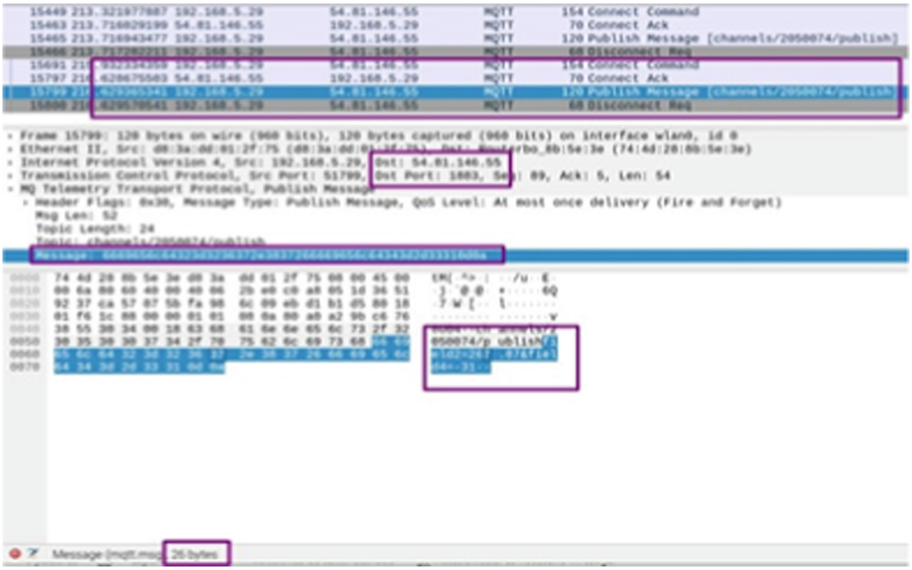

Fig. 12. Visualization platform ThingSpeak.

4.3 Testing of LoRa Wireless Communication

Communication tests were conducted at varying distances to verify communication between network nodes with the LoRa Gateway. The tests obtained data sent by the sensor as well as the RSSI of the signal. Table 1 illustrates a comparison of received signal intensities for varying distances using the following configuration: Spreading Factor (SF) of 7, Bandwidth (BW) of 125 kHz, and Code Rate (CR) of 4/5.

As can be seen in Table 1, the signal strength becomes weaker as the distance from the nodes to the Gateway increases, for longer distances the signal will be weaker and the connection between the nodes and the central node may even be lost.

Table 1. Distance and RSSI Measurements

Distance (m)	RSSI Node 1 (dBm)	RSSI Node 2 (dBm)
5	−59	−61
10	−64	−72
20	−76	−83
30	−84	−86
40	−89	−88
50	−90	−94
70	−110	−117

5 Conclusions

The developed system meets the project's needs by enabling the sensors to read data for water level measurements. Furthermore, LoRa wireless communication technology is used to transmit this data. By analyzing the collected data, it's possible to determine the variation in the water level and relate it to the climatic conditions of the area.

Sensor nodes continually transmit the river level's value to display on the platform. Collecting this data makes it possible to determine if the level is consistent, increasing, or decreasing. From this data, we can analyze whether there is rainfall or drought in the area.

Tests establish correct module configurations according to LoRa requirements since the data collected from sensor nodes can transmit to the Gateway for processing and visualization.

LoRa communication technology widely employed in wireless sensor networks interconnects devices separated over long distances. This feature sets it apart from other wireless communication technologies.

References

1. Narváez Narváez, K.S., Contreras Pérez, V.A.: Design and development of a prototype IoT sensor network using LoRaWAN technology for monitoring indoor and outdoor environmental parameters. Universidad Politécnica Salesiana. Sede Guayaquil, Guayaquil (2020)
2. Maldonado Borda, C.A., Pineda Cusba, L.: Design of a wireless network for the management and control of an integral system of irrigation systems. Universidad Distrital Francisco José de Caldas, Bogotá (2016)
3. Koike, Y., Takyu, O.: Water level monitoring system based on 429MHz LoRa with packet level index modulation. In: 2023 Fourteenth International Conference on Ubiquitous and Future Networks (ICUFN), Paris, France, pp. 76–81 (2023). https://doi.org/10.1109/ICUFN57995.2023.10199961
4. Prakash, C., Barthwal, A., Acharya, D.: FLOODWALL: a real-time flash flood monitoring and forecasting system using IoT. IEEE Sens. J. **23**(1), 787–799 (2023). https://doi.org/10.1109/JSEN.2022.3223671

5. Ashokkumar, N., Arun, V., Prabhu, S., Kalaimagal, V., Srinivasan, D., Shanthi, B.: Monitoring and warning of flooding conditions using IoT based system. In: 2023 9th International Conference on Advanced Computing and Communication Systems (ICACCS), pp. 1199–1203. Coimbatore, India (2023). https://doi.org/10.1109/ICACCS57279.2023.10112930
6. Kumar, M., Sapkal, A., Tiwari, V.: Ganga water quality monitoring system IoT based. In: 2018 IEEE Punecon, Pune, India, pp. 1–5 (2018). https://doi.org/10.1109/PUNECON.2018.8745406.
7. Nawar,p A.K., Altaleb, M.K.: A low-cost real-time monitoring system for the river level in Wasit province. In: 2021 International Conference on Advance of Sustainable Engineering and its Application (ICASEA), Wasit, Iraq, pp. 54–58 (2021). https://doi.org/10.1109/ICASEA53739.2021.9733092
8. Kadir, E.A., Siswanto, A., Rosa, S.L., Syukur, A., Irie, H., Othman, M.: Smart sensor node of WSNs for river water pollution monitoring system. In: 2019 International Conference on Advanced Communication Technologies and Networking (CommNet), Rabat, Morocco, pp. 1–5 (2019). https://doi.org/10.1109/COMMNET.2019.8742371
9. Pratama, R.P., Rusdinar, A., Wibawa, I.P.D.: Floating robot control system for monitoring water quality levels in Citarum River. In: 2019 IEEE International Conference on Internet of Things and Intelligence System (IoTaIS), Bali, Indonesia, pp. 206–211 (2019). https://doi.org/10.1109/IoTaIS47347.2019.8980393
10. Camacho, A., Rodriguez, E., Bajaña, J., Jonathan, P., William, C.: WSN networks for monitoring the banks of the San Pablo River in La Maná Canton. Cotopaxi. Universidad Técnica de Cotopaxi, La Maná (2019)
11. CATSENSORS: LoRa and LoRaWAN technology. Retrieved from CATSENSORS (2021). https://www.catsensors.com/es/lorawan/tecnologia-lora-y-lorawan
12. LoRa Alliance: What are LoRa® and LoRaWAN®? Retrieved from SEMTECH.COM. LoRa Alliance (2022). https://lora-developers.semtech.com/documentation/tech-papers-and-guides/lora-and-lorawan/
13. VISTRONICA S.A.S.: MODULO TRANSCEPTOR LORA RFM95: Article title (2023). https://www.vistronica.com/comunicaciones/wifi/modulo-transceptor-lora-rfm95-868mhz-detail.html

Innovation and Development

A Voice-Based Emotion Recognition System Using Deep Learning Techniques

Carlos Guerrón Pantoja[1], Edgar Maya-Olalla[1(✉)], Hernán M. Domínguez-Limaico[1], Marcelo Zambrano[1,2], Carlos Vásquez Ayala[1], and Marco Gordillo Pasquel[1]

[1] Universidad Técnica del Norte, Avenida 17 de Julio 5-21 y General María Córdoba, 100105 Ibarra, Ecuador
eamaya@utn.edu.ec

[2] Instituto Superior Tecnológico Rumiñahui, Avenida Atahualpa 1701 y 8 de Febrero, 171103 Sangolquí, Ecuador

Abstract. The project aims to create an emotion recognition system based on voice using deep learning techniques. The system is based on supervised learning with artificial neural networks, enabling it to accurately predict emotions. The system's potential usage in detecting depression pathologies in the psychological area gives rise to its development. The system is designed using the KDD (Knowledge Discovery in Database) methodology and utilizes an existing database containing audio with various emotions. These audios are subjected to Multilevel Wavelet transform, decomposing the original signal into sub-signals with specific characteristics for each audio to form a training data set that is subsequently normalized, followed by the generation of the LSTM neural network architecture. Performance tests are eventually conducted on patients with depressive pathology, involving the application of the "Beck test", which indicates the severity of depression experienced by the patient. As a result, the individual reads a text that is recorded, followed by the process of feature extraction and emotion recognition performed with the pre-trained neural network. The outcome indicates that 50% of the patients exhibit severe depression, while the remainder displays milder symptoms, which is supported by the emotions detected by the system alongside the administered test.

Keywords: Emotion Recognition · Wavelet Transform · deep learning · emotion recognition

1 Introduction

Emotion recognition can determine human attitude through speech-based emotional cues. Therefore, detecting human emotions is crucial for personal healthcare and mental well-being [1]. Emotions are an innate aspect of human beings, and they reflect a range of moods including sadness, anger, happiness, and neutrality. However, issues may arise due to emotional imbalance, including depression which significantly impacts a person's usual functioning, well-being, and

M. Z. Vizuete et al. (Eds.): CI3 2023, LNNS 1040, pp. 155–172, 2024.
https://doi.org/10.1007/978-3-031-63434-5_12

quality of life [2]. Artificial intelligence (AI) is currently a popular trend, with many research projects utilizing this technique to gain new insights and strategies that enhance people's lives. The research aims to study how people's emotions are expressed through their speech patterns and to create a machine-learning reference criterion that is inspired by the biological neural networks of the human brain. These elements are composed in a way that mimics the biological neurons in their most common functions. These elements are organized in a manner that resembles that of the human brain [3].

To conduct the research, it is important to discuss various concepts that aid in the development of the system. This starts with the voice, which is a sound produced by the vibration of vocal cords in living organisms and has qualities such as timbre, intensity, and quality [4]. The process of extracting acoustic parameters of vocal utterances is based on the idea that variations in speech are caused by different states of excitation or valence in the speaker. These variations can be estimated by different wave parameters [5]. The approach for Speech Emotion Recognition (SER) incorporates two main phases: feature extraction and feature classification [6]. One method of feature extraction is the multi-level modeling method. This method uses the Continuous Wavelet Transform (CWT) to model hierarchical prosodic features, such as an initial signal and energy contour [7].

A neural network is a computational model that emulates the behavior of the human brain. It consists of interconnected artificial neurons, represented by nodes or vertices, and connections, represented by edges. In a neural network, the fundamental element is the artificial neuron. It emulates its natural counterpart found in the brain [8].

The main focus of this research is to create an emotion recognition system using deep learning techniques. This system will detect emotions in patients who are attending consultations. The goal is to implement this system in patient care to provide better support to psychologists and offer improved diagnoses to the patient based on professional judgment.

The cascade model will facilitate the selection of system requirements during the system development process, which comprises several successive phases. For instance, the analysis phase addresses the concepts covered in the project. Another phase of the project is the design and specifications where the programming, training based on the Knowledge Discovery in Databases (KDD) methodology, implementation, functional testing, and finally a verification of the results obtained will be made.

Finally, we obtain the results of the tests conducted with the system on various individuals. We classify the effectiveness of measuring emotions and determine the percentage of emotions measured. We identify the emotion(s) with the lowest percentage of accuracy, precision, and sensitivity, enabling the system administrator to consider these values and use this tool effectively.

2 Development

The creation process of the speech emotion recognition system includes multiple stages such as emotion audio acquisition, signal preprocessing, feature extraction, training data preparation, and neural network training. The entire process is aligned with the Knowledge Discovery in Databases (KDD) methodology, represented in Fig. 1

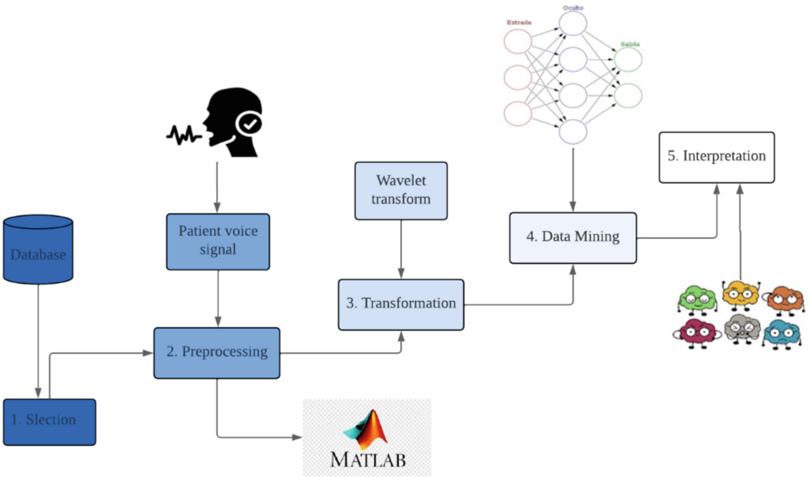

Fig. 1. Generalized KDD process.

2.1 Obtaining Audio of Emotions

Classical data mining tasks require two types of data: a training dataset that trains the algorithm on the problem-specific data and a test dataset that evaluates the quality of the algorithm. Thus, it was necessary to generate at least one audio recording for each human emotion during the data collection phase. However, due to the lack of Spanish audio data, a Mexican audio dataset known as the Mexican Emotion Speech Database (MESD) is utilized.

MESD provides single-word utterances for the affective prosodies of anger, disgust, fear, happiness, neutrality, and sadness with Mexican cultural conformation. The database was retrieved from the Kaggle repository, a scientific community focused on machine learning. The database is licensed for free use, however, proper credit should be given to its author, Saurabh Shahane.

The database consists of single-word utterances expressing affective prosodies of anger, disgust, fear, happiness, neutrality, and sadness. The affective prosodies are selected according to Mexican cultural adaptation. The Multilingual Everyday Speech Dataset (MESD) was recorded by adult actors and non-professional children. Three female, two male, and six child voices are included in the dataset. In this study, a database of 864 voice recordings is evaluated (see Table 1).

Table 1. Database prosodies

Database	MESD
Interpreter	Men, Women, Children
Size	864 recordings
Prosodias	Anger, disgust, fear, happiness, neutral, sadness
License	Free
Sampling frequency	48 kHz

The audio signals corresponding to different emotions are analyzed. Each emotion has specific characteristics that can be reflected by analyzing the corresponding graph of the audio signal. The important characteristics of each emotion can be highlighted by analyzing the obtained raw data. Accordingly, the audio of "Up", which was expressed in the emotion of Anger, was selected. Figure 2 displays the signal corresponding to anger. The first part of the figure shows the signal over time, while the second part shows its frequency spectrum. In Fig. 3, the amplitude of the signal starts with short peaks that are segmented over some samples. This is followed by a gradual increase in amplitude, culminating in very high peaks in the positive and negative axes. This signal is compared to the way anger is expressed vocally, as it begins with a soft tone that ends in a high tone producing a signal as seen in the graph. The signal's energy reaches up to -20dB, as illustrated in the spectrum graph.

2.2 Signal Preprocessing

Preprocessing is a procedure performed on the audio files before analysis, which may include resizing, changing the sample rate, enhancing quality, and extracting features.

It is important to note that the audio files in the database have a bandwidth of 48000 Hz, but their bandwidth is reduced to 16000 Hz after resizing. Thus, all the audio files in the database have a bandwidth of 16000 Hz.

For the audio files obtained in the previous section, the sampling rate of each element is reviewed. This is done to ensure that all the audio files have standardized parameters. To achieve this, the resampling function in MATLAB is utilized. This function alters the sample rate of an audio file to a desired rate. This process is demonstrated in Fig. 4.

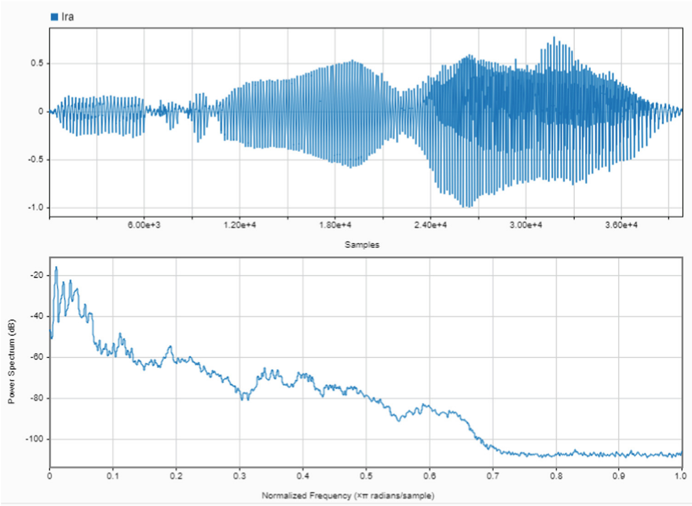

Fig. 2. Plot of anger signal versus time.

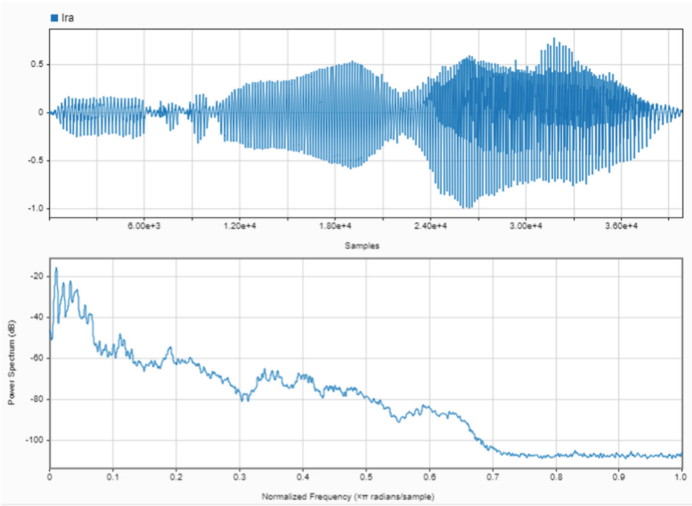

Fig. 3. Plot of the spectrum of the anger signal.

The audio to be processed is read first. Then, it is approximated by rational fractions using the rat function. Next, the sample rate is changed from the current one to the desired one by applying the resample function. Finally, the resulting audio is played back and saved in the desired direction. This process is repeated for each audio file in the folder.

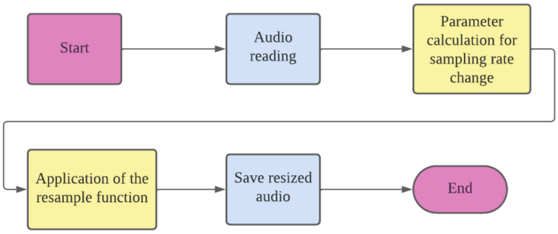

Fig. 4. Process for the audio sampling rate change.

After changing the sample rate, a data store is created with the addresses and names of each audio file. This is done to control variable generation, especially concerning their size in megabytes. The process shown in Fig. 5 is used for this purpose.

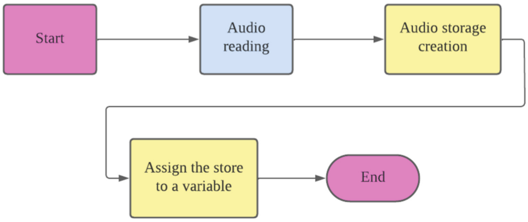

Fig. 5. Process for creating the data warehouse.

2.3 Feature Extraction

This process involves identifying and extracting unique features numerically from emotional audio recordings. The extraction of significant features is performed using wavelet transform in Matlab. To do so, one must follow a logical sequence of five steps, involving reading audio, calculating multilevel wavelet decomposition, quantifying signal entropy, and associating the features with corresponding emotions.

The main concept is to decompose the signal into a sequence of subspaces using chosen wavelet functions (Symmlet and Daubechies). This decomposition is usually accomplished by shifting (right or left) and scaling (amplifying or attenuating) the chosen wavelet function. By doing so, the signal is projected into the area represented by the particular scaling and translation.

In the issue of emotion recognition, the signal energy of the audio signal is recognized as one of the most crucial characteristics. A straightforward approach to extract features would be to employ the signal energy that is available in each subspace or node. Once you acquire each node's feature value, assemble them side by side, and that constitutes your feature vector (refer to Fig. 6).

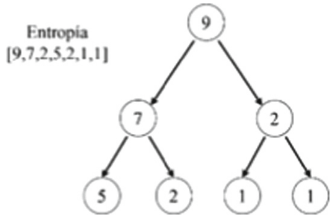

Fig. 6. Example of feature extraction for three levels of decomposition.

To illustrate the process described above, we proceed to calculate the wavelet transform for each considered emotion type. The anger signal is subjected to a wavelet decomposition of the Daubechies-4 family with seven levels of decomposition. As a consequence of using seven levels of decomposition, 255 features are obtained ($2^0 + 2^1 + 2^2 + 2^3 + 2^4 + 2^5 + 2^6 + 2^7 = 255$), as illustrated in Fig. 7.

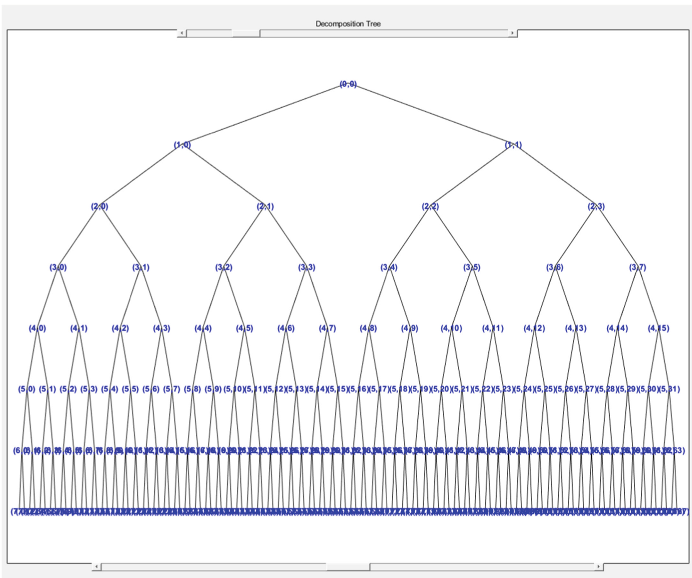

Fig. 7. 7-level wavelet decomposition tree for the emotion of anger.

The first two elements of the final decomposition level are presented, which correspond to the approximation coefficients displayed in Fig. 8. The approximation coefficient exhibits a much clearer signal when compared to the original audio signal, where the amplitude varies constantly.

Emotion audio labeling is the process of assigning emotions to audio. After obtaining the characteristics of the emotion audio, the data is associated with the relevant emotion through a process known as audio labeling. To achieve this, a binary logic, shown in Table 2, is used. Each vector of extracted characteristics is associated with a corresponding binary vector, as shown in Table 2, to label the audio. This labeling process is performed for all available audio in the database.

Table 2. The logic for emotion detection

Ira	Disgust	Fear	Happiness	Neutral	Sadness
1	0	0	0	0	0
0	1	0	0	0	0
0	0	1	0	0	0
0	0	0	1	0	0
0	0	0	0	1	0
0	0	0	0	0	1

2.4 Preparation of Training Data

After processing emotional audio and identifying and extracting signal characteristics, three matrices are created. To accomplish this, the matrix resulting from identifying and extracting characteristics is divided into three groups based on the percentages 80%, 10%, and 10%, which correspond to the training, validation, and testing data, respectively.

The normalization process adjusts the data set to scale values that differ from the original ones. In the obtained data set, the normalization process is performed. This process establishes a certain range for the data set so that it enters the neural network and is trained in a manner that helps the network comprehend the incoming data. The input dataset contains both maximum and minimum values. The data undergoes normalization, which establishes a range of [0,1]. The normalization process takes the negative data as the minimum and the maximum value as the highest. Finally, with the help of Eq. (1), the data can be normalized within the desired range.

$$X' = \frac{X - X_{\min}}{X_{\max} - X_{\min}} \tag{1}$$

where:

- X' represents the normalized value of each datum in the dataset.

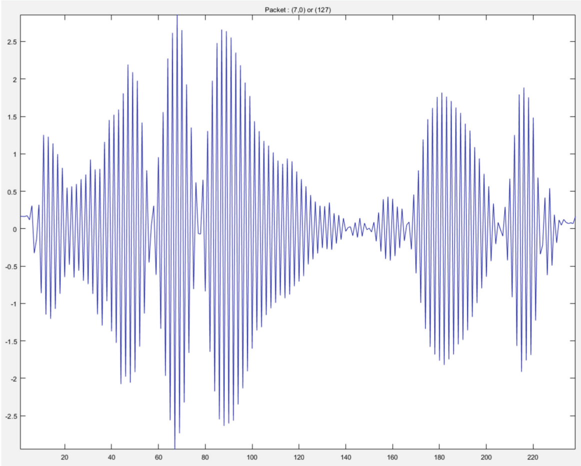

Fig. 8. Approximation coefficient, level 7 associated with the emotion of anger.

In contrast, the detail coefficient indicates that the signal is predominantly present during speech pauses (refer to Fig. 9).

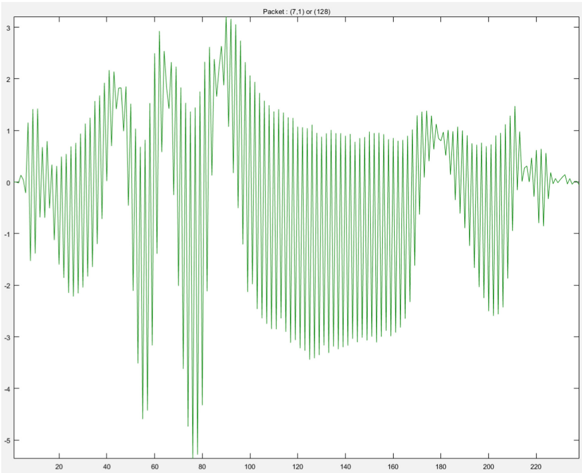

Fig. 9. Detail coefficient, level 7 associated with the emotion of anger.

- The value we wish to normalize is represented by X.
- The value of the minimum data found in the data set is denoted by $X_{\min}$.
- The maximum value found in the data set is represented by $X_{\max}$.

The prepared data set has been normalized, as shown in Fig. 10.

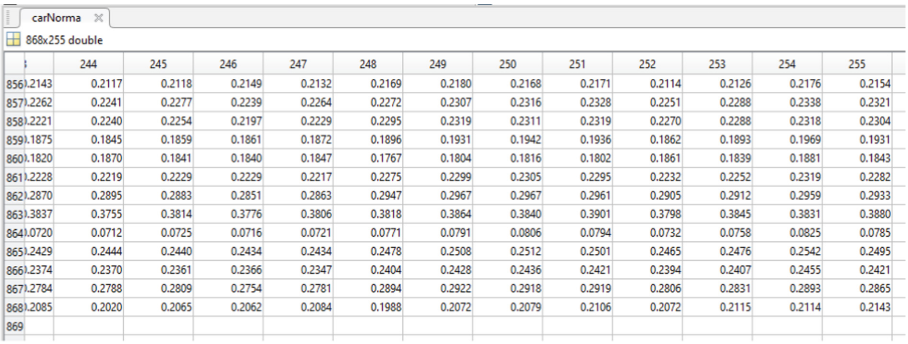
carNorma

868x255 double

	⁝	244	245	246	247	248	249	250	251	252	253	254	255
856	).2143	0.2117	0.2118	0.2149	0.2132	0.2169	0.2180	0.2168	0.2171	0.2114	0.2126	0.2176	0.2154
857	).2262	0.2241	0.2277	0.2239	0.2264	0.2272	0.2307	0.2316	0.2328	0.2251	0.2288	0.2338	0.2321
858	).2221	0.2240	0.2254	0.2197	0.2229	0.2295	0.2319	0.2311	0.2319	0.2270	0.2288	0.2318	0.2304
859	).1875	0.1845	0.1859	0.1861	0.1872	0.1896	0.1931	0.1942	0.1936	0.1862	0.1893	0.1969	0.1931
860	).1820	0.1870	0.1841	0.1840	0.1847	0.1767	0.1804	0.1816	0.1802	0.1861	0.1839	0.1881	0.1843
861	).2228	0.2219	0.2229	0.2229	0.2217	0.2275	0.2299	0.2305	0.2295	0.2232	0.2252	0.2319	0.2282
862	).2870	0.2895	0.2883	0.2851	0.2863	0.2947	0.2967	0.2967	0.2961	0.2905	0.2912	0.2959	0.2933
863	).3837	0.3755	0.3814	0.3776	0.3806	0.3818	0.3864	0.3840	0.3901	0.3798	0.3845	0.3831	0.3880
864	).0720	0.0712	0.0725	0.0716	0.0721	0.0771	0.0791	0.0806	0.0794	0.0732	0.0758	0.0825	0.0785
865	).2429	0.2444	0.2440	0.2434	0.2434	0.2478	0.2508	0.2512	0.2501	0.2465	0.2476	0.2542	0.2495
866	).2374	0.2370	0.2361	0.2366	0.2347	0.2404	0.2428	0.2436	0.2421	0.2394	0.2407	0.2455	0.2421
867	).2784	0.2788	0.2809	0.2754	0.2781	0.2894	0.2922	0.2918	0.2919	0.2806	0.2831	0.2893	0.2865
868	).2085	0.2020	0.2065	0.2062	0.2084	0.1988	0.2072	0.2079	0.2106	0.2072	0.2115	0.2114	0.2143
869													

Fig. 10. Normalized database with range [0,1].

2.5 Neural Network Training

This is a three-step process: building the LSTM model, parameterizing, and training the neural network. The architecture of the LSTM model is created using MATLAB's Deep Network Designer application, in which two models are built and tested to determine the most optimal model for emotion prediction. The general architecture adopted for the neural network starts with 255 input layer neurons and 6 output layer neurons. In Fig. 11 shows the LSTM architecture used to train the network.

Building the LSTM Model. The neural network models presented in this study are composed of multiple layers, including the input layer, intermediate layers, and output layers. An aspect of particular significance is the activation of the input layer with a data set characterized by dimensions of $255(C) \times 1(B) \times 1(T)$. These dimensions correspond to the features derived from the wavelet transform, signifying that the application of dissimilar multilevel wavelet transforms on an audio input could potentially lead to inaccurate classification outcomes.

Parameterization and Training Process. Upon defining the neural network model, the subsequent phase involves the meticulous configuration of training parameters. While there is variability in the selection of the algorithm and learning rate, certain factors such as the number of epochs and the minimum batch size remain consistent throughout this phase.

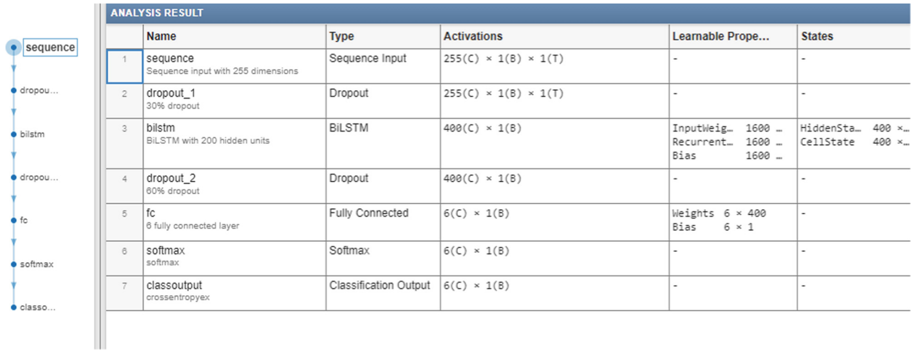

	Name	Type	Activations	Learnable Prope...	States
1	sequence Sequence input with 255 dimensions	Sequence Input	255(C) × 1(B) × 1(T)	-	-
2	dropout_1 30% dropout	Dropout	255(C) × 1(B) × 1(T)	-	-
3	bilstm BiLSTM with 200 hidden units	BiLSTM	400(C) × 1(B)	InputWeig... 1600 ... Recurrent... 1600 ... Bias 1600 ...	HiddenSta... 400 ×... CellState 400 ×...
4	dropout_2 60% dropout	Dropout	400(C) × 1(B)	-	-
5	fc 6 fully connected layer	Fully Connected	6(C) × 1(B)	Weights 6 × 400 Bias 6 × 1	-
6	softmax softmax	Softmax	6(C) × 1(B)	-	-
7	classoutput crossentropyex	Classification Output	6(C) × 1(B)	-	-

Fig. 11. BiLSTM neural network architecture with 7 layers for emotion classification.

The chosen algorithm for this study is the Gradient Descent method. This strategic choice stems from its ability to progressively enhance training efficacy over successive epochs, thereby facilitating the minimization of loss or error functions. The determination of the appropriate number of epochs, as depicted in Table 3, commences from the third epoch onward. This decision is informed by meticulous testing, which indicates that optimal training outcomes are achieved within this timeframe. As such, a total of 50 epochs are judiciously employed for conducting the comprehensive tests mandated by this research.

In establishing the optimal minimum number of batches, a comprehensive consideration of the overall data set is undertaken. In this instance, the dataset comprises a total of 868 instances, representing the maximum number of emotion-laden audio samples available. To facilitate a meticulous division of this dataset, an iterative approach is undertaken. This entails partitioning the data into smaller, manageable batches, each tailored to ensure effective training.

The initial batch size selected is 62, which is subsequently reiterated across 14 epochs. Additionally, a batch size of 217 is implemented, repeated four times throughout the epochs. Finally, the total batch size of 868 is engaged and deployed once across the epochs to encompass the entirety of the dataset.

Regarding the learning rate, a judiciously standardized value of 0.005 is employed. This selection is rooted in its intermediate characteristic, rendering it both compatible and recommended for integration with the Gradient Descent algorithm. Notably, a higher learning rate would impede algorithm convergence, while an excessively low value would significantly prolong the algorithm's weight optimization process.

The graphical representation shown in Fig. 12 corresponds to the results obtained from the first test performed, under the parameterization parameters meticulously outlined in Table 3. A noticeable feature within the graph is the manifestation of overtraining within the neural network architecture. This conspicuous overtraining phenomenon can be attributed to the adoption of remarkably small batch sizes that are insufficient for the effective operation of the system under the given parameter set.

Table 3. Parameters for testing with the LSTM neural network model

Parameter	Test 1	Essay 2	Essay 3
Algorithm	Gradient decrease	Gradient decrease	Gradient decrease
Number of epochs	50	50	50
Minimum lot size	62	217	868
Learning rate	0.005	0.005	0.005

The consequences of using such parameter values go beyond overtraining. They culminate in the prolonged period required for the training process, which significantly lengthens the path to achieving the desired results. Furthermore, the confluence of markedly elevated loss values and concurrently diminished accuracy levels substantiates the limited efficacy of the chosen parameterization. Consequently, the pursuit of optimal results necessitates a recalibration of parameter selection, striking a judicious balance between the architectural nuances of the network and the complexity of the task at hand.

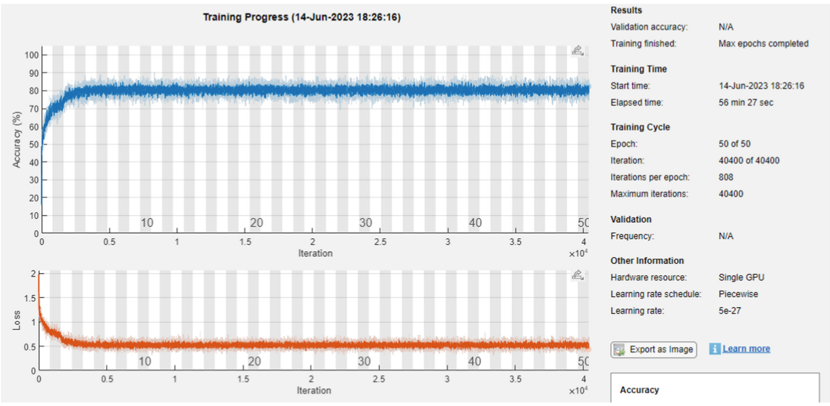

Fig. 12. Accuracy and error result of the first trial applying the LSTM model.

In Fig. 13 gives a visual representation of the training process of the network carried out according to the parameters prescribed in the second test, as described in Table 3. It can be seen that the application of the parameters set for this test leads to consistent results.

In Table 3, the redundancy of the fourth epoch becomes conspicuous, as an observed trend reveals the stability of the accuracy and the parameters from the second epoch onwards. In addition, there is a noticeable reduction in the execution time of the training, depending on the inherent characteristics of the

CPU, which have a significant impact on the temporal dynamics of the training. This correlation confirms the central role of the CPU in influencing the efficiency and duration of the training process.

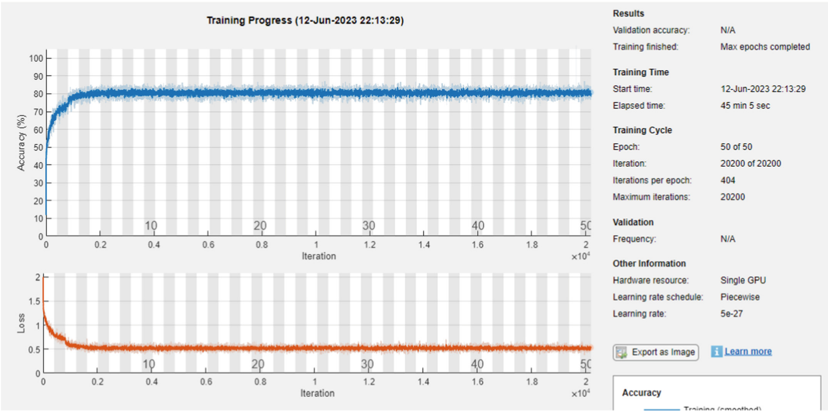

Fig. 13. Accuracy and error result of the second test applying the LSTM model.

In Fig. 14 summarizes the results derived from the final trial, which mirror the results observed in Trial 2. Notably, this final study includes an expanded range of epochs and batch sizes. It is pertinent to emphasize that a consistent pattern similar to that observed in Study 2 is evident, with the stabilization of training occurring from the third epoch onward. The observed stability of training renders further epochs unnecessary, implying that a saturation point has been reached in terms of refining model performance through additional epochs.

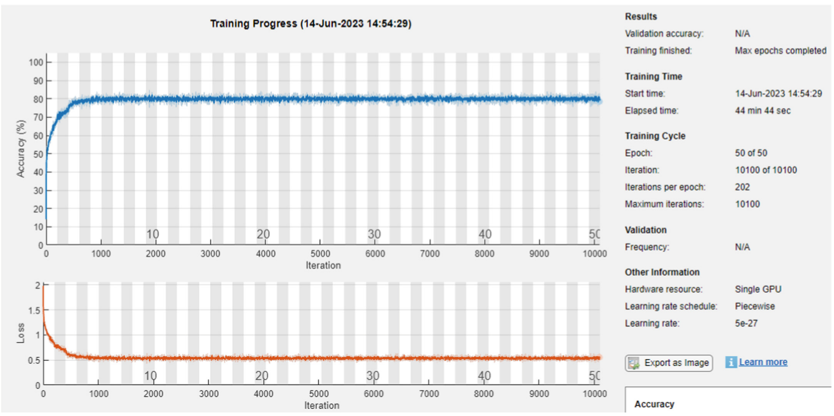

Fig. 14. Accuracy and error result of the third trial applying the LSMT model.

Throughout the neural network training process, careful examination reveals the inherent stability of the learning rate set at 0.005, as opposed to its counterpart at 0.01. As a result, the minimum batch loss exhibits a persistent equilibrium across trials 2 and 3. Significantly, Trial 2 emerges as the optimal training model, characterized by the adoption of a batch size of 217 and the judicious partitioning of the dataset into cohesive segments aligned with the overall size of the dataset. This strategic segmentation avoids the imprudent injection of the entire dataset into the network for training purposes. Conversely, the first batch iteration reveals elevated loss levels, but as the iterations progress, significant loss reduction becomes apparent.

This observed trend bodes well as it anticipates a convergence toward minimal batch losses as the iterations are completed. Finally, it is inferred that after the third epoch, the training reaches a plateau and exhibits consistent performance without further accuracy improvement.

The careful delineation of the parameterization data is comprehensively presented in Table 4. In this tabular format, optimal data parameters are meticulously elucidated, which collectively embody the most favorable configurations for training efforts.

Table 4. Selected training parameters for the neural network

Parameter	Value
Algorithm	Gradient decrease
Number of epochs	3
Minimum lot size	217
Learning rate	0.005

3 Results

This section briefly summarizes the results of the performance of the speech-based emotion recognition system in two different phases. Firstly, the efficiency ratio and the percentage of inaccuracy corresponding to each emotion considered are examined, starting with a comprehensive analysis of the confusion matrix for the trained model. Subsequently, an independent evaluation is carried out with six randomly selected individuals to determine the diagnostic categorization of depression, from mild to severe, for each patient.

The contributions made by this research are multifaceted. First and foremost is the theoretical contribution that underscores the core tenets of this investigation. It encompasses facets ranging from sound representation in speech to sound characterization, the neural networks integral to deep learning and their interconnection with emotion recognition, as well as a juxtaposition with conventional depression detection methods.

Another distinctive contribution is the novel approach to signal characterization. Here, multilevel wavelet decomposition plays a central role. This methodology assigns numerical values to signals depending on the chosen level of decomposition, here at level 7. This complex process results in a comprehensive collection of 255 signal features for each emotional category, meticulously encapsulated in the database.

In addition, this research proposes a linkage between the results derived from the emotion recognition system and the administered depression assessment tests. This synergy complements the psychological domain by providing insights into effective interventions for the treatment of depression.

To critically evaluate the efficiency of the proposed emotion recognition technique, we present the initial model's confusion matrix, as shown in Fig. 15. This analytical lens serves to illuminate the efficiency ratio and the percentage of inaccuracy attributed to each emotion, thus enriching the overall evaluation of the experimental results.

In the first scenario, the accuracy is 73.5%. Although this figure seems relatively modest in the context of the development of neural network systems, it is essential to contextualize this performance. The limited number of audio samples in the database is a prominent factor, limiting the network's ability to reach a superior level of training. In addition, the chosen model and the manner of signal feature extraction inherently influence the accuracy of the results obtained.

The field of emotion recognition is still relatively young. While the earliest investigations date back to 2016, the substantial body of research has proliferated since 2018, highlighting its dynamic and evolving nature. Acknowledging the complex nature of emotion recognition-where variability in emotional expression across individuals poses a challenge literature references are instructive. For example, in [5] reported an effectiveness rate of 56.71% for the neural network used in their research. Similarly, [10] obtained results between 70% and 75%. While the algorithms and databases used are different from the present study, the congruence of the accuracy percentages is noteworthy.

In contrast, the effectiveness of the emotion "anger" is 82.7%, with an associated error rate of 17.3%. Similarly, the emotion "disgust" reaches an effectiveness of 76.1%, paired with a misclassification rate of 23.9%. The emotion "Fear" has a recognition rate of 53.6%, while 46.4% of the cases are misclassified. Similarly, the emotion "happiness" is identified with an efficiency of 50.7% but experiences a misclassification rate of 49.3%. In parallel, the states "neutral" and "sad" manifest themselves as 79.7% and 90.3% correctly classified instances, alongside 20.3% and 9.7% misclassified cases, respectively.

Similarly, the predictive results for the emotion "anger" show an efficiency of 77.6% with an error rate of 22.2%. For the emotion "Fear", the prediction accuracy is 74% with an error rate of 26%. Meanwhile, for the emotion "Disgust", the efficiency rate is 84.4%, coupled with an error rate of 18.6%. "Happiness" has an accuracy of 60%, with an error of 40%. Similarly, "neutral" has an efficiency of 69.2% and an error of 30.8%, while "sadness" has an accuracy of 73.7% and an error of 26.3%.

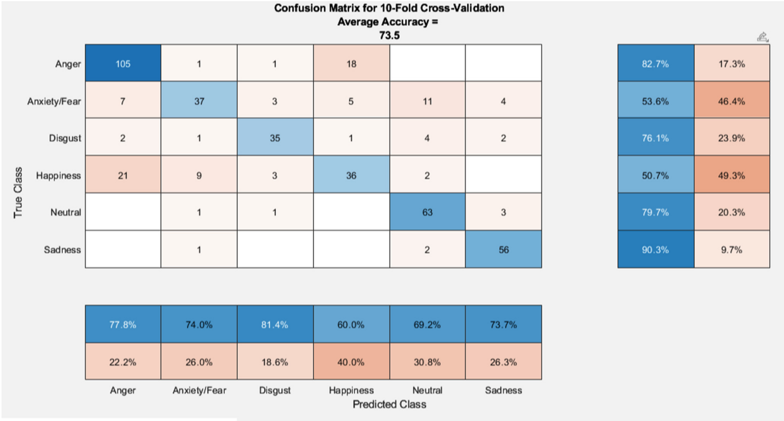

Fig. 15. Confusion matrix of the LSTM model.

The rigorous testing process includes patient consent, audio analysis, feature extraction, and emotion categorization. A systematic 7-step procedure, as illustrated in Fig. 16, is meticulously followed within this testing framework.

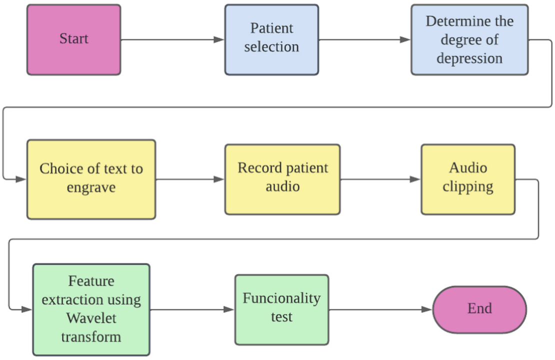

Fig. 16. Confusion matrix of the LSTM model.

The neural network response indicates that the audio input is indicative of the emotion "sadness", as shown in Fig. 17. This result is consistent with the diagnosis of major depression previously confirmed by the Beck test. The schematic shows how the audio labeling was performed. During the prediction phase, the neural network generates values in its six output layers. These values range from 0 to 1, with the value closest to 1 being the expected outcome. To reflect this process, the Simulink diagram uses an adder to effectively round these values to either 1 or 0, thus generating the result graph.

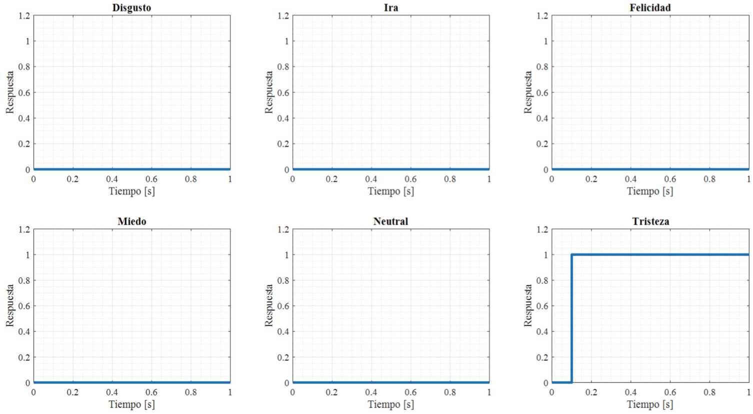

Fig. 17. Response of the emotion recognition system for Individual 1.

Finally, Table 5 is a summary of the results of the emotion detection for each individual. The chart shows the age of the person, the emotion identified by the system, the level of depression determined by the tests administered, and the scores obtained.

Table 5. Summary of the results obtained in the neural network

Individual	Genre	Age	Excitement	Pathology	Test score
Individual 1	Female	18–25	Sadness	Severe Depression	36
Individual 2	Male	18–25	Fear	Mild depression	13
Individual 3	Male	18–25	Fear	Mild depression	16
Individual 4	Female	18–25	Fear	Mild depression	18
Individual 5	Male	18–25	Sadness	Severe Depression	37
Individual 6	Female	18–25	Sadness	Severe Depression	53

4 Conclusions

The voice-based emotion recognition system proves its feasibility by establishing a correlation between the emotions detected by the system and the patient tests administered, thereby facilitating the recognition of the patient's depression level. In this regard, it is estimated that approximately 66.6% of the female participants in the sample are suffering from major depression, while this estimate is 33.3% for the male participants. In addition, the viability of deep learning techniques, particularly neural networks, has been demonstrated.

The Knowledge Discovery in Databases (KDD) architecture was used in the design of the system, including steps such as database acquisition, audio processing, feature extraction, and network training. During neural network training, two models were constructed and analyzed to determine the optimal model for the research. As a result, critical parameters influencing the training of the neural network were identified, including the optimization algorithm (gradient descent), the number of epochs (3), the minimum batch size (217), and the learning rate (0.005).

The overall effectiveness of the neural network was 73.5%. In terms of emotion-specific effectiveness and error rates, the following results were obtained: anger achieved effectiveness of 82.7% with an error rate of 17.3%. Similarly, disgust was identified with 76.1% effectiveness and 23.9% false classifications. Similarly, the network recognized fear with a 53.6% accuracy rate, while 46.4% were misclassified. Happiness was detected with 50.7% effectiveness, accompanied by a 49.3% misclassification rate. Finally, the neutral state and sadness were accurately identified at 79.7% and 90.3%, respectively, with misclassifications at 20.3% and 9.7%.

It is important to note that the effectiveness of the neural network depends significantly on the quality of the extraction of the emotional audio features, as well as the chosen parameterization for the network training. The performance of the network can only be definitively determined through experimentation, using analogous studies from the scientific community as a guide.

References

1. Kaur, G., Pandey, P.S.: Emotion recognition system using IOT and machine learning-a healthcare application. In: Proceeding of The 23rd Conference of Fruct Association, Haryana, 2018, Conference 2016, LNCS, vol. 9999, pp. 1–13. Springer, Heidelberg (2016)
2. Orozco, W.N., Baldares, M.J.V.: Addressing depression: intervention in crisis. Dome J. 19–35 (2012)
3. Olabe Basogain, X..: Artificial neuron networks and their applications, Escuela Superior de Ingeniería de Bilbao, p. 79 (2015)
4. Jahangir, R., Teh, Y.W., Hanif, F., Mujtaba, G.: Deep learning approaches for speech emotion recognition: state of the art and research challenges, vol. 80, no. 16. Multimedia Tools and Applications (2021). https://doi.org/10.1007/s11042-020-09874-7
5. Zloteanu, M., et al.: Speech emotion recognition with deep learning. Sensors **11**(2), 1–18 (2022). https://doi.org/10.1016/j.specom.2021.11.006
6. Hansen, L., Zhang, Y.P., Wolf, D., Sechidis, K., Ladegaard, N., Fusaroli, R.: A general- izable speech emotion recognition model reveals depression and remission. Acta Psychiatr. Scand. **145**(2), 186–199 (2022). https://doi.org/10.1111/acps.13388
7. Sisman, B.: Machine Learning for Limited Data Voice Conversion, National University of Singapore, Singapore (2019)
8. Toshinori, M.: Fundamentals of the new Artificial Intelligence, 2a edn. Springer, Cleveland (2008)
9. Ganapathy, A.: Speech emotion recognition using deep learning techniques. ABC J. Adv. Res. **5**(2), 113–122 (2016). https://doi.org/10.18034/abcjar.v5i2.550
10. Sandoval, V.: Emotion recognition by voice, p. 60 (2019)

Data Mining Applied to the HFC Network to Analyze the Availability of Telecommunication Services

Shirley Alarcón-Loza(✉) and Karen Estacio-Corozo

Instituto Superior Tecnológico ARGOS, Guayaquil, Ecuador
galarcon@tecnologicoargos.edu.ec

Abstract. The failures that affect the telecommunications service in hybrid fiber-coaxial networks (HFC) can be anticipated, through data analysis, to minimize the impact on service availability and users. This work seeks to analyze the causes that affect the performance of HFC networks in Ecuador, through a predictive model for their timely detection and application of anticipated works. The base studied included the components and causes that affected the availability of television and telephony service in a HFC network in 2020, from a sample of 17707 records. For the research, the dependent variable CATEGORY CAUSE is considered, and the objective was to analyze the causes that affect the telecommunications service. The KDD methodology was used and, from the use of WEKA software, classification algorithms were established to determine suitable predictive features, being the causes, the type of event, and the network components, the most significant. The results showed that, for the television service, the best classification algorithm was J48, with a precision value of 68.668% and an area under the curve (ROC Area) of 0.913. For the telephony service, the best classification algorithm was Random Tree, with a precision of 73.666% and an area under the curve of 0.969. The conducted research demonstrated the importance of data mining in the process of analyzing the causes of the impact on television and telephone services.

Keywords: HFC network · Hybrid fiber-coaxial networks · Data Mining · Classification Algorithm

1 Introduction

In recent years, technology has produced a large volume of data worldwide that is stored daily in database servers without being evaluated and then deleted without any action being taken. Today, the trend is to use the data and transform it into valuable information by applying computational models that can predict situations. In this context, data mining is a science that allows problem-solving through data analysis, applying techniques and methods that allow the discovery of patterns [29], which is why it has gained great popularity and is used in various disciplines.

Within the field of telecommunications, there are hybrid fiber optic and coaxial networks (HFC) that provide broadband services to transmit various services such as

M. Z. Vizuete et al. (Eds.): CI3 2023, LNNS 1040, pp. 173–185, 2024.
https://doi.org/10.1007/978-3-031-63434-5_13

telephony, television [8], Internet, and data. In an HFC network, two main sections are distinguished: the inside plant and the outside plant.

The inside plant refers to a segment of the network located inside a building or facility, where the Headend equipment, such as the cable modem termination system (CMTS) and the routing equipment play a fundamental role in the management and distribution of the transmission and reception of the signals of the configured services are located. Figure 1 details the aforementioned scheme [28].

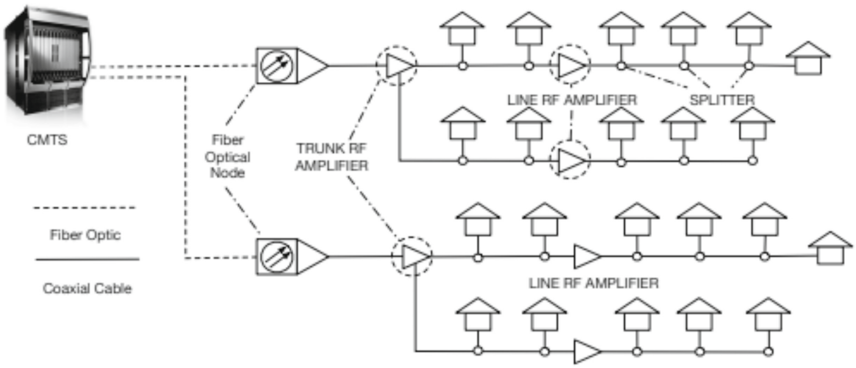

Fig. 1. HFC network architecture [14]

The outside plant represents the area outside the building or facility, where the fiber optic and coaxial cables that connect the network to customer locations are located. This segment is a compound of several sectored areas of optical nodes that are connected through highly reliable fiber optic connections.

In the event of a failure, it is easy to identify the exact point because each fiber node is designed to limit any signal interference. A fiber node, which typically uses multiple line amplifiers, distribution, and possibly splitters, is responsible for connecting the last mile of the network where the customer's cable modem or terminal equipment is installed. The last amplifier located before reaching the end customer is known as the end-line amplifier [26].

1.1 HFC Network Service Failures

In modern HFC networks, covering millions of users, operators must ensure high availability of network access. This need has become very important due to the accelerated growth of activities requiring telecommunication services, making it essential to quickly detect and locate any network faults. However, this task is not easy due to the number of devices present in typical HFC networks [7].

In a conventional HFC network monitoring system [18], transponders are installed to monitor active elements such as optical nodes, amplifiers, power supplies, and transmitters. The transponders allow direct monitoring and control of the aforementioned devices and elements, providing a wide range of detected parameters and service failures related to specific causes.

However, this system has some disadvantages, among which is the cost of monitoring due to the need to use equipment dedicated exclusively to this activity. In addition, the transponders are located in outdoor environments, which exposes them to various environmental conditions that trigger equipment malfunctions or loss of remote management, which generates false alarms and increases operation and maintenance costs by sending technical personnel for review [5].

On the other hand, it is an opportunity and an excellent benefit for Internet Service Providers (ISPs) to create a heat map that shows the devices identified as the root cause of problems affecting services [12]. In this way, if recurring problems are detected in a certain area, technicians attend to the exact spot to perform maintenance work and improve the overall network quality, without the need for it to be related to a specific incident. This approach is useful when faced with problems that are difficult to diagnose accurately. Consequently, by having a broader and longer-term view of problematic devices, ISPs can anticipate problems, optimize the network, and improve the user experience [13]. Table 1, compiles the most relevant cases on reported HFC network failures.

Table 1. Literature review on HFC network failures

Study	Cause	Component	Works related
Noise in upstream network channels	Noise Interference	CMTS	[30]
Cause of network cable failures	Noise	Fiber optic connector and cable	[12, 14]
Network failures	Several	CMTS, Access Point, Amplifier	[26]
RF amplifiers monitoring	Power failure	RF Amplifiers	[22]

The customer-centricity strategy has revolutionized how companies satisfy their customers, as service-oriented companies have recently been given great importance in terms of customer care and satisfaction. Despite this, it is still a challenge to manage the decision-making on what to offer to gain customer loyalty [3].

Based on this foundation, the objective of this article is to analyze the causes that affect the performance of HFC networks in Ecuador, through a predictive model. For this purpose, the data of the chosen sample was organized, the Knowledge Discovery in Databases (KDD) methodology was applied, and the Waikato Environment for Knowledge Analysis (WEKA) program was used to generate decision trees and knowledge rules through classification algorithms, and the results obtained were interpreted.

2 Materials and Methods

In the development of this article, the information was very important to obtain the results, since the data alone did not constitute a clear reality of any situation related to the affectation of television and telephony services in HFC networks. In this sense, the origin of the data, the treatment given to them, the data mining methodology used, the processing in the corresponding software, and the interpretation of the acquired results are explained.

2.1 Database and Resources

The study was focused on various events that affected the television and telephony service of the HFC network, which is managed by a private company. The characteristics of these events include whether they were fortuitous, programmed, or emergent. The causes correspond to failures, electrical interruptions, and physical damage, among others. The cause category includes the components that have failed, and the type of cause refers to failures originating in the telecommunications network itself or outside it.

Table 2 shows the population corresponding to the 50691 events in 2020 that meet the aforementioned characteristics. These events caused the interruption of the telecommunications service, generating discomfort in the users. Based on this aspect, the sample was selected using the non-probabilistic technique by convenience, considering the affectation of television and telephony services in the HFC network.

Table 2. Population distribution and sample used.

Population		Sample	
Events	Telecommunications service	Events	Telecommunications service
50691 service impact records in 2020	Television Telephony Internet Data	17707 service impact records in 2020	Television Telephony

For this study, a database of 17707 cases of damage was considered, according to the sample described, with the characteristics shown in Table 3. The type of event refers to whether the situation was a fortuitous event, scheduled maintenance, or an emergency. The causes were equipment damage, various electrical failures, accidents, redesign due to pole movement or urban regeneration, attenuation, misalignment, noise, intermittency, and signal weakness, among others. The category of the cause considered the affected equipment such as coaxial cable, amplifiers, sources, transmitters, UPS, and couplers, among others. In addition, it is considered whether the causes were due to internal or external factors.

Table 3. Features of the telecommunications, television, and telephony service impact in 2020.

Features	Description	Features	Description
Event Type	Situation in which the service was affected	Cause	Reason for service interruption
Category Cause	Component or device where the failure occurs	Cause Type	Origin of the cause that affects service

For data processing and information generation, WEKA software [23] version 3.8.6 was used, based on a high-level programming language that hosts various machine learning algorithms that allow the analysis of a large set of data. This technological resource is open source and supports data formats including ARFF, CSV, and LibSVM.

2.2 Methodology

The methodology applied in this work is a cross-sectional correlational design, aimed at a process of knowledge discovery in databases (KDD) [11]. It is a methodology for the data mining process that allows data cleaning before processing and also considers the understanding of the problem. This methodology, according to [19], consists of five phases, and its application for this article is described below:

Selection Stage. Data are generated in each of the events that affect telecommunications networks, which are stored in the corresponding software and are collected in a database, so it is of great importance that they receive some treatment to discover patterns associated with the state of HFC networks that provide television and telephony services. By identifying this scenario, the present research was proposed to analyze the causes that affect the operation of HFC networks through a predictive model to identify the cause of the affectation, as well as the faulty component for telecommunications companies to make timely decisions at the time of problems that disturb a large number of users [25]. For this purpose, the data mining classification technique was used and the best algorithms were validated from the participant sample.

Pre-processing Stage. In this phase, the database containing the causes affecting telecommunication services was used, constituting 50691 records of 4 different fields. The data were collected, stored, and filtered in Microsoft Excel, so that 17707 records of 4 fields were organized, shown in Table 3.

Transformation Stage. To determine the causes and their categories, a dependent variable has been chosen, a nominal type, and data mining classification techniques will be applied to this variable in WEKA software. The dependent variable that directly affects the availability of the telecommunications service and, therefore, generates user discomfort, is the variable CATEGORY CAUSE. Table 4 lists the variables that were entered into WEKA.

Table 4. Description of the variables considered in the impact on television and telephony services.

Variables	Meaning	Type
EVENT TYPE	Unintentional Programmed Emergent	Nominal
CAUSE	Accidents: attenuation, cut-off, damage Faults: high resource consumption, electrical, undetermined, mismatch, water or noise intrusion, sulfation, inhibition, signal level, intermittency, breakage, loss of connectivity Scheduled work Theft	Nominal
CATEGORY CAUSE (Dependent variable)	Amplifier, Fiber optic and coaxial cable, UPS, Source, Optical Node, Connector, Coupler, Splice, Receiver, Transmitter, Feeder, CMT, Switch, Servidor, Multiplexer, RF Headend	Nominal
CAUSE TYPE	Internal External	Nominal dichotomous

Data Mining Stage. Based on the test data set that allows analyzing the causes of the impairment of television and telephony service in HFC networks, three experiments were carried out with the dependent variable CATEGORY CAUSE; applying the classification algorithm that considers the best attributes [9] to reduce the processing work.

The classification algorithms [29] used to identify the causes of TV and telephony service impairment in HFC networks were J48 [1], Random Forest, and Random Tree [24] decision trees. In addition, the Cross-Validation [2, 21] evaluation and validation mode were applied, which provides an average accuracy per dependent variable based on N iterations run on the data set. In Table 5, the area under the curve (ROC-Area) [10, 15] and Accuracy [16] have been used as indicators for the quality assessment of the applied classification algorithm.

Table 5. Quality assessment of the applied algorithms.

Algorithm	CATEGORY CAUSE Television		CATEGORY CAUSE Telephony	
	Accuracy	ROC Area	Accuracy	ROC Area
J48	68.668%	0.913	73.636%	0.969
Random Forest	68.661%	0.913	73.606%	0.969
Random Tree	68.661%	0.913	73.666%	0.969

Interpretation Stage. In this paper, the predictive model [4, 20] was formed by the application of classification algorithms known as decision trees [17, 23] in WEKA. Several tests were executed, according to Table 5; the J48 classification algorithm was applied to analyze the causes affecting the availability of television services in HFC networks.

Twenty-eight knowledge rules were generated (see Fig. 2) indicating the causes of service impairment; those that presented more cases are explained below:

A) The CAUSE was a damage in the Fiber Optic Cable and the EVENT TYPE was fortuitous, then there was service affectation and 336 cases were located;
B) The CAUSE was a damage in the HFC Passive Connector 500 and the EVENT TYPE was programmed, then there was service affectation and 154 cases were located;
C) The CAUSE was an electrical failure in the UPS air conditioning and the CAUSE TYPE was external, then there was service affectation and 123 cases were located;
D) The CAUSE was an electrical failure in the Source Amplifiers, then there was an affectation of the service and 183 cases were located;
E) The CAUSE was an accident damage in the Fiber Optic Yarn and the EVENT TYPE was fortuitous, then there was an affectation of the service and 107 cases were located;
F) The CAUSE was a mismatch failure in the PAD Equalizer Amplifier, then there was affectation of the service and 409 cases were located.
G) The CAUSE was a noise ingress failure in the Coaxial Cable Drop, then there was affectation of the service and 111 cases were located;
H) The CAUSE was an inhibition failure in the Television Multiplexer Module, then there was service affectation and 3839 cases were located;
I) The CAUSE was a programmed work in the UPS air conditioning, then there was service affectation and 1025 cases were located;
J) The CAUSE was a programmed work and the EVENT TYPE was emergent in the OTN Node, then there was service affectation and 1902 cases were located;
K) The CAUSE was a failure due to loss of connectivity in the Core Service IPS Switches Interface, so the service was affected and 857 cases were located;
L) The CAUSE was an electrical failure in the Source Batteries, so the service was affected and 217 cases were located; and,
M) The CAUSE was a failure due to the high use of resources in the Television Multiplexor and the EVENT TYPE was fortuitous, so the service was affected and 4798 cases were located.

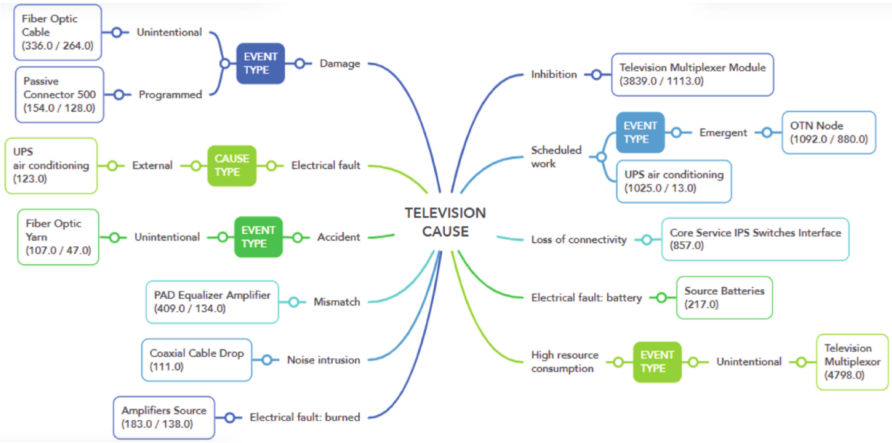

Fig. 2. Knowledge rules of the J48 algorithm for television service.

Similarly, the Random Tree classification algorithm was applied to analyze the causes affecting the availability of telephony service in HFC networks. Thirty knowledge rules were generated (see Fig. 3) indicating the causes of service impairment. Those with the highest number of cases are explained below:

A) The CAUSE was a damage in the fiber optic cable and the EVENT TYPE was fortuitous, then there was service affectation and 335 cases were located;
B) The CAUSE was a damage in the HFC Passive Connector 500 and the EVENT TYPE was programmed, then there was service affectation and 155 cases were located;
C) The CAUSE was an electrical failure in UPS Air Conditioning and the EVENT TYPE was incidental and the CAUSE TYPE was external, then there was service affectation and 307 cases were located;
D) The CAUSE was a burnout electrical failure in Amplifiers Source and the EVENT TYPE was incidental, then there was service affectation and 169 cases were located;
E) The CAUSE was a mismatch failure in PAD Equalizer Amplifier and the EVENT TYPE was programmed, then there was service affectation and 330 cases were located;
F) The CAUSE was a noise ingress failure in the Coaxial Intake, then there was service affectation and 111 cases were located;
G) The CAUSE was an electrical failure in Battery Sources, then there was an affectation of the service and 217 cases were located; and,
H) The CAUSE was a failure due to high use of resources in the Core Service IPS Servers Hardware, then there was an affectation of the service and 1026 cases were located.

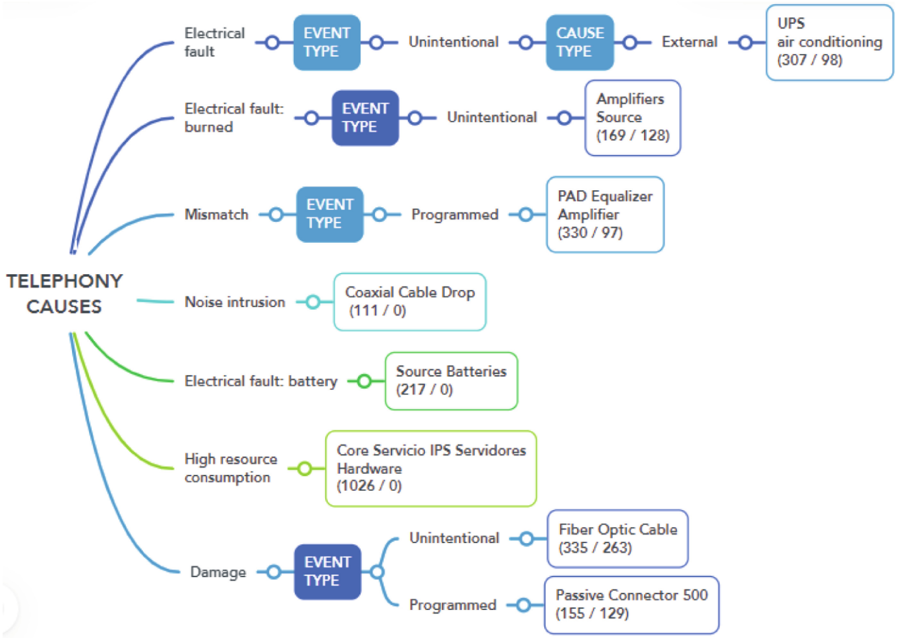

Fig. 3. Knowledge rules of the Random Tree algorithm for telephony service

3 Results

For the dependent variable CATEGORY CAUSE, algorithms that generate decision trees were applied to identify the most influential predictive attributes. In the case of the television service, the J48 algorithm was used and in the case of the telephone service, the Random Tree algorithm was used; both obtained a good percentage of accuracy and quality margin, according to the evaluation of Table 5. In both cases, service impairment was considered by evaluating the most significant causes.

The results of the television service (see Fig. 4), showed as a predominant factor the failures caused by the high use of resources in the multiplexer, causing total or partial inhibition in each of the modules due to traffic overloads, capacity limitations, configuration problems and hardware failures, so that this problem was divided into two independent causes for further treatment.

In the same way, programmed works represented another common cause of service affectation. These works were carried out within the Headend where OTNs, switches, Core routers, and CMTS were installed, which massively converged the configuration of the services of thousands of clients [6]. Likewise, adequate air conditioning of a Headend was considered essential to ensure optimal operation of electronic equipment, maintaining efficient energy use, stability, and performance of the network [27].

The results for the telephony service (see Fig. 5) showed that failure due to high resource usage was a predominant factor in the failure of the HFC network. This occurs when the resources of the IP core servers are saturated due to high traffic volume or excessive load of configured services, which results in degraded performance or service interruption.

Fiber optic cable damage [14] was identified as the second leading cause of failure in the HFC network. This part of the fiber optic cable is represented as the primary segment of the network, which runs from the optical node to the start of radio frequency signal distribution on the coaxial cable and goes to the last mile of customers. In addition, failure due to mismatch or miscalibration in the amplifiers was one of the causes with the greatest impact on the network's performance [22].

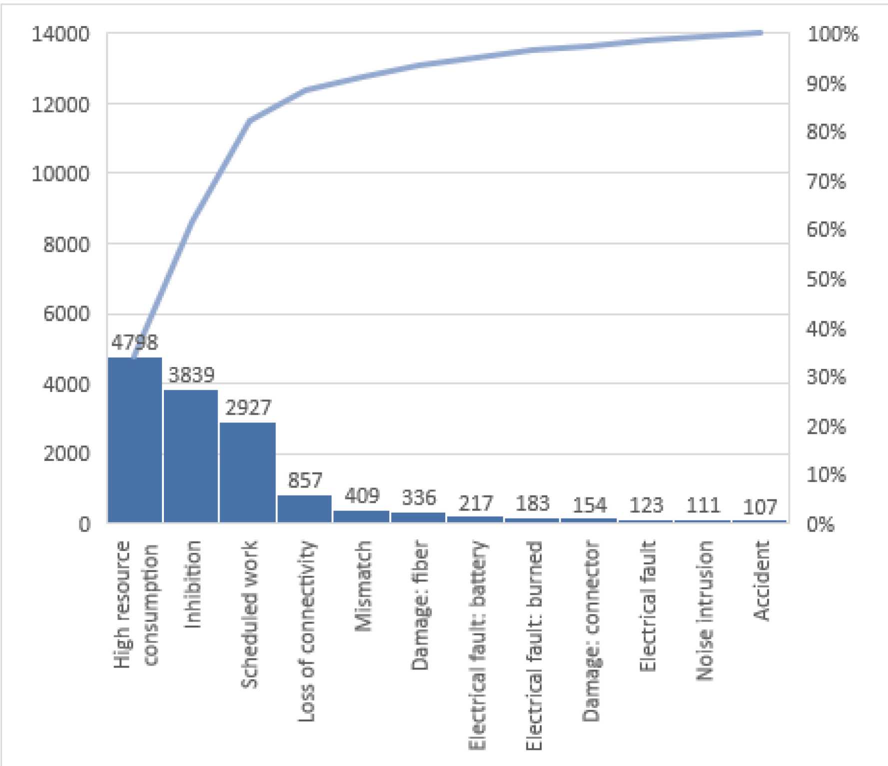

Fig. 4. Causes affecting TV service availability in an HFC network

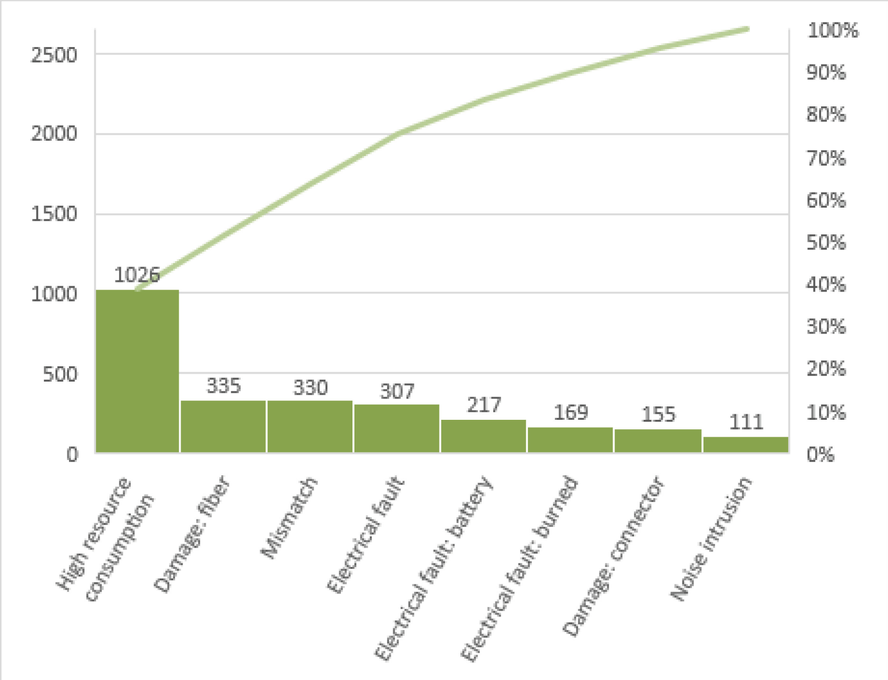

Fig. 5. Causes affecting the availability of telephony service in an HFC network.

4 Conclusions

In this case, it was evidenced that the high use of resources and the poor performance of the HFC network components directly influence the availability of the television service, so public and private companies should take preventive and corrective measures to improve the service. There are a large number of incidents at the Headend since this is the starting point of the network where the services of each of the customers are configured and converged massively, and when a failure occurs in any of its components, it can trigger a generalized service disruption.

Concerning the telephony service, the traffic overload in the IP Services Core Servers is caused by the high use of resources due to the reception and processing of a large amount of data. If the traffic load exceeds the capacity of the hardware to handle it, it can lead to resource saturation, resulting in degraded performance or even equipment inhibition. Core IP equipment can be inhibited to protect itself from complete collapse, this happens when there is a sudden increase in demand for the allocated bandwidth or because of widespread congestion in the network.

On the other hand, the secondary segment of the HFC network, composed of the coaxial cable and amplifiers, can also contribute to failures. The amplifiers are necessary to maintain the quality and strength of the signal as it is distributed over the coaxial cable. If there are power failures, malfunctions, mismatches, or wear, they can cause signal degradation, affect the quality of service, as well as affect the correct operating and signal-to-noise levels in the network terminal equipment. It would be interesting to identify and analyze the data collected from fiber optic networks, to generate new research that considers internet services and examines other factors that influence service availability. For the data mining approach, it is suggested to develop new predictive models with other algorithms, to have a better accuracy in the classification of data and obtain high-quality results.

References

1. Akinola, S., Oyabugbe, O.: Accuracies and training times of data mining classification algorithms: an empirical comparative study. J. Softw. Eng. Appl. **8**, 470–477 (2015)
2. Alabdulwahab, S.: Feature selection methods simultaneously improve the detection accuracy and model building time of machine learning classifiers. Symmetry **12**(9), 03–20 (2020)
3. Alzoubi, H., Alshurideh, M., Al Kurdi, B., Inairat, M.: Do perceived service value, quality, price fairness, and service recovery shape customer satisfaction and delight? A practical study in the service telecommunication context. Uncertain Supply Chain Manage. **8**, 579–588 (2020)
4. Attwal, K., Dhiman, A.: Exploring data mining tool-Weka and using Weka to build and evaluate predictive models. Adv. Appl. Math. Sci. **19**(6), 451–469 (2020)
5. Benhavan, T., Songwatana, K.: HFC network performance monitoring system using DOCSIS cable modem operation data in a 3-dimensional analysis. In: 4th Joint International Conference on Information and Communication Technology, Electronic and Electrical Engineering (JICTEE), pp. 1–5. IEEE, Chiang Rai (2014)
6. Campo, W., Rueda, D., Taimal, I., Arciniegas, J.: Analysis of the DOCSIS protocol for distribution of TDi applications and contents in an HFC network. Revista Avances en Sistemas e Informática **6**(3), 119–132 (2009)
7. Chan, H.N., Martinez, B.C., Gomez, R.M., Granados, J.R.: Integrated multi-purposed testbed to characterize the performance of internet access over hybrid fiber coaxial access networks. In: Gregori, E., Conti, M., Campbell, A.T., Omidyar, G., Zukerman, M. (eds.) NETWORKING 2002: Networking Technologies, Services, and Protocols; Performance of Computer and Communication Networks; Mobile and Wireless Communications, NETWORKING 2002, LNCS, vol. 2345, pp. 996–1007. Springer, Berlin (2002). https://doi.org/10.1007/3-540-47906-6_81
8. Ciciora, W., Farmer, J., Large, D., Adams, M.: The History of Modern Cable Television Technology, 2nd edn. Morgan Kaufmann Publishers, San Francisco (2003)
9. Dinakaran, S., Thangaiah, P.: Role of attribute selection in classification algorithms. Int. J. Sci. Eng. Res. **4**(6), 67–71 (2013)
10. Fawcett, T.: An introduction to ROC analysis. Pattern Recogn. Lett. **27**(8), 861–874 (2006)
11. Fayyad, U., Piatetsky-Shapiro, G., Smyth, P.: From data mining to knowledge discovery in databases. AI Mag. **17**(3), 37 (1996)
12. Heiler, G., Gadermaier, T., Haider, T., Hanbury, A., Filzmoser, P.: Identifying the root cause of cable network problems with machine learning. arXiv abs/2203.06989 (2022)
13. Heiler, G., Gadermaier, T., Haider, T., Hanbury, A., Filzmoser, P.: Improving cable network maintenance with machine learning. arXiv, abs/2203.06989 (2022)
14. Hu, J., Zhou, Z., Yang, X., Malone, J., Williams, J.: CableMon: improving the reliability of cable broadband networks via proactive network maintenance. In: 17th USENIX Symposium on Networked Systems Design and Implementation, pp. 619–632. NSDI 20, Santa Clara (2020)
15. Janssens, A., Martens, F.: Reflection on modern methods: revisiting the area under the ROC Curve. Int. J. Epidemiol. **49**(4), 1397–1403 (2020)

16. Juba, B., Le, H.: Precision-recall versus accuracy and the role of large data sets. In: Proceedings of the 37th AAAI Conference on Artificial Intelligence, pp. 4039–4048. AAAI Press, Washington (2019)
17. Kingsford, C., Salzberg, S.: What are decision trees? Nat. Biotechnoly **26**(9), 1011–1013 (2008)
18. Milan, S., Ina, M., Cica, Z.: Performance monitoring challenges in HFC networks. In: 13th International Conference on Advanced Technologies, Systems, and Services in Telecommunications (TELSIKS), pp. 385–388. IEEE, Serbia (2017)
19. Pareek, M., Bhari, P.: A review report on knowledge discovery in databases and various techniques of data mining. OAIJSE **5**(12), 79–82 (2007)
20. Preet, K., Singh, A.: Exploring data mining tool - WEKA and using WEKA to build and evaluate predictive models. Adv. Appl. Math. Sci. **19**(6), 451–469 (2020)
21. Scholz, M., Forman, G.: Apples-to-apples in cross-validation studies: pitfalls in classifier performance measurement. Int. J. Res. Stud. Sci. Eng. Technol. **6**(11), 40–52 (2010)
22. Sánchez, D., Vega, J., Rueda, D., Rodríguez, A.: Remote monitoring of RF amplifiers in HFC networks: voltage drop detection due to power blackouts. In: Congreso Internacional de Innovación y Tendencias en Ingeniería, pp.1–6. IEEE, Bogotá (2022)
23. Sharma, P.: Analysis of various decision tree classification algorithms using WEKA. Int. J. Recent Innov. Trends Comput. Commun. Comp. **3**(2), 684–690 (2015)
24. Sheela, Y., Krishnaveni, S.: A comparative analysis of various classification trees. In: International Conference on Circuit, Power and Computing Technologies, pp. 1–8. IEEE, Collam (2017)
25. Simakovic, M., Cica, Z., Drajic, D.: Big-data platform for performance monitoring of telecom-service-provider networks. Electronics **11**(14), 2224 (2022)
26. Simakovic, M., Cica, Z.: Detection and localization of failures in hybrid fiber-coaxial network using big data platform. Electronics **10**(23), 2906 (2021)
27. Suárez, I., Escobar-Díaz, A., Vacca, H.: Unidades de climatización para centro de datos. Vínculos **16**, 128–147 (2019)
28. Wauters, T., et al.: HFC access network design for switched broadcast TV services. IEEE Trans. Broadcast. **53**(2), 588–594 (2007)
29. Witten, I., Frank, E., Hall, M.: Data Mining: Practical Machine Learning Tools and Techniques. Elsevier Science & Technology, San Francisco (2011)
30. Zhang, L., Ma, Y., Liu, K., Zeng, Y.: Research of the noise characteristic on the upstream channel for HFC network. In: 2nd International Conference on Signal Processing Systems, pp. 426–430. IEEE, Dalian (2010)

Optimization of the B10s1 Engine for Corsa with Adaptation of the Cylinder Head of a Spark-Ignition Engine and Validation on a Chassis Dynamometer to Verify Its Power

Jose Vicente Manopanta Aigaje[1,2](✉)

[1] Instituto Tecnológico Universitario Ismac, Quito, Ecuador
vmanopanta@tecnologicoismac.edu.ec
[2] Universidad Internacional SEK, Quito, Ecuador

Abstract. In the automotive fleet, the improvement of performance and power have a significant growth, these parameters are evidenced in high-end vehicles with high costs. In common vehicles, these improvements can be obtained with adaptations to the combustion engine. The objective of this research is to improve the performance of the engine by adapting a cylinder head. A Chevrolet Corsa B10S vehicle is selected. The engine power without modification is determined using a chassis dynamometer. The impact on the mechanical performance of the vehicle is given by the adaptation and modification of the cylinder head of an Aveo Activo 16 valves with independent ITBs for the intake manifold, modifications in the exhaust manifold with independent outputs (header), improving the intake and exhaust of gases in the spark-ignition engine. The method used will be the experimental one, making adjustments in the distribution with two camshafts and timing belt, optimizing the maintenance. It is also concluded that as the percentage of air-fuel increases, a better torque and power performance will be obtained in relation to the standard engine.

Keywords: Tuning · Adaptation · Power · Performance

1 Introduction

This theoretical and practical research will take into consideration that motor racing competitions in Ecuador have been practiced since 1930 in cities such as Quito, Guayaquil, Riobamba, Cuenca and Ambato. In 1985 the Tungurahua Automóvil Club (Tungurahua Automobile Club) (TAC) was created and new divisions were formed. One of the categories characterized by the high competitive level in the province, is the 0 to 1150 cc category, dominated by the presence of Suzuki Forsa 1 vehicles [1]. Engine tuning is possible because all manufacturers have over-dimensioned them to obtain safety and reliability margins that ensure their operation in adverse conditions. It is possible to reduce these safety margins to acceptable minimums in order to considerably increase engine performance without jeopardizing the engine service life [2]. In conventional

M. Z. Vizuete et al. (Eds.): CI3 2023, LNNS 1040, pp. 186–198, 2024.
https://doi.org/10.1007/978-3-031-63434-5_14

spark-ignition engines, efficient combustion requires the use of fuels that ensure fast and safe starting of the engine regardless of the outside temperature, guarantee a carbon-free combustion process, reduce the formation of pollutants, and produce minimum deterioration of the main engine parts [3]. The physical-chemical properties of the fuel used must allow the fuel to evaporate to form a very homogeneous fuel-air mixture in the combustion chamber. In spark-ignition engines (SIE) the above process depends on factors such as: the type of fuel, the proper design of the intake system, heat transfer conditions, the presence of waste gases, engine speed, leakage in the chamber due to compression losses and the effects of mixture agitation [4]. The addition of bridges and bores in the cylinder head proves to be very effective as it considerably reduces emissions. In addition, a slight change in the configuration of the bridges and bores can change the flow directions and patterns and vary the way the gases react, which can further reduce emissions [5]. Sha et al. (2015) [6] experimentally investigated the effects of pre-chamber volume and nozzle diameter on the resultant ignition characteristics. It was found that a larger pre-chamber provides higher ignition energy, which results in shortened flame development angle and combustion duration. At a given pre-chamber volume, nozzle diameter mainly affects the combustion duration [7]. The research begins with the aforementioned background, and due to contamination and lack of performance in spark-ignition and compression-ignition engines, the low level of energy consumption of organic materials as energy sources that guarantee an optimal performance in internal combustion engines. The main purpose of this project is the adaptation of the cylinder head of a spark-ignition engine and validation on a chassis dynamometer for the verification of its developed power after the respective modifications of the cylinder head with its respective elements that involve a better performance in the engine.

2 Method

2.1 Applied Test Vehicle

The research will be experimental and a Chevrolet Corsa 1.3 Standard 4-cylinder 1,300 cm^3 gasoline engine, with an indirect injection in the intake manifold, equipped with a three-way catalytic converter of the year 1997 will be used; the vehicle with the lowest fuel consumption and most sold in Ecuador in those years. Table 1 describes the technical specifications of the vehicle.

2.2 Combustion Chamber (Cylinder Head) Features

It is made of aluminum, which helps to dissipate heat. The design of the cylinder head is simple, easy to reproduce and install; given the intake stroke, the mixture reaches the cylinder with little speed, the turbulence is almost null, the combustion is slow and prone to detonation due to the long length of the flame [8]. The measurement of the volume of the combustion chamber can be seen in Fig. 1 with the help of a graduated burette in ml and an acrylic piece.

The mathematical models are generated from the following equations.

Table 1. Chevrolet Corsa 1.3L Standard Technical Data Sheet

Characteristics	Units
Make	Chevrolet
Model	Corsa Wind
Year	1997
Compression Ratio	9.4/1
Torque	111 Nm
Horsepower	60 CV
Bore	77.6 mm
Top Speed	164 km/h
Acceleration, 0–100 km/h	14.8 s
Max Power	60 CV DIN AT 5800 rpm
Displacement	1389 cm^3
Max Torque	111 Nm DIN AT 3400 rpm
Valves	2 valves per cylinder
Fuel	Gasoline
Engine	Inline four
Firing order	1-3-4-2

Fig. 1. Measurement of the combustion chamber volume

Piston volume measurement [9]

$$Compressed\ Vol. = \text{Piston } Vol. + Chamber\ Vol. + \text{Gasket Vol.} \tag{1}$$

$$Compressed\ Vol. = 14{,}4 + 22{,}2 + 4{,}65 = 41.25\ cm^3$$

Calculation of the compression ratio of the engine

$$Rc = \frac{Compressed\ Vol. + Displacement\ Vol.}{Compressed\ Vol.} \tag{2}$$

$$Rc = \frac{41{,}25 + 343.67}{41.25} = 9.33 : 1$$

With the help of the mathematical models [9] and the corresponding adaptation, calculations are made to obtain the tuned or modified compression ratio that will allow observing the changes in the displacement values, comparing the results of this experiment where a burette is used to have a great accuracy in the liquid measurements and precision instruments to avoid errors in this experiment, as shown in Table 2.

Table 2. Compression Ratio Technical Data

	Engine without Modification	Engine with Modification
Displacement Vol	343.67 cm3	343.67 cm^3
Gasket Vol	4.65 cm^3	3.66 cm^3
Chamber Vol	22.2 cm^3	22 cm^3
Piston Vol	14.4 cm^3	14.4 cm^3
Compressed Vol	41.25 cm^3	40.06 cm^3
Compression Ratio	9.33:1	9.57:1

2.3 Valve Mechanism System

The project involves a traditional OHV type distribution system and a DOHC type system with the variation of two camshafts, improving the engine performance and gas intake and exhaust [10]. The adaptation is based on the use of a cylinder head from a Chevrolet Aveo vehicle in the monoblock of the Corsa vehicle. The DOHV valve system performs an exhaustive work in the gas recirculation. Figure 2 shows several characteristics of the valves both in standard and modified or tuned form, applying an inclination of 30 ° to the valve seat [11].

Fig. 2. Camshaft and valve configuration

Table 3 shows the characteristics of the intake and exhaust valves with their standard and modified values for the experimentation with a Corsa Wind vehicle with the engine tuned.

Table 3. Valve System

	Standard Condition	Modified Condition
Intake Valve Measurement		
Retainer Diameter	39.2 mm	28.58 mm
Valve Length	105.1 mm	101.58 mm
Valve Stem	7.1 mm	5.86 mm
Valve Seat	45°	30°
Exhaust Valve Measurement		
Retainer Diameter	31 mm	26 mm
Valve Length	112.5 mm	101.34 mm
Valve Stem	105.1 mm	5.85 mm
Valve Seat	45°	30°

2.4 Intake and Exhaust System of the Spark-Ignition Engine

The cylinder head has the gas intake mainly by means of ITB ducts which are used for the recirculation of gases and managing a proper combustion. Figure 3 shows the ITBs that allow greater air intake. Table 4 details the characteristics and values for standard and tuned measures proposed in this research. In addition, Figs. 2, 3 and 4 show the measurement processes established to obtain the data in the cylinder head [12]. The engines are fed with ethanol-gasoline blends and the users are responsible for performing the tuning, without following a recommended instruction and carrying out the tests in any chassis dynamometer. The service technicians, with their experience rather than formal training, are the ones that perform the engine tunings when operating with fuel not provided by the manufacturer [13].

Intake valve timing has a significant effect on the engine air exchange process. During engine start conditions, the engine valve strategy is to delay the intake valve timing and speed up the exhaust valve timing to ensure the lowest residual exhaust gas and maximum fresh air [14]. The sizing of the manifold nozzles is relevant to appreciate the modification as a consequence of the new performance desired from the vehicle engine, according to Table 5.

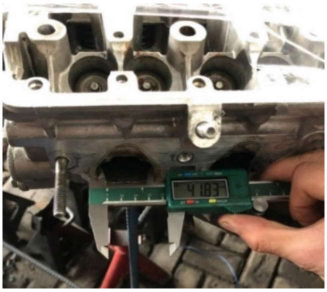

Fig. 3. Measurement of the intake manifold nozzle diameter

Table 4. Gas recirculation cylinder head ducts and valve springs

	Engine Without Modification			Engine with Modification		
Cylinder head intake nozzles						
	Diameter (mm)	Length (cm)	Volume (cm^3)	Diameter (mm)	Length (cm)	Volume (cm^3)
CYLINDER 1	33.0	35	500	40.73	18.5	238.7
CYLINDER 2	33.0	35	500	40.73	18.5	238.7
CYLINDER 3	33.0	35	500	40.73	18.5	238.7
CYLINDER 4	33.0	35	500	40.73	18.5	238.7
Cylinder head exhaust nozzles						
	Diameter (mm)	Length (cm)	Volume (cm^3)	Diameter (mm)	Length (cm)	Volume (cm^3)
CYLINDER 1	30.0	22	530	33	26	530
CYLINDER 2	30.0	22	530	33	26	530
CYLINDER 3	30.0	22	530	33	26	530
CYLINDER 4	30.0	22	530	33	26	530
Cylinder head springs						
	Diameter (mm)	Length (mm)	Thickness (mm)	Diameter (mm)	Length (mm)	Thickness (mm)
CYLINDER 1	29.50	30.50	3.05	27.1	40.42	3.48
CYLINDER 2	29.50	30.50	3.05	27.1	40.42	3.48
CYLINDER 3	29.50	30.50	3.05	27.1	40.42	3.48
CYLINDER 4	29.50	30.50	3.05	27.1	40.42	3.48

Fig. 4. Measurement of the ITB diameter

Table 5. Manifold nozzles and cylinder head height

	Engine Without Modification	Engine with Modification
Measurement of the cylinder head height		
	mm	mm
Height	96	130.4
Measurement of the exhaust manifold nozzle diameter		
	Diameter (mm)	Diameter (mm)
CYLINDER 1	30	33
CYLINDER 2	30	33
CYLINDER 3	30	33
CYLINDER 4	30	33
Measurement of the intake manifold nozzle diameter		
	Diameter (mm)	Diameter (mm)
CYLINDER 1	33	40.73
CYLINDER 2	33	40.73
CYLINDER 3	33	40.73
CYLINDER 4	33	40.73

2.5 Determination of the Developed Power

For the measurement process, the drive wheels or front wheels of the car rest on four rollers. The rollers rotate with a known moment of inertia. There is a sensor that registers the rotational speed of the rollers and systematically sends the speed information to the computer. [15] (For this chassis dynamometer, only computerized measurement is admissible). The main test in this study is in the chassis dynamometer, where the SAENZ PERFORMANCE INERTIAL CHASSIS DYNOS-N 08–19 was used, which allows simulating a speed profile as a function of time to perform dynamic tests on diesel and gasoline vehicles. It allows to load several test cycles of the different legislations for which they were designed, determining in an exact way the values of power and torque of the vehicle.

Fig. 5. Dynamometer characteristics

Figure 5 shows a sequential representation of the process and the model of tests performed on the vehicles. This is a chassis dynamometer (Fig. 6).

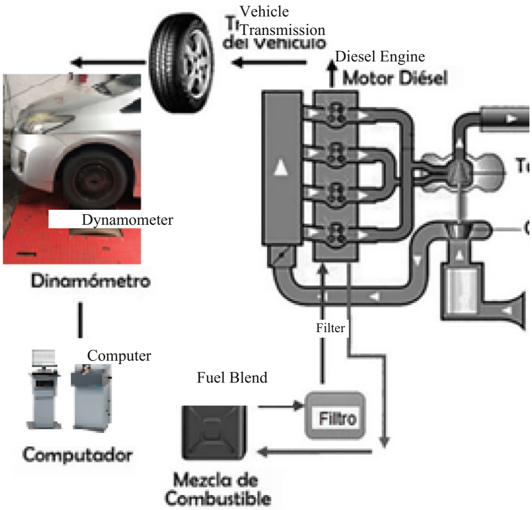

Fig. 6. Chassis dynamometer structure

The power and torque test protocols were performed under the ISO 1585 and ISO 3173 standards; following the test protocol: verify that the diameter of the wheels is equal to or greater than 13-inch rim (Wheels of the Corsa vehicle are 175/70/13). Verify the cleanliness of the test site both in the tire tread and in the dynamometer (Fig. 7).

Secure the vehicle with straps to prevent it from slipping off the rollers; enter the technical data concerning the vehicle to be tested into the software; check the gear and transmission ratio of the unit, which must be 1:1; make sure that the engine temperature is in the range of 85°-90°, otherwise it must pass an engine warm-up period to reach such temperature; start the cooling fan of the dynamometer; start the measurement test; accelerate the vehicle with the pedal fully depressed in the test gear until reaching the

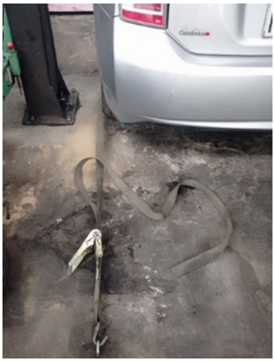

Fig. 7. Security straps and anchoring of the vehicle.

desired speed called "rpm cut" (4500–6000 rpm); when the "rpm cut" has been reached, depress the clutch, leaving the gear engaged. The dynamometer decelerates to a stop [16, 3] (Fig. 8).

Fig. 8. Dynamometer tests

3 Results

3.1 Vehicle Power Without Modification of the Cylinder Head

The power values generated by the engine of the Corsa 1.3 vehicle are obtained with tests. The static test with load was carried out, using the chassis dynamometer, under the ISO 1585 Standard, performing three tests for each case and obtaining the result to be evaluated. Figure 9 shows the results of the tests on the equipment. The results of

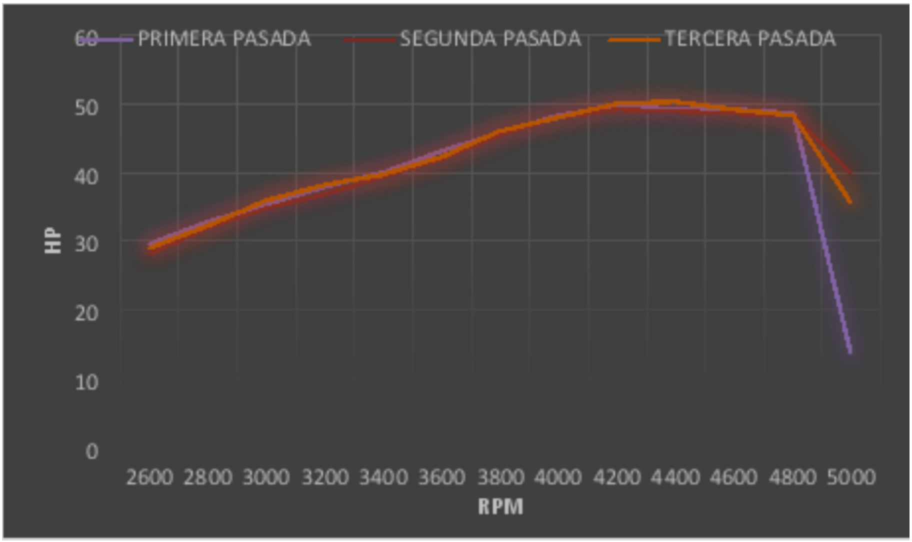

Fig. 9. Vehicle power without the cylinder head modification during three runs

the power values obtained for the vehicle with the dynamometer are as follows. The test was run three times in a row using premium gasoline. In this test, it can be observed that the curves generated do not show a major difference according to the values.

3.2 Vehicle Power with the Cylinder Head Modification

Next, the power parameters generated by the engine of the Corsa 1.3L vehicle are presented. The static test with load was carried out using the chassis dynamometer, under the ISO 1585 Standard. Three consecutive tests were performed obtaining the result shown in Fig. 10, which indicates the power curves obtained with the dynamometer, using premium gasoline. In addition, it is shown that there is no great difference between the values obtained.

Table 6 shows the results obtained in the dynamometer with a power increase of 8 hp, where it is confirmed that the adaptation of the cylinder head of the Aveo vehicle to the engine of the Corsa vehicle has been efficient.

3.3 Discussion of the Results on the Obtained Power

The engine could be fueled by gasoline, ethanol or a blend of both in any proportion. The fuel injection system was controlled by an electronic module for engine development, which allowed optimizing the blend ratio and ignition timing for the whole speed range tested [17].

In Fig. 10, an irregular line representing the torque curve as a function of revolutions per minute of the Corsa Wind 1.3L engine can be seen. The graph starts at 2200 RPM with a torque of 50 hp, when approaching 2300 RPM there is an abrupt change, a rise in the graph curve up to 68 hp and at 5500 RPM rises to almost 69 hp and drops at 2000

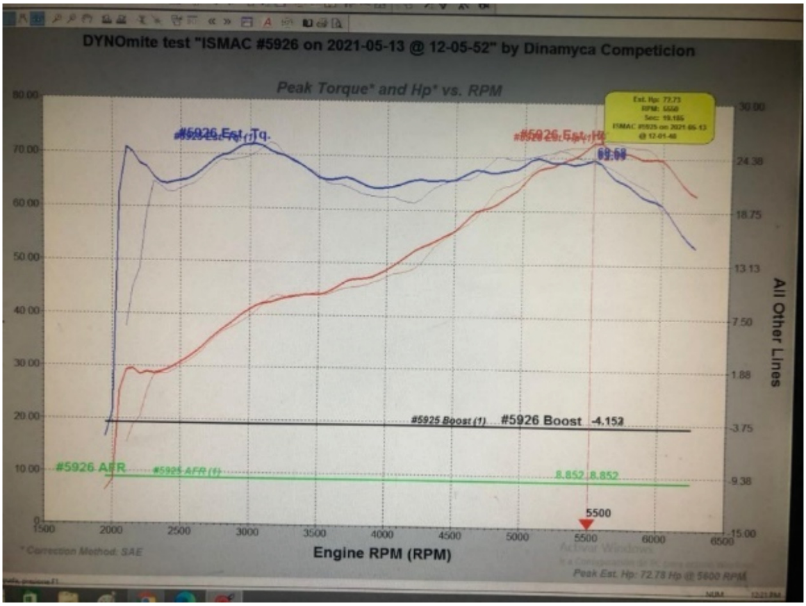

Fig. 10. Vehicle power with the cylinder head modification during three runs

Table 6. Test results of the tuned engine

Dynamometer	Power	RPM
First test	68.58 hp	5500 rpm
Second test	69.58 hp	5500 rpm
Third test	68.58 hp	5500 rpm

RPM to 30 hp, it rises again to almost 50 hp at 2700 RPM and then there is a rise and fall of torque, rises and falls again until it stabilizes from 3500 RPM [18].

The tests carried out and the values obtained are used to analyze the behavior of the vehicle, which will be used to develop the pertinent analysis regarding the performance of the engine. We will proceed as follows, working with the average power values obtained [12]. Figure 9 shows the power variation differences for the standard working tests and the cylinder head modification, clearly evidenced in the chassis dynamometer.

It is then established according to the measurements made that there is an increase of 30.08% in the performance at 4400 rpm with respect to the engine power with the modifications of the cylinder head, and it is clearly seen in Table 6 the difference between the performance of power before and after the modifications of the cylinder head. All the tests were carried out with the premium gasoline that is commercialized in the country. Several authors show similar data, confirming the increased engine efficiency [4] (Fig. 11).

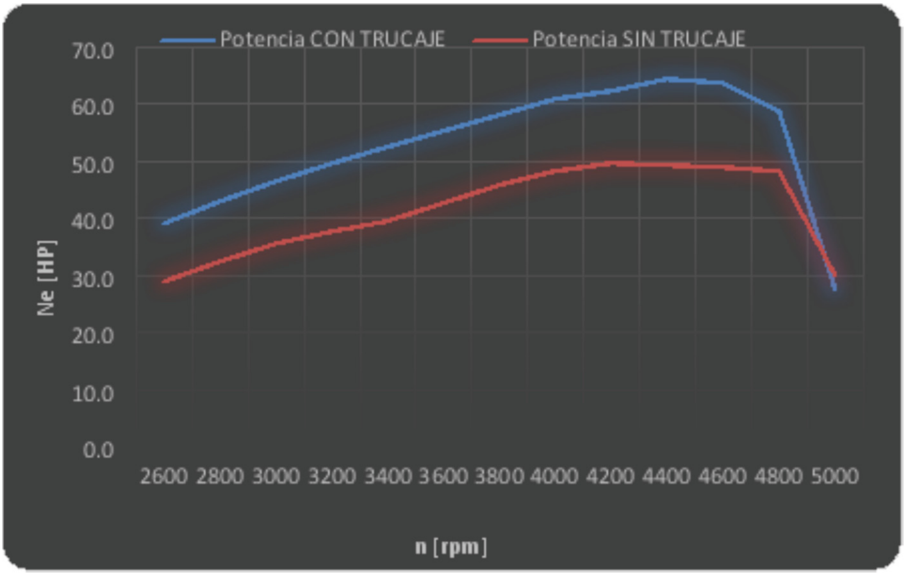

Fig. 11. Developed powers before and after the engine cylinder head tuning.

4 Conclusions

An analysis is made by researching the adaptations and modifications in the cylinder head and engine tuning to find the best performance and yield. In the analyzed studies, it has been found that the best angle of the valve seats is at 30 degrees in the intake and exhaust nozzles and ducts of the cylinder heads, and they are truly relevant and have the greatest influence on the performance of the engine's ITBs (Individual throttle body)**.**

The measurements performed show an increase in power performance of 8 hp in general during the course of the engine operation from idle to maximum power. Therefore, with the modifications and specifically at the maximum power at 4500 rpm, an increase of 13.08% measured in the chassis dynamometer was observed as a result of the modifications of the cylinder head of the Aveo vehicle with respect to the standard cylinder head of the Corsa Wind vehicle.

References

1. Repositorio de la Universidad de Fuerzas Armadas ESPE: Artículo Científico - Estudio y análisis teórico práctico del comportamiento de un motor SUZUKI G10 previo y posterior a su trucaje
2. Herrera Martínez, J.J.: Trucaje de un motor Renault 1022 CC referencia R850 de serie (2016)
3. Jovaj, M.: Motores de automovil, Editorial MIR, Mosc˙(1982)
4. Lukanin, V.: Motores de combustion interna, Editorial MIR, Mosc (1985)
5. Indudhar, M.R., Banapurmath, N.R., Rajulu, K.G., Patil, A.Y., Javed, S., Khan, T.M.Y.: Optimization of piston grooves, bridges on cylinder head, and inlet valve masking of home-fueled diesel engine by response surface methodology. Sustainability **13**(20), 11411 (2021)

6. Shah, A., Tunestal, P., Johansson, B.: Effect of pre-chamber volume and nozzle diameter on pre-chamber ignition in heavy duty natural gas engines, SAE technical paper (2015)
7. Ge, H., Bakir, A.H., Yadav, S., Kang, Y., Parameswaran, S., Zhao, P.: CFD optimization of the pre-chamber geometry for a gasoline spark ignition engine. Front. Mech. Eng. **6**, 599752 (2021)
8. Kalghatgi, G.T., McDonald, C.R., Hopwood, A.B.: An experimental study of combustion chamber deposits and their effects in a spark-ignition engine, SAE Technical Paper (1995)
9. Kindler, H.: Matemática Aplicada Para La Técnica Del Automóvil. Barcelona España: Reverté (2007)
10. Gillieri, S.: Preparación de Motores de Serie para Competición. Barcelona España: CE (2006)
11. Rosales, J.P.F., Revelo, J.D.G., Cárdenas, E.M.C., Paz, P.A.M.: Determinación experimental de la eficiencia mecánica de un motor de combustión interna de encendido provocado por medio de las curvas de torque y potencia. Polo del Conoc. **7**(7), 1735–1759 (2022)
12. Romero-Piedrahita, C.A., Mejía-Calderón, L.A., Carranza-Sánchez, Y.A.: Estudio de sensibilidad del desempeño durante el calentamiento en vacío de un motor de combustión interna a cambios en su relación de compresión, el contenido de etanol en la mezcla combustible con gasolina y el material de la culata. Dyna **85**(204), 238–247 (2018)
13. Galindo, J., Climent, H., De la Morena, J., Pitarch, R., Guilain, S., Besançon, T.: A methodology to study the interaction between variable valve actuation and exhaust gas recirculation systems for spark-ignition engines from combustion perspective. Energy Convers. Manag. **250**, 114859 (2021)
14. MAUT 014 TRABAJO DE GRADO.pdf (utn.edu.ec)
15. Corsini, A., Di Antonio, R., Di Nucci, G., Marchegiani, A., Rispoli, F., Venturini, P.: Performance analysis of a common-rail diesel engine fuelled with different blends of waste cooking oil and gasoil. Energy Procedia **101**, 606–613 (2016)
16. Yu, S., Zheng, M.: Future gasoline engine ignition: a review on advanced concepts. Int. J. Engine Res. **22**(6), 1743–1775 (2021). https://doi.org/10.1177/1468087420953085
17. Costa, R.C., Sodré, J.R.: Hydrous ethanol vs. gasoline-ethanol blend: engine performance and emissions. Fuel **89**(2), 287–293 (2010)
18. Modificación mecánica y electrónica de un motor Corsa Wind 1300 cc distribución OHC con la implementación de una unidad de control electrónico programable y un sistema de distribución DOHC de 16 válvulas

Analysis of the Reliability of the Calibration of a Camera Through the Knowledge of Its Extrinsic Parameters

Henry Díaz-Iza[1](✉), Harold Díaz-Iza[2], Wilmer Albarracín[1], and Rene Cortijo[1]

[1] Universidad Tecnológica Israel, Quito, Ecuador
hdiaz@uisrael.edu.ec
[2] Universitat Politècnica de València, Valencia, Spain

Abstract. Camera calibration methods support their concepts on pinhole camera models to obtain the intrinsic and extrinsic parameters of a camera. These methods consider the different nonlinearities caused by the lens to determine their results. The different calibration algorithms, to verify whether the parameters of the model are acceptable, use a mathematical factor known as back-projection error that, as much as it approximates to zero, indicates whether the theoretical mathematical model of a camera fits well with the real camera model. In this study, the aim is to analyze the reliability of the calibration results of a camera by comparing the extrinsic parameters (position and orientation) delivered by the algorithms of Tsai, Zhang, and Faugeras with different camera positions and orientations taken using an ABB manipulator robot.

Keywords: Camera calibration · Error analysis · Computer vision

1 Introduction

In computer vision, digital cameras play a significant role in developing vision applications. Digital cameras allow improvements in image definition, resolution, and optical quality. In addition, they have advanced processing capabilities that enable additional features such as fast autofocus, face detection, and burst image capture. These enhancements have significantly impacted various industries and vision applications, expanding possibilities in photography, video surveillance, augmented reality, medicine, robotics, and more.

Calibration of a camera is essential in obtaining accurate measurements of a scene from captured images. For this reason, it is essential to perform a camera calibration with complete assurance that the parameters obtained are as close as possible to values that guarantee an accurate real measure of a scene. Calibration enables a mathematical representation of their physical and geometrical properties and their orientation and position according to a reference plane [1–3].

M. Z. Vizuete et al. (Eds.): CI3 2023, LNNS 1040, pp. 199–210, 2024.
https://doi.org/10.1007/978-3-031-63434-5_15

The basic idea of calibration is to describe a projection model that relates the coordinate systems of the camera and the reference world. In other words, a calibration permits obtaining intrinsic parameters (optical center and focal length) and extrinsic parameters (position and orientation of a camera according to a reference framework) [4,5].

Although there are a variety of calibration methods, all of them use the reprojection error to validate their results [6]; however, in practice, this mathematical factor does not ensure that the camera model is correct due to the coupling between intrinsic and extrinsic parameters that makes the algorithms in one way or another look for a solution to the system that may or not be adequate.

Even though most camera calibration algorithms solve the acquisition of intrinsic and extrinsic parameters, the question arises as to how reliable are the parameters obtained from the calibration. In general terms, this work aims to implement and analyze the most commonly used calibration algorithms in the field of vision and to assess the reliability of the extrinsic parameters by comparing the extrinsic parameter results of the algorithms with the position and orientation values of the camera taken with the help of an IRB140 robot of ABB.

The article is structured as follows: Sect. 2 describes the camera model commonly employed in calibration and the different calibration methods implemented. Section 3 details the results of the experiments performed. Finally, Sect. 4 mentions the conclusions

2 Methods

The camera calibration methodology is divided into two stages. The first stage consists of obtaining the intrinsic and extrinsic camera parameters by applying the most popular calibration algorithms, Zhang and Tsai for 2D and Tsai and Faugeras for 3D, over synthetic data to validate the algorithms. The second stage is responsible for analyzing the reliability of the extrinsic parameters obtained by applying the algorithms over real data and comparing the extrinsic parameter results with the real camera position obtained with the help of the IRB140 robot [7]. The camera model consists of two parameters to consider: intrinsic and extrinsic. The intrinsic parameters model the camera image sensor, i.e., internal geometry and optical characteristics. The extrinsic parameters, on the other hand, measure the position and orientation of the camera with respect to a world coordinate system.

The model of a camera is based on the approximation of the internal geometry, position, and orientation of the camera in the scene. Several camera models depend on the desired accuracy; one of the most widely used is the Pinhole model. In general, this model allows obtaining the necessary data to calculate the geometric information that an image possesses, i.e., they describe a mathematical projection between an object in 3D and 2D image space.

2.1 Pinhole Camera Model

The pinhole model is the most straightforward and practical type of camera model. It operates by projecting a point in the scene onto the image plane through the intersection of a line passing through the point and the center of projection [4,8], as shown in Fig. 1.

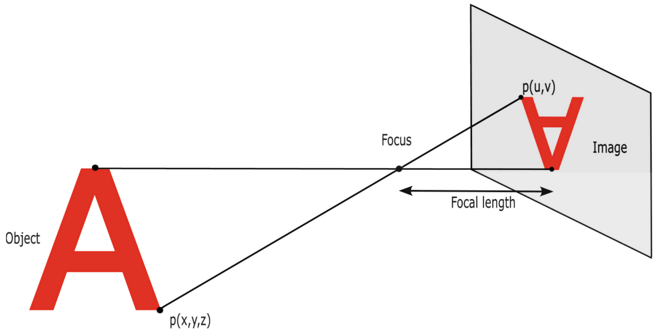

Fig. 1. Pinhole Camera Model [9]

The pinhole model utilizes a projection matrix to convert the three-dimensional coordinates of object points into their corresponding two-dimensional image coordinates, as expressed by Eq. 1.

$$m = P \cdot M \tag{1}$$

where $M = [X_\omega, Y_w, Z_\omega, 1]^T$ represents the vector that contains the coordinates of the world reference system, P is the projection or camera matrix used to transform the world coordinates into the projected point $m = [u, v, 1]^T$ over the image, the units of m are pixels.

2.2 Methods of Calibration

Calibrating a camera is essential for obtaining accurate scene measurements from captured images. The quality of the calibration will have a direct impact on the accuracy of the measurements made based on those images. For this reason, it is necessary to perform a reliable camera calibration and to obtain parameters as close as possible to the valid values. This commitment implies making the right decisions regarding the chosen calibration method and using it correctly.

Calibration involves obtaining the parameters that describe the camera model including their linear and nonlinear components. Several methods are currently available for performing this calibration; some use specific templates, while others dispense with them altogether.

The Hall [10] and Faugeras-Toscani [7] linear calibration methods are commonly used with 3D templates and employ least-squares techniques to obtain the model parameters. By the other hand, nonlinear calibration methods such as Tsai's [11] with 3D or 2D templates and Zhang's [12] with 2D templates employ a two-stage technique. In the first stage, a linear model is calculated based on the calibration data; this provides initial estimates of data for the camera parameters. In the second stage, a nonlinear optimization is performed using the initial estimates parameters as a starting point. This optimization process refines the camera parameters to further improve the calibration accuracy. By combining both linear and nonlinear techniques, the calibration process achieves more accurate and reliable results. The algorithms and their main characteristics used in this work are briefly described below.

Hall Calibration Method. The Hall method [7,10] is based on an implicit calibration whose objective is to find the linear relationship between the 3D points of the scene with the 2D points projected on the image plane. This relationship is shown in the Eq. 2

$$\begin{pmatrix} s^I X_d \\ s^I Y_d \\ s \end{pmatrix} = \mathbf{A} \begin{pmatrix} {}^W X_w \\ {}^W Y_w \\ {}^W Z_w \end{pmatrix} \tag{2}$$

where $({}^W X_w, {}^W Y_w, {}^W Z_w)^T$ expresses a 3D point from the world (scene), $({}^I X_d, {}^I Y_d)^T$ is the 2D point in pixel with respect to the image coordinate system, s is an scale factor, and A is a 3 by 4 transformation matrix proposed by Hall.

Faugeras-Toscani Calibration Method. To obtain a complete model, Faugeras-Toscani [7,13] proposes a slightly different method than that proposed by Hall for the estimation of the calibration matrix. Faugeras-Toscani obtains the intrinsic and extrinsic parameters by equating his calibration matrix with that proposed by Hall. The relationship is shown in the equation

$$\begin{pmatrix} s^I X_d \\ s^I Y_d \\ s \end{pmatrix} = \begin{pmatrix} \alpha_u & 0 & u_0 & 0 \\ 0 & \alpha_v & v_0 & 0 \\ 0 & 0 & 1 & 0 \end{pmatrix} \begin{pmatrix} r_{11} & r_{12} & r_{13} & t_x \\ r_{21} & r_{22} & r_{23} & t_y \\ r_{31} & r_{32} & r_{33} & t_z \\ 0 & 0 & 0 & 1 \end{pmatrix} \begin{pmatrix} {}^W X_w \\ {}^W Y_w \\ {}^W Z_w \\ 1 \end{pmatrix}, \tag{3}$$

then

$$\begin{pmatrix} s^I X_d \\ s^I Y_d \\ s \end{pmatrix} = \mathbf{A} \begin{pmatrix} {}^W X_w \\ {}^W Y_w \\ {}^W Z_w \\ 1 \end{pmatrix} \tag{4}$$

where $({}^W X_w, {}^W Y_w, {}^W Z_w)^T$ expresses a 3D point from the world (scene), $({}^I X_d, {}^I Y_d)^T$ is the 2D point in pixel with respect to the image coordinate system, s is an scale factor, A is a 3 by 4 transformation matrix, $(\alpha_u, \alpha_v, u_0, v_0)$ are the intrinsic parameters and $(r_1, r_2, r_3, t_x, t_y, t_z)$ are the extrinsic parameters.

Tsai Calibration Method. The Tsai method [7,11] models the radial distortion of the lens but assumes that there are camera parameters that the manufacturer provides. This method reduces the number of calibration parameters at the first stage when parameter estimation is started.

The Tsai method has some limitations, among which we can mention that in its model, it only involves radial and not tangential distortions; however, these distortions are often not considered necessary, so the method has been widely extended and used in applications that require higher accuracy.

Zhang Calibration Method. The Zhang method [9,14] is the most widely used in computer vision; in the first instance, the method is based on obtaining an approximation of the camera model by a linear method. This approximation is refined by applying a maximum likelihood criterion iteratively. Calibration with this method is mainly performed with a point plane or a 2D grid. Zhang mentions that for the method to work correctly, it is necessary to take at least three images from different positions and orientations; however, the number of images can be reduced if some intrinsic parameters are fixed.

3 Results and Discussion

A series of images captured from various camera positions were used to extract intrinsic and extrinsic parameters. Different algorithms were implemented to estimate these parameters, firstly using synthetic data to verify the correct functioning of the algorithm to finally using the algorithms with real data. The data obtained from the application of the algorithm over the different images taken were used to verify whether the extrinsic parameters resulting from the calibration algorithms fit the camera positions and orientations by taking the positions acquired with the help of an ABB IRB 140 robot as a reference. The system overview is shown in Fig. 2 and consists of a Canon EOS 700D camera, 2D/3D calibration templates, ABB IRB 140 robot, and measurement pointer. For further reference of the implemented system and acquired data, refer to [15].

3.1 Description of the Experiments Performed

The acquired images have a 5184 $\times$ 3456 [pixels] resolution, and the focal distance of the camera is 18 [mm]. The data acquisition was performed in two parts; first, the coordinates of the reference points (corners) of the template were taken with a pointer mounted as an end-effector on the robot. Second, the coordinates and orientations of the different camera locations were taken according to the orientation and position of the robot.

The images were acquired from a camera in the robot as an end-effector and from different camera positions and orientations reached by IRB 140 robot. The robot position data displayed on the Flexpendant were recorded. For the detection of points of the 2D template, necessary for the calibration of the camera, were obtained by the vision tools of Matlab software. Specifically, the

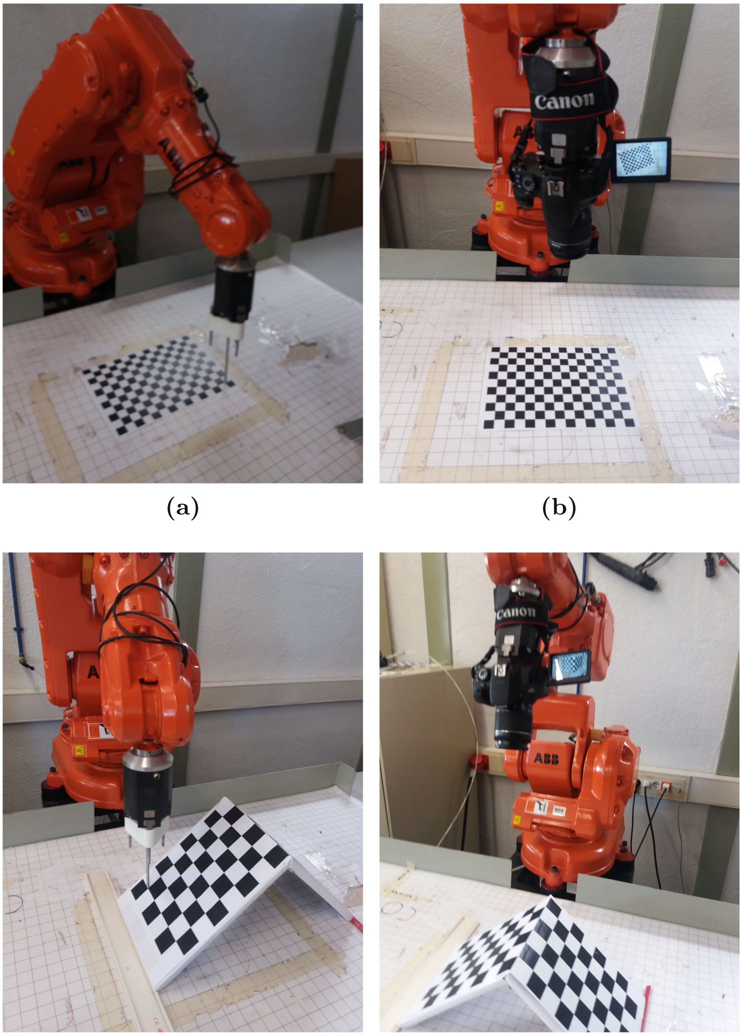

(a) (b) (c) (d)

Fig. 2. System used for calibration: pointer and 2D template(a), camera and 2D template(b), pointer and 3D template(c), camera and 3D template(d).

detectCheckerboardPoints function was used to identify the points of the 2D template. On the other hand, the detection of points for a 3D template was performed manually using as a reference the measurement of each point by the robot.

3.2 Tsai and Zhang Method for 2D

Tsai and Zhang's algorithms used a set of 16 images. The extrinsic parameters (camera position and orientation) resulting from the calibration of each image have been compared with the coordinates acquired by the ABB robot. Figure 3 shows the back-projection error of each image used for calibration. It is observed that the maximum back-projection error for Tsai's method is 4.2 pixels and a mean of 3.07 pixels, and for Zhang's method, the maximal back-projection error is 3.7 pixels and a mean of 2.33 pixels. This error means there is no significant difference (depending on the application) between the extrinsic parameters given by both algorithms and the values taken by the robot.

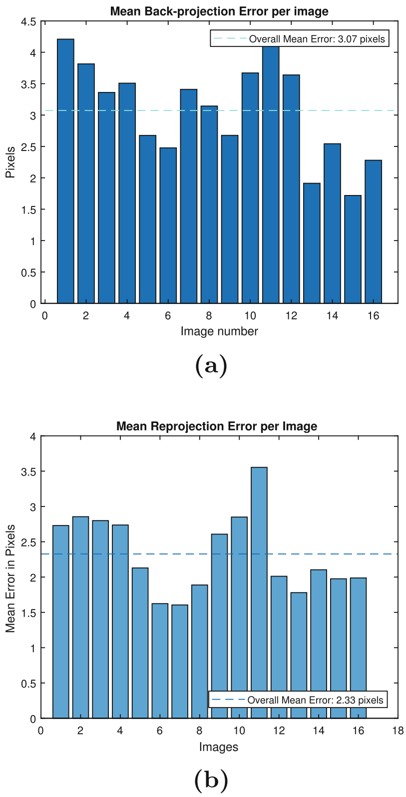

Fig. 3. Back-projection error: Tsai 2D (a) y Zhang (b)

By applying the inverse transform to the extrinsic parameter matrix resulting from the calibration, we can obtain the camera position and orientation that were compared with those acquired by the ABB robot. Figure 4 shows the camera position and orientation error by comparing the robot coordinates as a reference with the extrinsic parameters provided by the Tsai 2D and Zhang 2D algorithms

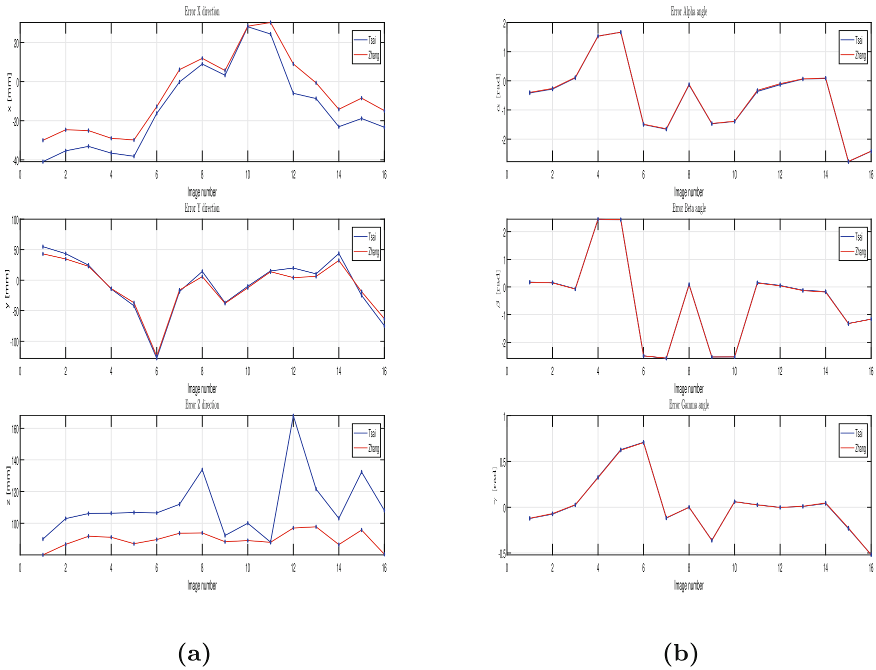

Fig. 4. Tsai 2D and Zhang 2D: Position error (a) and orientation error (b) of the camera.

for each image. The results show that the orientation errors of the camera are similar in both algorithms; in addition, little difference errors can be seen in x and y directions, but a significant difference is shown in the z direction, meaning that the algorithms are inefficient to detect depth, this problem could be due to that the algorithms only take into a count a single camera, to solve the problem with depth the use of a stereo-vision system is recommended.

Figure 5 shows graphically how the different actual camera positions lie over those delivered by the Tsai 2D and Zhang 2D calibration algorithm.

3.3 Tsai and Faugeras Method for 3D

A set of 6 images was used for the Tsai and Faugeras 3D algorithms. The extrinsic parameters (camera position and orientation) resulting from the calibration of each image have been compared with the coordinates acquired by the ABB robot. Figure 6 shows the back-projection error of each of the images used for calibration; it is observed that the average reprojection error of 20.17 pixels for the Tsai algorithm and 11.91 pixels for the Faugeras 3D algorithm. This error means that the difference between the extrinsic parameters given by the algorithms and the values taken by the robot is significant.

Applying the inverse transform to the extrinsic parameter matrix yields the position and orientation of the camera concerning the calibration template; these

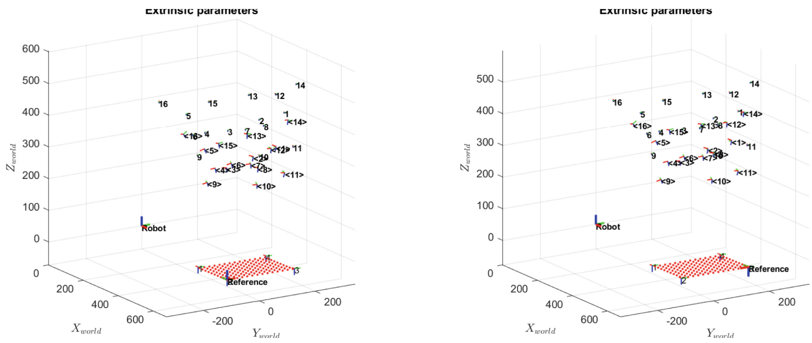

(a) (b)

Fig. 5. Calibration comparison of extrinsic parameters.The actual camera positions are above those delivered by the algorithm: Tsai 2D (a) and Zhang (b).

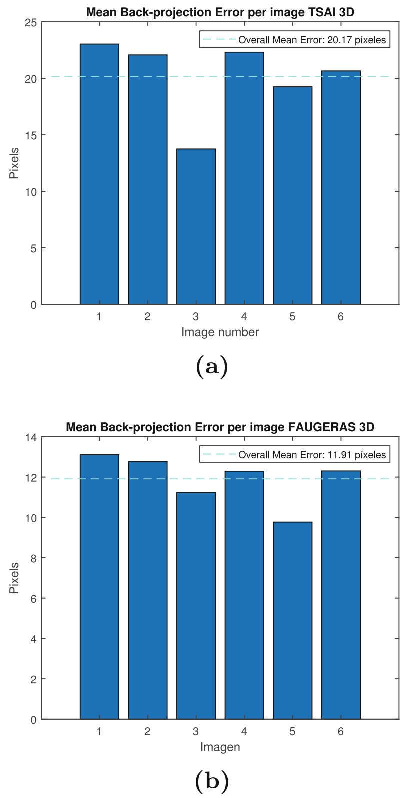

Fig. 6. Back-propagation error: Tsai 3D (a) and Faugeras 3D (b).

results were compared with the values obtained from the robot and are shown in Fig. 7. As before, the results show that the orientation errors of the camera are similar in both algorithms; in addition, little difference errors can be seen in x and y directions, but a significant difference is shown in the z direction. Although the algorithms are designed to detect depth, they are inefficient in detecting it. This problem might be due to the algorithms only considering a single camera, a stereo-vision system could be used to solve the problem.

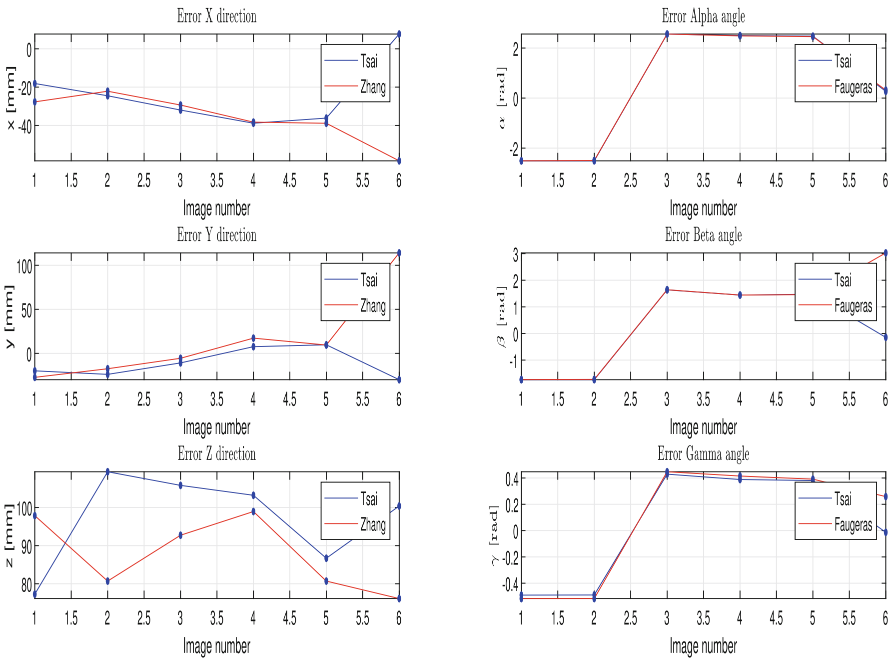

(a) **(b)**

Fig. 7. Tsai 3D and Faugeras 3D: Error of camera position (a) and orientation (b).

Figure 8 shows graphically that the actual camera positions do not match those delivered by both the Tsai 3D and Faugeras 3D algorithms, as the actual position is offset from that resulting in the algorithms.

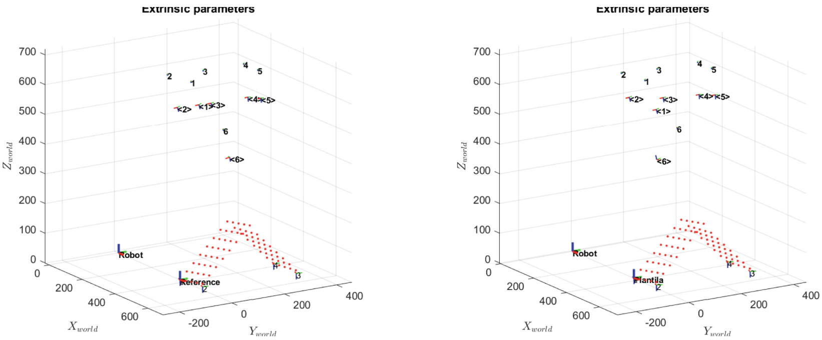

(a) (b)

Fig. 8. Comparison of extrinsic parameter calibration: Tsai 3D (a) and Faugeras 3D (b).

4 Conclusions

In our study, the different camera calibration methods showed a specific deviation from the reference values (measurements taken by the robot) in both orientation and translation. However, the 2D Zhang and 3D Faugeras calibration methods had the best approximated extrinsic parameters concerning the reference. Additionally, the results demonstrate that the back-projection error in the 2D calibration methods is small in comparison with the 3D calibration methods; however, this small error does not guarantee that the extrinsic coordinates are the same that the reality coordinates, as shown by the results obtained. Our results underscore that practical experiments provide an essential piece of information to distinguish which algorithm has the best performance at the time to calibrate a camera.

References

1. Viala, C.R.: Caracterización y optimización del proceso de calibrado de cámaras basado en plantilla bidimensional. Ph.D. thesis, Tesis doctoral, Universidad Politécnica de Valencia. Capitulo 2: El modelo de la cámara-2.7 Homografias p. 29 (2006)
2. Förstner, W., Wrobel, B.: Photogrammetric computer vision, pp. 141–159. Chapter robust estimation and outlier detection, Springer, Berlin (2016). https://doi.org/10.1007/978-3-319-11550-4
3. Ricolfe-Viala, C., Esparza, A.: The influence of autofocus lenses in the camera calibration process. IEEE Trans. Instrum. Meas. **70**, 1–15 (2021)
4. Hornberg, A.: Handbook of Machine and Computer Vision: The Guide for Developers and Users. Wiley, Hoboken (2017)
5. Chen, C.H.: Handbook of Pattern Recognition and Computer Vision. World Scientific, Singapore (2015)
6. Chatterjee, C., Roychowdhury, V.P.: Algorithms for coplanar camera calibration. Mach. Vis. Appl. **12**(2), 84–97 (2000)

7. Salvi, J., Armangué, X., Batlle, J.: A comparative review of camera calibrating methods with accuracy evaluation. Pattern Recogn. **35**(7), 1617–1635 (2002)
8. Hui, Z., Hua, W., Huinan, G., Long, R., Zuofeng, Z.: A real-time camera calibration system based on opencv. In: Proceedings of SPIE, vol. 9631, pp. 96311T–1 (2015)
9. Isern González, J.: Estudio experimental de métodos de calibración y autocalibración de cámaras (2003)
10. Hall, E.L., Tio, J.B., McPherson, C.A., Sadjadi, F.A.: Measuring curved surfaces for robot vision. Computer **15**(12), 42–54 (1982)
11. Tsai, R.: A versatile camera calibration technique for high-accuracy 3d machine vision metrology using off-the-shelf tv cameras and lenses. IEEE J. Robot. Autom. **3**(4), 323–344 (1987)
12. Burger, W.: Zhang's camera calibration algorithm: in-depth tutorial and implementation. In: HGB16-05, pp. 1–6 (2016)
13. Faugeras, O.: Three-Dimensional Computer Vision: a Geometric Viewpoint. MIT Press, Cambridge (1993)
14. Zhang, Z.: Flexible camera calibration by viewing a plane from unknown orientations. In: Computer Vision, 1999. The Proceedings of the Seventh IEEE International Conference on, vol. 1, pp. 666–673. IEEE (1999)
15. Díaz Iza, H.J.: Valoración de la fiabilidad de los resultados de calibrado de una cámara conociendo sus parámetros extrínsecos. UPV (2018)

Design and Construction of a Prosthetic Finger with Distal Phalanx Amputation

Enrique Mauricio Barreno-Avila[1](✉), Segundo Manuel Espín-Lagos[2], Diego Vinicio Guamanquispe-Vaca[2], Alejandra Marlene Lascano-Moreta[2], Christian Israel Guevara-Morales[2], and Diego Rafael Freire-Romero[3]

[1] Postgraduate Faculty, Universidad Técnica de Manabí, Av. Urbina y Portoviejo, 130105 Portoviejo, Ecuador
ebarreno3907@utm.edu.ec

[2] Faculty of Civil and Mechanical Engineering/Technology and Transfer Center (CTT), Universidad Técnica de Ambato, Av. los Chásquis, 180207 Ambato, Ecuador

[3] Harbert International Establishment S de RL, de las Magnolias S8-216, Quito, Ecuador

Abstract. There is a large number of workers who have suffered an accident at work in most companies is common phalangeal and transfalangeal amputations is the case of the company Dico-Val, where a few years ago a worker suffered an accident where he lost part of the finger specifically the distal phalanx, in this way, obtaining a prosthesis in order to recover the physical capacity of workers becomes imperative; Therefore, the present research of analysis of mechanism alternatives proposes the design of a mechanically driven prosthesis of the distal phalanx of the hand using bibliographic information and analysing different types of prosthesis; comparative analysis of 3D printing materials was performed, a comparative study between design applications and laminators required for the use of 3D printing was performed, different types of prosthesis were analysed focusing on the selection of alternatives of the type of mechanism, which helps the flexion and extension movements, and the type of material for the design parameters. Finally, the results were positive as the computational verification efforts were obtained; concluding that a functional prosthesis was obtained and the selected 3D printing material (PLA) provided sufficient strength for the prosthesis to perform prehension actions.

Keywords: Distal phalanx · Finger prosthesis · Mechanism · Anthropometry · Kinematic analysis

1 Introduction

Various prosthetic hands (or fingers) have been created for amputees who lost a finger or hand in an accident or complication. These prosthetic hands can be can be classified into three types, depending on the pattern and level of amputation of the patient: Type 1 (middle or proximal phalanx), Type 2 (affects only the wrist) and Type 3 (affects the thumb and part of the metacarpals) [1–3].

M. Z. Vizuete et al. (Eds.): CI3 2023, LNNS 1040, pp. 211–224, 2024.
https://doi.org/10.1007/978-3-031-63434-5_16

Because the proximal interphalangeal (PIP) or metacarpophalangeal (MCP) joints may move, prosthetic hands for Type 1 patients have been created as finger modules that employ a linking mechanism powered by the patient's body [4, 5].

The human hand has a wide range of degrees of freedom, a high force-to-weight ratio (including the source of energy), a low factor of form (compactness), and a complex sensory system. Each of the bases of the fingers has two degrees of freedom, with the exception of the thumb, which has five degrees and two joints that allow for flexion and extension motions. The other degree of freedom (GDL) is located in the palm, which curves the surface where the bases of the toes are located [6, 7].

A prosthesis is a device created to replace a missing part of the human body [8]. Its purpose is to improve the user's quality of life by helping him or her to perform tasks for which the missing body part would normally be needed or by serving as an aesthetic accessory [9]. They say that when choosing the type of prosthesis, several factors have to be taken into account, such as the degree of amputation, the functionality and the economic aspect of the device [10].

The aim of prostheses for distal phalangeal amputations is to restore some (as many as possible) of the lost functions, rather than to replace the missing limb, with the primary goal of improving the quality of life of patients who have undergone some form of amputation [11].

However, the development and fabrication of handmade partial prostheses is not a recent development [7].

This paper will depict the design and explain the construction of a finger prosthesis with distal phalanx amputation. As such, this research will focus on determining a mechanical system to simulate a distal phalanx prosthesis with features that can be attached to the residual limb. Furthermore, to design a model of a distal phalanx prosthesis capable of performing prehension movements of the finger and, finally, to simulate the operation of the prosthesis using software. Finally, to build a finger prosthesis for the distal phalanx using 3D printing techniques [12, 13].

2 Methodology

This section discusses the most important considerations to be taken into account when designing a prosthesis of the distal phalanx and the different working mechanisms to subsequently build a prototype containing suitable and efficient materials and also describes the most appropriate methods to carry out the technical research work.

2.1 Materials

Comparisons were made with other prosthesis models with different types of materials and mechanisms, to find possible advantages and disadvantages that help to make an adequate and improved design for the construction [14].

The materials used for the construction of the 3D printed mechanism are listed in Table 1.

Table 1. 3D printing materials.

Material	Durability	Flexibility	Bed temperature	Waste
PLA (Polylactic Acid)	Good	Little or none	25 °C–60 °C	Biodegradable Recyclable
ABS (Acrylonitrile Butadiene Butadiene Styrene)	High	Little or none	90 °C–100 °C	No biodegradable Recyclable
TPU (Thermoplastic Polyurethane)	High	High	25 °C–60 °C	No biodegradable Recyclable
PETG (Polyethylene Terephthalate)	High	Little or none	70 °C–80 °C	No biodegradable
PC (Polycarbonate)	Very High	None	90 °C–105 °C	No biodegradable Recyclable

The design software and laminators required for the use of 3D printing are currently in use due to their characteristics; either learning type or licensing costs [15, 16]. These aspects are shown in Table 2.

Table 2. Comparative study of design applications and laminators required for the use of 3D printers.

Software	Description	Learning Difficulty	Cost of Licences
Tinkercad	Online 3D modelling software, popular for its simplicity and ease of use	Little or none	Free
Blender	Dedicated to modelling, lighting, animation and the creation of three-dimensional graphics	Very High	Free
Fusion 360	3D CAD product modelling and design, manufacturing, electronics and mechanical engineering.	Medium	$495USD/year No Free
SketchUp	Allows design, 3D modelling for video games or filming movies.	Medium	$299USD/year No Free

(*continued*)

Table 2. (*continued*)

Software	Description	Learning Difficulty	Cost of Licences
Simplify 3D	Printing simulation, support structures, multiple extruder optimisation, mesh generation	Medium	$149USD/Year No Free
Ultimaker Cura	The print parameters can be modified and then converted to G-code	Easy	Free
Matter Control	Allows you to design, cut, organise and manage your 3D prints	Easy	Free
Slic3r	Slic3r is a free 3D cutting engine software for 3D printers. It generates G-code from 3D CAD files	Medium	Free

Prostheses manufactured with 3D printing technologies offer many advantages in all aspects of the human being, in contrast to standard prostheses they have some disadvantages in terms of the following factors: functionality, high prices and unaesthetics are shown in Table 3.

Table 3. Comparative study of design applications and laminators required for the use of 3D printers.

	3D printed prosthetics	Standard prosthesis
Lifetime	They last between 7 and 10 years. It does not require a complete replacement of the prosthesis, it is sufficient to replace the part that is malfunctioning or damaged	The entire prosthesis needs to be replaced after 2 to 3 years depending on your physical activity
Availability factor	The work is carried out together with a doctor and a specialist in the use of 3D printing technology. Orders can also be placed with companies specialising in 3D printing	Only upon request
Couplings	It is made to measure according to the patient's needs. Each piece is modelled according to the specifications of the prototype used	Tailor-made, physical therapy is necessary
Price	From $500 to $700 approx	From $5,000 to $10,000 depending on the amputation, material and functionality required by the patient

The particularities of the prototype finger prosthesis are intended to positively impact the needs of the patient, focusing on the grasping functions of the human hand. Since no patients were involved in the realisation of this project, the design specifications below were based on the improvement needs considered significant (operation, cost and maintenance) compared to other types of prostheses marketed in the country.

2.2 Calculation of Anthropometric Measures

Sample for Anthropometric Measurements. The project focuses on people with disabilities related to distal phalanx dissection; however, some people are more at risk due to the industrial activities they perform. Therefore, the sample was taken from a population of 120 workers. The sample was taken from 60 male workers with the aim of finding out the ergonomic measurements of the right hand.

Before extracting the percentile value, it is necessary to obtain several important data such as: range, class mark and interval factor which are directly proportional to the percentile value. This calculation process is seen in the Fig. 1.

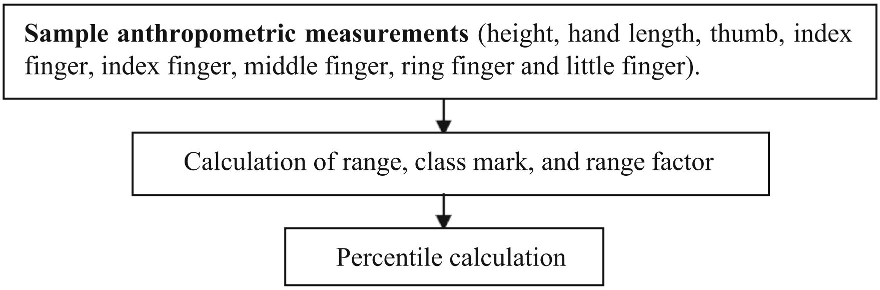

Fig. 1. Anthropometric measurement calculation sequence.

2.3 Selection of the Mechanism

This selection was carried out in three pre-projects. The first one assumes a mechanism when flexing the proximal phalanx, two tensor shafts attached to the sides restrict the movement of the bar behind this phalanx, causing its linear movement in the direction of the joint, as can be seen in Fig. 2.

In the second sketch, the bars are no longer on the sides but on the back of the hand and finger, creating a spider shape in the plan view. As can be seen in Fig. 3.

The third pre-project focuses on the adjustment of the person affected by distal phalanx by means of rings to make them feel comfortable. The aim is to understand the user's perception and to achieve the right position for each joint. This can be seen in Fig. 4.

Finally, the geometry of each phalanx and the anchorage of the prosthesis will be relatively similar for each option, as shown in Fig. 5.

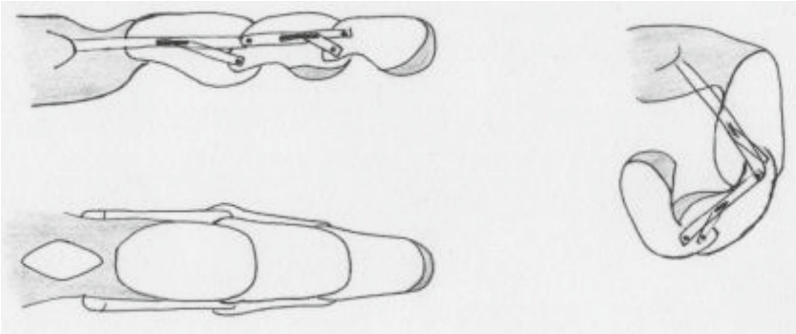

Fig. 2. Free body diagram for the distal phalanx.

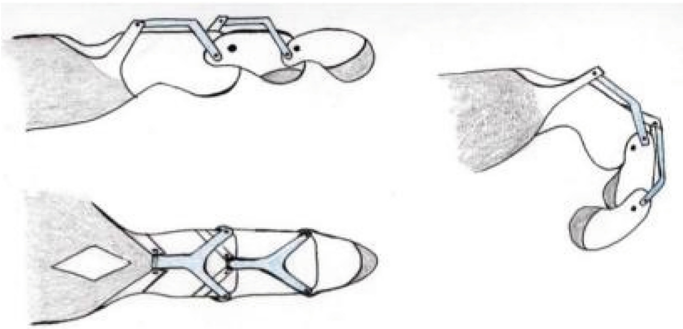

Fig. 3. Y-connection scheme for the distal phalanx

Fig. 4. Suitable dimensions for the prosthesis

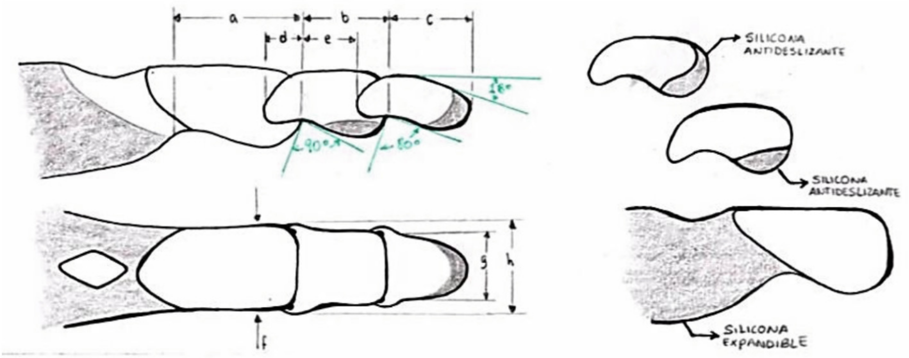

Fig. 5. Genereral scheme for the prosthesis

2.4 Calculation of Forces for Each Phalanx

Free body analysis is structured by body diagram, simulating phalanges as beams, and force of 0.66 kgf or 6.47N.This is illustrated in Fig. 6.

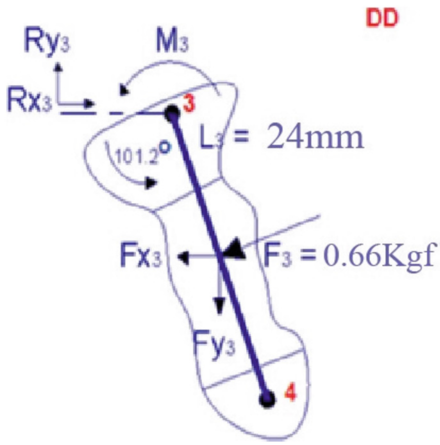

Fig. 6. Free body force diagram for the distal phalanx

The proposed design consists of a four-bar mechanism, activated by the movement of the matrix and the second one generated continuously. The aim is to correct the fourbar mechanism to respect the proposed range of articulation seen in the Fig. 7. The middle finger is chosen for its higher incidence and utility. The design, methodology and calculations can be reproduced for any four-handed finger. The distance $r2$ is the length of the matrix, and the inputs to solve the system are the values of $r2$ and θ2.

Figure 6 shows how the movement of the phalanx coincides with the movement of the previous one, confirming the complete movement of the joint. For this 4-bar mechanism, points “A” and “B” are fixed, by rotating the first arrangement, $r2$, point “D” will move

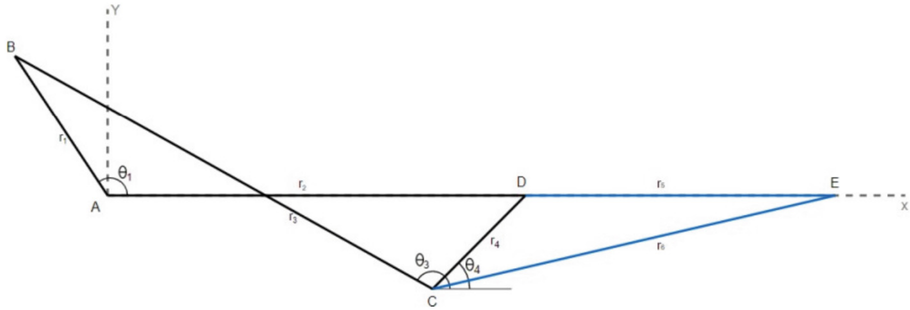

Fig. 7. Schematic diagram of 4-busbar system

an angle θ2; which will produce a rotation of bar *r*4 and it is precisely this rotation that will cause bar *r*5 to no longer be aligned with bar *r*2, that is, by moving the proximal phalanx we have a movement of the middle and distal one.

The distribution of phalanges in the human hand has several positions for grasping objects, and the trajectory is supposed to be circular and have extension movements. The synthesis of the device is presented under two conditions: three trajectory points and two support points (*Q*1 and *Q*2). With these variables, the shape of the link can be defined and compared with ergonomic measurements, as it is seen in the Fig. 8.

The linking mechanism, which consists of the trajectory and its magnitude, is checked by anthropometric measurements. The proximal phalanx is replaced by the transverse mechanism, while the middle and distal phalanges are also part of the link. The link between the middle and distal phalanges is not necessary in the model, as they can be selected in the modelling process by maintaining an angle of inclination of 7 degrees with respect to the neutral axis, as it is seen in the Fig. 9.

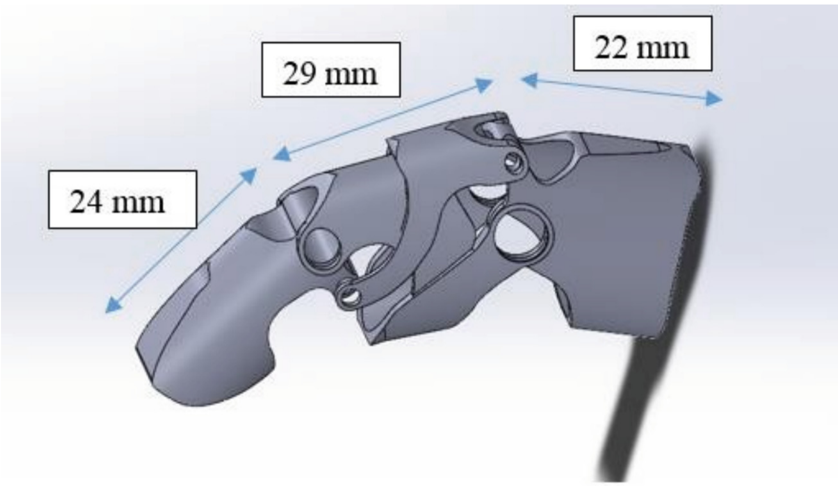

Fig. 8. Distal phalanx mechanism with anthropometric measurements

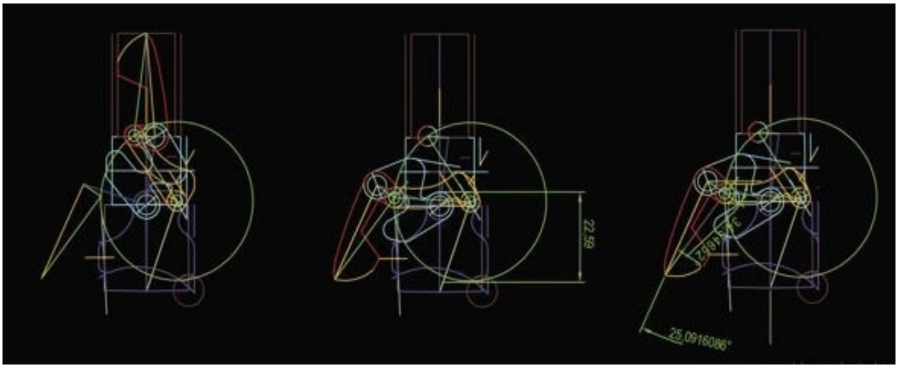

Fig. 9. Movement of the phalanx mechanism

2.5 Movement of the Phalangeal Mechanism.

The values of forces exerted at each support point are shown in Fig. 4. An analysis using 2 mm diameters, from orifices to 23 mm, was used to represent the most important case. Results for Von Mises equivalent effort, displacement, and safety factor for each arrangement are presented. Pines and pines were removed in all pieces to obtain better color gradient images within these regions.

Table 4 presents a detailed report on the accuracy of the convergence analysis, using a method of using smaller elements in possible regions to produce high levels of error.

Table 4. Convergence by Adaptive-h method.

Accuracy level	98%
Accuracy balance	50
Max. no. of loops	5
Mesh thickness application	Disable

The table presents the loads and boundary conditions applied to the proximal link model for the finite element analysis with an accuracy of 98%. Furthermore, It is also necessary to establish mesh parameters so that the analysis can reach a convergence of results seen in the Fig. 10.

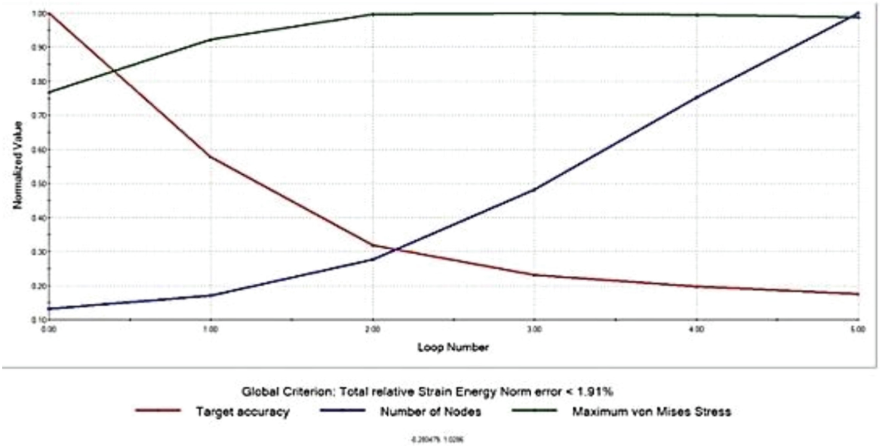

Fig. 10. Convergence of results for the proximal phalanx model.

2.6 Stress Analysis of Components

The stress analysis was carried out in Solidworks software, which had to be analysed part by part since, if it was analysed as an assembly, the software ended up analyzing it as a single part, thus giving misleading results. The values of the forces exerted at each support point were taken from Fig. 4.

Mesh parameters must be established in order for the analysis to get findings that are converging. The details of the mesh characteristics used for the proximal phalanx model are shown in Table 5.

Table 5. Mesh information - Details

Total number of nodes	192286
Total number of elements	122131
Maximum aspect ratio	17,331
% of elements with aspect ratio <3	94,4
The percentage of elements whose aspect ratio is >10	0,118
Percentage of distorted elements	0
Time to complete the grid (hh;mm;ss)	00:00:02

3 Results

3.1 Load Analysis Results

Finally, the results of the finite element analysis with the loads and restraints established on the proximal, medial, and distal phalanx model are obtained. Table 6 presents the results of the Von Mises stress, displacement and deformation analyses from the proximal, medial, and distal links shown in the Fig. 10.

Table 6. Mesh information - Details

Type	Proximal link		Medial link		Distal link	
	Min	Max	Min	Max	Min	Max
Stresses by Von Mises	5,916e + 03N/ m^2 Node: 58395	1,119e + 08N/ m^2 Node: 2013	1,351e + 03N/ m^2 Node: 73564	9,650e + 07N/ m^2 Node: 478	8,197e + 02N/ m^2 Node: 74638	1,085e + 0N/ m^2 Node: 273
URES: Resultant displacements	0,000e + 00m m Node: 58	1,102e + 00m m Node: 29963	–	–	–	–
ESTRN: Equivalent strain	5,408e-06 Element: 8735	9,163e-02 Element: 45240	1,896e-06 Element: 62	6,218e-02 Element: 83654	1,000e-10 Element: 62	9,915e-07 Element: 3562

These analyses were performed element by element, therefore, the most representative analysis for this prosthetic element was obtained for the ESTRN: Equivalent strain deformation analyses results from each element. This can be seen in Fig. 11.

Simulated proximal and medial matrix displacement is 0 to 1 mm, and the maximum displacement values in the distal phalanx are 0.009 mm. The Von Mises stress in the medial and proximal phalanges is higher, at 0.99 MPa and 8.92 MPa, respectively. The results represent less than 1% of the yield strength, but the analysis is performed with a load of 6.47N, which generates reactions not exceeding 12N. To know the maximum strength by tensile analysis, analyse with high load.

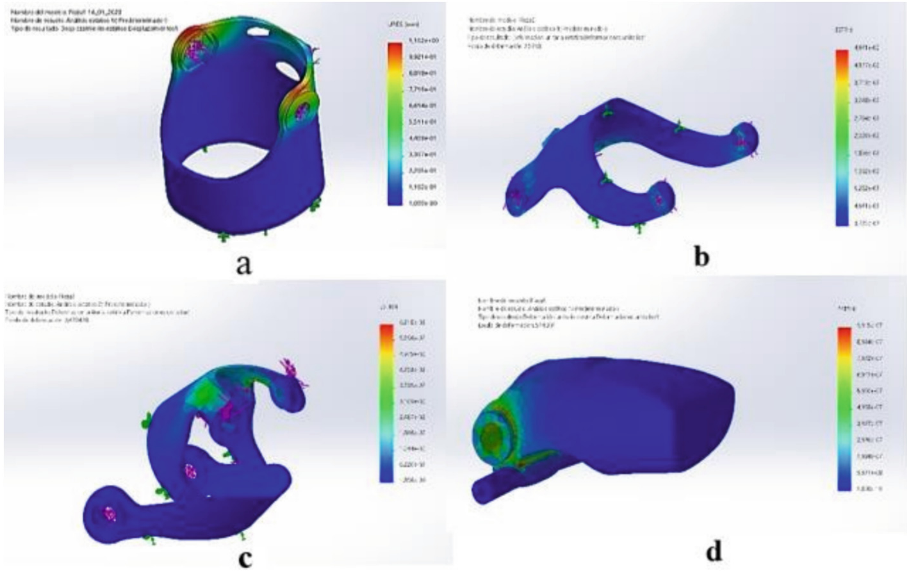

Fig. 11. ESTRN: Equivalent strain deformation analyses results: a) proximal link, b) connecting piece, c) medial link, and d) distal link

Subsequently, from Fig. 10 and Fig. 11 the values are taken to elaborate Table 11 where the comparison of the resulting values for each part with the PLA material is shown (Table 7).

Table 7. Static results generated in Solidworks software for PLA

Von Mises Max. (MPa)				Displacement (mm)			Safety factor Min.		
Phalange	Proximal	Distal	Medial	Proximal	Distal	Medial	Proximal	Distal	Medial
PLA material	0.001	0.965	8.92	0.99	0.000062	0.000647	3	3	3

3.2 Costs Estimation

Table 8 shows the estimated cost values for each part and prosthesis for a distal finger.

Table 8. Estimated cost of finger prosthesis per piece in US dollars.

Part	Printing cost*	Printing time (h)	Filament costs**	Part weight (gr)	Total cost per part***
Proximal	5.54	0.82		0.95	0.74
Medial		0.79		1.14	0.88
Distal		1.6	13.99	4.32	3.36
connecting piece		0.56		0.7	0.54

*The cost of printing on a Stratasys Mojo printer was calculated in USD per hour of printer usage
**Filament cost was evaluated in USD per gram
***Cost per part = printing cost x printing time + filament cost x part weight

Table 9 shows the cost data for printing a prosthesis for an adult.

Table 9. Estimated cost of finger prosthesis per piece in US dollars.

	Costs of production
3D printing	5.54$
Pin and screw	1.74$
Anti-slip silicone	1.00$
Labour	50% surcharge on the total value
Total	16.56$

4 Conclusions

This research aimed to develop a device that can perform flexion and extension movements with an angular amplitude of 32° for the middle phalanx and 30° for the distal phalanx. The device is purely mechanical, requiring no external power source. The four-bar mechanism is influential for designing mechanical prosthetic phalanges, as it responds to prehension, the same movement humans use for certain activities.

Certain 3D printing material (PLA) was selected for its strength, allowing for a cylindrical grip with weights up to 1 kg. The PLA+ case had a maximum Von Mises stress of 9 MPa, representing a safety factor of 3. This technological advance can greatly benefit patients with limb or limb amputation, providing information on designing and manufacturing 3D printed prostheses for patients with distal phalanx damage from work accidents. This low-cost, functional, and aesthetic prosthesis can improve patients' confidence, physical appearance, and self-esteem.

To ensure proper prosthesis manufacturing, consider shrinkage in polymers and a ±2% dimensional tolerance. Explore resistant polymers similar to the human body without affecting user health. Measure cylindrical grip strength and conduct experimental verification with the prosthesis and user for future research.

References

1. Difonzo, E., Zappatore, G., Mantriota, G., Reina, G.: Advances in finger and partial hand prosthetic mechanisms. Robotics **9**(4), Art. n.o 4, dic. (2020). https://doi.org/10.3390/robotics9040080
2. Fajardo, J., Ferman, V., Cardona, D., Maldonado, G., Lemus, A., Rohmer, E.: Galileo hand: an anthropomorphic and affordable upper-limb prosthesis. IEEE Access **8**, 81365–81377 (2020). https://doi.org/10.1109/ACCESS.2020.2990881
3. Ryu, W., Choi, Y.Y., Choi, J., Lee, S.: Development of a lightweight prosthetic hand for patients with amputated fingers. Appl. Sci. **10**(10), Art. n.o 10 (2020). ene. https://doi.org/10.3390/app10103536
4. Koudelkova, Z., et al.: Verification of finger positioning accuracy of an affordable transradial prosthesis. Designs **7**(1) (2023). https://doi.org/10.3390/designs7010014
5. del Piñal, F.: The indications for toe transfer after minor finger injuries. J. Hand Surg. Br **29**(2), 120–129 (2004). https://doi.org/10.1016/j.jhsb.2003.12.004
6. Cuellar, J.S., Plettenburg, D., Zadpoor, A.A., Breedveld, P., Smit, G.: Design of a 3D-printed hand prosthesis featuring articulated bio-inspired fingers. Proc. Inst. Mech. Eng. H **235**(3), 336–345 (2021). https://doi.org/10.1177/0954411920980889
7. Moreira, A.H.J., Queirós, S., Fonseca, J., Rodrigues, P.L., Rodrigues, N.F., Vilaca, J.L.: Real-time hand tracking for rehabilitation and character animation. In: 2014 IEEE 3nd International Conference on Serious Games and Applications for Health (SeGAH), pp. 1–8, May 2014. https://doi.org/10.1109/SeGAH.2014.7067086
8. Bregoli, C., et al.: Osseointegrated metallic implants for finger amputees: a review of the literature. Orthop. Surg. **14**(6), 1019–1033 (2022). https://doi.org/10.1111/os.13296
9. Markus, A.T., Sobczyk, M.R., Perondi, E.A.: Modeling, control, and simulation of a 3-degrees of freedom mechanism actuated by pneumatic artificial muscles for upper limb prosthesis application. J. Mech. Robot. **15**(1) (2023). https://doi.org/10.1115/1.4054084
10. Draycott, J.: Prosthetics and Assistive Technology in Ancient Greece and Rome. Cambridge University Press, Cambridge (2022). https://doi.org/10.1017/9781009168410
11. Cevik, P., Schimmel, M., Yilmaz, B.: New generation CAD-CAM materials for implant-supported definitive frameworks fabricated by using subtractive technologies. Biomed. Res. Int. **2022**, 3074182 (2022). https://doi.org/10.1155/2022/3074182
12. Barreno-Avila, A.F., Monar-Naranjo, M., Barreno-Avila, E.M.: Fusion deposition modeling (FDM) 3D printing parameters correlation: an analysis of different polymers surface roughness. In: IOP Conference Series: Materials Science and Engineering, vol. 1173, no. 1, p. 012071 (2021). ago. https://doi.org/10.1088/1757-899X/1173/1/012071
13. Barreno-Avila, E., Moya-Moya, E., Barreno-Avila, A.: Optimización de parámetros del proceso de corte con láser para Polimetilmetacrilato y Policloruro de vinilo. CienciAmérica **9**(4), 43–50 (2020). dic. https://doi.org/10.33210/ca.v9i4.342
14. Capsi-Morales, P., et al.: Comparison between rigid and soft poly-articulated prosthetic hands in non-expert myo-electric users shows advantages of soft robotics. Sci. Rep. **11**(1), Art. n.o 1, dic. (2021). https://doi.org/10.1038/s41598-021-02562-y
15. Barreno-Avila, E., Moya-Moya, E., Pérez-Salinas, C.: Rice-husk fiber reinforced composite (RFRC) drilling parameters optimization using RSM based desirability function approach. Mater. Today Proc. **49**, 167–174 (2022). ene. https://doi.org/10.1016/j.matpr.2021.07.498
16. Barreno Avila, E., Balladares-Pazmiño, M., Barreno-Avila, A., Espín, S.: Black- berry (Rubus Glaucus) Natural-Fiber Reinforced Polymeric Composites: An Overview of Mechanical Characteristics, pp. 300–315 (2021). https://doi.org/10.1007/978-3-030-72212-8_22

Vehicle Braking and Suspension Systems: Redesign of Preventive and Corrective Maintenance Processes in Automotive Workshops in Southern Quito

Jorge Ramos(✉), Paúl Caza, Cristian Guachamin, Pamela Villarreal, Rodrigo Díaz, Patricio Cruz, and Edisón Criollo

Instituto Tecnológico Universitario Vida Nueva, Quito, Ecuador
jorge.ramos@istvidanueva.edu.ec

Abstract. Mechanical design analysis using technologies such as FEM, CAD (Computer Aided Design) and CAE (Computer Aided Engineering) is a common practice in engineering to determine the behavior of mechanical stresses and deformations in a multifunctional machine. In the specific case of a multifunctional machine for the maintenance of the brake and suspension system of cars, it is important to consider the maximum weight of a car, which in this case is set at 1.5 tons (1.5T). This specification provides a reference for the load and strength analysis of the machine. The use of FEM technology allows a detailed analysis of the structural behavior of the machine. Using the finite element method, the machine is divided into smaller elements to represent its geometry and material. Then, appropriate loading conditions and constraints are applied to simulate the forces and moments acting on the machine during its operation. CAD software is used to create the 3D model of the multifunctional machine, including geometric details, components and assemblies. The CAD model can be imported into the FEM analysis software to generate a finite element mesh and apply load conditions. The CAE software allows the analysis and simulation of the results obtained from the FEM model. It provides tools to visualize and evaluate mechanical force, deformation and other relevant parameters at different points of the machine. It can also help to identify critical areas where high levels of force or deformation occur, allowing design and optimization decisions to be made.

Keywords: Brake system · Suspension system · Vehicle · Maintenance · Pneumatics

1 Introduction

Nowadays, the versatility of the maintenance processes applied to the different systems that make up the automobile is due to the advance of technology both in tools and equipment used by technicians, depending on the useful life of the automobile [1–3]. In the automotive industry market, there is a great variety of this type of resources that seek

M. Z. Vizuete et al. (Eds.): CI3 2023, LNNS 1040, pp. 225–237, 2024.
https://doi.org/10.1007/978-3-031-63434-5_17

to optimize times and reduce labor risk factors [4]; however, the purchasing power of most multi-brand workshops prevents them from having the technologically advanced machines available [5, 6].

The design and simulation processes supported by software of great computation-al capacity help to determine the physical and mechanical behaviors, predicting the maximum and minimum values of forces and displacements to which they will be subjected, which currently minimizes manufacturing costs for companies, but nevertheless, represent components that are difficult to acquire [7]. Under this reality, the manufacture of a multifunctional machine, which gathers the characteristics of several of them in one, turns out to be the answer to this reality, which will allow to have an equipment that provides the reliability to apply preventive and corrective maintenance processes in the brake and suspension systems, minimizing the risk of accidents, optimizing resources and providing high quality technical services [8–11].

2 Brake and Suspension System

Brake and suspension systems are an essential part of the structural geometry of vehicles which, through their components, are exposed to physical and mechanical loads such as exposure to temperature variations, friction, rubbing, shocks, humidity, bending, etc. [12, 13].

Therefore, they must meet a series of mechanical requirements to provide the necessary safety for both the driver and the occupants under any driving conditions, regardless of the different types, marks and models of vehicles in general [14–18].

As mentioned by Bauzá Francisco [19] in his research on braking systems in light vehicles, the objective of the brakes is to stop the car with a very short distance and in the shortest time according to the needs of the driver [20], under the principle of surface friction, dissipating a large amount of energy into the environment in the form of heat [21].

On the other hand, a suspension system has the purpose of absorbing the irregularities of the road on which the vehicle moves and that these are not transmitted to its interior, thus avoiding the corresponding discomfort to its occupants. In this context, Camilo Gavilanes [22] has extended in his research the analysis and importance of the suspension system of light vehicles through a digital model, noting how it influences the behavior under exposure to different loads and how this improves or affects the comfort of its occupants, under simulations in computer programs. It is very common to assimilate the term suspension only to the shock absorbers because they are very important in the geometry of the car and they support the greatest amount of load, however they are a series of elements that achieve the purpose of this system, and it is here where you get the different variants and types of these systems that make up the structure of the car [23, 24].

2.1 Brakes

Mechanical Brake System. This system is used for parking braking (parking brake), using simple mechanisms by a cable by the action of ratchet and locking that has in addition to an adjustment according to the needs of the driver, the following figure shows the characteristics of this system with its constituent components [25] (Fig. 1).

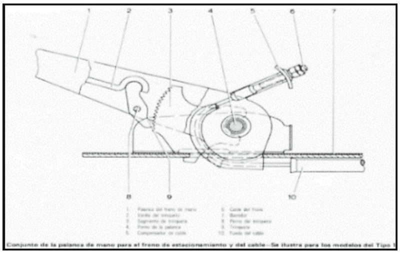

Fig. 1. Mechanical braking or parking system. [2]

Hydraulic Brake System. The brake systems that use a hydraulic fluid and the physical principle of Pascal for its operation are the most used in vehicles today, the hydraulic fluids used in these systems meet the DOT regulations that depend heavily on their boiling points both wet and dry in addition to this they are incompressible that under high loads come to act practically as a solid come to amplify the force transmitted in a circuit formed by pipes that have physical properties to withstand high pressures and temperatures generated in the system [26]; To achieve this multiplication and force is the sequential operation of a series of mechanical components such as a brake servo, a hydraulic pump, pipes, reaching the clamps that through cylinders make contact between sur-faces with the brake discs or pads against the drum, which will depend on the type of circuit that has the vehicle [27].

The figure shows a conventional brake circuit using hydraulic operation (Fig. 2).

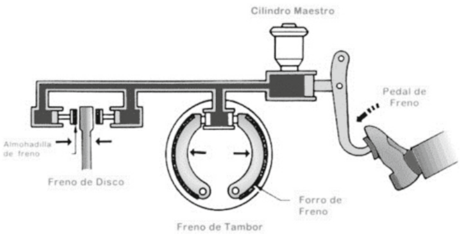

Fig. 2. Hydraulic brake circuit [6]

2.2 Suspension

As mentioned by Mitsubishi Motors [28], the suspension system of a car is a set of elements that have great elasticity capacity with high rates of support deformation loads, which provide stability and control under different driving conditions in addition to providing a high degree of comfort to its occupants. The suspension of an automobile has the function of absorbing the unevenness of the terrain over which it travels.

In a simple suspension system, spring steel linkage components are used in the form of: leaf springs, coil springs, torsion bars, stabilizer bars, etc.

The suspension components must have excellent elastic properties, but their disadvantage is that they have little capacity to absorb mechanical energy, so they can-not be mounted alone in the suspension, requiring the assembly of an element that restrains the oscillations produced in its deformation. The figure shows the constituent elements of a suspension system [29] (Fig. 3).

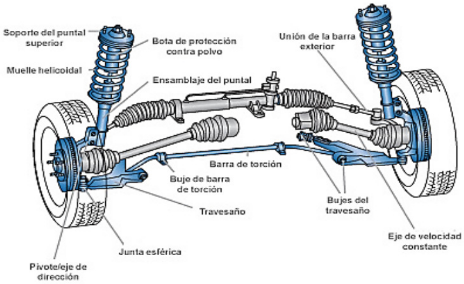

Fig. 3. Suspension system components [8]

2.3 Breakdowns in the Brake and Suspension System

Failures of Brake System. The brake system is extremely important, it is in charge of controlling the dis-placement based on friction, the elements used are subjected to high temperature; each of the components contributes to the reduction of speed. The elements that make up the braking system usually show wear and deterioration that after a certain mileage it is necessary to revise.

The failures that frequently occur are linked to wear and tear, among the most frequent are the following:

- Wear brake linings, whether disc or drum, due to friction between the materials.
- The wear of friction materials such as discs or drums, these materials are made of different materials that withstand high temperatures, however, a thermal shock causes deformation or even breakage.
- High temperature due to emergency braking causes overheating of the friction material, which leads to evaporation of the brake fluid and thus to a constant failure in braking efficiency.
- Low brake fluid level may be an indicator of friction material wear or premature fluid leakage through the brake cylinder seals.
- When the brake pedal is pressed, it moves too low to stop the vehicle, causing a feeling of insecurity.
- The materials produce a scraping noise when braking and even a clanking sound.

- Crystallized brakes due to high temperatures generate a permanent squealing noise or in certain braking conditions.
- The brake servo helps reduce braking force, however, a failure in the vacuum system often results in excessive brake pedal harshness and poor braking.
- Efficiency loss
- Unbalance is another brake system failure generally attributed to the distribution of braking force causing the vehicle to roll sideways under braking.

Suspension System Failures. The elements that make up the suspension system usually show wear and deterioration that must be checked after a certain mileage [30].

The failures that frequently occur are linked to component wear or breakage of elastic elements to the deterioration of shock absorbers. Among the failures considered high risk are the following:

- Excessive elastic oscillation, which increases when passing an irregularity in the roadway and even when crossing a speed breaker.
- The steering axle does not maintain the direction of the vehicle, tending to change the trajectory to one side or the other.
- Irregular tire wear is one of the signs of suspension system failure.
- Suspension squeaking indicates exposure of the articulating elements to oxidizing substances and implies a lack of maintenance and lubrication.
- Excessive vibration of the steering wheel occurs when driving at speeds above 80 km/h.
- If the car is parked and without load, and the car is leaning towards a certain side-wall, an anomaly in the elastic elements is established.
- When going over bumps or irregularities in the road, you feel a strong shock in the area where the tires are located means deterioration in the articulation points of the arms or shock absorbers.
- Shock absorbers with loss of efficiency to reduce the oscillations of the elastic elements.

3 Methodology

According to the question posed at the beginning of the research according to the objective of the study, it has a qualitative approach that allows analyzing the design and modeling of an equipment that allows performing the maintenance of brake and suspension systems of vehicles in multi-brand workshops, considering the operation and applicability that will be developed to generate a redesign of the existing plat-forms, which is intended to reduce the safety risks to which operators are exposed during the various activities, for this reason the following bibliographic, descriptive and experimental research techniques will be used to generate the progress of the investigation [31].

Through corrective and preventive maintenance, it will be possible to analyze the failures or defects that the braking and suspension system of the vehicle may have, by using tools and equipment according to the problems during the inspection of the vehicle.

3.1 Statistical Analysis

The validation of the data under the ANOVA statistical model based on the results obtained in the surveys applied, determine a confidence level of 95% in the feasibility of the construction of this multifunction machine for use in the maintenance process for the brake and suspension systems, for which the following treatments were pro-posed:

Sample 1: PROCESSING 1 (Operation of the mechanical workshop)
Sample 2: PROCESSING 2 (Maintenance of light vehicles)
Sample 3: PROCESSING 3 (Activities performed in the workshop)
Sample 4: PROCESSING 4 (Maintenance of brakes)
Sample 5: PROCESSING 5 (Maintenance of suspension)
Sample 6: PROCESSING 6 (equipment and tools used in the ABC of brakes)
Sample 7: PROCESSING 7 (Tools FOR suspension system maintenance)
Sample 8: PROCESSING 8 (Incidents or occupational accidents have generated)
Sample 1: 45 values in the range de 1,0 a 5,0
Sample 2: 45 values in the range of 5,0 a 15,0
Sample 3: 45 values in the range of 2,0 a 7,0
Sample 4: 45 values in the range of 5,0 a 15,0
Sample 5: 45 values in the range of 2,0 a 7,0
Sample 6: 45 values in the range of 5,0 a 15,0
Sample 7: 45 values in the range of 4,0 a 4,0
Sample 8: 45 values in the range of 2,0 a 2,0

Means with confidence intervals are constructed in such a way that, if two means are equal, their intervals will overlap 95.0% of the time.

It is observed in the graph the intervals selecting, being the representation of the means of and if they are significantly different from others, as it is interpreted in the Table 1.

Table 1. Table of averages with confidence intervals of 95,0%

	Error Est.				
	Cases	*Media*	*(s groups)*	*Lower Limit*	*Upper Limit*
PROCESSING 1	45	4,3111	0,311791	3,87751	4,74472
PROCESSING 2	45	7,3333	0,311791	6,89973	7,76694
PROCESSING 3	45	5,0	0,311791	4,5664	5,4336
PROCESSING 4	45	6,2222	0,311791	5,78862	6,65583
PROCESSING 5	45	5,0	0,311791	4,5664	5,4336
PROCESSING 6	45	6,1111	0,311791	5,67751	6,54472
PROCESSING 7	45	4,0	0,311791	3,5664	4,4336
PROCESSING 8	45	2,0	0,311791	1,5664	2,4336
Total	360	4,9972			

The table shows the means with the 95% confidence level, this method used in the research was used to discriminate between the means is Fisher's Least Significant Difference (LSD) procedure. With this method there is a risk of 5.0% in saying that each pair of means is significantly different, when the real difference is equal to 0.

3.2 Structural Design Analysis

The equipment designed and built is oriented for its application in the automotive field, for preventive and corrective maintenance processes in vehicles [32]. Based on the reference of a vehicle, it is considered that the most relevant part of the multifunction machine represents the structure of the hydraulic lift, which was dimensioned based on its technical characteristics, as shown in Table 2 below.

Table 2. Technical specifications of hydraulic elevator

Technical characteristics of the hydraulic elevator		
Load support	Load support	4 swivel arms, symmetrical
	Capacity	3 T
	length of swivel arm at the front, min	600 mm
	length of swivel arm at the front, max	1070 mm
	length of swivel arm at rear, min	600 mm
	length of swivel arm at rear, max	1070 mm
	distance between supports, max	2300 mm
	Diameter of loading platform	120 mm
Lifting height	lift height	1850 mm
	minimum support height	110 mm
	height adjustment of the silver-loading shape	35 mm
Speed	lifting time	40 s
	descent time (under load)	40 s
Dimensions	dimensions length	2350 mm
	Width	3050 mm
	Height	790 mm
	Input width	2000 mm
	Weight	900 kg

Based on the functionality of the hydraulic elevator, it must withstand loads of great magnitude, so its design and structure must correspond to withstand the influence of these and under different operating conditions.

The simulation of the application of point loads as deformation and displacement on the main arm of the hydraulic elevator is shown below.

In order to generate data on the elevator's behavior under structural loads, the simulation process is generated in the SolidWorks environment, determining stress values and displacements, which are represented in the following figures (Fig. 4).

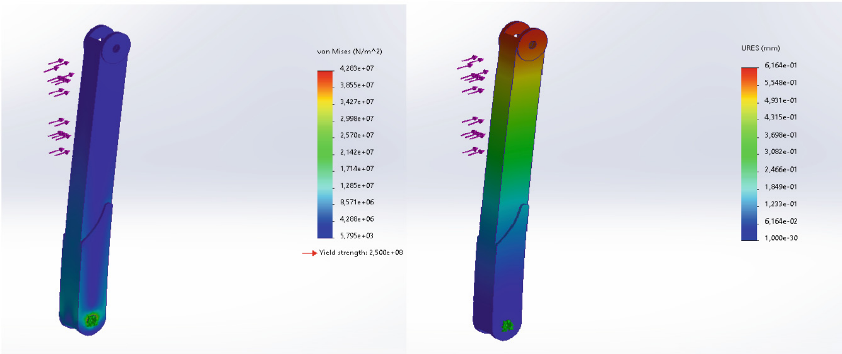

Fig. 4. Simulation of structural loads on the elevator main elevator arm

For the simulation, the point load was applied on the pad considering that it is the element that will support the vehicle load, this magnitude is equivalent to 2500 [N], the same that is distributed over the four pads in the same way.

In the simulation of the extendable arm, the quality of the meshing is another important factor during the finite element analysis, in Fig. 40 you can see the mixed mesh size, which has a value of 0.78 [mm] (Fig. 5).

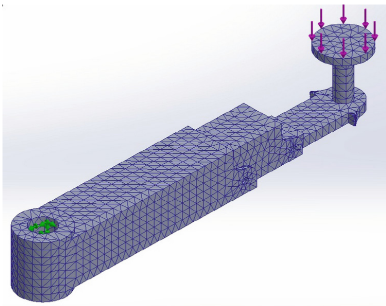

Fig. 5. Application of loads and constraints to analyze the behavior of the main arm pad

Figure 6 shows the results of the maximum and minimum deflection in the analyzed structural system according to the load assigned to the most critical structural element, observing that the maximum deflection is 2.1 [mm] which is a significantly small value in consideration to the magnitude and size of the system, in addition the maximum Von Misses force is presented where a maximum value of 2.51 [N/mm^2] is indicated, if the yield force of the material is considered, it can be observed that the value is lower, so the system cannot fail.

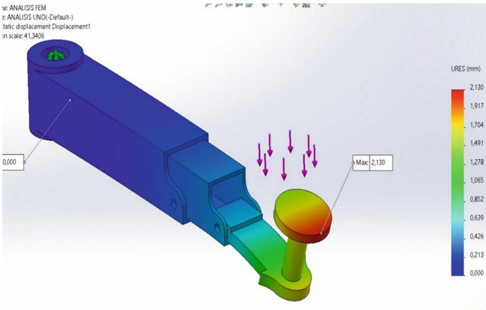

Fig. 6. Von Misses analysis on the extendable arm

3.3 Dimensioning of the Pneumatic and Hydraulic System

Vehicle Lifting System. A hydraulic system is one in which the application of power is generated, transmitted and controlled through the circulation of oil through the circuit. The system as such can be divided into three main parts which are the motor, pump, control valves and cylinder or actuator including the pipes that allow the connection of the system.

Cylinder and pump selection. The parameters to generate the correct selection of the hydraulic equipment are related to three main factors which are:

- Maximum load: 3000 kg
- Stroke: 35.5 cm
- Speed: 6 [cm/s]

In the present investigation the hydraulic cylinder has a stroke of 35.5 cm according to the hydraulic cylinder catalog, based on this selection it can be determined that:

Piston Rod Diameter. The calculation of this parameter is made considering the minimum diameter that the shank must have and is related to the slenderness that the element must have, since it is subjected to compression loads. The safety factor used for this type of buckling case is 3.0.

$$F = \frac{\pi^2 \times I \times E}{L^2 \times n} \tag{1}$$

Considering that it is a circular section, the moment of inertia is calculated with the following equation:

$$I = \frac{D^4 \times \pi}{64} \tag{2}$$

Considering the force of 30,000 [N], with a modulus of elasticity of 206.8 GPa, in conjunction with the force and inertia equations mentioned above, the minimum stem diameter to be considered can be determined.

$$F = \frac{\pi^3 D^4 E}{64 L^2 n} \tag{3}$$

$$D = \sqrt[4]{\frac{64FL^2n}{\pi^3 E}}$$

$$D = \sqrt[4]{\frac{64 \times 30000 \times 355^2 \times 3}{\pi^3 \times 206.8x10^3}}$$

$$D = 336.46\,[\text{mm}]$$

According to the calculation, it can be estimated that the minimum diameter to be considered in the stem to avoid buckling failures is 168 [mm], due to the load that the hydraulic element will support.

Hydraulic System Pressure. For the calculation of the system pressure, it is necessary to know the piston area of the cylinder, considering the previous calculation of the piston diameter, we proceed to calculate it with the following equation:

$$P = \frac{F}{A} \tag{4}$$

$$P = \frac{30000[N]}{\frac{\pi \times (0.2)^2}{4}}$$

$$P = 954.92\,[\text{kPa}]$$

Working Fluid Flow Rate. It is also necessary to know the flow rate to determine the required pump power. For which the data of this parameter is related to the elevation speed and the piston area.

$$Q = A \times V \tag{5}$$

Pump Power. The pump power is determined by knowing the previously calculated flow rate and system pressure, with the following equation:

$$P_{ot} = Q \times P \tag{6}$$

The motor to be selected for the construction of the machine must have a power of 2.5 [hp] with a pump flow rate of 1.88 [m^3/s].

4 Discussion and Results

This section presents the results obtained and analyzed during the research, in which it has been possible to study elements that are part of a multifunctional machine used in the maintenance of the brake and suspension system as a preventive part of the mechanical, ergonomic and physical risks for the operators.

In the process of design and construction of the multifunctional machine for the maintenance of the brake and suspension system, an adequate selection of materials and forming processes was carried out, considering that they comply with the technical requirements that allow the handling of the vehicle, which allows reducing accidents or damages caused to the operator's health.

Of the elements that make up the machine, it was determined that the cushion is the most critical component, since it will support the load of the vehicle, so after per-forming a finite element analysis it was observed that the maximum and minimum deflection in the structural system analyzed in terms of the load assigned to the most critical structural element, noting that the maximum deflection is 2.1.

Taking into account the conditions to which the machine will be subjected, which were calculated through finite element analysis, observing the zones of influence and load distribution in the arms that will support the weight of the vehicle during the revision and maintenance of the brake and suspension system.

A key factor in the design of the machine was the ease with which the operator can manipulate the equipment and tools required in the process of maintaining the brakes and suspension of a vehicle, reducing the time factor in the repair of the systems.

5 Conclusions

In this research, a study of the mechanical elements that constitute a multifunctional machine was carried out from the mechanical and safety point of view for the operator in unauthorized mechanical workshops, in which production, work times, maintenance and ergonomic, mechanical and physical risks to which the operator is ex-posed were compared. According to the study carried out, it was identified that the workshops are looking for the implementation of equipment that allows them to better handle the repair and maintenance of the vehicle's brake and suspension system.

Through mechanical design analysis using FEM, CAD and CAE technology, it is possible to evaluate the behavior of mechanical forces and deformations in a multi-functional machine for the maintenance of the brake and suspension system of automobiles. This helps to ensure that the machine is strong and safe enough to withstand the expected loads during operation, considering the maximum weight of a car of 1.5 tons.

It is recommended that future research be carried out to analyze the design of new components that will allow a preventive maintenance analysis of conventional and automatic transmission systems, steering systems and complementary engine systems, taking into account automation and control technology.

References

1. Bonavía, T., Marín, J.A.: An empirical study of lean production in the ceramic tile industry in Spain. Int. J. Oper. Manage. (2006)
2. Bouhmala, J.: Los secretos de una buena suspensión | AMORTIAUTOS. AMORTIAUTOS SAS (2020). https://amortiautos.com/los-secretos-una-buena-suspension/
3. Braglia, M., Carmignani, G., Zammori, F.: A new value stream mapping approach for complex production systems. Int. J. Prod. (2006)
4. Brembo. Mantenimiento del sistema de frenos (n.d.). https://www.brembo.com/es/automóviles/aftermarket/conductores/manutenzione-impianto-frenante. Accessed 20 Mar 2022

5. Gavilánez Endara, C.: Análisis e Importancia de Sistema de Suspensión de Ve-hículos Livianos Mediante Modelo Digital. UNIVERSIDAD SAN FRANCISCO DE QUITO USFQ (2016)
6. Giraldo Gutiérrez, C.A.: Control Predictivo con Restricciones de Suspensión Vehicular Activa. https://www.researchgate.net/publication/320981475_Control_predictivo_con_restricciones_de_suspension_vehicular_activa. Accessed 20 Mar 2022
7. Crabill, J., et al.: Production operations level transition-tolean description manual. Center for Technology, Policy, and Industrial Development. Massachusetts Institute of Technology (2000)
8. Bauzá Fernández, F.J.: Estudio del sistema de frenado en los vehículos ligeros (turismos). Universidad Técnica de Cataluña (2018)
9. García León, R.A., Acosta Pérez, M.A., Flórez Solano, E.: Análisis del compor-tamiento de los frenos de disco de los vehículos a partir de la aceleración del proceso de cor-rosión. Tecnura **19**(45), 53–63 (2015). https://doi.org/10.14483/UDISTRITAL.JOUR.TECNURA.2015.3.A04
10. Gómez, J.: Mantenimiento preventivo de suspensión. Doctor Auto. https://www.doctorauto.com.mx/2019/06/17/mantenimiento-preventivo-del-sistema-de-la-suspension-del-automovil/
11. Rodriguez Pinzon, H.R.: Consideraciones cinematicas y dinamicas para el desarrollo de control a un sistema de suspensión. https://www.researchgate.net/publication/328589913_CONSIDERACIONES_CINEMATICAS_Y_DINAMICAS_PARA_EL_DESARROLLO_DE_CONTROL_A_UN_SISTEMA_DE_SUSPENSION. Accessed 20 Mar 2019
12. Rodríguez Pinzón, H.R.: Diseño y construcción de un sistema para medir el desgaste en forros de frenos de disco. https://www.researchgate.net/publication/332725197_Diseno_y_construccion_de_un_sistema_para_medir_desgaste_en_forros_de_frenos_de_disco. Accessed 20 Mar 2022
13. Correa-Arciniegas, J.: Mapas mecánicos y dinámicos de frenos de disco bajo diferentes condiciones de operación. https://www.researchgate.net/publication/357438518_Propuesta_del_sistema_de_frenos_para_un_vehiculo_Baja_SAE. Accessed 20 Mar 2022
14. Correa-Arciniegas, J.: Propuesta de sistema de frenos para un vehículo Baja SAE. https://www.researchgate.net/publication/357438518_Propuesta_del_sistema_de_frenos_para_un_vehiculo_Baja_SAE. Accessed 20 Mar 2022
15. Rivera-López, J.E.: Análisis térmico y fluido dinámico de un freno de disco automotriz conpilares de ventilación tipo aerodinámico. https://www.researchgate.net/publication/337614379_Thermal_and_fluiddynamic_analysis_of_an_automotive_disc_brake_with_ventilation_pillars_aerodynamic_type. Accessed 20 Mar 2022
16. Gallardo, J.M.: Investigación de la rotura en servicio de amortiguadores de automóviles (2016). https://www.researchgate.net/publication/242230029_INVESTIGACION_DE_LA_ROTURA_EN_SERVICIO_DE_AMORTIGUADORES_DE_AUTOMOVILES. Accessed 20 Mar 2022
17. Obregón Sánchez, L.M.: Diseño y construcción de un módulo didáctico de en-trenamiento para frenos de aire de camiones. UNIVERSIDAD INTERNACIONAL DEL ECUADOR FACULTAD DE INGENIERÍA AUTOMOTRIZ (2013)
18. Mecánica Automotriz, F.: Reparación del sistema de frenos convencionales y ABS (2018). www.mecanica-facil.com
19. Mantenimiento preventivo del sistema de frenos. El Universo. https://www.eluniverso.com/entretenimiento/2018/11/21/nota/7060449/frene-embrague-adecuadamente/
20. Mendez Cuello, A., Velez Cely, M., Monar Monar, W.: Diseño del sistema de freno regenerativo de automóviles híbridos. Rev. Politécnica **37**(2), 10 (2016). https://revistapolitecnica.epn.edu.ec/ojs2/index.php/revista_politecnica2/article/view/451/pdf

21. Trejo, O.: Sistema de inferencia difuso de estructura variable para el control de suspensión mecánica (2016). https://www.researchgate.net/publication/343135582_Sistema_de_inferencia_difuso_de_estructura_variable_para_el_contro_de_suspension_mecanica
22. Padilla, L.: Elaboración de hojas de operación estándar para el mantenimiento del ser-vicio mayor de una empresa automotriz del Sur de Sonora (2018). http://www.ecorfan.org/republicofperu/research_journals/Revista_de_Ingenieria_Industrial/vol2num6/Revista_de_Ingenier%C3%ADa_Industrial_V2_N6_1.pdf
23. Razmi-Ishak, M., Abu-Bakar, A.R., Belhocine, A., Mohd-Taib, J., Wan-Omar, W.Z.: Brake torque analysis of fully mechanical parking brake system: theoretical and experimental approach. Ingeniería Invest. Tecnol. **19**(1), 37–49 (2018). https://doi.org/10.22201/fi.25940732e.2018.19n1.004
24. García-León, R.A.: Análisis del caudal en un disco de freno automo-triz con álabes de ventilación tipo NACA 66-209, utilizando velocimetría por imágenes de partículas (2019). https://www.researchgate.net/publication/342734012_Analisis_metalografico_y_materiales_de_los_frenos_de_disco/related. Accessed 20 Mar 2019
25. García-León, R.A.: Estudio y análisis térmico del diseño de formas de paletas para discos de freno en automoción industria (2020). https://www.researchgate.net/publication/342734012_Analisis_metalografico_y_materiales_de_los_frenos_de_disco/related
26. García-León, R.A.: Análisis de los principales mecanismos de falla en tres frenos de disco automotrices (2020). https://www.researchgate.net/publication/357114147_ANALISIS_DE_LOS_PRINCIPALES_MECANISMOS_DE_FALLA_EN_TRES_FRENOS_DE_DISCO_AUTOMOTRICES
27. Zamora, R.S.: Material de friccion sin asbesto para frenos y embragues con compuesto de baritina (2022). https://www.researchgate.net/publication/287215845_Material_de_friccion_sin_asbesto_para_frenos_y_embragues_con_compuesto_de_baritina
28. Simulación, A.D.: Manual de Mantenimiento de Frenos. Manual De Metodo-logia Da Pesquisa Aplicada À Educação **6**, 1–56 (2019)
29. Systems, B.: What is a braking system ? How does a braking system work ? 1 (n.d.)
30. TEOJAMA COMERCIAL. Recomendaciones para el mantenimiento de la Sus-pensión de Camiones. Blog - Teojama (2018). https://www.teojama.com/blog/recomendaciones-mantenimiento-la-suspension-cami-ones/#:%7E:text=Revisar%20el%20engrase%20de%20chasis,y%20balanceo%20cada%2010.000%20kil%C3%B3metros
31. Jayaraj, T.: Diseño optimizado para freno magnetorreológico usando métodos DOE (2015). https://www.researchgate.net/publication/326106876_Amortiguadores_inteligentes_y_reologia
32. Yogesh Kumar, Estudio sobre el Comportamiento Dinámico del Sistema de Suspensión Wishbone (2022). https://www.researchgate.net/publication/258683057_Study_on_Dynamic_Behaviour_of_Wishbone_Suspension_System

Cylinder Head Tuning of a Spark-Ignition Engine and Validation on a Chassis Dynamometer to Verify Its Power

Jose Vicente Manopanta Aigaje[1,2](✉), Jonathan Daniel Hurtado Muñoz[2], Jefferson Marcelo Peringueza Chuquizan[2], and Fausto Neptali Oyasa Sepa[2,3]

[1] Universidad Internacional SEK, Quito, Ecuador
vmanopanta@tecnologicoismac.edu.ec
[2] Instituto Tecnológico Universitario Ismac, Tumbaco, Ecuador
[3] Universidad Israel, Quito, Ecuador

Abstract. The research is motivated by the high levels of contamination and lack of efficiency, especially due to the exponentially increasing vehicle fleet in Ecuador, the proposal is to modify several components and characteristics of the cylinder head such as the combustion chamber, the valve mechanism system, the intake and exhaust system of the spark-ignition engine, which will result in changes to the power of the engine and thus the vehicle and this was measured in the chassis dynamometer since this result can be obtained directly through the vehicle. With the present research you can achieve a bulwark of machining in the elements of the engine where the calculated theory is reflected in practice and in the chip starting that will be given to the cylinder head linking fuel consumption and compression ratio, the engines look good or bad according to the power sought experimentally. In conclusion, from the measurements made, in general there is an increase in the power performance of 30.08% with the modifications and specifically at the maximum power at 4400 rpm, measured in the chassis dynamometer, which were the result of the modifications of the cylinder head of the engine with respect to the standard cylinder head of the vehicle's engine.

Keywords: Cylinder head tuning · Spark-ignition engine · Compression ratio · Power · Chassis dynamometer

1 Introduction

A small portion of vehicles are replaced by new models every year. Standards for passenger cars, for example, now cover almost two-thirds of their overall energy use, up from 50% a decade ago. For some developing countries that have not yet established standards, the import of second-hand vehicles is an important feature of their market with many of these imports no longer meeting the standards of the exporting country [1].

M. Z. Vizuete et al. (Eds.): CI3 2023, LNNS 1040, pp. 238–250, 2024.
https://doi.org/10.1007/978-3-031-63434-5_18

Each country's economy is directly or indirectly dependent on fossil fuels, gradually shrinking through massive industrialization, transportation and population growth [2]. In addition, concerns about climate imbalances, global warming and the commitments made by developed countries to improve the security of energy supply and encourage the use of renewable energies are just some of the factors that make biodiesel an interesting alternative [3].

The addition of bridges and bores in the cylinder head proves to be very effective as it considerably reduces emissions [4]. In addition, a slight change in the configuration of the bridges and bores can change the flow directions and patterns and vary the way the gases react, which can further reduce emissions [5, 6]. The effect of speed, load, and blend ratio on the competence of a multi-cylinder indirect injecting diesel power unit was investigated by Adam et al. (2015), using statistical tool, Box-Behnken design (BBD) based on RSM to predict and assess their net effects on the responses, such as torque, power, BSFC, and BTE. Blends of 5–20% volume of BDF (prepared from a mixture of palm and rubber seed oils) to diesel fuel were prepared Load was found to be the most effective input, both individually and in combination, in contrast to the blending and speed variables [7]. A strong influence of speed on the results was observed, except for torque, while their combined effect was not vital, except for BSFC and BTE [8].

Sha et al. (2015) [9] experimentally investigated the effects of pre-chamber volume and nozzle diameter on the resultant ignition characteristics. It was found that a larger pre-chamber provides higher ignition energy, which results in shortened flame development angle and combustion duration. At a given pre-chamber volume, nozzle diameter mainly affects the combustion duration [10].

The research was initiated in response to the high levels of contamination and lack of efficiency, especially in the automotive fleet [11], due to the scarce energetic use of organic materials as energy sources that guarantee an optimal performance in internal combustion engines. The main objective of this project is the modification of the cylinder head of a spark-ignition engine and validation in a chassis dynamometer for the verification of its developed power after the adjustments in these variables.

2 Method

2.1 Applied Test Vehicle

For the experimental investigations, a Citroën 1.4 Standard K2d 4-cylinder 1,360 cm^3 gasoline engine, with indirect injection in the intake manifold, naturally aspirated and equipped with a conventional three-way catalytic converter from 1998 was used; selected because it is one of the most sold automobiles in ecuador in those years [12]. Table 1 describes the specifications of the vehicle.

Table 1. Citroën 1.4 Standard K2d Technical Data Sheet

Characteristics	Units
Make	Citroën
Model	Saxo
Year	1998
Compression Ratio	9.3/1
Torque	114 Nm
Horsepower	75 CV
Bore	75 mm
Top Speed	164 km/h
Acceleration, 0–100 km/h	14.8 s
Max Power	76 CV DIN AT 5800 rpm
Displacement	1360 cm^3
Max Torque	111 Nm DIN AT 3400 rpm
Valves	8 valves
Fuel	Gasoline
Engine	Inline four
Firing order	1-3-4-2

2.2 Characteristics of the Cylinder Head for the Combustion Chamber Area

The design of the cylinder head is simple, easy to reproduce and install [13]; given the intake stroke, the mixture reaches the cylinder with little speed, the turbulence is almost null, the combustion is slow and prone to detonation due to the long length of the flame [14]. Figure 1 shows the measurement of the combustion chamber volume, as the main value in this tuning process, in addition to the calculation of the engine compression ratio measured, applying the following equations.

Piston volume measurement

$$\begin{gathered} Piston\,Vol. = 10cm^3 \\ Compressed\,Vol. = \text{Piston } Vol. + Chamber\,Vol. + \text{Gasket Vol.} \\ Compressed\,Vol. = 10 + 25.5 + 6.87 = 42.37\,\text{cm}^3 \end{gathered} \tag{1}$$

Calculation of the compression ratio of the engine

$$\begin{gathered} Rc = \frac{Compressed\,Vol. + Displacement\,Vol.}{Compressed\,Vol.} \\ Rc = \frac{42.37 + 343.67}{42.37} = 9.11\,a\,1 \\ Chamber\,Vol. = 25.5\,\text{cm}^3 \end{gathered} \tag{2}$$

As a consequence of the calculations, we obtain the tuned or modified compression ratio that will show the results of this experiment [15], as described in Table 2.

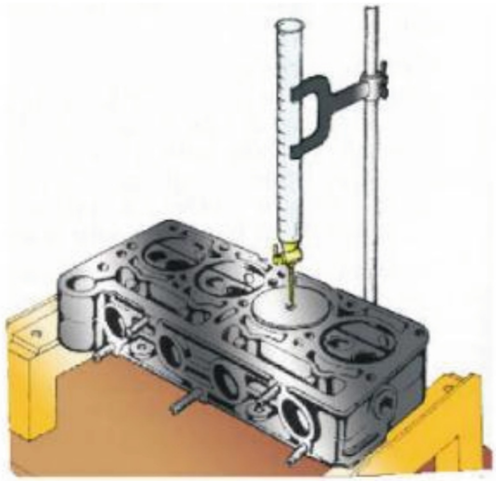

Fig. 1. Measurement of the combustion chamber volume

Table 2. Compression Ratio Calculations

	Engine without Modification	Engine with Modification
Displacement Vol.	343.67 cm^3	343.67 cm^3
Gasket Vol.	6.87 cm^3	6.87 cm^3
Chamber Vol.	25.5 cm^3	24.8 cm^3
Piston Vol.	10 cm^3	10 cm^3
Compressed Vol.	42.37 cm^3	41.67 cm^3
Compression Ratio	9.11 : 1	9.25 : 1

2.3 Valve Mechanism System

The valve system performs an exhaustive work in the recirculation of gases and manages a proper combustion. Table 3 shows several characteristics of the valves both in standard form and in modified or tuned form applied in the study proposed in this research [16].

Table 3. Valve System

	Standard Condition	Modified Ccndition
Intake Valve Measurement		
Retainer Diameter	36.5 mm	36.5 mm
Valve Length	112.69 mm	112.69 mm
Valve Stem	0.7 mm	0.6 mm
Valve Seat	45°	30°
Exhaust Valve Measurement		
Retainer Diameter	29.2 mm	29.2 mm
Valve Length	112.5 mm	112.5 mm
Valve Stem	0.7 mm	0.6 mm
Valve Seat	45°	30°

2.4 Intake and Exhaust System of the Spark-Ignition Engine

The cylinder head has several ducts that are mainly useful for the recirculation of gases and managing a proper combustion. Table 4 shows several features measured for both standard form and modified or tuned form that characterize the study proposed in this research [17]. In addition, Figs. 2, 3 and 4 show the measurement processes established to obtain the data in the cylinder head [18].

Fig. 2. Measurement of the exhaust manifold nozzle diameter

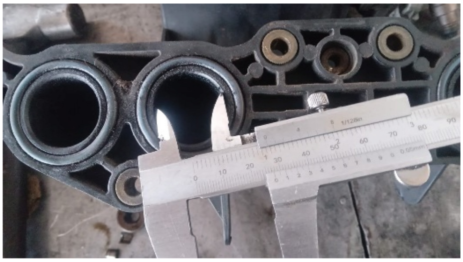

Fig. 3. Measurement of the intake manifold nozzle diameter

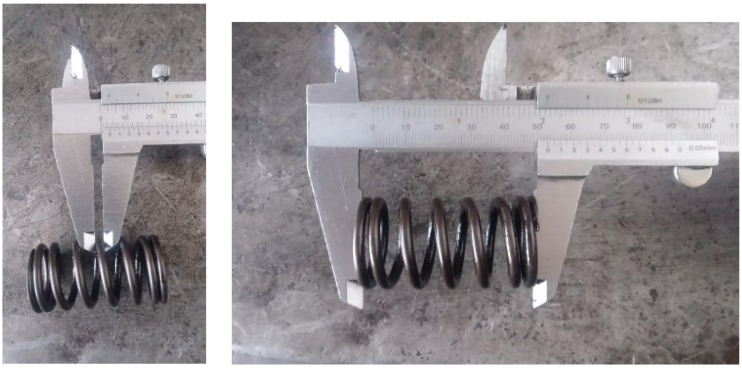

Fig. 4. Measurement of the cylinder head springs

Table 4. Gas recirculation cylinder head ducts and valve springs

	Engine without Modification			Engine with Modification		
Cylinder head intake nozzles						
	Diameter (mm)	Length (cm)	Volume (cm^3)	Diameter (mm)	Length (cm)	Volume (cm^3)
CYLINDER 1	29.40	8.5	66.5	31	8.5	67.2
CYLINDER 2	29.40	8.5	66.5	31	8.5	67.2
CYLINDER 3	29.40	8.5	66.5	31	8.5	67.2
CYLINDER 4	29.40	8.5	66.5	31	8.5	67.2
Cylinder head exhaust nozzles						
	Diameter (mm)	Length (cm)	Volume (cm^3)	Diameter (mm)	Length (cm)	Volume (cm^3)
CYLINDER 1	28.0	6	45.0	33	6	47.0

(*continued*)

Table 4. (*continued*)

	Engine without Modification			Engine with Modification		
CYLINDER 2	28.0	6	45.0	33	6	47.0
CYLINDER 3	28.0	6	45.0	33	6	47.0
CYLINDER 4	28.0	6	45.0	33	6	47.0
Cylinder head springs						
	Diameter (mm)	Length (mm)	Thickness (mm)	Diameter (mm)	Length (mm)	Thickness (mm)
CYLINDER 1	28.80	52.10	3.60	32.40	47.30	4.50
CYLINDER 2	28.80	52.10	3.60	32.40	47.30	4.50
CYLINDER 3	28.80	52.10	3.60	32.40	47.30	4.50
CYLINDER 4	28.80	52.10	3.60	32.40	47.30	4.50

The measurements of the manifold nozzles are relevant to observe its modification as a consequence of the new performance to be obtained in the vehicle's engine, according to Table 5.

Table 5. Manifold nozzles and cylinder head height

	Engine without Modification	Engine with Modification
Measurement of the cylinder head height		
	mm	mm
Height	111.2	110.4
Measurement of the exhaust manifold nozzle diameter		
	Diameter (mm)	Diameter (mm)
CYLINDER 1	31	34.80
CYLINDER 2	31	34.80
CYLINDER 3	31	34.80
CYLINDER 4	31	34.80
Measurement of the intake manifold nozzle diameter		
	Diameter (mm)	Diameter (mm)
CYLINDER 1	27.5	27.5

(*continued*)

Table 5. (*continued*)

	Engine without Modification	Engine with Modification
CYLINDER 2	27.5	27.5
CYLINDER 3	27.5	27.5
CYLINDER 4	27.5	27.5

2.5 Determination of the Developed Power

The main test in this study is the chassis dynamometer, where the chassis dynamometer SAENZ PERFORMANCE INERTIAL CHASSIS DYNOS-N 08-19 was used, which allows simulating a speed profile as a function of time to perform dynamic tests on diesel and gasoline vehicles [19]. It allows to upload different test cycles of the different legislations or self-designed cycles in order to be able to determine exactly the amounts of developed power. Figure 5 shows schematically the model of the testing process performed on the vehicles. The torque and power tests were performed on the chassis dynamometer [20].

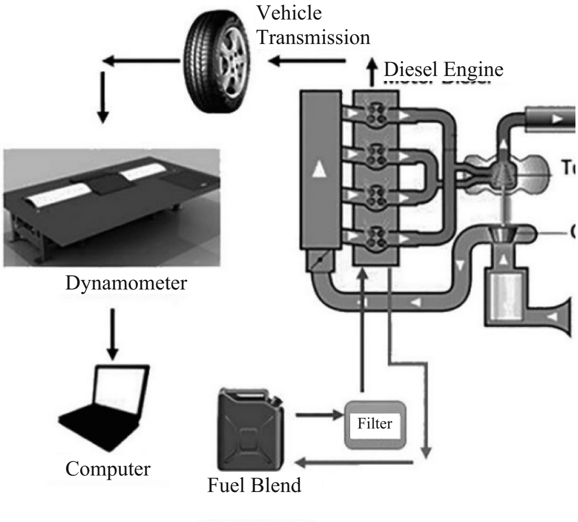

Fig. 5. Test setup on the chassis dynamometer

Power and torque test protocol. The evaluation of the performance obtained on the output shaft through the dynamometer was performed under ISO 1585 and ISO 3173 standards [3]; following the test protocol: verify that the diameter of the wheels is equal to or greater than 13 rim and that they comply with the weight capacity established by the manufacturer; place the test vehicle on the dynamometer rollers; verify that the tire tread is free of stones; lower the lift and leave the wheels resting on the rollers;

check the alignment of the wheel assembly with respect to the dynamometer rollers by rotating the wheels at a maximum speed of 20 km/h; secure the vehicle with straps to prevent it from slipping off the rollers; check the safety of the test area; enter the technical data concerning the vehicle to be tested into the software; check the gear and transmission ratio of the unit, which must be 1:1; make sure that the engine temperature is the normal operating temperature, otherwise it must pass an engine warm-up period to reach such temperature; start the cooling fan of the dynamometer; start the measurement test; accelerate the vehicle with the pedal fully depressed in the test gear until reaching the desired speed called "rpm cut" (4500–6000 rpm); when the "rpm cut" has been reached, depress the clutch, leaving the gear engaged. The dynamometer decelerates to a stop [21].

3 Results

3.1 Vehicle Power Without Modification of the Cylinder Head

The power parameters generated by the engine of the Citroën 1.4 vehicle with the different tests. The static test with load was carried out, using the chassis dynamometer, under the ISO 1585 Standard, performing three tests for each case and obtaining the result to be evaluated. Figure 6 shows the evolution of the tests on the equipment [22]. Here are the results of the measurement of the power obtained for the vehicle with the dynamometer. The test was run three times in a row using premium gasoline. In this test, it can be observed that the curves generated do not show a major difference according to the values.

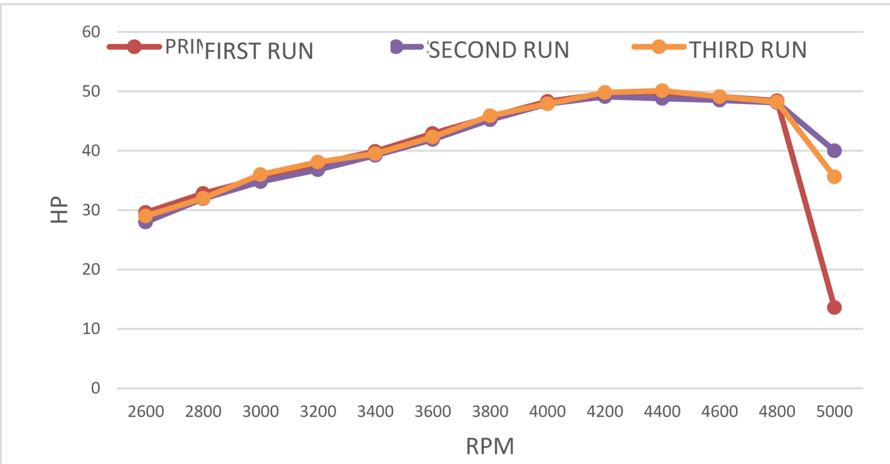

Fig. 6. Vehicle power without the cylinder head modification during three runs

3.2 Vehicle Power with the Cylinder Head Modification

The power parameters generated by the engine of the Citroën 1.4 vehicle with the different tests. The static test with load was carried out, using the chassis dynamometer, under the ISO 1585 Standard, performing three tests for each case and obtaining the result to be evaluated [23]. Figure 7 shows the power curves obtained with the dynamometer. The test was run three times in a row using premium gasoline. In addition, it can be observed that there is not a major difference among the values [24].

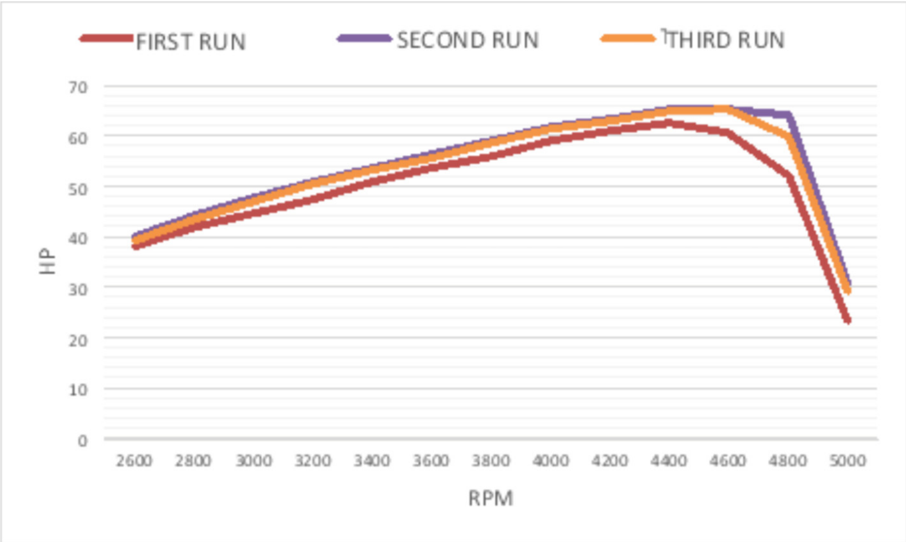

Fig. 7. Vehicle power with the cylinder head modification during three runs

3.3 Discussion of the Results on the Obtained Power

The tests carried out and the values obtained are used to analyze the behavior of the vehicle, which will be used to develop the pertinent analysis regarding the performance of the engine. We will proceed as follows, working with the average power values obtained [25]. Figure 8 shows the power variation differences for the standard working tests and the cylinder head modification, clearly evidenced in the chassis dynamometer.

It is then established according to the measurements made that there is an increase of 30.08% in the performance at 4400 rpm with respect to the engine power with the modifications of the cylinder head, and it is clearly seen in the comparative graph the difference between the performance of power before and after the modifications of the cylinder head. All the tests were carried out with the premium gasoline that is commercialized in the country [26]. Several authors show similar data, confirming the increased engine efficiency [5].

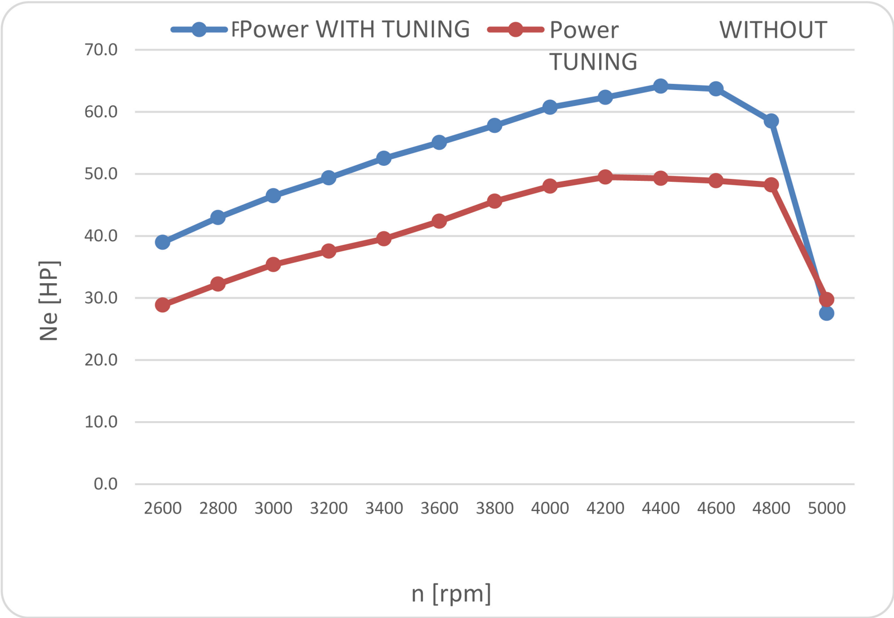

Fig. 8. Developed powers before and after the engine cylinder head tuning.

4 Conclusions

In conclusion, a research analysis is made about the modifications in the engine cylinder head to find the best configuration and the best performance. In the studies analyzed, it has been found that the valve, nozzles and ducts of the cylinder head are truly relevant and have the greatest influence on the engine performance.

The measurements performed show an increase in power performance in general during the course of the engine operation from idle to maximum power. Therefore, with the modifications and specifically at the maximum power at 4400 rpm, an increase of 30.08% measured in the chassis dynamometer was observed as a result of the modifications of the engine cylinder head with respect to the standard cylinder head of the vehicle's engine.

References

1. Cozzi, L., et al.: World energy outlook 2020, pp. 1–461. International Energy Agency Paris, France (2020)
2. Afzal, S., et al.: Exhaust emission profiling of fatty acid methyl esters and NO x control studies using selective synthetic and natural additives. Clean Technol. Environ. Policy **20**, 589–601 (2018)
3. Rocha-Hoyos, J.C., Llanes-Cedeño, E.A., Celi-Ortega, S.F., Peralta-Zurita, D.C.: Efecto de la Adición de Biodiésel en el Rendimiento y la Opacidad de un Motor Diésel. Inf. Tecnol. **30**(3), 137–146 (2019)

4. Menaca, R., Bedoya-Caro, I.D.: Una revisión del uso del hidrógeno en motores de encendido por compresión (diésel) y un análisis de su posible uso en motores duales en Colombia. Rev. UIS Ing. **21**(3), 33–54 (2022)
5. Indudhar, M.R., Banapurmath, N.R., Rajulu, K.G., Patil, A.Y., Javed, S., Khan, T.M.Y.: Optimization of piston grooves, bridges on cylinder head, and inlet valve masking of home-fueled diesel engine by response surface methodology. Sustainability **13**(20), 11411 (2021)
6. Ogden, J.M., Williams, R.H., Larson, E.D.: Societal lifecycle costs of cars with alternative fuels/engines. Energy Policy **32**(1), 7–27 (2004)
7. Shrivastava, P., Verma, T.N., Samuel, O.D., Pugazhendhi, A.: An experimental investigation on engine characteristics, cost and energy analysis of CI engine fuelled with Roselle, Karanja biodiesel and its blends. Fuel **275**, 117891 (2020)
8. Adam, I.K., Aziz, A.R.A., Yusup, S.: Determination of diesel engine performance fueled biodiesel (rubber seed/palm oil mixture) diesel blend. Int. J. Automot. Mech. Eng. **11**, 2675 (2015)
9. Shah, A., Tunestal, P., Johansson, B.: Effect of pre-chamber volume and nozzle diameter on pre-chamber ignition in heavy duty natural gas engines. SAE technical paper (2015)
10. Ge, H., Bakir, A.H., Yadav, S., Kang, Y., Parameswaran, S., Zhao, P.: CFD optimization of the pre-chamber geometry for a gasoline spark ignition engine. Front. Mech. Eng. **6**, 599752 (2021)
11. Demeulenaere, X.: The use of automotive fleets to support the diffusion of alternative fuel vehicles: a rapid evidence assessment of barriers and decision mechanisms. Res. Transp. Econ. **76**, 100738 (2019)
12. Ocaña, B.V., Zavala, A.F., Erazo, C.V.: "Trucaje del cabezote del motor del vehículo Chevrolet Astra para competencias rally", 593 Digit. Publ. CEIT **7**(6), 192–201 (2022)
13. Perumal Venkatesan, E., et al.: Performance and emission reduction characteristics of cerium oxide nanoparticle-water emulsion biofuel in diesel engine with modified coated piston. Environ. Sci. Pollut. Res. **26**, 27362–27371 (2019)
14. Kalghatgi, G.T., McDonald, C.R., Hopwood, A.B.: An experimental study of combustion chamber deposits and their effects in a spark-ignition engine. SAE Technical Paper (1995)
15. Mohiuddin, K., Kwon, H., Choi, M., Park, S.: Effect of engine compression ratio, injection timing, and exhaust gas recirculation on gaseous and particle number emissions in a light-duty diesel engine. Fuel **294**, 120547 (2021)
16. Rosales, J.P.F., Revelo, J.D.G., Cárdenas, E.M.C., Paz, P.A.M.: Determinación experimental de la eficiencia mecánica de un motor de combustión interna de encendido provocado por medio de las curvas de torque y potencia. Polo del Conoc. **7**(7), 1735–1759 (2022)
17. Galindo, J., Climent, H., De la Morena, J., Pitarch, R., Guilain, S., Besançon, T.: A methodology to study the interaction between variable valve actuation and exhaust gas recirculation systems for spark-ignition engines from combustion perspective. Energy Convers. Manag. **250**, 114859 (2021)
18. Romero-Piedrahita, C.A., Mejía-Calderón, L.A., Carranza-Sánchez, Y.A.: Estudio de sensibilidad del desempeño durante el calentamiento en vacío de un motor de combustión interna a cambios en su relación de compresión, el contenido de etanol en la mezcla combustible con gasolina y el material de la culata. Dyna **85**(204), 238–247 (2018)
19. Yang, Z., Deng, B., Deng, M., Huang, S.: An overview of chassis dynamometer in the testing of vehicle emission. In: MATEC Web of Conferences, vol. 175, p. 2015 (2018)
20. Alagumalai, A.: Internal combustion engines: progress and prospects. Renew. Sustain. Energy Rev. **38**, 561–571 (2014)
21. Corsini, A., Di Antonio, R., Di Nucci, G., Marchegiani, A., Rispoli, F., Venturini, P.: Performance analysis of a common-rail diesel engine fuelled with different blends of waste cooking oil and gasoil. Energy Procedia **101**, 606–613 (2016)

22. Chen, L., Wang, Z., Liu, S., Qu, L.: Using a chassis dynamometer to determine the influencing factors for the emissions of Euro VI vehicles. Transp. Res. Part D Transp. Environ. **65**, 564–573 (2018)
23. Bae, C., Kim, J.: Alternative fuels for internal combustion engines. Proc. Combust. Inst. **36**(3), 3389–3413 (2017)
24. Abd-Alla, G.H.: Using exhaust gas recirculation in internal combustion engines: a review. Enery Convers. Manag. **43**(8), 1027–1042 (2002)
25. Yu, S., Zheng, M.: Future gasoline engine ignition: a review on advanced concepts. Int. J. Engine Res. **22**(6), 1743–1775 (2021). https://doi.org/10.1177/1468087420953085
26. Costa, R.C., Sodré, J.R.: Hydrous ethanol vs. gasoline-ethanol blend: engine performance and emissions. Fuel **89**(2), 287–293 (2010)

Additive Manufacturing of the Acceleration Body of the Corsa Evolution Analyzing the Type of Meshing

Denis Ugeño(✉), Víctor López, Pamela Villarreal, Cristian Guachamin, Jhon Jara, and Jorge Ramos

Instituto Superior Universitario Vida Nueva, Quito, Ecuador
denis.ugeno@istvidanueva.edu.ec

Abstract. Additive manufacturing, also known as 3D printing, has revolutionized the manufacturing industry by enabling the creation of complex parts in an efficient and customized manner. In the case of the Corsa Evolution's throttle body, additive manufacturing has been used to produce this key component of the air intake system. In terms of meshing type analysis, meshing in additive manufacturing refers to the internal structure of the 3D printed part. Meshing can vary in terms of density and design, which directly affects the properties and performance of the final part. The additive manufacturing of the acceleration body of the Corsa Evolution has allowed the production of a customized and efficient component. The analysis of the type of mesh in this process plays a crucial role in optimizing the performance of the final part, taking into account factors such as strength, weight and airflow.

Keywords: Additive manufacturing · 3D printing · Meshing · FEM analysis · CFD analysis

1 Introduction

Reverse engineering has evolved in leaps and bounds these last two decades, enabling a continuous improvement in design processes, therefore, [9] mentions that "in this way designers as architects, engineers will have a much clearer idea of what is being built, with the possibility of minimizing errors when building mechanical elements".

The obtaining of the geometry of the mechanical elements through a 3D scan has gained strength in recent times so [10] affirmed the following:

The function of a 3D scanner is to measure and digitize a physical model, for this it collects samples of the geometry of the object, extracting a cloud of points that will be processed and analyzed to determine its position in space and obtain a three-dimensional model or reconstruction of the object.

For example, you can create replacement parts that correspond to the original design of damaged existing parts, or use reverse engineering processes to integrate complex surfaces of sturdy objects into fasteners with 3D-printable guides, which are useful when you want to modify handmade or mass-produced products [16].

M. Z. Vizuete et al. (Eds.): CI3 2023, LNNS 1040, pp. 251–266, 2024.
https://doi.org/10.1007/978-3-031-63434-5_19

However, despite the advances, the use of composite materials in different automotive parts still has great challenges: how do the mechanical properties of compo-site materials influence the performance and durability of the car's acceleration body?

In this research, we propose to address the question posed through a multidisciplinary approach that combines composite materials theory, solid mechanics and de-sign engineering. Through experiments and theoretical analyses, seeking to obtain accurate and reliable information on how composite materials influence the performance, strength and durability of acceleration bodies.

2 Additive Manufacturing

Additive manufacturing is a technology that is currently being applied for the manufacture of complex parts, [14]. "the technology known as Additive Manufacturing (AM), as it is known internationally, basically consists of manipulating material at the micrometric scale and depositing it very precisely to build a solid" (p. 34).

Taking into account the above, additive manufacturing may vary according to the following parameters:

- Cost
- Type of material
- Maintenance
- Velocity
- Thickness
- Precision

2.1 FMD (Fused Deposition Modeling) Printing

From the point of view of "fused deposition modelling (FDM) is a 3D printing technology based on extrusion. The manufacturing materials used in FDM are thermoplastic polymers and come in filament form", On the other hand, with FDM technology, "a part is manufactured by selectively depositing molten material layer by layer in a path defined by the CAD model. Due to its high precision, low cost and wide selection of materials [17].

According to [14] "FDM technology uses the manufacturing input material in the form of thermoplastic filaments that are liquefied and re-solidified into the de-sired shape according to the defined CAD model (Fig. 1).

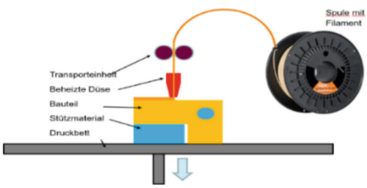

Fig. 1. This graph represents the fundamental elements of FMD printing, taken form [12]

In this type of printing [3] mentions that a very important aspect must be taken into account regarding the filament, so the filament for FMD printing must reach a liquid state so that the individual layers of the model can be added. This must be properly heated and introduced into a thin nozzle. This produces a thin thread of plastic that is used to make layers that overlap to form the 3D component.

Advantages of Fused Deposition 3D Printing. This type of technology, used mainly in sectors such as aeronautics, automotive, health and consumer goods, among others, constitutes a new model in the way parts and products are manufactured. It has numerous advantages that have made it a modality widely used by companies, in addition to any new technology, it also has its limitations, therefore, the following table shows the advantages and limitations of additive manufacturing (Table 1).

Table 1. Advantages and limitations of additive manufacturing

Advantages	Limitations
Geometric complexity, customization	AM Technologies in Development
Creative freedom	Peripheral and auxiliary processes
Adaptation to the market	Lack of knowledge of designers
Access to new market niches	Availability and cost of raw materials
Integrated mechanisms	Surface finish
Weight reduction, lightened products	Manufacturing speed
Reduced time to market	Product quality and process repeatability
Reduction of intermediate process costs	Limited size of parts
Hybrid processes	Cost of machinery

As for the FDM process, these are the most important factors that make it one of the most popular 3D printing technologies.

- FDM is known as one of the cheaper options for 3D printing compared to its counterparts that are more expensive like SLA o SLS
- The manufacturing material is cheaper and widely available which makes printing prototypes and design improvements less expensive than with other technologies.
- The FDM process is fast in terms of printing speed, since the manufacturing filaments are readily available and there is no problem with printing time.

Technical Specifications for FMD. Taking into account the advantages of fused deposition 3D printing, the technical specifications for FMD technology are presented below (Table 2).

Table 2. Technical specifications for FMD technology of 3D printing [17]

Standard delivery time	Minimum 4 days (or 48 h for models using the quick management service), depending on the size of the part, number of components and degrees of finish
Standard accuracy	±0,15% (with a lower limit of ±0,2 mm)
Layer thickness	0.18–0.33 mm (varies depending on material selected)
Minimum wall thickness	1 mm
Maximum dimensions of the construction area	There are no limits to dimensions, as components can be created with different parts. The maximum size is machine is 914 × 610 × 914 mm
Surface structure	Unfinished parts usually have a rough surface, but it is possible to apply any type of surface finish. Parts produced using FDM can be painted and coated

2.2 Filling 3D Printing

Infill is very important in 3D printing, since this filling pattern can be adjusted from 0% to 100% so [2] mentions the following:

- When doing 3D printing there are several parameters that one can control that give the final finish to the piece and one of the most important is the filling
- The filling is how the part to be printed is filled and this parameter determines many characteristics of the part. It influences weight, strength, printing speed, part cost, and even its ability to float.

Fill Density. The density of the filling is a characteristic that 3D printing technology has, so you can modify the percentage of filling material of the piece at the time of printing, con-figured the weight, resistance and time of printing, in Fig. 7 the percentage of filling is shown in a triangular pattern (Fig. 2).

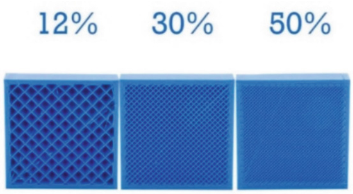

Fig. 2. In the figure you can see the percentage of meshing of a mechanical component [2].

When using software such as Cura or Prusa Slicer, you can choose the percentage of fill of the piece to be printed, default from 20% to 100% fill, so [2] mentions the following:

If you want to use exhibition pieces, the same ones that are going to be exhibited on a shelf or models and do not support loads that may affect their structure, it is recommended to use a filling from 0% to 15%.

If you want to use standard functional parts, the same ones that will be supporting moderate loads such as that of a simple mechanism, it is recommended to use a filling from 15% to 50%, modifying its robustness and printing speed.

If it is going to be used for mechanical parts, a filling percentage from 50% to 100% is recommended, so they will always be supporting combined stresses or as they are commonly called, cyclic stresses, requiring more material [2].

2.3 Materials for Additive Manufacturing

Carbon Fiber. According to the research of [11] mentions that "this fiber is one of the most used in the industrial field so it is composed of carbon atoms, the same that has a diameter of 5 to 10 um", therefore Alegre Gago [5] mentions that "over the years it has gained strength in many sectors because it provides great resistance and can even overcome the resistive stress of the conventional materials", in the same way it offers a low, but compared to other metals for the reason that it provides, it should be noted that carbon fiber in its pure state offers a resistance of 5 times more than that of steel.

The following table shows the characteristics of carbon fiber, highlighting its mechanical properties for printing tensile and bending specimens (Table 3).

Table 3. Properties of carbon fiberglass

Typical Material Properties			
Physical Properties	Unit	Value	Method
Density	g/cm^3	1,35	ISO 1183
Moisture absorption	%	–	
Tensile strength	MPA	76	ISO 527
Tensile elongation @ breakage	%	7,5	ISO 527
Flexible strength	MPA	110	ISO 178
Bending modulus	GPA	6,2	ISO 178
Impact resistance with notches	kJ/m^2	6	ISO 180
Young's module	GPA	220	ISO 178
Impact resistance without notches	kJ/m^2	60	ISO 180
Poisson coefficient		0,25	
Recommended 3D printing temperature	°C	240–260	–

(*continued*)

Table 3. (*continued*)

Typical Material Properties			
Physical Properties	Unit	Value	Method
Recommended bed temperature	°C	60–70	–
Bed surface	–	modification Glass plate	–
Active cooling fan	%	50	–
Recommended 3D printing speed	mm/w	40–70	–

ABS Plus Fiber. According to the research of [4], mentions that "ABS Plus, is a versatile material that has special properties such as greater resistance and lower processing contraction than standard ABS", therefore Alegre Gago [5] mentions that this fiber "is ideal for mechanical and technical processing. In addition, 3D printing with ABS Plus is faster than with other standard ABS.

On the other hand, [16] mentions that "the possible applications of ABS PLUS are prototypes, electronic components or decorative objects, but mainly the applications of this material find their space in industry, in products that require greater durability".

The following table shows the printing characteristics of ABS fiber BONUS (Table 4).

Table 4. Printing features of ABS Plus fiber

Characteristics	Value
Printing temperature	250–270 °C
Bed temperature	90–110 °C
Closed chamber	recommended
Fan	0–10%
Flowrate	95–105%
Print speed	35–60 mm/s
Surface	glass, Kapton tape, ABS juice
Retraction (direct)	2–3 mm
Retraction (Bowden)	4–6 mm
Retraction speed	20–45 mm/s
Drying conditions	60 °C/4h

3 Methodology

3.1 DOE Experimental Design

The design of experiments (DOE) is a statistical approach that will be applied for the optimization of the research project, that is, it will help to obtain the factorial experimental design, the number of possible combinations or treatments and the number of specimens.

3.2 Factorial Experimental Design

The effects that occur in the study of most experiments that are developed Many experiments, is due to different causes in the research process, so [13] states that "the factorial design is understood as one in which all possible combinations of factor levels are investigated in each complete trial or replica of the experiment".

Other authors mention the following about factorial experimental design:

Two types of elements are present in the object of study. The planning factor (k) is the measurable variable that acts on the object of investigation and takes a certain value in a given test. Planning factors can be quantitative and/or qualitative [15].

The factorial design lies in all possible combinations of levels with factors. According to [15] mentions that "a factorial arrangement is represented by Eq. 1.

$$n^k \tag{1}$$

where:

K = It is the number of factors

n = the number of levels

To apply the factorial design for the calculation of the combinations of the specimens, the type of mesh in 3D printing, the printing speed and printing temperature with their respective levels are taken into account, the same as presented in Table 5.

Table 5. Factors and levels to be applied in the unifactorial design for the calculation of the number of combinations of the specimens

Factors	Levels
Type of meshing	Triangular (A1) Grid (B1) Gromoid (C1)
Print speed	35 mm/s (D1)
Printing temperature	275 °C (E1)

Applying the mathematical model of factorial design yields the following:

$$3^1 \times 1^1 \times 1^1 = 3 \tag{2}$$

Analyzing the value obtained, it can be deduced that 3 treatments need to be performed with their respective combinations, the same as presented in Table 6.

Table 6. Treatments and combinations of test tubes to be performed

Treatment	Combinations	Response variable
T1 (Carbon Fiber)	A1 + D1 + E1	5 units
T2 (ABS PLUS)	B1 + D1 + E1	5 units
T3 (PETG)	C1 + D1 + E1	5 units

Interpreting Table 5, the following can be mentioned:

- Treatment 1 shall be printed 5 units with triangular mesh at the speed of 35 mm/s with a temperature of 275 °C.
- Treatment 2 shall be printed 5 units with the mesh type grid at the speed of 35 mm/s with a temperature of 275 °C.
- Treatment 3 shall be printed 5 units with gyroid meshing at a speed of 35 mm/s with a temperature of 275 °C.

Number of Repetitions of the Experiment. For the results of the experimental design, aspects such as the following variables are taken into account, such as: maximum elasticity force and breaking force, as a background the type of meshing, the printing speed and finally the printing temperature variable, where these variables are intentionally manipulated for the calculation of the number of repetitions, is considered. as visualized in Eq. 3.

$$n = \left(\frac{40 \times \sqrt{n'' \times \sum x^2 - (\sum x)^2}}{\sum x} \right)^2 \tag{3}$$

where:

N'' = Number of preliminary observations
Σ = Sum of values
x = Value of observations
40 = A constant for a 95% confidence level and a 5% error

To apply the mathematical model for the experimental design, the following considerations must be taken into account:

If > 5 the number of missing specimens must be drawn up
If (n < =) 5 will be sufficient with the test specimens.

Evaluation of the Mechanical Properties of the Prototype. Once determined the combinations of the specimens according to the experimental design, we proceed to the design of the tensile and bending specimens for their characterization, using the ASTM D3039-14 and D7264 standards respectively, to guarantee the standardized tests that allow to determine the mechanical properties, in the table the variables that must be considered for the development of the process considered the validation of the mechanical properties of the prototype are presented (Table 7).

Table 7. Dependent and independent variables for prototyping validation considering mechanical properties

Independent variables	Dependent variables
Type of meshing	Tractive effort Stress curve Deformation Deflection effort Deflection curve
Material	Carbon fiber, ABS plus and PETG

Design of Tensile and Flexural Specimens According to ASTM D3039-14 and D7264. The research also focuses on the experimental type for the reason that test tests were carried out through the design and construction of specimens, obtaining the mechanical properties of the same with carbon fiber, ABS PLUS and PETG, these results will be obtained by applying the ASTM 3039–14 standard for tensile tests, the same one that mentions that said specimen must have a thickness of 3 mm, 250 mm in length and 59 mm in width (Fig. 3).

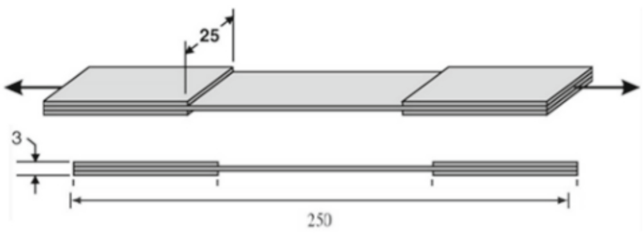

Fig. 3. Tensile test specimen according to ASTM D3039-14

On the other hand, the ASTM-D7264 standard designed for bending tests, which mentions that the specimen must have the measurements: 160 mm long, 13 wide, and 4 thick (Fig. 4).

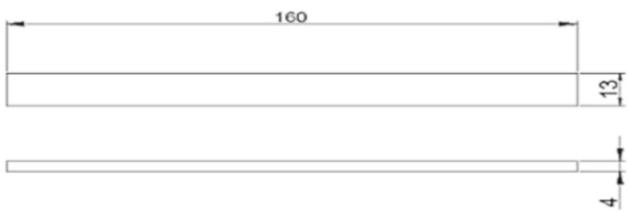

Fig. 4. Specimen for bending test according to ASTM D7264

Once the regulations for the manufacture of specimens have been analyzed, it was designed in SolidWorks, in this way it can be transported in STL format for the configuration of the printing in the Prusa Slicer software, as shown in Fig. 5.

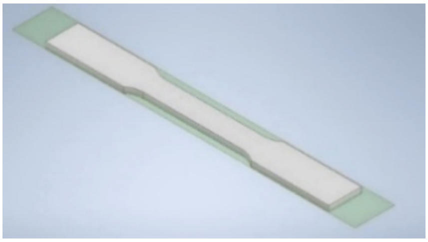

Fig. 5. CAD design of specimen to bend and tensile according to the regulations

Parameters for Printing the Initial Tensile and Bending Specimens. The parameters that are taken into account for the analysis of the printing of the specimens in the Prusa Slicer software with the Infill triangular type, grid and Gyroid, after the CAD design, was the printing speed the same as the value of 35mm/s, also the temperature, taking into account that the printing temperature of the carbon fiber PETG and ABS Plus are almost similar (2400 °C–2600 °C and 2500 °C–2700 °C), Recom-mended bed temperature for each of the fibers is (600 °C–700°C and 900 °C–1000 °C), manufacturing the specimens with carbon fiberglass, ABS Plus and PTG, taking into account that the mesh type grid is used for mechanical parts, gyroid is used for organic parts and triangular is used for mechanical parts.

FEM Simulation. Finite element analysis decomposes a real object into a large number (thousands to hundreds of thousands) of finite elements, such as small cubes. Mathematical equations make it possible to predict the behavior of each element. A computer then adds up all the individual behaviors to predict the actual behavior of the object. It is for this reason that we proceed to perform this type of simulation in the acceleration body of the Chevrolet Corsa, using the SIMSOLID software, considering the mass of the vehicle, its speed to determine the efforts and displacements in real time in case of a frontal impact, modulus of elasticity, Poisson coefficient, density and load, both original material, carbon fiber, PETG and ABS PLUS.

Now to know the impact force of the 2000-kg car traveling at 20 m per second that crashes into a wall, directly affecting the internal combustion engine, Eq. 4 is used.

$$F = \frac{0.5 \times m \times v^2}{d} \tag{4}$$

where:

F = impact force (N)
M = mass of the vehicle (kg)
V = vehicle speed
D = transformation coefficient (0.75)

When replacing the corresponding values, a load of 53.33 KN was obtained, this load will be the one applied in the simulation.

Table 8 shows the general conditions that were taken into account for the development of the first analysis of the acceleration body with the materials mentioned above.

Table 8. General considerations taken into account for the finite element analysis of the acceleration body with different materials

General conditions for FEM-conventional material analysis	
Velocity	72 km/h
Modulus of elasticity	73000 GPA
Poisson coefficient	0,33
Material	Aluminio
Density	2780 kg/m^3
Strength	53,33 kN
General conditions for FEM-carbon fiber analysis	
Velocity	72 km/h
Modulus of elasticity	62 GPA
Poisson coefficient	0,4
Material	Fibra de carbono
Density	1,35 g/m^3
Strength	53,33 kN
General conditions for the EMF analysis of ABS plus	
Velocity	72 km/h
Modulus of elasticity	1800 MPA
Poisson coefficient	0,42
Material	ABS plus
Density	1,07g/cm^3
Strength	53,33 kN
General conditions for FEM-PETG analysis	
Velocity	72 km/h
Modulus of elasticity	2200 MPA
Poisson coefficient	0,42
Material	PETG
Density	12700 kg/m^3
Strength	53,33 kN

Once the general configuration characteristics for FEM simulation in SIMSOLID have been identified, a general environment of that configuration is displayed in Fig. 6.

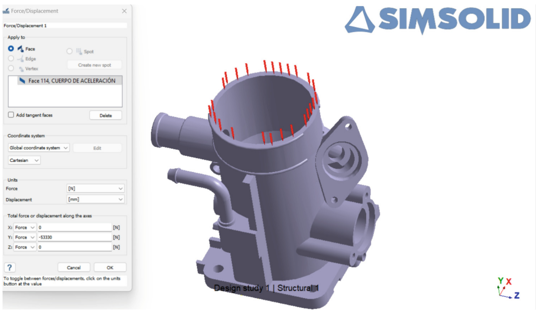

Fig. 6. Configuration in the SIMSOLID software the FEM simulation of the acceleration body of the Chevrolet Corsa

As can be seen in Fig. 36, the maximum displacement suffered by the acceleration body with the load of 53.33 KN is 0,048 mm right at the top, so in that sector it should be reinforced.

The maximum effort produced by the mechanical element when subjected to the load of 53.33 kN, is 224.8 MPa, and the minimum is 8.210e−5 MPa, so it is very resistant to frontal impacts.

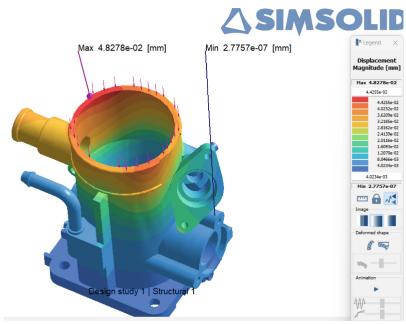

Fig. 7. Analysis of displacements and forces of the acceleration body according to Von Misses with the original material

4 Results and Discussion

4.1 Results

The analysis reveals that the acceleration body experiences a maximum displacement of 157 mm at the top when subjected to a load of 53.33 kN. This information suggests the need to reinforce that specific area of the acceleration body. Reinforcing this area will ensure that the component can withstand the load and prevent possible failures or excessive deformations. The analysis provides a solid basis for taking preventive measures and ensuring safe and reliable performance of the acceleration body.

Automotive auto parts, on the other hand, experience a maximum effort of 217 MPa and a minimum effort of 6.38e−5 MPa. These values indicate a wide difference between maximum and minimum stress, suggesting an uneven distribution of loads along the element. This situation is worrisome, as it can lead to excessive stress concentrations in certain areas, which could lead to unacceptable failures or deformations. It is necessary to address this problem by designing reinforcements or redistribution of loads to ensure a more even distribution of stress along the mechanical element. This will help prevent potential structural failures and ensure safe and reliable operation of the component (Fig. 8).

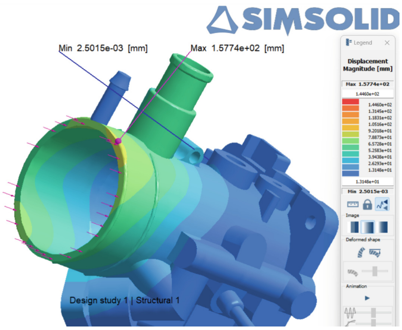

Fig. 8. Analysis of displacements and forces of the acceleration body with carbon fiber

4.2 Discussion

The analysis reveals that the maximum displacement of the element is 5.41 mm, while the minimum displacement is 8.84e−5 mm. These values indicate a not so significant difference in the displacements along the element, which may be ideal. It is important to consider that such a small minimum displacement may indicate a lack of stiffness or strength in certain areas of the element.

On the other hand, the analysis reveals that the maximum stress on the element is 215 MPa, while the minimum effort is 6.339e−5 MPa. These values indicate a wide difference between the maximum and minimum stresses, suggesting an uneven distribution of loads along the element, taking into account that it can withstand high loads before its deformation (Fig. 9).

Based on the results, it was determined that the minimum deformation in the component is 7,23e−5 mm, while the maximum deformation is 4,43 mm.

These values indicate a significant difference in the deformations experienced along the component. Importantly, such low minimum deformation could be indicative of areas of the component that are experiencing insufficient load or lack the stiffness needed to adequately withstand the applied forces.

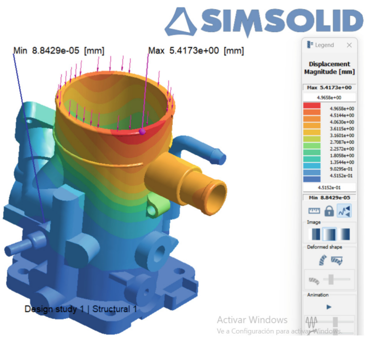

Fig. 9. Analysis of displacements and forces of the acceleration body with ABS PLUS

On the other hand, according to the results of the analysis, it was determined that the maximum effort in the component is 2,15e2 MPa, while the minimum effort is 6,339e−5 MPa. These values reveal a wide difference between the maximum and minimum stresses experienced on the component. The existence of such a low mini-mum effort can indicate areas of the component that are subjected to very low loads so it would be a suitable composite material for the manufacture of the acceleration body of the Chevrolet Corsa.

5 Conclusions

In the study of additive manufacturing of the throttle body for the Corsa Evolution, a comprehensive analysis of the meshing technique used in finite element simulations was carried out. The choice of meshing type significantly impacts the accuracy and efficiency of the simulations. The results demonstrated that the selected meshing approach, in combination with the powerful tool SimSolid, allowed for reliable outcomes in a considerably reduced timeframe compared to conventional simulation methods. This optimization of the meshing technique not only enhanced the analysis speed but also contributed to a deeper understanding of the structural behaviors and performance of the additively manufactured throttle body.

The application of 3D printing through fused filament fabrication with carbon fiber filament and ABS Plus has proven to be an effective strategy for enhancing the performance of the Corsa Evolution throttle body. The incorporation of carbon fiber bolstered the structural strength and durability of the component, enabling it to withstand the mechanical and thermal demands it faces under operating conditions. Additionally, the use of ABS Plus as a complementary material provided greater toughness and dimensional stability to the component. This combination of materials and the 3D printing process resulted in a throttle body that not only met performance standards but also provided an advantage in terms of volumetric efficiency.

The additive manufacturing study of the Corsa Evolution throttle body highlights the innovative potential and feasibility of 3D printing technology in the automotive industry. The integration of finite element simulations through SimSolid and the use of advanced materials such as carbon fiber and ABS Plus represent a significant advancement in optimizing the design and manufacturing of automotive components. This considers technical characteristics, geometry, and materials in accordance with mechanical and physical properties to enhance performance, enabling the creation of highly efficient and durable products.

References

1. Alvarez C.K.L., Lagos C.R.F., Aizpun, M.: Influencia del porcentaje de relleno en la resistencia mecánica en impresión 3D, por medio del método de Modelado por Deposición Fundida (FDM). Ingeniare Rev. Chilena Ingeniería **24**(ESPECIAL), 17–24 (2020). https://doi.org/10.4067/S0718-33052016000500003
2. Colombia, B.: Microscopio Trinocular Amscope Soporte de Pluma—3.5X-90X/Luz LED 54. BIOWEB® Colombia (2022). https://colombia.bioweb.co/products/microscopio-trinocular-amscope-boom-stand-3-5x-90x-luz-led-54
3. Dong, C., Davies, I.J.: Flexural properties of macadamia nutshell particle reinforced polyester composites. Compos. B Eng. **43**(7), 2751–2756 (2021). https://doi.org/10.1016/j.compositesb.2021.04.035
4. Fiberlogy. ABS PLUS | Filamento ABS con mayor resistencia. Fiberlogy (2022). https://fiberlogy.com/es/filamentos/abs-plus/. Accessed 21 June 2022
5. Goldschmidt, B.: Infill en Cura: Los mejores patrones de relleno. All3DP (2022). https://all3dp.com/es/2/infill-cura-relleno-impresion-3d/
6. Ikustec. Escaneado 3D de Piezas—Mediciones de precisión. Ikustec (2021). https://ikustec.com/escaneado-3d-de-piezas/
7. Ineo 3D, C. Ineo—Fabricación aditiva—Modelado por deposición fundida (FDM) (2022). https://www.ineo.es/es/tecnologias/modelado-deposicion-fundida-fdm. Accessed 12 July 2022
8. González-Estrada, O.A., Martínez, E.: Evaluación de las propiedades tribológicas de materiales compuestos de matriz metálica (MMCs) procesados por técnicas de fabricación aditiva con haz láser (SLM). Rev. UIS Ingenierías **16**(1), 101–114 (2019)
9. Loste, J., Lopez-Cuesta, J.M., Billon, L., Garay, H., Save, M.: Transparent polymer nanocomposites: an overview on their synthesis and advanced properties. Prog. Polym. Sci. **89**, 133–158 (2019)
10. Miranda, M.F.: Universidad Internacional SEK. Panorama, pp. 5–20 (2020)
11. Möhring, H.C., Brecher, C., Abele, E., Fleischer, J., Bleicher, F.: Materials in machine tool structures. CIRP Ann. Manuf. Technol. **64**(2), 725–748 (2019). https://doi.org/10.1016/j.cirp.2019.05.005
12. Pucha Tambo, M.V.: Caracterización de materiales compuestos con matriz foto polimérica reforzados con fibras de abacá y cabuya mediante impresión 3D (2020). http://localhost:8080/xmlui/handle/123456789/3138
13. Rocha-Hoyos, J.C., Llanes-Cedeño, E.A., Peralta-Zurita, D., Pucha-Tambo, M.: Caracterización mecánica a flexión de materiales compuestos con matriz foto polimérica reforzados con fibras de abacá y cabuya mediante impresión 3D. Ingenius **22**, 100–112 (2020). https://doi.org/10.17163/ings.n22.2020.10
14. Tapia Cabrera, J.E.: Evaluación de las propiedades de amortiguamiento de materiales fabricados por impresión 3D y reforzados con nanotubos y fibras de carbono (2020). https://tesis.pucp.edu.pe/repositorio/handle/20.500.12404/15674
15. Vázquez Núñez, M.: Desarrollo de polímeros conductores para circuitos fabricados mediante impresión 3D (2020). https://ruc.udc.es/dspace/handle/2183/28409

16. Villarreal Bolaños, C.A.: Alternativa para la construcción de autopartes vehicular por medio de la ingeniería inversa e impresión 3D. Caso de estudio tapa de distribución inferior del Chevrolet Spark 2019 (2019). http://localhost:8080/xmlui/handle/123456789/3303
17. Xometry, E.: Tecnología de impresión 3D por deposición fundida. Xometry Europe (2022). https://xometry.eu/es/impresion-3d-por-modelado-por-deposicion-fundida-fdm-vision-general-de-la-tecnologia/
18. 3DWorks. Altura de Capas y Resolución en la Impresión 3D. 3DWorks (2021). https://www.3dworks.cl/post/altura-de-capaseade. Sector automotor en cifras. https://www.aeade.net/wp-content/uploads/2021/04/Sector-en-Cifras-Resumen.pdf. Accessed 25 May 2021

Analysis of Airborne Particles in Powder Coating Process

Caza Paúl(✉), Villarreal Pamela, López Víctor, Díaz Rodrigo, and Cruz Patricio

Instituto Superior Tecnológico Vida Nueva, Quito, Ecuador
paul.caza@istvidanueva.edu.ec

Abstract. This study focuses on the analysis of particles generated during the electrostatic painting process and aims to measure air quality and atmospheric pollution. A study was conducted to evaluate the effectiveness of a cyclone-type extractor system in reducing particle emissions and improving air quality in industrial painting environments. The analysis focuses on understanding the characteristics of particles generated during the electrostatic painting process, including their size, composition, and potential impact on air quality. Various sampling techniques and analytical methods are used to measure and analyze particle concentrations in the ambient air. The effectiveness and efficiency of the cyclone-type extraction system are evaluated, providing insight into its crucial role in reducing particle emissions and improving environmental conditions. This contributes to the development of strategies and technologies aimed at minimizing air pollution in industrial painting operations.

Keywords: Air quality · industrial safety · spay · extraction system · power coating

1 Introduction

The application of electrostatic painting using the spray method is a technique currently being employed in numerous industries to achieve high-quality coatings. This process involves the dispersion of electrically charged paint particles into to the surface to be painted, harnessing the electrostatic energy between the particles and the metallic surface. As the particles move towards the substrate, a uniform layer is formed, providing optimal characteristics and properties such as protection, adhesion, aesthetic appearance, hardness and resistance to environmental and chemical agents.

However, during the electrostatic painting spray process, fine particulate matter is generated and remains suspended in the air, posing challenges in terms of air quality and workplace safety. These suspended particles can vary in size, shape and composition, depending on various factors such as the type of electrostatic paint, spray conditions, equipment configuration and substrate characteristics.

The particulate matter generated in the electrostatic painting application process can have significant consequences for both the coating quality and the health and environment. Suspended airborne particles can negatively affect the appearance and durability

M. Z. Vizuete et al. (Eds.): CI3 2023, LNNS 1040, pp. 267–280, 2024.
https://doi.org/10.1007/978-3-031-63434-5_20

of the final finish, causing defects such as rough texture, thickness irregularities, and poor adhesion. Moreover, exposure to these particles can pose health risks to workers, as some particles may contain toxic or irritant compounds.

2 Contamination

2.1 Air Pollution

It can be stablished that atmospheric pollutions have different emission sources (both natural and anthropogenic) that have a negative effect on the atmosphere. According to these considerations, pollutants can be classified by different aspects such as origin, form of emission, physical state, reactivity and composition, as mentioned above, they can be of natural origin or generated by people and industries [18].

The negative effects generated by these pollutants can be related to premature damage to materials by altering the properties of soil and water, affecting people, causing death due to oxygen substitution, causing skin cancer, destruction of the ozone layer and damage to plantations [12].

Ozone Layer Destruction. Ozone can be considered a reactive gas that cause oxidation in some materials. This damage is generally caused by different pollutants such as NOx, VOCs, CH4 and CO, which are associated with fossil fuels, causing damage to health and the environment due to the level of toxicity and corrosive properties.

It can be mentioned that the ozone layer weakens due to the decrease in the concentration of O3, which causes the formation of ozone holes, this factor is related to diseases related to skin cancer, premature aging of the skin, among others.

Photochemical Pollution. Photochemical pollution is known as acid smog, a mixture of primary and secondary pollutants, which in the presence of sunlight cause severe damage to the biosphere and materials [19]. This process occurs in polluted atmospheres with a high SO2 content, which is composed of high levels of suspended particles, humidity, and cold temperatures, causing it to form a layer of cold air and preventing warmer air from rising. The harmful effects on human health are related to irritation of eyes and mucous membranes, asthmatic attacks, bronchitis, among others.

Air Quality. Air quality can be determined through the analysis of the concentration of different types of pollutants, taking into account the criteria of intake and emission.

For this purpose, a measurement and quantification of the pollutants present in the atmosphere is performed on the sample, which allows a comparison with the legal limit values, thus guaranteeing that the air quality is in accordance with the permitted limits. The procedure to be performed to analyze the air quality considers:

Sampling the same which depends on some factors such as time of day, weather conditions, emission at the site. In accordance with the Ecuadorian Air Quality Standard, Table 1 shows the alert, alarm and emergency levels for the concentration of pollutants to be considered [13].

Table 1. Concentration of pollutant types

Type of pollutants	Alert	Alarm	Emergency
Carbon monoxide 8-h average concentration (µg/m3)	15000	30000	40000
Ozone average concentration 8-h average(µg/m3)	200	400	600
Nitrogen dioxide 1-h average concentration (µg/m3)	1000	2000	3000
Sulfur dioxide 24-h average concentration (µg/m3)	200	1000	1800
Particulate Matter PM10 Concentration in 24 h (µg/m3)	250	400	500
Particulate Matter PM2.5 Concentration in 24 h (µg/m3)	150	250	350

2.2 Mechanical Processes

In fine particle recovery systems, the cyclone is analyzed because it is one of the most efficient equipment for separating and recovering particulate matter, thus helping to reduce the environmental damage caused by industrial processes. The most used control technologies or systems to help reduce particulate matter emission pollution are the cyclone, Venturi scrubber, electrostatic precipitator and baghouse [3].

The main objective of these mechanical processes is to collect as many of the particles emitted in different industrial processes as possible before they are released int the environment [10]. These separators are found in different types considering the separation system to be used, in this research we intend to analyze the efficiency and effectiveness of cyclone type separators.

Cyclone. The cyclone is a device used in systems for extracting and recovering airborne dust particles. Its operation is primarily based on the principle of centrifugal force. The contaminated air, along with the particulate matter, enters the cyclone through a tangential inlet in a spiral form, creating a rotating vortex motion. This rotation pushes the particles towards the cyclone's walls [2].

The particles with higher density separate and fall into the bottom of the cyclone, where they accumulate in a collection container. Meanwhile, the clean air, now free of particles, continues its path towards the cyclone's outlet. It is established that to increase the efficiency of the mechanism, the following should be considered:

- Particulate size
- Particulate properties
- Cyclone design parameters
- Particulate inlet diameter in relation to gas outlet

3 Methodology

Sampling will be carried out using manual equipment that will allow analyzing the concentration of contaminants generated by the dust particles obtained in situ from the analysis of the cyclone-type mechanical system in the electrostatic paint application process.

From the analysis carried out in the sampling, it can be observed that all the values considered in the analysis are related to the pressure generated by the compressor, since fluidization and pulverization depend on it, according to the calibration generated in the equipment. In the manual sampling process, different samples were taken considering the following aspects shown in the table.

3.1 Cyclone Dimensional Analysis

Once the required equations are established, different dimensional analysis techniques can be applied to determine the dimensions and relationships between the various variables of the cyclone. These dimensions are related to the cyclone's diameter, cone height, and the size of the inlet and outlet for air [6].

It is important to highlight that dimensional analysis considers practical limitations in the investigation, such as space constraints, cyclone installation, and the selection of optimal materials that can withstand the working conditions in the electrostatic painting process.

Technical Operating Parameters. To analyze the technical parameters of the cyclone operation in the powder paint application process, it is intended to tabulate the pressure-dependent variables of the electrostatic equipment which generates an optimum performance in the collection of suspended particles in the paint chamber, for which the following parameters are considered [7]:

- The blower motor has an air flow capacity of m3/h 1050. This allows to have higher absorption of dust particles.
- According to the design the diameter of cyclone is 800 mm. Considering the efficiency and efficacy within the collection process which allows to reduce atmospheric pollution.
- The climatic conditions of the painting chamber are to room temperature, which is a suitable factor for electrostatic adhesion on the metal surfaces to be coated.
- According to the implemented system, the vacuum inlet velocity to the cyclone is 190 mbar. Therefore, it is considered an essential factor in the study.

TOPSIS Comparative Analysis. For the multicriteria analysis, a selection is made from several criteria that directly affect the dependent variables such as: environmental pollution, energy consumption of the equipment, work efficiency, equipment manufacturing cost, maintenance cost, construction complexity and operation safety, with all these elements the TOPSIS analysis is developed, which consists of choosing the most efficient option for the analysis of the collection system of suspended particles in the environment. The equipment analyzed are Venturi scrubber collector, cyclone collector, electrostatic precipitator, and bag filter, as shown in Table 2.

This alternative consists of selecting a minimum distance with respect to a positive ideal distance, considering a greater distance from an anti-ideal alternative. The selection is determined based on seven criteria and four alternatives. The criteria must be reliable and meet the parameters, maximizing the acceptance criteria (Table 3).

Table 2. Criteria for selected alternatives

Criteria	Production capacity (%)	Energy consumption (kW/h)	Environmental contamination (kg)	Production (kg)	Investment	Maintenance cost $/year	Production Volume (gr)
Oven Infrared	90	10	65	120	17000	2500	800
Oven Electrical resistors	90	7,26	10	120	14000	1200	1000
Oven Burners	85	5,2	90	120	20000	2000	500
Oven Convection	70	5,4	85	120	17000	1500	400

Table 3. Weighted table of variables

Criteria	Environmental contamination (%)	Energy consumption (kW/h)	Efficiency	Manufacturing cost (USD)	Maintenance cost $/year	Construction complexity (%)	Handling safety (%)
Venturi Scrubber	65	10	90	7690	2500	90	26
Cyclone	10	5,2	90	6000	1200	85	45
Electrostatic precipitator	90	7,26	90	9500	1200	90	24
Bag filter	85	5,4	90	6300	1500	90	21

In Table 4, the normalized matrix generated in the TOPSIS multicriteria analysis is presented. It is obtained by taking the square root of each criterion and dividing it by the sum of the squares.

Table 4. TOPSIS standardized analysis matrix

Criteria	Production capacity (%)	Energy consumption (kW/h)	Environmental contamination (kg)	Production (kg)	Investment	Maintenance cost $/year	Production Volume (gr)
Oven Infrared	90	10	65	120	17000	2500	800
Oven Electrical resistors	90	7,26	10	120	14000	1200	1000
Oven Burners	85	5,2	90	120	20000	2000	500
Oven Convection	70	5,4	85	120	17000	1500	400

(*continued*)

Table 4. (*continued*)

Criteria	Environmental contamination (%)	Energy consumption (kW/h)	Efficiency	Manufacturing cost (USD)	Maintenance cost $/year	Construction complexity (%)	Handling safety (%)
Venturi Scrubber	0,463	0,6918	0,5	0,512	0,7410	0,5068	0,4264
Cyclone	0,0713	0,3597	0,5	0,3999	0,3557	0,4787	0,7380
Electrostatic precipitator	0,6420	0,5022	0,5	0,6332	0,3557	0,5068	0,3936
Bag filter	0,6063	0,3736	0,5	0,4199	0,4446	0,5068	0,3444

Table 5 displays the weighted normalized decision matrix, where each acceptance criterion is assigned a percentage weight according to a specific percentage ranking. This ranking is determined by multiplying the normalized matrix by the assigned percentage weight.

Table 5. Weighted normalized matrix of the multicriteria selection criteria

Criteria	Production capacity (%)	Energy consumption (kW/h)	Environmental contamination (kg)	Production (kg)	Investment	Maintenance cost $/year	Production Volume (gr)
Oven Infrared	90	10	65	120	17000	2500	800
Oven Electrical resistors	90	7,26	10	120	14000	1200	1000
Oven Burners	85	5,2	90	120	20000	2000	500
Oven Convection	70	5,4	85	120	17000	1500	400
Criteria	Environmental contamination (%)	Energy consumption (kW/h)	Efficiency	Manufacturing cost (USD)	Maintenance cost $/year	Construction complexity (%)	Handling safety (%)
Venturi Scrubber	0,125	0,187	0,095	0,056	0,067	0,025	0,013
Cyclone	0,019	0,097	0,095	0,044	0,032	0,024	0,022
Electrostatic precipitator	0,173	0,136	0,095	0,070	0,032	0,025	0,012
Bag filter	0,164	0,101	0,095	0,046	0,040	0,025	0,010

Finally, the “Euclidean” distance is determined, which represents the distance at which the point of maximum performance in the performance score corresponds to the best alternative in the alternatives ranking from an ideal value to an alternative.

Table 6. Euclide distance or ranking of alternatives

Criteria	Production capacity (%)	Energy consumption (kW/h)	Environmental contamination (kg)	Production (kg)	Investment	Maintenance cost $/year	Production Volume (gr)
Oven Infrared	90	10	65	120	17000	2500	800
Oven Electrical resistors	90	7,26	10	120	14000	1200	1000
Oven Burners	85	5,2	90	120	20000	2000	500
Oven Convection	70	5,4	85	120	17000	1500	400

Positive Ideal Solution	Negative Ideal Solution	Performance Score Pi	Ranking Alternatives Ci
0,140	0,061	0,303	2
0,043	0,179	0,805	1
0,163	0,057	0,260	4
0,149	0,087	0,368	3

In the multicriteria analysis using the TOPSIS method, four teams are presented as options, each fulfilling the best characteristics for collecting airborne dust particles. The evaluation focuses on variables that directly impact the manufacturing of the equipment. The results indicate significant differences among the teams, the TOPSIS analysis shows a high Euclidean distance value for the cyclone system, considering it as the best alternative based on the multi-criteria criterion.

3.2 Factorial Experimental Design

The experimental design is based on two variables such as the particles suspended in the environment considering two different positions inside the paint booth, and two different speeds of the blower in the dust extraction system suspended in the environment are also considered. Table 6 details each of the factors involved in the analysis (Table 8).

Table 7. Variable denomination

Criteria	Production capacity (%)	Energy consumption (kW/h)	Environmental contamination (kg)	Production (kg)	Investment	Maintenance cost $/year	Production Volume (gr)
Oven Infrared	90	10	65	120	17000	2500	800
Oven Electrical resistors	90	7,26	10	120	14000	1200	1000
Oven Burners	85	5,2	90	120	20000	2000	500
Oven Convection	70	5,4	85	120	17000	1500	400

Table 8. The statement of variables used in the experimental design

Variable Designation	
Treatment 1	Treatment 1 Total suspended particulate matter 1 (TSP)/Velocity 1
Treatment 2	Treatment 2 Total suspended particulate matter 1 (TSP)/Velocity 2
Treatment 3	Treatment 3 Total suspended particulate matter 1 (TSP)/Velocity 3
Treatment 4	Treatment 4 Total suspended particulate matter 1 (TSP)/Velocity 4

For the declaration of variables, we start from two very important elements such as the variation of the position of measures or dust collection system inside the cabin and the linear velocity that affects the cyclone is also considered in order to have a higher efficiency factor in the particle collection system. Table 7 details the statement of each of the variables (Table 9).

Table 9. Codification of variables

Criteria	Production capacity (%)	Energy consumption (kW/h)	Environmental contamination (kg)	Production (kg)	Investment	Maintenance cost $/year	Production Volume (gr)
Oven Infrared	90	10	65	120	17000	2500	800
Oven Electrical resistors	90	7,26	10	120	14000	1200	1000
Oven Burners	85	5,2	90	120	20000	2000	500
Oven Convection	70	5,4	85	120	17000	1500	400

Using Stat graphics software, the comparative samples in the results of the statistical summary are presented in Table 10, which shows the values of the number of counts or

Table 10. Coding of variables used in the experimental design

Statement of Variables	
Total suspended particulate matter 1 (TSP)	Particulate matter measured at the back of the spray booth
Total suspended particulate matter 2 (TSP)	Particulate matter measured at the top of the paint booth
Total suspended particulate matter 3 (TSP)	Blower linear velocity (1.43 m/s)
Total suspended particulate matter 4 (TSP)	Blower linear velocity (1.76 m/s)

analyses studied in each treatment, the larger the coefficient of variation, the greater the difference in deviation between the measured values [9] (Tables 11 and 12).

Table 11. Statistical summary

Criteria	Production capacity (%)	Energy consumption (kW/h)	Environmental contamination (kg)	Production (kg)	Investment	Maintenance cost $/year	Production Volume (gr)
Oven Infrared	90	10	65	120	17000	2500	800
Oven Electrical resistors	90	7,26	10	120	14000	1200	1000
Oven Burners	85	5,2	90	120	20000	2000	500
Oven Convection	70	5,4	85	120	17000	1500	400

Table 12. Results obtained using stat graphics software for the average standard deviation between the tests generated

	Count	Average	Standard Deviation	Variation Coefficient	Minimum	Maximum
Analysis I	4	79,135	21,87	27,63%	46,34	90,86
Analysis II	4	66,71	20,12	30,17%	39,69	86,52
Analysis III	4	97,96	81,88	83,58%	40,46	219,11
Analysis IV	4	38,95	10,17	26,11%	30,24	50,59
TOTAL	16	70,69	45,03	63,71%	30,24	219,11

Table 13 shows the results of standardized kurtosis and standardized bias, where information is presented and indicates that the data entered and the measurements obtained come from a normal curve and normal values ranging between –2 and 2, if the data were outside this range they are also known as outliers that should not be considered, therefore, it is considered that the number of tests is correct for this analysis in taking measurements of particulate matter suspended in the air.

In the Anova table, the P-value of the F-ratio is presented, which in this case is 1.27, the estimated coefficient between groups. It can be observed that the P-value is greater

Table 13. Statistical analysis standardized kurtosis and skewness

	Range	Standardized skewness	Standardized kurtosis
Analysis I	44,52	–1,62	1,62
Analysis II	46,83	–0,74	0,24
Analysis III	178,65	1,5	1,42
Analysis IV	20,35	0,25	–1,72
TOTAL	188,87	4,17	6,73

than or equal to 0.05, indicating that there is no statistically significant difference among the four variables. This result is obtained with a confidence level of 95%, as shown in Table 14.

Table 14. Anova table

Source	Sum of squares	Mean square	F Ratio	P-value
Between groups	7352,14	2450,71	1,27	0,3274
Between groups	23014,7	1922,89		
Total (Corr)	30426,9			

Figure 1 shows the response through the block diagram by box and whisker, where the value of the mean is indicated, it is also observed that there are significant differences between the four treatments of analysis I and analysis IV, it is also visualized that analysis II and analysis III have a similar average in the value of the mean, the maximum and the minimum. In addition, in treatment III there is a very high dispersion among the assigned values, since the external values are far from the mean, and it is also observed that in treatment III one of its values has a high dispersion, thus being considered as the most defective treatment in the treatment of samples and reading in the tests.

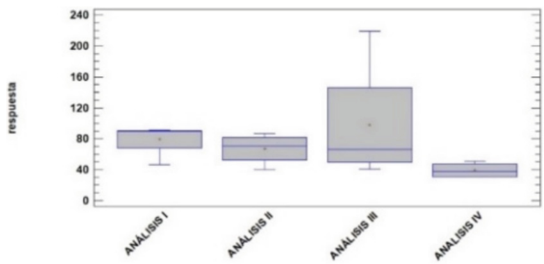

Fig. 1. Box and whisker plot

A very important factor to consider is the dispersion in the reading of the selected measurements, this factor depends on the condition under which each of the analyses were carried out, in case III a very high dispersion in the results is observed, what is recommended is to generate more measurements, on the other hand, in analysis I the reading measurements coincide in the same way, ore readings are recommended in order to have a significant difference, in analysis II it is observed that the samples were taken almost equally, as shown in Fig. 2.

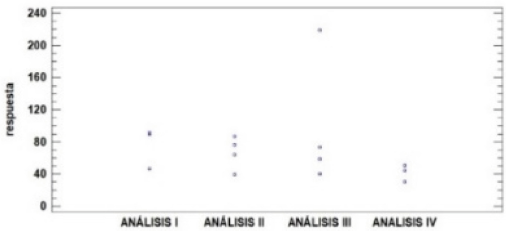

Fig. 2. Sample dispersion box

Finally, Fig. 3 shows the values obtained in the Anova analysis, indicating a dispersion factor P of 0.3274, which is a considerable value for a technical experimental analysis and considering that the sample readings in each of the treatments are similar, which makes it possible to take samples at any internal point of the space analyzed for the collection of suspended particles in the environment.

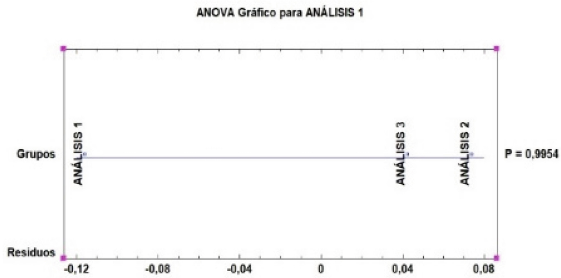

Fig. 3. Anova analysis

4 Results and Discussion

Finally, after conducting various air quality measurements in this research, it has been determined that the technical characteristics of powder coating, such as adhesion, temperature, and humidity, influence the spraying method on the metal surface to be coated, which poses a high risk to operators and the environment.

The ability of powder coatings to adjust their chemical composition according to the needs relies entirely on their components. Therefore, the materials chosen to design the particle collector must meet mechanical, chemical, and physical properties that ensure greater durability of the system used in the electrostatic painting process.

The technical parameters of the electrostatic painting equipment play a crucial role in the application of the coating on the metal component. Poor calibration of pressure, amperage, volumetric amount of powder coating, inadequate or lack of nozzle selection, and circuit closure can result in excessive overspray in the work area, placing maximum demand on the extraction system and application equipment.

From the obtained data, it can be observed that a cyclone type extraction and collection system with a filter ensures high efficiency in collecting suspended particulate matter in the air caused by application and poor practices by the operator or equipment. This, in turn, reduces air pollution and mitigates the risks to which the worker is exposed.

According to the CFD simulation, it was possible to verify and analyze that the cyclone-type system, due to centrifugal forces, generates a laminar flow, allowing for the collection of a high percentage of suspended particles in the working process. This was achieved thanks to the optimal design, which determined the post-construction dimensional analysis parameters, ensuring the proper functioning of the equipment.

Additionally, it has been established that the cyclone system will be driven by a blower that generates centrifugal movement through the use of blades. These blades, powered by the motor's pressure, enable a wide operating range and low energy consumption. This helps reduce the impact of powder coating on both operators and the environment.

The factorial analysis allowed us to determine the Anova graph, which shows a significant distance between the selected equipment, with a minimum distance below 0.05% of the P factor for the cyclone-type equipment selection. This achieves an efficiency and reliability of 95%, which is considered an optimal range in the technical and scientific field for selecting reliable equipment.

5 Conclusions

The present research contributed to the study of air quality through the implementation of a cyclone type extraction and collection system, analyzed based on different acceptance criteria or variables that meet the requirements of design, manufacturing, operation, and maintenance. This system has led to a reduction in ergonomic risks and environmental mitigation. The analysis of variables was performed using the TOPSIS multi-criteria selection method, which yielded results indicating that the cyclone-type system implemented in the electrostatic painting application process is ideal for separating particulate matter, which is collected in a container connected to the collection system, while clean air is recirculated into the environment without contaminants.

The design of the powder particle extraction and recovery system ensured high performance with a 95% efficiency in powder paint recovery, as determined through factorial analysis. Key parameters in the construction process were considered, such as the diameter of the cyclone, cone height, and the size of the air inlet and outlet. The latter is closely related to the airflow rate, density, and particle size. These parameters were carefully evaluated to optimize the system's performance and ensure effective recovery of the powder paint.

The extraction system meets the optimal specifications thanks to the blade design, allowing for the collection of 98% of the suspended powder paint particles in the air during the application in the paint booth. This ensures operator safety and environmental protection, as well as enabling the reuse of the collected paint for coating new metal elements.

It is recommended for future research to conduct a study that analyzes the climatic conditions according to the equipment's location, as they influence the air quality in industrial extraction and collection systems. Understanding the impact of factors such as weather, temperature, humidity, and air composition can provide valuable insights into the performance and efficiency of these systems under different environmental conditions. This information can be used to optimize the design and operation of industrial extraction and collection systems, leading to improved air quality and better environmental outcomes.

References

1. Arredondo, K., Muñoz, J., Carrillo, T.: Proyecto de mejora en los procesos de curado y pintura en una empresa de productos eléctricos. Rev. Aristas Investig. Básica y Apl. **6**(12), 239–243 (2019)
2. Cabina, T.: Nuevas cabinas de aspiración de pintura en polvo evolucionadas - Tecnicabina S.L. https://tecnicabina.com/nueva-cabina-aspiracion-pintura-polvo/. Accessed 20 June 2021
3. Company Spectris, "Contaminación por partículas y Seguridad Ambiental". https://mx.omega.com/technical-learning/contaminacion-por-particulas-y-seguridad-ambiental.html. Accessed 24 Aug 2021
4. Dalmar protecciones y "Cabinas de pintura en polvo". http://blog.proteccionesypinturas.com/cabinas-de-pintura-en-polvo/. Accessed 28 Sep 2021
5. "Parlamento Europeo P9_TA(2023)0318 Calidad del aire ambiente y una atmósfera más limpia en Europa" (2020)
6. El sitio de la pintura en polvo, "Recuperación de Pintura en Polvo en la Fabricación". http://pinturaenpolvo.org/recuperacion-de-pintura-en-polvo. Accessed 20 Jan 2022
7. He, H., Lou, J., Li, Y., Zhang, H., Wei, X.S.: Effects of oxygen contents on sintering mechanism and sintering-neck growth behaviour of FeCr powder. Powder Technol. **329**, 12–18 (2020). https://doi.org/10.1016/J.POWTEC.2020.01.036
8. Industria elaboradora de pinturas, "Guía para el control y prevención de la contaminación industrial". http://www.ingenieroambiental.com/4014/pinturas.pdf. Accessed 05 July 2020
9. IPM Integraciones y proyectos metálicos S.A. "Cabinas para aplicar la pintura electrostática Metalmecánica, Proyectos Metálicos y Pintura Electrostática". http://ipmsadecv.com/cabinas-para-aplicar-la-pintura-electrostatica. Accessed 20 Jan 2021
10. Kleine Deters, J., Zalakeviciute, R., Rybarczyk, Y.: Modeling PM $_{2.5}$ urban pollution using machine learning and selected meteorological parameters. J. Electr. Comput. Eng. **2020**, 1–14 (2020). https://doi.org/10.1155/2017/5106045
11. Li, Y., Zhang, W., Wang, Y.: Effect of spray powder particle size on the bionic hydrophobic structures and corrosion performance of Fe-based amorphous metallic coatings. Surf. Coat. Technol. **437**, 128377 (2022). https://doi.org/10.1016/j.surfcoat.2022.128377
12. Ministerio para la Transición Ecológica, "Partículas en suspensión". https://www.miteco.gob.es/es/calidad-y-evaluacion-ambiental/temas/atmosfera-y-calidad-del-aire/emisiones/prob-amb/particulas.aspx. Accessed 23 Feb 2020

13. Norma Española, "UNE-EN 50050-1: Equipo manual de pulverización electrostática" (2020)
14. Raoelison, R., Sapanathan, T., Langlade, C.: Cold gas dynamic spray technology: A comprehensive review of processing conditions for various technological developments till to date. Addit. Manuf. **19**, 134–159. https://doi.org/10.1016/J.ADDMA.2020.07.001
15. Rodríguez Guerra, A., Cuvi, N.: Air pollution and environmental justice in Quito, Ecuador. Fronteiras **8**(3), 13–46 (2019). https://doi.org/10.21664/2238-8869.2019v8i3.p13-46
16. Rojas, J.: Reciclado y recuperación de pintura en polvo, Dianetl. https://dialnet.unirioja.es/servlet/articulo?codigo=6733852. Accessed 13 Sep 2020
17. Secretaria del Ambiente, "Norma Ecuatoriana de la Calidad del Aire (2021). http://www.quitoambiente.gob.ec/ambiente/index.php/norma-ecuatoriana-de-la-calidad-del-aire
18. Tapia Núñez, L.: Norma De Calidad Del Aire Ambiente o Nivel De Inmisión Libro Vi Anexo, no. 4 (2019)
19. Valencia, A., Suárez Castaño, R., Sánchez, A., Cardozo, M.B., Buitrago, C.: Gestión de la contaminación ambiental: cuestión de corresponsabilidad Management of Environmental Pollution: a matter of co-responsibility (2019)

Climatic Pattern Analysis Using Neural Networks in Smart Agriculture to Maximize Irrigation Efficiency in Grass Crops in Rural Areas of Ecuador

Evelyn Bonilla-Fonte, Edgar Maya-Olalla, Alejandra Pinto-Erazo, Ana Umaquinga-Criollo, Daniel Jaramillo-Vinueza, and Luis Suárez-Zambrano(✉)

Universidad Técnica del Norte, Avenida 17 de Julio 5-21 y General María Córdoba, 100105 Ibarra, Ecuador
{eamaya,lesuarez}@utn.edu.ec

Abstract. This project describes the development of a system that allows to improve the efficiency of a sprinkler irrigation system based on sensor networks and artificial neural networks. The WSN network is composed of a sensor node, a central node, and an actuator node. The sensor node consists of soil moisture, UV radiation, temperature, and rain sensors. The data collected by the sensor node is sent to the central node or Gateway through LoRa communication where the neural network is trained. The neural network makes predictions of irrigation status it predicts when the crop needs irrigation. Subsequently, the actuator node executes order sent from central node; activates or deactivates the solenoid valve allowing or denying the water flow to the sprinklers. A comparison between the manual irrigation system and the automated system with the neural network, where it is verified that automated system reduces water consumption and contributes to the development grass crop.

Keywords: LoRaWAN · smart irrigation · neural network · precision agriculture

1 Introduction

In [1], a drip irrigation system specifically designed for vegetable crops has been developed, utilizing fuzzy logic as its foundation. This system comprises a Wireless Sensor Network (WSN) that wirelessly collects and transmits data to a control station through Zigbee technology. At the control station, the data is analyzed, and the solenoid valve's opening time for crop irrigation is determined. Parameters such as irrigation durations and solenoid valve operation times are managed. Although this system automates part of the process, it still relies on operator intervention and does not harness IoT-oriented communication technologies.

M. Z. Vizuete et al. (Eds.): CI3 2023, LNNS 1040, pp. 281–298, 2024.
https://doi.org/10.1007/978-3-031-63434-5_21

On the other hand, in [2], a drip irrigation control system applying machine learning techniques to precision agriculture in alfalfa crops is proposed. Data is collected from a Sensor Network, as described in [3], consisting of input parameters processed in an artificial neural network that decides whether irrigation is necessary. Wireless communication is achieved through LoRaWAN modules. However, this system lacks an IoT platform enabling real-time sensor data visualization and access from any location and moment.

Considering the aforementioned projects focused on addressing drip irrigation challenges in greenhouses for various crops, we propose the design of an intelligent irrigation system tailored to open-field agriculture, with a focus on grass cultivation using the sprinkler irrigation method. This system acquires data from a Wireless Sensor Network used as input variables for an Artificial Neural Network that establishes behavioral rules. This enables the system to make predictions and determine whether the crop requires irrigation or not. The algorithm's resulting decision is wirelessly transmitted to an actuator node responsible for activating a solenoid valve controlling water flow in the grass crop via sprinklers. The process continues as described below.

Starting from the design, programming, implementation, and testing of a LoRa-based Wireless Sensor Network (WSN) [4] for a smart irrigation system in a grass cultivation area in the rural zone of the Tocachi parish, Pedro Moncayo canton in Pichincha province, real-time sensor data is collected. This data is visualized and analyzed through an IoT platform. In addition, key parameters of the wireless link such as path loss, receiver power, signal-to-noise ratio, link budget, and Fresnel zone are analyzed. During this phase, artificial intelligence techniques and neural net-works are applied to improve the efficiency of the sprinkler irrigation system in the grass cultivation. Behavior rules are established, and predictions are made to determine the appropriate time for irrigation. The commands are transmitted through the LoRa wireless link to an actuator node with a solenoid valve. Comparative tests are also conducted between the grass cultivation using the automated irrigation system and the cultivation that continues to use manual irrigation. Aspects such as grass growth, leaf coloration, plant height, and root size are evaluated. The document is structured into sections covering the materials and methods used, hardware and software design, results and discussion obtained through the neural network, as well as conclusions and recommendations.

2 Methods

The proposed topology consists of three nodes: Sensor Node, Central Node (Gateway), and Actuator Node [5], as shown in Fig. 1.

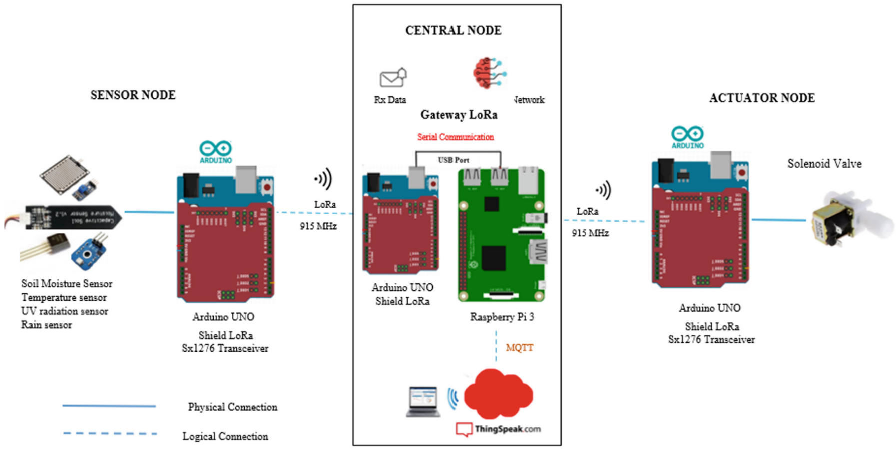

Fig. 1. General System Architecture

2.1 Current Situation

In the first phase, a star-type communication [6] was established using LoRa technology [7] between the Sensor and Actuator nodes towards the Gateway, located in the central node. The data collected by the sensors is transmitted to the central node through the MQTT protocol [8] and displayed on an IoT platform. In the second phase, the neural network is trained to predict irrigation in the grass cultivation. The central node is responsible for sending the command to the actuator node to activate or deactivate the solenoid valve. The execution of the neural network takes place on a Raspberry Pi 3 using Python programming, selected for its low computational load. The actuator node consists of an Arduino UNO and a LoRa transceiver. A 4-channel Relay Shield module is also used to control the opening or closing of the solenoid valve. Once the wireless connection is established, the sensor node's variable data is stored in the Gateway. However, these data cannot be transformed into useful information for the automatic sprinkler irrigation system without proper processing.

2.2 System Design

The soil moisture, temperature, UV radiation, and rain sensors collect data through the sensor node, which is used as a training set for an artificial neural network that makes predictions on when the crop needs to be irrigated and sends a command to the central node to activate or stop irrigation through the solenoid valve. To provide a visual understanding of how the neural network operates in the system, Fig. 2 is shown.

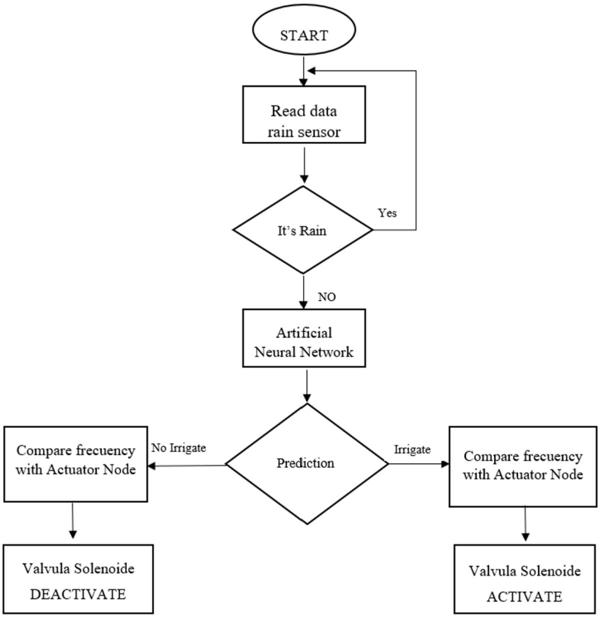

Fig. 2. Flowchart of the neural network application

2.3 Power Supply

The system is powered with 3–5 volts at the sensor node, as well as 3.7–12 V at the actuator node, since each node consumes 173.36 mA and 323.3 mA, respectively, in normal state. The actuator node, like the sensor node, has a lithium battery charging system through a solar panel. The power board includes a TP4056 module for charging the lithium battery and a DC-DC boost converter MT3608 that converts the 3.7V input voltage to 12V to power the solenoid valve.

2.4 System Encoding

The actuator node uses the same LoRa communication parameters as the central node. The training of the neural network is conducted in five stages.

The stages are developed as follows:

Data Collection. It involves gathering data acquired by the sensors in the WSN network, which serves as input for the neural network learning process.

Data Processing. This process involves managing the data obtained from variables such as soil moisture and UV radiation. A total of 8822 data points were obtained, and ranges were assigned to determine a decision based on these two variables: soil moisture and UV radiation.

The node issues a command to not irrigate if the soil is moist or very moist, regardless of the UV radiation. On the other hand, it is decided to irrigate when the soil is dry or very dry, if the UV radiation is low, moderate, or high. If the UV radiation is high, the decision is not to irrigate. Figure 3 presents four ranges for the soil condition and five ranges for UV radiation. The decision to irrigate (1) or not irrigate (0) the grass crop is based on the soil condition and UV radiation.

DATASET

SOIL MOISTURE SENSOR		
Wet	200-298	1
Moist	299-349	2
Dry	350-449	3
Very dry	450-550	4

UV RADIATION SENSOR		
Low	(1-2)	1
Moderate	(3-4-5)	2
High	(6-7)	3
Very high	(8-9-10)	4
Extremely high	11	5

Decision	
Irrigate	1
No Irrigate	0

Soil Moisture			Uv Radiation			Decision	
Very dry	491	4	Moderate	3	2	Irrigate	1
Very dry	489	4	Moderate	3	2	Irrigate	1
Very dry	489	4	Moderate	3	2	Irrigate	1
Very dry	489	4	Moderate	3	2	Irrigate	1
Very dry	483	4	Moderate	3	2	Irrigate	1
Very dry	484	4	Moderate	3	2	Irrigate	1
Very dry	482	4	Moderate	3	2	Irrigate	1
Very dry	481	4	Low	2	1	Irrigate	1

dataset | Hoja3 | train | train_2 | Hoja1 | Hoja2

Fig. 3. Treatment of soil moisture and UV radiation data

Creation of the Neural Network. The structure of the neural network is defined with input, output, and hidden layers. The number of neurons in each layer is determined. The input layer receives data from the environmental variables, the output layer provides the response of the neural network, and the hidden layer captures specific features of the environment being modeled [9]. In the input layer, two neurons are used for soil moisture and UV radiation variables, while in the output layer, one neuron is used for the irrigation decision (to irrigate or not to irrigate). The number of neurons in the hidden layer is not fixed but can be calculated using the geometric pyramid rule. For a three-layer network with a single hidden layer, Eq. 1 [9] is used.

$$h = \sqrt{m \cdot n} \tag{1}$$

where h is the initial number of neurons in the hidden layer, m is the number of neurons in the output layer, and n is the number of neurons in the input layer, it is obtained that the number of neurons in the hidden layer is 1.4 neurons. However, it would not be feasible to have enough data for prediction. Therefore, the number of neurons in a network with two hidden layers, h1 for the first hidden layer and h2 for the second hidden layer, is determined following Eq. 2 and Eq. 3 [10].

$$h_1 = m \cdot r^2 \tag{2}$$

$$h_2 = m \cdot r \tag{3}$$

where:

$$r = 3\sqrt{\frac{n}{m}} = 3\sqrt{\frac{2}{1}} = 4.24 \tag{4}$$

Replacing the values in Eqs. 2 and 3, we find that the number of neurons in the first hidden layer is 18, and in the second hidden layer it is 4,24.

$$h_1 = 1 \cdot (3\sqrt{2})^2 = 18 \tag{5}$$

$$h_2 = 1 \cdot 3\sqrt{2} = 4.24 \tag{6}$$

To obtain the optimal number of neurons, it is necessary to train and evaluate the network with different numbers of neurons for the hidden layers until achieving satisfactory performance. Therefore, the flow described in Fig. 4 should be followed.

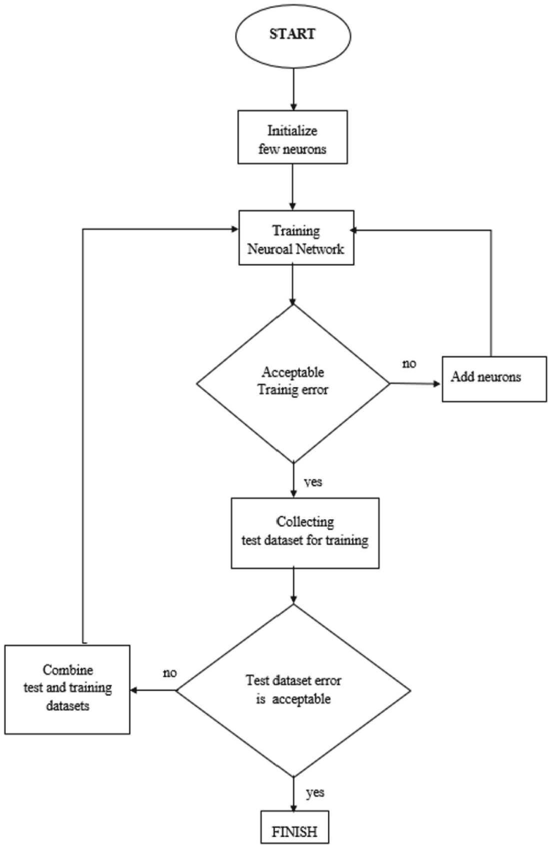

Fig. 4. Flowchart to determine the number of neurons and hidden layers. Adapted from "Design of Multilayer Neural Networks". [11]

Training the Neural Network. The development environment is set up using the Anaconda Navigator interface, which provides access to Jupiter Notebook as a web application. This allows for importing the necessary libraries to execute the neural network training code. The training dataset with 8822 rows and three columns: humidity, radiation, and decision. The data is graphically visualized, where the X-axis represents soil moisture, and the Y-axis represents UV radiation. In the graph, the gray area indicates the irrigation decision made by the system, while the red area indicates that the system should not irrigate (Fig. 5).

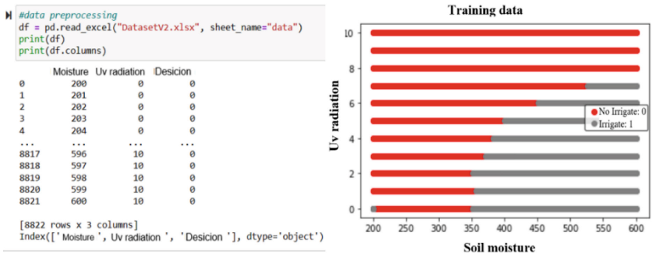

Fig. 5. Data preprocessing and graphical representation of trained data.

The first model initially consists of an input layer, two hidden layers, and an output layer, with eighteen neurons in the first hidden layer and four neurons in the second hidden layer [12]. However, this model fails to achieve the desired prediction and does not fit the training data properly. Therefore, in the second model, it is decided to increase the number of neurons in the hidden layers to twenty neurons. Although this model shows positive results, it does not fulfill the prediction for values according to the training data. Therefore, it is decided to increase the number of neurons in each hidden layer to one hundred neurons, according to the third training of the neural network, which allows for more accurate predictions with respect to the dataset. Hence, this model is selected as the most suitable one, See Fig. 6, Fig. 7, Fig. 8.

Activation Functions: These are used to establish the relationship between nodes when moving from one layer to another. In the hidden layers, the ReLU function is used to transform the input values by nullifying the negatives and preserving the positives. On the other hand, in the output layer, the sigmoid function is used, which produces an output in the range of 0 to 1, suitable for binary classification [13].

Learning Algorithm: The backpropagation algorithm is used, which allows the transmission of an input pattern through the different layers of the neural network to obtain an output. Then, a training stage is conducted where the network weights are adjusted to improve its performance.

Hyperparameters: They allow controlling the training process of this model, which can be divided into two phases: compilation and fitting.

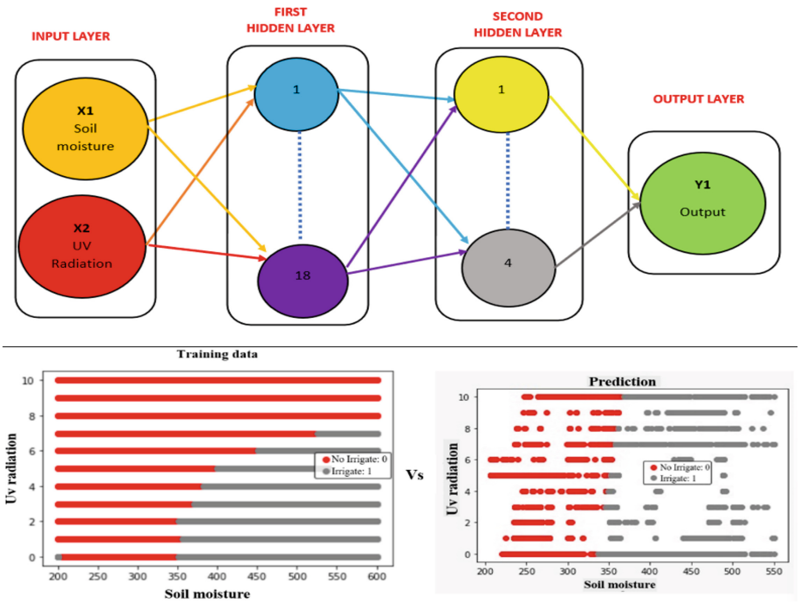

Fig. 6. Training result with the first model.

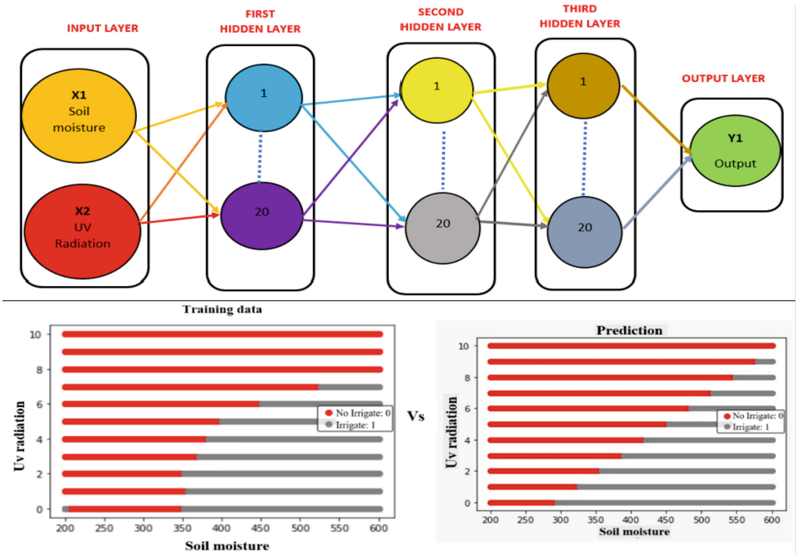

Fig. 7. Training Result with the second model.

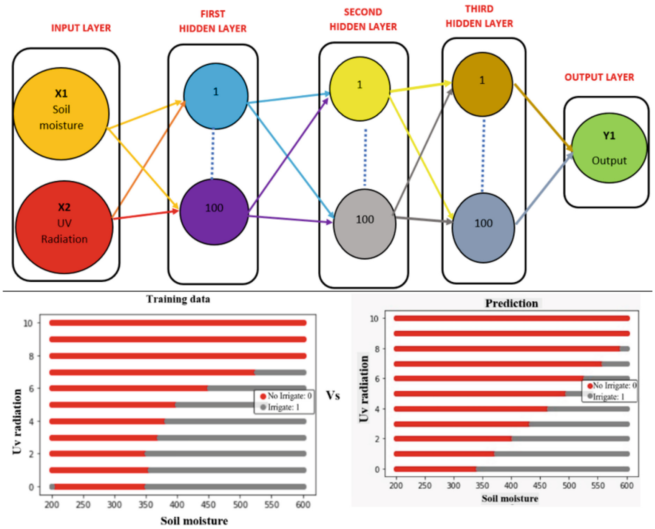

Fig. 8. Training Result with the third model

Compilation: The optimizer, loss function, and list of metrics are defined.

– Optimizer: In this model, the Adam optimizer is used, which adapts the learning rates individually for each parameter. A higher value of this parameter will require more epochs (training iterations) to make subtle changes to the weights in each update.
– Loss function: In this case, the Binary Cross-Entropy loss function is used, which evaluates how accurate the model's predictions are. This function compares the output of the sigmoid function (sigmoid activation function) with the two possible categories: 1 (irrigate) and 0 (do not irrigate).
– List of metrics: Accuracy represents the fraction of correct predictions made by the model, while loss indicates how incorrect the model's predictions have been. If the prediction is perfect, the loss will be zero. These aspects help measure the performance and quality of the model during its training and evaluation.

Fitting: These include the inputs (x) and outputs (y), representing the soil moisture, UV radiation data, and the irrigation results, respectively. The batch size is also included, which defines the number of data points used in each update of the internal parameters. Additionally, the number of epochs is specified, indicating how many times the entire dataset is worked with. Lastly, the validation split is mentioned, determining the percentage of in-put data used exclusively for evaluating the model during training. In this study, it corresponds to 0.3 of the totals provided data.

Testing and Validation of the Neural Network: There are a lot of record of training metrics for each epoch. This includes the model's loss and accuracy during training, as well as the loss and accuracy of the validation dataset. The metric "accuracy" represents the accuracy of the training dataset, while "val_accuracy" represents the accuracy of the validation dataset. On the other hand, "loss" corresponds to the loss of the training dataset, and "val_loss" represents the loss of the validation dataset. The accuracy in both the training and validation datasets indicates that the model has been fully trained, as there is no observed increase in the accuracy trend in the later epochs.

2.5 Actuator Node

The central node utilizes the predictions from the neural network to control the solenoid valve that regulates the water flow to the sprinklers in the grass crop. Communication between the central node and the actuator node is established using LoRa, with a transmission power of 20 dBm, spreading factor SF7 [14], bandwidth of 125 kHz, and error coding rate of 4/5. These parameters are observed in Fig. 9.

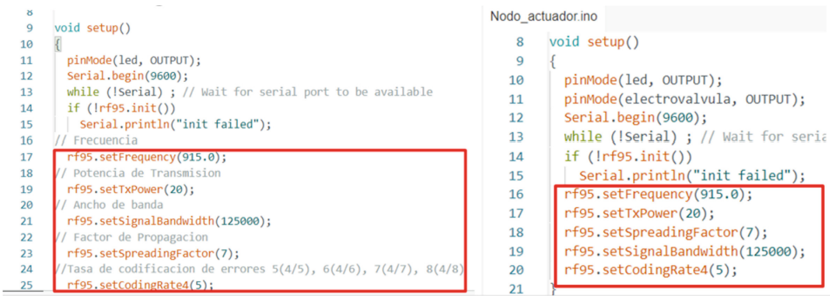

Fig. 9. Basic configurations of the central node and actuator node.

3 Results and Discussion

After designing the sensor network, an electrical test of the system was realized. During this test, sensor information was collected and wirelessly received at the central node using LoRa technology. Additionally, the behavior prediction of the neural network and actuator node was performed.

3.1 Electrical Test

Figure 10 shows the verification of the activation of each device in the system through LED indicators. Functionality tests were performed on the power board, first without the solar panel connection, and then with the solar panel connected.

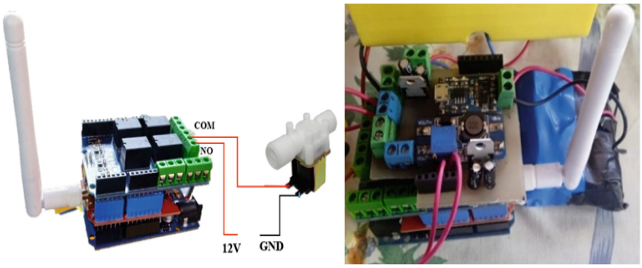

Fig. 10. Actuator node powered by a lithium battery.

3.2 Neural Network Prediction

The environmental variable data captured by the sensors and the predictions from the neural network can be visualized on the central node using the Tonny Python integrated development environment shell. For the neural network training model to run, the rainfall sensor value needs to be above 500, indicating the absence of rain.

In Fig. 11, the following details can be observed: in the first section, the rainfall sensor value is 1023, which activates the model execution. The UV radiation sensor shows a value of 0 (indicating low UV radiation), and the soil moisture sensor exceeds 450 units, indicating that it is very dry. As a result, the neural network prediction is "Irrigate" with a value of 1.0. On the other hand, in the second section, the soil moisture sensor value is below 350, indicating that the soil is moist. In this case, the neural network prediction is "Do not irrigate".

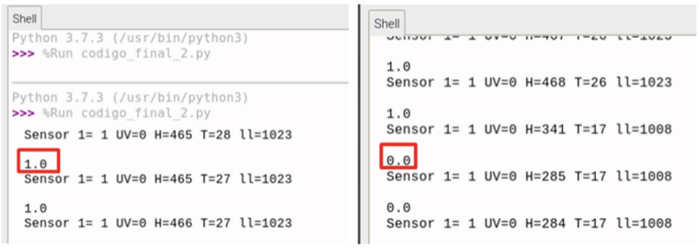

Fig. 11. Neural Network Prediction. Case 1 - Irrigate. Case 2 - Don't irrigate.

3.3 Actuator Node Behavior

The system communicates wirelessly via LoRa from the central node to the actuator node, which is located 160 m away. The system is protected by a sealed casing, shielding the devices from external agents such as water, heat, and humidity, as shown in Fig. 12.

Fig. 12. Sensor, central, and actuator nodes that make up the wireless sensor network (WSN).

In the prototype shown in Fig. 13, the following components are located as follows: the sensor node is situated 160 m away in the grass crop, the central node is in the user's home and is protected from external agents. Lastly, the actuator node is placed in the secondary pipe of the plot, and the solenoid valve is responsible for activating and deactivating the water flow according to the irrigation prediction sent by the central node.

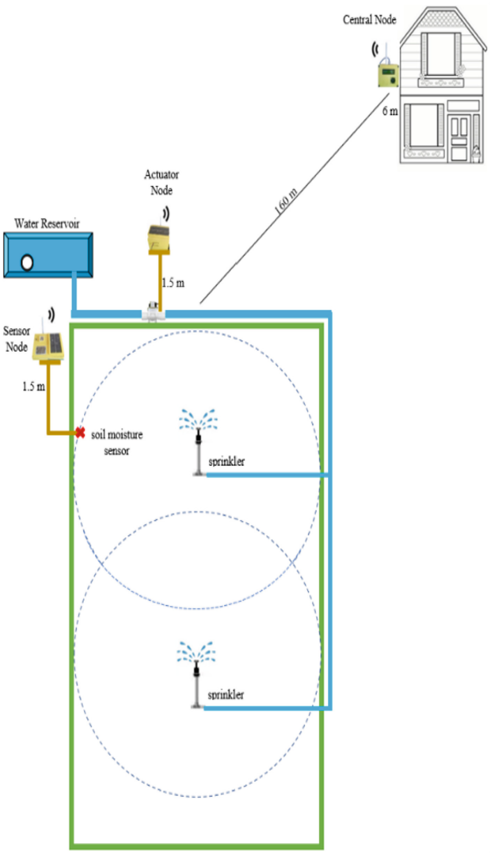

Fig. 13. Location of the nodes in the plot.

3.4 Water Consumption Analysis

The system undergoes testing on a 1000 m^2 plot equipped with two rotating sprinklers. In manual irrigation mode, the sprinklers operate continuously for 3 to 5 h, assuming full irrigation. With the automated system, the time and water consumption are calculated from the moment the neural network predicts the need for irrigation until it stops when the soil reaches the desired moisture level.

In Fig. 14, the system activates irrigation (1) at 18:08 and stops it (0) at 18:46, with an irrigation time of less than one hour on a completely dry grass plot.

Date	Soil moisture	Temperature	UV Radiation	Irrigation Prediction	Rain
2022-10-05T18:08:56	415	21	0	1	0
2022-10-05T18:10:23	416	21	0	1	0
2022-10-05T18:10:48	415	22	0	1	0
2022-10-05T18:11:07	415	23	0	1	0
2022-10-05T18:11:27	414	22	0	1	0
2022-10-05T18:11:48	415	21	0	1	0
2022-10-05T18:12:14	440	22	0	1	0
2022-10-05T18:12:34	453	21	0	1	0
2022-10-05T18:13:08	480	23	0	1	0
2022-10-05T18:15:12	482	22	0	1	0
2022-10-05T18:16:33	483	22	0	1	0
2022-10-05T18:17:59	484	56	0	1	0
2022-10-05T18:19:25	484	21	0	1	0
2022-10-05T18:20:45	480	21	0	1	0
2022-10-05T18:22:12	479	21	0	1	0
2022-10-05T18:25:38	477	21	0	1	0
2022-10-05T18:26:57	451	22	0	1	0
2022-10-05T18:27:17	472	22	0	1	0
2022-10-05T18:29:37	463	21	0	1	0
2022-10-05T18:32:58	439	21	0	1	0
2022-10-05T18:33:19	430	21	0	1	0
2022-10-05T18:33:43	450	22	0	1	0
2022-10-05T18:34:12	467	15	0	1	0
2022-10-05T18:34:32	462	15	0	1	0
2022-10-05T18:35:00	451	15	0	1	0
2022-10-05T18:35:24	440	15	0	1	0
2022-10-05T18:35:51	410	15	0	1	0
2022-10-05T18:36:14	405	15	0	1	0
2022-10-05T18:37:37	400	15	0	1	0
2022-10-05T18:38:04	398	16	0	1	0
2022-10-05T18:39:28	398	21	0	1	0
2022-10-05T18:40:48	395	22	0	1	0
2022-10-05T18:41:23	391	21	0	1	0
2022-10-05T18:43:27	391	18	0	1	0
2022-10-05T18:44:14	385	16	0	1	0
2022-10-05T18:45:34	364	15	0	1	0
2022-10-05T18:46:28	341	16	0	0	0

Fig. 14. Database of the irrigation status, retrieved from ThingSpeak. 1 = Irrigate, 2 = No irrigate

Table 2 presents a comparison of the results obtained between the manual irrigation system vs the automated irrigation system with the neural network over a period of 15 days (Table 1).

3.5 Grass Crop Analysis

An evaluation of the grass crop's development is conducted after the defoliation stage when implementing the automated irrigation system with the neural network. Over a 15-day period, the growth and leaf coloration are observed as the plant recovers its leaf area. Figure 15 presents three images: the first shows the grass during the defoliation stage, the second shows the crop using the automated irrigation system, and the third shows the grass crop using manual irrigation.

The results are remarkable and evident. The automated irrigation system has successfully provided appropriate water dosing, reflected in the emergence of new leaves with elongated growth and vibrant green color. Additionally, it has generated uniform regrowth in the grass crop. In Fig. 16, it can be observed that in the automated irrigation system, the roots are thin, elongated, and abundant, unlike the manual irrigation system where the roots are smaller, thicker, and have not achieved sufficient depth.

Table 1. Water consumption using the manual irrigation system vs the automated irrigation system.

Day	MANUAL IRRIGATION SYSTEM		AUTOMATED IRRIGATION SYSTEM	
	time (hours)	Consumption (m3)	time (hours)	Consumption (m3)
1	5:00	5.4	1:30	1.62
2	3:00	3.24	1:36	1.72
3	0:00	0	0:55	0.99
4	5:00	5.4	1:35	1.7
5	3:00	3.24	1:36	1.72
6	3:00	3.24	1:35	1.7
7	0:00	0	2:11	2.35
8	3:00	3.24	0:00	0
9	5:00	5.4	1:50	1.98
10	0:00	0	2:28	2.66
11	5:00	5.4	0:00	0
12	3:00	3.24	2:04	2.23
13	3:00	3.24	2:17	2.46
14	0:00	0	0:00	0
15	5:00	5.4	1:42	1.83
	TOTAL: 46.44		TOTAL: 22.03	

Fig. 15. a. Defoliation, b. Grass with automated irrigation, c. Grass with manual irrigation.

Fig. 16. Root size with manual irrigation and automated irrigation.

4 Conclusions

- The electrical test demonstrated that the power supply board continuously provides power to the actuator node for approximately 22 h.
- The TP5046 charging module features a micro-USB port to recharge the system's battery with 5 V, if necessary.
- The neural network's response to environmental variables is optimal, activating when the rain sensor indicates the absence of rain, which prevents unnecessary activation of the irrigation system. Additionally, the accuracy of the predictions made by the neural network has been verified.
- The communication between the central node and the actuator node is successful, as they are located at the same distance and use the same LoRa communication parameters, ensuring efficient transmission and reception of information.
- The behavior of the actuator node is correct, activating the solenoid valves if the neural network prediction is "Water" and properly deactivating them if the prediction is "No Water."
- An automated sprinkler irrigation system has been successfully implemented using artificial neural networks to predict irrigation in grass crops.
- The neural network model used consists of an input layer with two neurons, three hidden layers with one hundred neurons each, and an output layer. After experimentation, it was determined that 5000 training epochs are optimal for effective learning without overfitting.
- According to the predictions of the neural networks, it is observed that the sprinkler irrigation system irrigates the crop during dawn and dusk, which promotes water absorption and soil filtration by reducing evaporation compared to direct sun exposure.
- It has been found that the manual sprinkler irrigation system consumes approximately 46.44 mm^3 of water, while the automated system with neural networks consumes around 22.03 mm^3, representing a difference of 15.89 mm^3. These results demonstrate that the automated system significantly improves the efficiency of sprinkler irrigation.
- While the growth and development of a grass crop depend on factors such as soil and nutrients, proper water distribution in the crop contributes positively to its development.

5 Recommendations

- It is crucial to ensure that the gateway has a stable internet connection to achieve efficient packet routing and enable data visualization in the cloud.
- To enhance the precision of irrigation prediction, it is advisable to incorporate supplementary variables, such as wind speed and the occurrence of mist/fog, given their significance in a sprinkler irrigation system. By considering these factors, the accuracy of the irrigation predictions can be improved, resulting in more efficient water distribution and optimized irrigation practices.

– To ensure optimal performance, it is recommended to perform an initial charge of the sensor and actuator nodes' lithium batteries through the micro-USB port. This will help maximize their battery life and overall functionality. By starting with a full charge, the nodes will be better equipped to carry out their tasks effectively and reliably in the automated irrigation system.
– It is important to ensure a clear line of sight between the end node and the gateway, as the presence of obstacles can weaken the transmitted signal. This may require adjustments in the network design during the development process.
– Careful selection of data used to train the neural network is crucial, as the network will learn from this data. The quality and representativeness of the data will influence the network's ability to make accurate predictions.
– Determining the optimal number of layers and neurons in the hidden layer of a neural network can be challenging. It is recommended to perform testing and adjustments to find the appropriate configuration, as this process may require a trial-and-error approach.
– Like the layer and neuron configuration, finding the right number of training epochs or iterations also involves a trial-and-error process. An optimal number of iterations must be found that avoids both overfitting and underfitting of the network.

References

1. Leandro, S.: Diseño de un sistema de riego inteligente para cultivos de hortaliza basado en Fuzzy Logic en la granja La Pradera de la Universidad Técnica del Norte, Universidad Técnica del Norte, 2019
2. Dario, C.: Diseño de un sistema para el control de riego mediante técnicas de aprendizaje automático aplicadas a la agricultura de precisión en la granja La Pradera de la Universidad Técnica del Norte, Universidad Técnica del Norte, 2020
3. Dominguez, A.: Diseño de una red de sensores inalámbricos LPWAN para el monitoreo de cultivos y materia orgánica en la granja experimental La Pradera de la Universidad Técnica del Norte, Universidad Técnica del Norte, 2020
4. Santamaría, F., Archila, D.: Estado Del Arte De Las Redes De Sensores Inalámbricos. Tecnol. Investig. Acad. **1**(2) (2013)
5. Fernández, R., et al.: Redes inalámbricas de sensores: teoría y aplicación práctica, 2009
6. Nayibe, C.C., Tibaduiza, D., Aparicio, L., Caro, L.: Redes de sensores inalámbricas. J. Pediatr. Adolesc. Gynecol. **24**(6), 404–9 (2011)
7. Semtech, Semtech SX1276 (2020). https://www.semtech.com/products/wireless-rf/lora-transceivers/sx1276
8. Poursafar, N., Alahi, M.E., Mukhopadhyay, S.: Long-range wireless technologies for IoT applications: a review. In: Proceedings of the International Conference on Sensing Technology, ICST, vol. 2017-Decem, pp. 1–6 (2017). https://doi.org/10.1109/ICSensT.2017.8304507
9. Zepeda Hernandez, J.Á., Aguilar Castillejos, A.E., Hernandez Sol, Á., Salgado Gutiérrez, M.C.: Metodología para determinar la topología, patrones de parámetros eléctricos y entrenamiento de una Red Neuronal Artificial para un control inteligente. Rev. Tecnol. Digit. **5**(1), 103–113 (2015)

10. Pano Azucena, A.D.: Realización FPGA de una Red Neuronal Artificial para Reproducir Comportamiento Caótico, p. 97 (2015)
11. ESCOM, Diseño de redes neuronales multicapa (2019). https://es.slideshare.net/mentelibre/diseo-de-redes-neuronales-multicapa-y-entrenamiento. Accessed 14 July 2023
12. ¿Qué es una red neuronal? — TIBCO Software. https://www.tibco.com/es/reference-center/what-is-a-neural-network. Accessed 14 July 2023
13. Acevedo, E., Serna, A., Serna, E.: Principios y características de las redes neuronales artificiales. Desarrollo e innovación en ingeniería, no. March 2019, pp. 173–183 (2017)
14. Solera, E.: Modulación LoRa: long range modulation. Medium 1–10 (2018)

Data Lake Optimization: An Educational Analysis Case

Viviana Cajas-Cajas[1(✉)], Diego Riofrío-Luzcando[2], Joe Carrión-Jumbo[1], Diana Martinez-Mosquera[3], and Patricio Morejón-Hidalgo[1]

[1] Universidad Internacional SEK, Quito, Ecuador
{viviana.cajasc,joe.carrion,victor.morejon}@uisek.edu.ec
[2] Universidad San Francisco de Quito, Quito, Ecuador
driofriol@usfq.edu.ec
[3] Escuela Politécnica Nacional, Quito, Ecuador
diana.martinez@epn.edu.ec

Abstract. This study focuses on enhancing the performance of Universidad Internacional SEK's (UISEK) Data Lake by addressing challenges in computing resource consumption from a prior data lake implementation. Notably, data has been sourced from the Canvas Learning Management System based on the university's usage since 2019 for both implementations. The restructuring, carried out through three layers, successfully mitigated previous computing resource challenges.

Following the CRISP-DM framework, the new approach exhibited substantial improvements over the previous version. Results include a 73.1% reduction in the estimated size of the last dump, 51.7% more efficient storage utilization in the user behavior table, and a 4.3% improvement in CPU consumption. Additionally, showcased a 50% reduction in ingestion time.

The study emphasizes the significance of a well-organized Data Lake governance structure for streamlined data management. The presented improvements lay a solid foundation for future analyses and machine learning models. Moreover, the study underscores the role of automated processes in maintaining an updated Data Lake, ensuring its relevance for decision-making at UISEK. Overall, this work contributes to advancing the efficiency and performance of educational Data Lakes, providing valuable insights for decision-making and continuous enhancement of the educational experience.

Keywords: API REST · data lake · Data Science · HDFS · LMS Canvas · optimization

1 Introduction

"Data Lake" is a term coined in 2010 by Dixon (2010), sometimes erroneously associated solely with a marketing label. However, it refers to a massively scalable storage repository containing a large amount of raw data in its native format until further processing systems (engine) are needed, capable of ingesting data without compromising data structure.

M. Z. Vizuete et al. (Eds.): CI3 2023, LNNS 1040, pp. 299–309, 2024.
https://doi.org/10.1007/978-3-031-63434-5_22

Additionally, it can integrate SQL and NoSQL database approaches, online analytical processing (OLAP), and online transaction processing (OLTP) capabilities. For this reason, McClure (2016), notes that yesterday's unified storage is today's enterprise data lake.

In this context, the Data Lake serves as a storage system for managing and analyzing data in line with institutional objectives. It addresses the challenge of heterogeneous data volumes within a business that are complex to process for decision-making.

Processes related to teaching and learning generate a vast amount of data with multiple potential applications. Cantabella et al. (2019) suggest that the current trend is towards harnessing Big Data to understand how university students experience and build knowledge, a valuable insight for universities assessing the impact of the teaching-learning process. Analyzing and drawing conclusions through Big Data enables a more accurate understanding of student usage patterns and preferences for virtual platforms, facilitating improvements in both physical and virtual teaching methodologies in real-time.

This work presents the case of the International SEK University (Universidad Internacional SEK Ecuador, 2023), offering undergraduate and postgraduate programs with a student community of 2500 as of 2023. The current issue is that data within Canvas's Learning Management System (LMS) isn't providing value to the administration because the analysis results are missing. Reasons for this include:

- Data not being processed.
- Many data points being forgotten.
- Loss of origin and purpose of the data.

As a partial solution, a proposal was made resulting in an initial architecture (Beltrán, 2022) outlined in a master's thesis. This involved implementing a Data Lake with Canvas LMS data from UISEK, storing it in a single repository with greater flexibility for subsequent data analysis, machine learning, and other applications. In the previous work, complete data was loaded into a Hadoop Distributed File System (HDFS) (Dwivedi & Dubey, 2014) directory created in a Hadoop environment through Canvas's API with Python scripts. Scripts were also generated to create directories in HDFS, tables in Hive, and automate data ingestion. Finally, a scheduled task was set up for daily execution of the described processes.

However, with daily use of the Data Lake, it was observed that computing resources, particularly RAM consumption, reached high limits. This was primarily attributed to a "requests" table, storing all records of each user, i.e., every click made by each student and teacher on the platform. Memory consumption occurred when updating the corresponding file for this table in HDFS, following the process explained in the aforementioned thesis.

Hence, a proposed architecture was introduced, focusing on restructuring the Data Lake into three layers (LT, STI, and CT). HDFS-created paths begin with /LT to identify the Academic Period directory, grouping unprocessed files for the same period, with data arriving in batches daily. Directories named LMS, SocialNetworks, WebServices, AcademisServices, and Sensors group data by source (Martinez-Mosquera et al., 2022).

This work presents the implementation and results of the proposed architecture outlined in the previously mentioned document.

2 Related Work

According to the findings of Romero & Ventura (2020), el Educational Data Mining (EDM) (Ashish et al., 2017) Educational Data Mining (EDM) (Ashish et al., 2017) emerged from the analysis of student-computer interaction log files that prevailed in the early years of the 21st century. The methods evolved from relationship mining to prediction, with a strong emphasis on learning and teaching, as evident in the work of Zaıane and Luo (Zaiane & Luo, 2001). They emphasized that the goal of EDM is to make learners effective, a focus contrasting with the early use of the term learning analytics (LA) by Mitchell & Costello (2000) to refer to business intelligence in e-learning.

Campbell et al. (2007) state that the growth of learning analytics is driven by the need to use insights gained from data analysis to make interventions aimed at improving learning, addressing factors such as the tension related to the impersonality of online systems, as addressed by Mazza & Dimitrova (2007). This sets the stage for a strong line of research in the field, leading to relevant studies related to the present work on data treatment in education:

Gewerc et al. (2016) conduct a case study of students using a social network as a learning context, employing Unicet and NetDraw as analytical tools with metrics such as network density to gauge collaboration intensity and node centrality. Using ADEGA, they extract information to analyze the content of student blog entries and automatically extract terms or words characterizing each entry. The results show interdependence between student-centered teaching and resulting Learning Analytics (LA) indicators.

Cravero et al. (2021) present an architecture for a Chilean university's Data Lake and metadata modeling, consisting of three data access zones, tested with a prototype implemented on AWS. It provides a metadata catalog for data analysts and third-zone (Gold) data for decision-makers, recording management indicators. The Data Lake manages data from survey files, relational databases, processed spreadsheets, and data stored in Data Warehouses. Additionally, applying ontologies highlights relationships between existing data. Future work aims to implement the Data Lake for all available data on a local server.

Oukhouya et al. (2022) propose a new big data architecture for educational systems covering multiple data sources. This architecture organizes data through layers, from managing different data sources to final consumption. The proposed approach includes the use of a data lake to modernize decision-making processes, particularly data warehouses and OLAP methods. It serves as a means of consolidating data for integrating heterogeneous data sources.

Seeling (2022) notes that despite the existence of various open-source Learning Management System (LMS) solutions allowing open access to data for learning analysis stakeholders, commercially prevalent solutions in the U.S. education system are often closed-code and closed-data. Therefore, this work provides an approach to enable research and implementations of open and open-source data within the confined environments of closed-code and closed-data commercial LMS implementations.

Kustitskaya et al. (2023) address the design of an educational database oriented towards educational management, primarily for student attention and learning analytics tasks. Implementing these principles may require significant changes to existing database infrastructures and training for university staff using database-related information systems.

All the aforementioned works underscore the growing importance of learning analytics for research and implementation in educational systems. However, none of them align precisely with the proposed approach. The following section details the methodology of the present work.

3 Methodology

The improvement of performance in data collection, storage, and querying within the Data Lake of Universidad Internacional SEK was addressed following the CRISP-DM framework (Schröer et al., 2021), providing a structured and systematic methodology. This approach breaks down into six interrelated stages, each crucial for the project's success.

The initial project phase focused on thoroughly understanding fundamental objectives, prioritizing the optimization of performance in data collection and storage within the university's Data Lake. A significant aspect was the creation of an on-premise virtualized environment to ensure a scalable and adaptable infrastructure, capable of meeting the institution's changing needs. Notably, the solution was installed on a cluster using commodity hardware with the following minimum specifications:

- Hypervisor Promox Virtual Environment
- 3 DataNodes
- 24 GB RAM
- 4 processors (2 sockets, 2 cores)
- Storage: 300 GB

Subsequently, a comprehensive analysis of data obtained from the Canvas LMS system was conducted. This analysis included transforming records into fact and dimension tables, following a star schema. This structure allowed for a clearer and deeper understanding of the data, especially in terms of academic performance and student engagement.

Data preparation became an essential phase, encompassing the selection of tables, records, and attributes, as well as data transformation and cleaning for use in modeling tools.

In contrast to focusing on model implementation, the project prioritized improving the performance and infrastructure of the Data Lake, emphasizing efficiency in data management over the creation of analysis models.

Initially, data extraction occurred through a REST API (Sohan et al., 2017) connected to Canvas LMS, downloading the complete dump. However, this approach proved inefficient due to the massive consumption of computational resources when bringing in all data with each dump. The proposed solution involved modifying the API to allow incremental data consumption, significantly reducing computational load and improving storage efficiency.

The API now identifies and transmits only the updated data since the last extraction. This approach minimizes resource usage while ensuring the integrity and constant update of information stored in the data lake.

3.1 Implementation Process

Identification of Changes: The REST API now tracks updates in Canvas LMS since the last synchronization.

Incremental Transmission: Only modified or added data is transmitted to the data lake, avoiding redundancy of previously stored information.

Atomized Update: An atomized update process is implemented to ensure the coherence and consistency of data stored in the lake.

Equation 1 reflects the essence of the incremental approach, reducing computational load and optimizing data storage in the data lake.

$$Dt = Dt - 1 \cap D\Delta t \tag{1}$$

where:

Dt corresponds to the total data at time t,

Dt − 1 is the previously stored data, and

DΔt represents changes in data since the last synchronization.

$\cap$ denotes the set intersection operation, ensuring that Dt contains only the updated or added data since the last extraction.

Figure 1 shows the implemented architecture, where a modified REST API allows incremental data consumption, reducing computational load by identifying and transmitting only changes since the last synchronization. This data is stored in a data lake implemented with Hadoop Distributed File System (HDFS) (Dwivedi & Dubey, 2014), from where it is extracted and loaded into Hive internal tables for processing. Finally, visualization is achieved using any presentation tool.

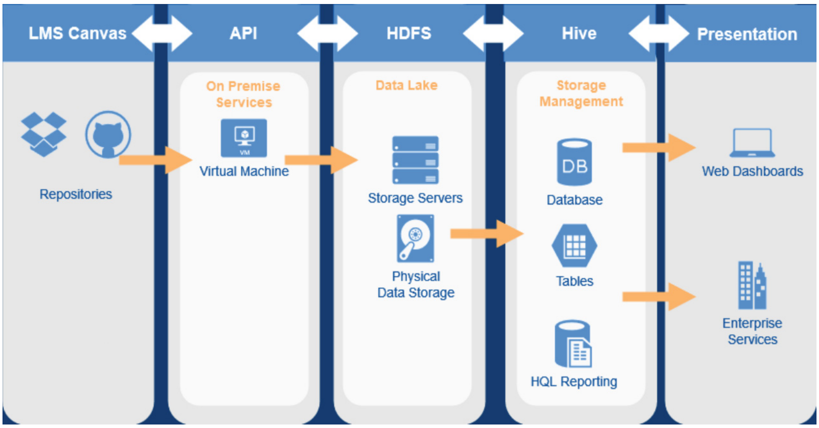

Fig. 1. Data Lake Architecture for Education.

The evaluation was a critical step in the process. Key metrics such as RAM and storage consumption were measured to compare a virtualized environment with the existing system, allowing for the assessment of the impact of improvements.

Finally, the results were deployed to ensure their effective utility. The acquired knowledge was presented clearly and accessibly to UISEK, considering specific needs and client skills to facilitate informed decision-making.

Additionally, an organizational data structure was established within the Data Lake, classifying historical and recent data in an orderly and accessible manner for use and analysis.

Complementary automated processes were implemented to generate the database and for the daily download and upload of the latest data from the Canvas Learning Management System. These automated processes ensure that the Data Lake is always updated and available for decision-making and educational analysis.

The structured approach throughout the different stages of the CRISP-DM framework has generated significant improvements in the infrastructure and performance of UISEK's Data Lake. These improvements ensure greater scalability, flexibility, and efficiency in data management and analysis, providing a valuable tool for decision-making and continuous enhancement of the educational experience.

3.2 Data Lake Governance

Structuring data in the Data Lake of Universidad Internacional SEK has been essential for organizing and classifying information logically and efficiently. A folder hierarchy has been adopted, all generated within the "bin" directory of the Hive installation, to facilitate data management and query. This organizational structure is presented in Fig. 2.

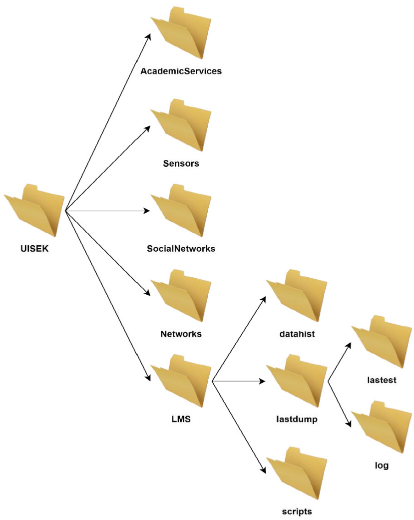

Fig. 2. Folder structure

The "LMS" subfolder within the "bin" folder of Hive contains specific subfolders:

- datahist: Stores historical data from the LMS, including past records and events relevant for the analysis and tracking of the LMS data's evolution over time.
- lastdump: Saves the latest data downloaded from the LMS, providing updated and relevant information for analysis and decision-making based on recent data.
- scripts: Stores codes used in database generation.
- Additionally, within the "lastdump" subfolder, two additional subfolders have been created:
- latest: Contains the most recently downloaded data, allowing quick and direct access to the most current information.
- log: Records events and activities related to the download and update of data in the last dump. This subfolder logs important data and metadata for detailed tracking of operations performed.

Furthermore, an automated process has been implemented for generating the database in the Data Lake, activated in the absence of the database or during the first execution of data download. This process involves a.py file that generates a.hql file with the necessary instructions to create the database and its corresponding tables. These instructions are executed in the Hadoop environment using appropriate commands.

Moreover, an automated process has been developed for the download and upload of the latest data from the Canvas Learning Management System (LMS). A file named "last_dump.py," located within the "lastdump" folder, performs this action, scheduled to run daily at 4 am using the Crontab tool (Xu et al., 2014). This process involves downloading files from the last dump via the Canvas Data API, verifying and copying them into the Hadoop environment (HDFS), maintaining a detailed record of activities and performance metrics. The next section presents the results obtained after applying the proposed approach.

4 Results

The results obtained after implementing the improvement of this Data Lake and automating the download and upload of the latest dump from LMS Canvas were analyzed, focusing on the resources used during the process and corresponding measures to evaluate the system's performance and efficiency on two virtual machines named DataLakeCANVASDev and DATACANVAS. DataLakeCANVASDev represents the previous version with the mentioned issues at the beginning of this article.

For this analysis, the available resources on the respective virtual machines were considered, where DataLakeCANVASDev has 300 GB of storage and 31.25 GB of RAM, while DATACANVAS has 300 GB of storage and 23.44 GB of RAM.

It is important to highlight the two different approaches implemented in the virtual machines DataLakeCANVASDev and DATACANVAS. In DataLakeCANVASDev, the combination of operations related to the download and upload of the lastDump, along with the historical file, posed memory management challenges. The gradual accumulation of data due to integrating the lastDump into the historical file made it difficult to precisely identify the individual size of the lastDump, estimated at approximately 3.4 GB at the end of the DataLakeCANVASDev version.

On the contrary, DATACANVAS implemented a more direct and efficient approach, where the lastDump is incorporated directly into the latest, avoiding additional operations that could impact memory management. This simplified strategy allowed a clear identification of the individual size of the lastDump, estimated at 915 MB, providing an accurate measure of its dimension compared to the complete dataset.

The results showed significant differences in the size of the "request" table between the two versions. In DataLakeCANVASDev, the table exhibited a size of around 282.89 GB, while in DATACANVAS, considering the inclusion of all data from the first dump, it presented a size of approximately 136.79 GB.

The implementation of the DATACANVAS version of the Data Lake revealed substantial improvements in performance and efficiency compared to the DataLakeCANVASDev version. Optimization of CPU and memory usage, along with a significant reduction in runtime, ensured a smoother and more effective experience in data collection, storage, and querying in the Data Lake of Universidad Internacional SEK. These improvements provide a solid foundation for data analysis and informed decision-making in the educational environment of the institution.

Table 1 presents a comprehensive summary of the results obtained, highlighting key similarities and differences in terms of storage, CPU, and efficiency. Both machines exhibit similar storage and CPU configurations, but there is a disparity in RAM, with 31.25 GB used in DataLakeCANVASDev and 23.44 GB in DATACANVAS.

Table 1. Comparison of Resources and Efficiency between DataLakeCANVASDev and DATACANVAS

Virtual Machines	DataLakeCANVASDev	DATACANVAS
Storage (GB)	300	300
RAM (GB)	31.25	23.44
CPU Consumption (%)	17.23	16.5
Ingestion Time (minutes)	20	10
Implementation Approach	Combination of operations	Direct and efficient approach
Estimated lastDump Size (GB)	Aprox. 3.4	0.915
"request" Table Size (GB)	282.89	136.79
Number of Records in "request" Table (millions)	7.32	39499.56

The choice of the implementation approach reveals a crucial point of differentiation: DataLakeCANVASDev opted for a combination of operations, while DATACANVAS implemented a direct and efficient approach. This strategic decision resulted in notable improvements, evidenced by the 73.1% reduction in the estimated size of the lastDump in DATACANVAS, decreasing from 3.4 GB to 0.915 GB.

Efficiency is further accentuated in the size of the "request" table, where DATACANVAS proves to be 51.7% more efficient than DataLakeCANVASDev, with a size of 136.79 GB compared to 282.89 GB, respectively. These results indicate substantial optimization in the system's performance and efficiency with the implementation of the DATACANVAS version of the Data Lake.

Furthermore, other previously unexplained key results are highlighted, where DATACANVAS shows more efficient CPU consumption, with a 4.3% improvement (17.23% vs. 16.5%). The ingestion time also experiences a significant improvement, halving from 20 min in DataLakeCANVASDev to 10 min in DATACANVAS. Additionally, the number of records in the "request" table sees an impressive increase of 538,852% in DATACANVAS, reaching 39,499.56 million records, compared to 7.32 million in DataLakeCANVASDev. These complementary results reinforce the overall conclusion of notable improvements in efficiency and performance with the implementation of DATACANVAS in the Data Lake environment. Finally, conclusions and future work are presented in the next section.

5 Conclusions and Future Work

The adoption of a star schema for data storage proved to be a wise choice, facilitating analysis and access to relevant information. Organizing data into fact and dimension tables allowed a clear separation of fundamental data, simplifying understanding and exploration. Data preparation processes, including selection, transformation, and cleaning, ensured the quality and consistency of stored information.

The differentiated approach between virtual machines in terms of operational efficiency is particularly noteworthy. The old version (DataLakeCANVASDev) involved additional operations such as data decompression, storage in files, and loading into the Hive database. In contrast, the new version (DATACANVAS) stands out for executing exclusively necessary operations, demonstrating a more efficient and results-focused approach.

The Data Lake provides a solid foundation for future analyses and models that can extract valuable insights for the university. Results from the DATACANVAS version exceeded expectations, showing a significant improvement in system performance and efficiency. Reduced memory and storage usage, along with an approximate runtime of 10 min for the download and upload process, ensure fast and up-to-date access to data.

The hierarchical organization of folders in the Data Lake, specifically in the "LMS" section, facilitated the storage and access of historical and latest dump data. This organized structure allows for easier management and intuitive navigation of information. The automation of downloading and loading the latest dump ensures that information is always updated and available for analysis and decision-making. The optimization in resource usage and overall system performance in the DATACANVAS version emphasizes the importance of having appropriate infrastructure and a well-defined strategy for data management.

Furthermore, the implementation of these automated processes ensures that the Data Lake is always up-to-date with the latest data from the LMS Canvas, providing Universidad Internacional SEK with access to current and relevant information for decision-making and educational analysis. This automation enhances the efficiency and reliability of the system, establishing the Data Lake as a powerful source of information for the institution.

As a future endeavor, the implementation of a machine learning model based on the Random Forest Classifier algorithm is proposed. This model aims to facilitate the identification of categories and classes, enabling proactive classification of students, like the approach taken by Rojas Pari (2021) in identifying performance patterns. This approach seeks to effectively anticipate problematic situations, such as low grades or dropouts, with the goal of intervening and providing necessary support in early stages.

Acknowledgments. We appreciate the financial support from Universidad Internacional SEK.

References

Ashish, D., Maizatul, A.I., Tutut, H.: A systematic review on educational data mining. IEEE Access **5**, 15991–16005 (2017)

Beltrán, V.: Implementación de un Data Lake de los datos de uso del LMS Canvas de la Universidad Internacional SEK. Universidad Internacional Sek (2022)

Campbell, J., DeBlois, P., Oblinger, D.: Academic analytics: a new tool for a new era. Educause Rev. **42**(4), 40–57 (2007)

Cantabella, M., Martínez-España, R., Ayuso, B., Yáñez, J.A., Muñoz, A.: Analysis of student behavior in learning management systems through a big data framework. Futur. Gener. Comput. Syst. **90**, 262–272 (2019)

Cravero, A., Lefiguala, I., Tralma, R., Gonzalez, S.: Data Lake para la dirección de análisis universitaria: Arquitectura y Metadata. RISTI: Revista Ibérica de Sistemas e Tecnologias de Informação, Extra **41**, 560–569 (2021)

Dixon, J.: James Dixon's Blog. Pentaho, Hadoop, and Data Lakes (2010)

Dwivedi, K., & Dubey, S. K. (2014). Analytical review on Hadoop Distributed file system. *In 2014 5th International Conference-Confluence The Next Generation Information Technology Summit (Confluence)*, 174–181

Gewerc, A., Rodríguez-Groba, A., Martínez-Piñeiro, E.: Academic social networks and learning analytics to explore self-regulated learning: a case study. IEEE Revista Iberoamericana de Tecnologias Del Aprendizaje **11**(3), 159–166 (2016)

Kustitskaya, T.A., Esin, R.V., Kytmanov, A.A., Zykova, T.V.: Designing an education database in a higher education institution for the data-driven management of the educational process. Educ. Sci. **13**(9), 947 (2023)

Martinez-Mosquera, D., Beltrán, V., Riofrío-Luzcando, D., Carrión-Jumbo, J.: Data lake management for educational analysis. In: 2022 IEEE Sixth Ecuador Technical Chapters Meeting (ETCM), pp. 1–5 (2022)

Mazza, R., Dimitrova, V.: CourseVis: a graphical student monitoring tool for supporting instructors in web-based distance courses. Int. J. Hum. Comput. Stud. **65**(2), 125–139 (2007)

McClure, T.: Yesterday's unified storage is today's enterprise data lake. Yesterday's Unified Storage is Today's Enterprise Data Lake (2016)

Mitchell, J., Costello, S.: International e-VET market research report: a report on international market research for Australian VET online products and services (2000)

Oukhouya, L., El Haddadi, A., Er-raha, B., Asri, H., Laaz, N.: A proposed big data architecture using data lakes for education systems. Emerg. Trends Intell. Syst. Netw. Secur. 53–62 (2022)

Rojas Pari, R.J.: Modelo de Aprendizaje Automático Supervisado para Identificar Patrones de Bajo Rendimiento Académico en los Ingresantes al Instituto de Educación Superior Pedagógico Público–Juliaca. Universidad Peruana Unión (2021)

Romero, C., Ventura, S.: Educational data mining and learning analytics: an updated survey. Wiley Interdiscip. Rev. Data Min. Knowl. Discov. **10**(3) (2020)

Schröer, C., Kruse, F., Gómez, J.M.: A systematic literature review on applying CRISP-DM process model. Procedia Comput. Sci. 526–534 (2021)

Seeling, P.: Enabling open source, open data for closed source, closed data learning management systems. In: ACM Digital Library (Ed.), In Proceedings of the 23rd Annual Conference on Information Technology Education, pp. 124–126 (2022)

Sohan, S.M., Maurer, F., Anslow, C., Robillard, M.P.: A study of the effectiveness of usage examples in REST API documentation. In: 2017 IEEE Symposium on Visual Languages and Human-Centric Computing (VL/HCC), pp. 53–61 (2017)

Universidad Internacional SEK Ecuador. (2023). Universidad Internacional Sek

Xu, L., Cao, S.X., Ma, L.M.: A strategy of database project task based on the Crontab. Appl. Mech. Mater. **610**, 611–614 (2014)

Author Index

M. Z. Vizuete et al. (Eds.): CI3 2023, LNNS 1040, pp. 311–312, 2024.
https://doi.org/10.1007/978-3-031-63434-5